Luminescence properties of $Gd_2O_3:Bi^{3+}$ co-doped Ln^{3+} as powder and thin films phosphor for solar cell application

By

Mogahid Hassan Mohammed Abdelrehman

(MSc)

A thesis submitted in fulfilment of the requirements for the degree of

PHILOSOPHIAE DOCTOR

in the

Faculty of Natural and Agricultural Sciences

Department of Physics

at the

University of the Free State

Republic of South Africa

***Promoter**:* Prof. H. C. Swart

Co-Promoter: Prof. R. E. Kroon

Co-Promoter: Prof. Abdelrhman Yousif Mohmmed Ahmed

November (2021)

Acknowledgements

I would like to express my sincere gratitude to the following individuals and institutions without which this thesis would be impossible:

- My promoter Prof H. C. Swart, for being my supervisor for his mentorship, positive attitude, guidance and support throughout this study, and especially for his confidence in me. Thank you a lot.
- My co-promoter, Prof R. E. Kroon for the support and valuable inputs towards this study, suggestions and discussions. I am grateful.
- My co-promoter Prof. Abdelrhman Yousif Mohmmed for his assistance and fruitful discussions.
- Prof E. Coetsee-Hugo for her assistance in X-ray photoelectron spectroscopy measurements.
- Mr. L. J. B. Erasmus for his patience and assistance in photoluminescence measurements and his help with the pulsed laser deposition synthesis.
- Dr. Emad Hasabeldaim for assisting with cathodoluminescence degradation measurement.
- Mr. Edward Lee, for all his assistance with the field-emission scanning electron microscope measurements.
- Mr. Anthonie Fourie for taking care of the chemicals.
- Friends and colleagues (staff and students) in the Department of Physics at the University of the Free State for their positive and impactful attitude, and the wonderful time we spent together.
- I am indebted to my lovely family, my parents, brother and sister for their endless love and constant assistance throughout my life.
- National Research Foundation (NRF), South African Research Chairs Initiative (SARChI) chair and the University of the Free State for financial support.
- But above all, I would like to thank the Almighty Allah for everything that he has given to me, for his blessing and guidance to finish this work.

Abstract

The main aim of this project is to study the luminescence properties of $Gd_2O_3:Bi^{3+}$ co-doped Ln^{3+}(Yb^{3+} and Er^{3+}) phosphor powder and thin films to improve the energy conversion efficiency of photovoltaics (PV) by using the solar spectral conversion principle for use in solar cell applications.

The luminescence properties of $Gd_2O_3:Bi^{3+}$ single doped was investigated. The effect of different annealing temperatures and different concentrations of Bi^{3+} on the luminescence properties were investigated. The combustion method was used to synthesize all the powders samples. The optimum Bi^{3+} doping concentration was found to be x = 0.003 and the optimum annealing temperature was found to be 1000 °C (2 h). An increase in the average crystallite size with increasing annealing temperature and a decrease with an increase in Bi^{3+} doping concentration were obtained. The morphological studies showed small particles (less than 100 nm) that started to agglomerate to form bigger particles with sizes up to close to 400 nm during thermal treatment at higher temperature. Diffuse reflectance measurements of the pure host material showed absorption bands at 250, 275 and 315 nm that were attributed to the 4f-4f transitions of the Gd^{3+} ions. The bandgap was found to be influenced by the annealing temperature, which was determined to be 5.09 eV for the as prepared Gd_2O_3 host and then increased with increasing temperature. For all the doped samples the strong band at about 227 nm was observed corresponding to inter-band transitions of the Gd_2O_3 matrix in addition to three bands located around 260, 335, and 375 nm corresponding to the excitation transitions of Bi^{3+} ions into the different sites (C_2 and S_6). The luminescent properties of $Gd_{2-x}O_3:Bi_x$ phosphor powder were investigated and the fluorescence spectra show that the luminescence was stimulated by the emission from two types of centers which exhibited efficient blue-green emission bands. The excitation and emissions that correspond to the $^1S_0 \rightarrow {}^3P_1$ transitions in the Bi^{3+} ion depend on the presence of Bi^{3+} in the two different sites (S_6 and C_2) of Gd_2O_3. Significant changes in the thermoluminescence (TL) intensity for the different annealing temperatures and different dopant concentration in the Gd_2O_3 were observed. The TL glow curves of the UV-irradiated samples showed a low temperature peak at about 364 K and a high temperature peak at 443 K for all the samples. Auger electron spectroscopy (AES) was

employed to analyse the surface chemical composition of the powder at a vacuum base pressure of 1.3×10^{-8} Torr and after back-filling with O_2 to a pressure of 1.0×10^{-7} Torr. Simultaneous monitoring of the cathodoluminescence (CL) and AES peak-to-peak heights (APPHs) during prolonged electron bombardment in vacuum and O_2 over time for 40 h was done. The CL emission of Gd_2O_3:Bi powder was found to be stable under electron irradiation.

Thin films were successfully prepared using the pulsed laser deposition technique. $Gd_{2-x}O_3:Bi_{x=0.003}$ phosphor that was optimized for blue luminescence was deposited on Si (100) substrates in vacuum and an oxygen atmosphere at different substrate temperatures. The background atmosphere and substrate temperature were found to significantly affect the microstructure and luminescence of the thin films. The thicknesses for the thin films were relatively constant around 100 nm. The CL emission intensity degradation in a vacuum and an oxygen atmosphere was checked synchronously with the APPHs using the same electron beam for both measurements. The effect of the electron bombardment on the surface state of the samples was studied by using AES and X-ray photoelectron spectroscopy (XPS). All major elements (gadolinium and oxygen) were located, with additional carbon and chlorine that were removed during the early stages of electron bombardment. The CL intensity of the thin films with a blue-green emission was stable under electron bombardment.

The Gd_2O_3 materials based on the Bi^{3+},Yb^{3+} phosphor powders were investigated for possible improvement of the photovoltaic conversion efficiency via spectral modification, utilizing the down-conversion (DC) process. The optical bandgap of Gd_2O_3 increased with additional doping. The DC emission was obtained successfully from Yb^{3+} co-doped $Gd_{2-x}O_3:Bi_{x=0.003}$ samples. The visible emission has blue and green bands related to the Bi^{3+} in the S_6 and C_2 symmetry of Gd_2O_3. The near-infrared (NIR) of DC emissions were centered at 976 nm and less intense peaks centered around 950 nm, 1025 nm and 1065 nm caused by the crystal field Stark splitting of the $^2F_{5/2}$ and $^2F_{7/2}$ energy levels corresponding to the Yb^{3+}: $^2F_{5/2} \rightarrow {}^2F_{7/2}$ transitions after absorption of a single UV photon. It was observed that the visible Bi^{3+} emission gradually decreased with the addition of Yb^{3+} ion concentration while the NIR emission increased due to energy transfer from Bi^{3+} to Yb^{3+} ions. There was a strong increase in DC emissions with doping by adding of Bi^{3+} ions compared with the samples doped by Yb^{3+} ions.

Er^{3+} co-doped $Gd_{2-x}O_3$:$Bi_{x=0.003}$ was investigated for up-conversion (UC) processes for the possible use in applications for c-Si SCs. The 980 nm infrared excitation was successfully converted into visible (green-orange-red) emissions and was confirmed for Er^{3+} doped Gd_2O_3 samples with and without the presence of Bi^{3+}. There was an increase in the UC emissions with the addition of Bi^{3+} compared to the sample doped with single Er^{3+} ions due to the enhancement in Er^{3+} emission. The UC emissions were observed at 520, 537, 560, 670 and 870 nm and were assigned to the $^2H_{11/2}$, $^4S_{3/2}$, $^4F_{9/2}$ and $^4I_{9/2} \rightarrow {}^4I_{15/2}$ transitions of the Er^{3+} ion. The results showed that the presence of Bi^{3+} ions improved the UC emission of the Er^{3+} ions.

The effect of different concentrations of Yb^{3+} on the luminescence of Gd_2O_3:Bi^{3+}, Er^{3+} phosphor powder was investigated successfully. The structure and morphology of the surfaces revealed that the phosphors were affected by an increasing concentration of the Yb^{3+} ions. There was a decrease in the crystallite size with an increase in the Yb^{3+} doping concentration. The successful UC emission spectra of $Gd_{1.977-x}O_3$:$Bi_{0.003}$, $Er_{0.02}$, Yb_x ($x = 0.0$, 0.01, 0.03, 0.06, 0.09 and 0.12) were studied under 980 nm infrared excitation. The UC visible emission spectra consisted of a series of green, red and NIR emission bands at 520, 537, 550, 560 and 670 nm and are ascribed to the $^4F_{5/2}$, $^4F_{7/2}$, $^2H_{11/2}$, $^4S_{3/2}$ and $^4F_{9/2} \rightarrow {}^4I_{15/2}$ transitions of the Er^{3+} ions, respectively. The intensity of the UC emission of the green, red and NIR emission bands of the Gd_2O_3:Er^{3+} was dependent on the introduction of the Bi^{3+} and Yb^{3+} into the matrix. Co-doping by Bi^{3+} ions strongly enhancing the UC green emission, while co-doping with Yb^{3+} ions enhanced the UC red emission intensity. The intensity for both the visible emission spectra of Er^{3+} monitored by using a 379 nm excitation wavelength and CL at 5 keV exhibited a reduction in the intensity with an increase in the Yb^{3+} concentration due to the energy transfers from Er^{3+} to Yb^{3+} by cross-relaxation in contrast to the UC emission results. Under the excitation at 375 nm the emissions were centered at 418 nm corresponding to the $^3P_1 \rightarrow {}^1S_0$ transition of the Bi^{3+} ions and in addition the peaks mentioned earlier corresponding to the transitions of the Er^{3+} ions.

Our results indicated that the obtained phosphors might be possibly used for applications in displays, lighting and as a luminescence layer used to modify the solar spectrum with the aim of improving the efficiency of solar cells.

List of Abbreviations

Phosphor, powder, thin films, gadolinium oxide, bismuth, combustion method, pulsed laser deposition, down-conversion, up-conversion, annealing, photoluminescence and cathodoluminescence.

AES – Auger electron spectroscopy
APPH – Auger peak-to-peak heights
Bi^{3+} – trivalent bismuth
Bi_2O_3 – bismuth oxide
C – carbon
CL – cathodoluminescence
Cl – chlorine
CIE – Commission Internationale de l’Eclairage
CET cooperative energy transfer
c-Si – crystalline silicon
CT – charge transfer
CET – Cooperative energy transfer
CU – Cooperative upconversion
DC – down-conversion
DR – Diffuse reflectance
DS – down-shifting
Eg – band gap
EDS – energy dispersive x-ray spectroscopy
Er^{3+} – Erbium
ET – energy transfer
ETU – ET Upconversion
ESSCR – Electron stimulated surface chemical reaction
ESA – Excited-state absorption
e-h – electron-hole
FEDs – field emission displays
FWHM – full width at half maximum

Gd – gadolinium

Gd_2O_3 – gadolinium oxide

IR – infrared

JCPDS – Joint Committee on Powder Diffraction Standards

LED – light emitting diode

Ln^{3+} – lanthanide

MAUD – Material Analysis Using Diffraction

NIR – near-infrared

O^{2-} – oxygen

PL – photoluminescence

PV – photovoltaic

PLD – Pulsed laser deposition

PMT – Photomultiplier tube

QC – quantum cutting

RE – Rare earth

SHS – self-propagation high-temperature synthesis

SC – solar cell

SEM – Scanning electron microscopy

Si – Silicon

TL – Thermoluminescence

UC – up-conversion

UV – Ultraviolet

UV – Vis Ultraviolet-visible

Vis – Visible

XRD – X-ray diffraction

XPS – X-ray photoelectron spectroscopy

Yb^{3+} – Ytterbium

Table of Contents

Chapter 1

Chapter 2

Chapter 3

Chapter 4

Photoluminescence, thermoluminescence and cathodoluminescence of optimized cubic Gd_2O_3:Bi phosphor powder …..……………………………………………............................66

Chapter 5

Chapter 6

Chapter 7

Chapter 8

List of Figures

List of Tables

Chapter 1

Introduction

This chapter serves as the introductory chapter on a research study about the luminescent properties of the $Gd_2O_3:Bi^{3+}$ *co-doped with* Ln^{3+} *(*Yb^{3+} *and* Er^{3+}*) in the powder and thin film form for solar cell applications. It also includes the motivation for the objectives of the study and provides the layout of the thesis.*

1.1 General overview

Recently, there has been a growing interest in searching for alternative solutions to non-renewable energy for use in various energy fields. Utilizing solar energy is one of the most widely applied fields of sustainable energy and an excellent way to reduce dependence on non-renewable and unclean energy resources and provide the world with its increasing energy needs because the sun will continue to supply the earth with solar energy for the next billions of years. The amount of energy that comes from the sun to the earth is more energy than we can consume, therefore photovoltaic (PV) technology used in solar cells (SCs) was developed to take advantage of the sun's radiation to combat the energy crises we face today. The most commonly used SCs are based on c-Si crystalline Si [1]. Unfortunately, the Si SCs have low limiting photoelectric conversion efficiency that responds to a narrow range of the solar spectrum due to a mismatch between the solar spectrum and the silicon maximum absorption spectrum. The high energy photons are not used efficiently (thermalization loss). The energy loss in a SC is due to the thermalization of charge carriers generated by the absorption of the high energy photons. Also, photons with energy lower than the SCs band gap are not absorbed by the SC (transparency loss) [2]. Thus, the main problem is that the silicon SCs can only convert a small part of the solar radiation energy into electrical energy. The experimental efficiency of crystalline silicon PV cells is about 25.0% which absorbs photons efficiently in different wavelengths depending on the properties of the materials used in their fabrication [3]. Current interest in the SCs field is focused on the fabrication of phosphors materials and the improvement of their efficiency. To optimize the utilization of the SCs and reduces the spectrum mismatch loss and thermal conversion losses, both down-conversion (DC) (also known as quantum cutting (QC)) and up-conversion (UC) approaches by luminescence materials are proposed to adapt the solar spectrum for better use by the SC [4]. The DC occurs when a material is lightly photoexcited at a shorter wavelength (a high-energy photon) resulting in the re-emission of light with a longer wavelength (into two lower-energy photons) [5]. The UC occurs when the material is photoexcited with a longer wavelength (two or more absorbed lower-energy photons) resulting in light emission with shorter wavelengths (one high-energy photon) [6]. These concepts will be discussed in more detail in chapter 2. In general, the phosphor materials emit light at the visible wavelength range and absorb light of shorter wavelengths such as in the ultraviolet (UV) range. The luminescence is strongly dependent on the dopants and defects present in the material. Trivalent rare earth (RE^{3+}) ions with numerous energy levels by a diversity of 4f-4f transitions are good candidates for doping luminescent materials for emissions in various applications [7]. These ions have received more attention for developing of highly efficient photon conversion processes due to their special properties when incorporated into a host matrix with desirable properties including low lattice phonon energy, appropriate refractive index, and chemical stability among others. The phosphors co-doped by the RE^{3+} have been used in photon conversion processes to improve the efficiency of SCs. The broad spectral range and diversity of the 4f-4f transitions have made their use possible in both DC and UC [7]. All RE^{3+} ions can act as sensitizers or activators to be used in photon conversion processes. The transition metals can also be used in combination with the lanthanide ions as activators or sensitizers. Bi^{3+} ion is one of the most famous trivalent post-transition metal ions that can be used as an excellent sensitizer ion when combined with lanthanide ions so that it can significantly absorb ultraviolet light and transfer energy to other luminescent centers [8].

1.2 Motivation

Silicon PV devices are able to convert only a portion of the solar spectrum to electricity. Therefore, researchers and developers are still conducting a lot of research and experiments to develop SCs and to improve their efficiency by the photons conversion process by using UC and DC applications. Figure 1.1 shows the possibility that DC and UC can be used to optimize the use of the solar spectrum if it does not take into account any losses other than spectral mismatch losses. The cyan part shows the energy conversion of the absorbed part of the solar spectrum for a c-Si solar, while the green part shows the probability of extra energy conversion if every photon with $E > 2E_g$ results in 2 NIR photons by DC process and the red part shows the probability of energy gain if every pair of photons with $0.5E_g < E < E_g$ is converted to 1 higher energy photon by an UC process [9].

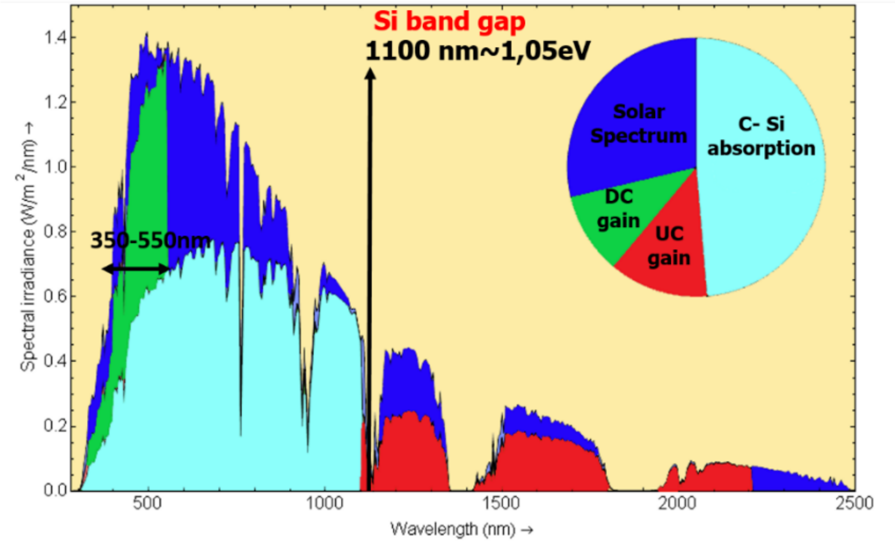

Figure 1.1: The potential gain for DC and UC for Si solar cell the cyan part shows the energy conversion of the absorbed part of the solar spectrum for a c-Si solar, the green part shows the probability of extra energy conversion by DC process and the red part the probability of energy gain by an UC process [10].

The Bi^{3+} ions with $6s^2$ electronic configuration can function as both an activator and a sensitizer for luminescent materials. Bi^{3+} provides a strong absorption of UV light, which can either be efficiently converted to longer wavelengths, which can be used (as an activator) or transfer energy to other luminescent centers, greatly enhancing the acceptable ion emission intensity. Thus, Bi^{3+} can be used as an excellent sensitizing ion. It has been demonstrated that the luminescence of Yb^{3+} [11], Nd^{3+} [12], Er^{3+} [13], Eu^{3+} [14] or Dy^{3+}, Ho^{3+} and Sm^{3+} [15] can be greatly enhanced through resonant energy transfer from Bi^{3+} to these ions. Amongst these ions, ytterbium (Yb^{3+}) is a unique rare-earth (RE) element with a +3 oxidation state that has shown great potential in enhancing the efficiency of crystalline silicon SCs. The Yb^{3+} emission can efficiently be absorbed by c-Si SC [16], because the luminescent quantum efficiency of Yb^{3+} approaching 100% and its unique emission from 900 to 1100 nm corresponds considerably with the bandgap of c-Si. Yb^{3+} has only two energy states, the $^2F_{7/2}$ ground state and $^2F_{5/2}$ excited state, separated by around 10,000 cm^{-1} which translates to emission at approximately 1000 nm [17], which makes it a highly effective ion to enhance the effectiveness of silicon SCs by a DC process without significant thermalization losses [18]. On the other hand, erbium (Er^{3+}) is one of the efficient RE ion candidates for UC luminescence processes due to its branched energy levels capable of pumping with infrared radiation. Since the fact that the $4f^n$ electron levels of Er^{3+} ion have dense energy levels present in a wide range of wavelengths from visible up to infrared, most of the UC research has also focused on excitation by infrared lasers by the 980 nm making it one of the most efficient ions for UC luminescence [19].

Luminescent materials nowadays have been used as the DC and UC layers for adapting the solar spectrum, to improve the silicon SC efficiency [20]. Trivalent rare earth oxides such as gadolinium oxide (Gd_2O_3) in comparison with other oxide materials have been the subject of great interest in optical properties and energy transfer that might exhibit good probability as a suitable host of the DC and UC mechanisms [21, 22]. Gd_2O_3 is a stable compound and has a 4f electron shell which makes its optical, chemical and electronic properties have high potential, which is suitable to work as a host of highly efficient optical transfer materials [11].

Luminescent materials used in applications can be found in various forms such as powders and thin films. Thin films are one of the most widely used forms of phosphor in SC applications due to their high quality electrical and luminescence properties compared with powder phosphors of the same composition [23]. Various techniques are often used to fabricate thin films such as electron-beam evaporation, sputtering, atomic layer deposition, H_2O-assisted atomic layer deposition, metal-organic chemical vapour deposition, sol-gel method, molecular beam epitaxy and pulsed laser deposition (PLD) [24]. Deposition techniques have an important role in controlling the properties of the film by changing the growth and deposition parameters, which is widely available in the PLD technique. Also the stability of the phosphor material is very important for the use in SCs applications. For the systematic investigation, we firstly investigated the luminescent properties of the Bi^{3+} ion single-doped Gd_2O_3 as a powder synthesized by the solution combustion synthesis and as thin films fabricated by the PLD technique and the stability of the phosphors under prolonged electron bombardment were investigated (see chapters 4 and 5), which emit blue-green luminescence and found to be generally stable under prolonged electron bombardment.

1.3 Research aim

To study, the luminescence properties of $Gd_2O_3:Bi^{3+}$ co-doped Ln^{3+} (mainly Yb^{3+} and Er^{3+}) phosphor as powder and thin films for possible DC and UC application in SCs.

1.4 The objectives of the study

- Prepare and characterize the $Gd_2O_3:Bi^{3+}$ phosphor powder by using the combustion methods.
- Study the luminescent properties and investigate the effect of heat treatment and dopant concentrations of the $Gd_2O_3:Bi^{3+}$ phosphor powder.
- Study the surface, chemical and the luminescence stability of the $Gd_2O_3:Bi^{3+}$ phosphor powder under prolonged electron beam irradiation.
- Prepare $Gd_2O_3:Bi^{3+}$ thin films by the PLD technique.
- Study the structure, morphology, chemical and luminescence stability properties of the films.
- Using different characterization techniques to investigate the luminescence of Ln^{3+} co-doped $Gd_2O_3:Bi$ phosphor powders for use in solar cell application namely; Yb^{3+} and Er^{3+} as DC and UC materials.
- To enhance the red luminescence of the $Gd_2O:Bi$, Er phosphors by co-doping with different concentrations of Yb^{3+} ions.

1.5 Thesis layout

This thesis is divided into eight chapters. Chapter 1 contains a brief introduction regarding the overview of the work and the aims of the study. Chapter 2 contains a brief background of the notions necessary to understand and explain the theoretical principles used in the study. The synthesis method and characterization techniques are covered and presented together with their principles in Chapter 3. Chapter 4 provides the study of photoluminescence, thermoluminescence and cathodoluminescence of Bi^{3+} ions in the Gd_2O_3 phosphor powder with different concentrations and different annealing temperatures. Also, the CL degradation of the phosphor was investigated. Chapter 5 focuses on photoluminescence, cathodoluminescence degradation and surface analysis of $Gd_{2-x}O_3:Bi_{x=0.003}$ PLD thin films including the study of the effect of the background atmosphere and different substrate temperatures on the thin films. Chapter 6 presents luminescence properties of Yb^{3+} and Er^{3+} co-doped into Gd_2O_3:Bi phosphor powder for use in solar cell application as DC and UC materials. Chapter 7 the effect of Yb^{3+} on the luminescence of Bi^{3+}/Er^{3+} co-doped Gd_2O_3 phosphor powder is presented. Chapter 8 gives the summary of the thesis results and suggestions for future work and also contains the publications and conference participation that followed from this thesis.

References

[1] B. S. Richards. Luminescent layers for enhanced silicon solar cell performance: Down-conversion. *Solar Energy Materials and Solar Cells,* **90(9)** (2006) 1189–1207. doi:10.1016/j.solmat.2005.07.001.

[2] P. Ramasamy, P. Manivasakan and J. Kim. Upconversion nanophosphors for solar cell applications. *Royal Society of Chemistry Advances.* **4(66)** (2014) 34873–34895. doi:10.1039/c4ra03919j.

[3] B. M. Van der Ende, L. Aarts, and A. Meijerink. Lanthanide ions as spectral converters for solar cells. *Physical Chemistry Chemical Physics*, **11(47)** (2009) 11081-11095. doi:10.1039/b913877c.

[5] X. Huang, S. Han, W. Huang and X. Liu. Enhancing solar cell efficiency: the search for luminescent materials as spectral converters. *Chemical Society Reviews,* **42(1)** (2013) 173–201. doi:10.1039/c2cs35288e.

[6] A. Ivaturi and H. Upadhyaya. Upconversion and Downconversion Processes for Photovoltaics. *A Comprehensive Guide to Solar Energy Systems,* **chapter 13** (2018) 279–298. doi:10.1016/b978-0-12-811479-7.00013-0.

[7] D. Li, W. Qin, P. Zhang, L. Wang, M. Lan, P. Shi. Efficient luminescence enhancement of $Gd_2O_3:Ln^{3+}$ (Ln = Yb/Er, Eu) NCs by codoping Zn^{2+} and Li^{+} inert ions. *Optical Materials Express*, **7(2)** (2017) 329–340. doi:10.1364/ome.7.000329.

[8] J. Xue, X. Wang, J. H. Jeong, X. Yan. Spectrum and Energy transfer in Bi^{3+}-Re^{n+} (n = 2, 3, 4) co-doped phosphors studies for extended optical applications. *Physical Chemistry Chemical Physics*. **20** (2018) 11516-11541. doi:10.1039/C8CP00433A.

[9] B. McKenna, R. C. Evans. Towards Efficient Spectral Converters through Materials Design for Luminescent Solar Devices. *Advanced Materials,* **29(28)** (2017) 16064911–160649123. doi:10.1002/adma.201606491.

[10] W. G. J. H. M. van Sark, A. Meijerink, R. E. I. Schropp. Solar spectrum conversion for photovoltaics using nanoparticles, in: Vasilis Fthenakis (Ed.), Third Generation Photovoltaics. *IntechOpen Limited, London, UK*, **Chapter 1** (2012) 1–28, doi:10.5772/39213.

[10] X. Y. Huang and Q. Y. Zhang. Near-infrared quantum cutting via cooperative energy transfer in $Gd_2O_3:Bi^{3+},Yb^{3+}$ phosphors. *Journal of Applied Physics,* **107(6)** (2010) 063505-063505-4. doi:10.1063/1.3354063.

[11] G.-X. Liu, R. Zhang, Q.-L. Xiao, S.-Y. Zou, W.-F. Peng, L.-W. Cao and J.-X. Meng. Efficient $Bi^{3+}\rightarrow Nd^{3+}$ energy transfer in $Gd_2O_3:Bi^{3+}$, Nd^{3+}. *Optical Materials,* **34(1)** (2011) 313–316. doi:10.1016/j.optmat.2011.09.003.

[12] S. K. Singh, K. Kumar and S. B. Rai. Optical properties and switching behavior in $Gd_2O_3:Er^{3+}$ nanophosphor. *Journal of Applied Physics*, **106(9)** (2009) 093520-093520-6. doi:10.1063/1.3259370.

[13] J. Fu, R. Pang, L. Jiang, Y. Jia, W. Sun, S. Zhang and C. Li. A novel dichromic self-referencing optical probe $SrO:Bi^{3+},Eu^{3+}$ for temperature spatially and temporally imaging. *Dalton Transactions*, **45(34)** (2016) 13317–13323. doi:10.1039/c6dt01552b.

[14] X. Y. Huang, J. X. Wang, D. C. Yu, S. Ye, Q. Y. Zhang and X. W. Sun. Spectral conversion for solar cell efficiency enhancement using $YVO_4:Bi^{3+}$, Ln^{3+} (Ln = Dy, Er, Ho, Eu, Sm, and Yb) phosphors. *Journal of Applied Physics*, **109(11)** (2011) 1135261- 1135267. doi:10.1063/1.3592889.

[15] D. Serrano, A. Braud, J.-L. Doualan, P. Camy, A. Benayad, V. Ménard, R. Moncorgé. Ytterbium sensitization in $KY_3F_{10}:Pr^{3+}$, Yb^{3+} for silicon solar cells efficiency enhancement. *Optical Materials*, **33(7)** (2011) 1028–1031. doi:10.1016/j.optmat.2010.07.023.

[16] E. Lee, R. E. Kroon, J. J. Terblans, H. C. Swart. Luminescence properties of $Y_2O_3:Bi^{3+},Yb^{3+}$ co-doped phosphor for application in solar cells. *Physica B: Condensed Matter*, **(535)** (2017) 102-105. doi:10.1016/j.physb.2017.06.072.

[17] J. J. Eilers, D. Biner, J. T. Van Wijngaarden, K. Krämer, H. Güdel, A. Meijerink. Efficient visible to infrared quantum cutting through downconversion with the Er^{3+}–Yb^{3+} couple in $Cs_3Y_2Br_9$. *Applied Physics Letters*, **96(15)** (2010) 151106/1-151106/3. doi:10.1063/1.3377909.

[18] G. Hai, L. Yunfeng, W. Dianyuan, Z. Weiping, Y. Min, L. Liren, X. Shangda. Blue upconversion of cubic $Gd_2O_3:Er$ produced by green laser. *Journal of Alloys and Compounds*, **376(1-2)** (2004) 0–27. doi:10.1016/j.jallcom.2003.12.020.

[19] R. M. Jafer, H. C. Swart, A. Yousif and E. Coetsee. The effect of different substrate temperatures on the structure and luminescence properties of $Y_2O_3:Bi^{3+}$ thin films. *Solid State Sci*, **53** (2016) 30–36. doi:10.1016/j.solidstatesciences.2016.01.005.

[20] Y. Zou, L. Tang, J.-L. Cai, L.-T. Lin, L.-W. Cao and J.-X. Meng. Combustion synthesis and luminescence of monoclinic $Gd_2O_3:Bi$ phosphors. *Journal of Luminescence*, **153** (2014) 210–214. doi:10.1016/j.jlumin.2014.03.02.

[21] S. Majeed and S. A. Shivashankar. Rapid, microwave-assisted synthesis of Gd_2O_3 and $Eu:Gd_2O_3$ nanocrystals: characterization, magnetic, optical and biological studies. *Journal of Materials Chemistry B*, **2(34)** (2014) 5585-5593. doi:10.1039/c4tb00763h.

[22] J. S. Bae, K. S. Shim, B. K. Moon, B. C. Choi, J. H. Jeong, S. Yi and J. H. Kim. Photoluminescence characteristics of $ZnGa_2O_{4-x}M_x:Mn^{2+}$ (M=S, Se) thin film phosphors grown by pulsed laser ablation. *Thin Solid Films*, **479(1-2)** (2005) 238–244. doi: 10.1016/j.tsf.2004.11.18.

[23] M. R. Byeon, E. H. Chung, J. P. Kim, T. E. Hong, J. S. Jin, E. D. Jeong, J. S. Bae, Y.D. Kim, S. Park, W. T. Oh, Y. S. Huh, S. J. Chang, S. B. Lee, I. H. Jung and J. Hwang. The effects for the deposition temperature onto the structural, compositional and optical properties of pulsed laser ablated Cu_2ZnSnS_4 thin films grown on soda lime glass substrates. *Thin Solid Films*, **546** (2013) 387-392. doi: 10.1016/j.tsf.2013.05.032.

Chapter 2

Background theory

This chapter presents a brief background of the notions necessary to understand and explain the theoretical principles used in this study.

2.1 Solar radiation

Recently, there has been a steadily increasing demand for energy in general and clean energy in particular, coupled with dwindling fossil fuel resources, increasing the need to move towards renewable energy supply technologies. Therefore, the use of energy from the sun is a sustainable and excellent way to reduce the dependence on non-renewable and unclean energy resources and provide the world with its increasing energy needs, because the sun will continue to supply the earth with solar energy for the next billions of years. Accordingly, it is expected that high-efficiency solar cell (SC) power generation can contribute significantly to the future of renewable energy to meet a large part of future energy consumption requirements [1]. A great deal of research has focused on improving the efficiency of SC by making better use of the spectrum coming from the sun via the photon conversion process and using the exploitation of the solar spectrum energy resource for global energy demand in the future. Generally, solar radiation is defined as the energy emitted by a distribution of electromagnetic waves emitted by the sun from a fusion reaction. The sun emits a nearly continuous spectrum extending from ultraviolet, visible, and infrared to electromagnetic radiation close to blackbody radiation with a temperature of about 5800 K [2]. However, it has been scientifically proven that the amount of solar energy that reaches the Earth within one hour is greater than the total human energy consumption during an entire year [3].

2.2 Solar cells

SCs are thin semiconductor devices that convert solar energy into useful electrical energy. The energy conversion consists of absorption of light (photon) energy-producing electron-hole pairs in a semiconductor and charge carrier separation. Once sunlight interacts with a solar cell, photons boost the electrons in the cell into a conduction band where these electrons can then be used to generate an electric current [2]. It is possible to make SCs from several different types of materials, of which crystalline silicon (c-Si) is the most popular with a market share of around 87% [4]. The c-Si is a semiconducting material with an indirect bandgap of about 1.12 eV. It can be doped with elements contributing fewer or more electrons than Si, producing p- or n-type silicon. The experimental efficiency of c-Si photovoltaic cells is about 25.0%. Such cells mostly absorbs photons efficiently in the near-infrared (NIR) region (E_g = 1.12 eV, 1000 nm) while they show very low spectral response in the short-wavelength range [5].

Luminescent materials have a significant role in the manufacture of the optical and electronic devices, some of which can also be used in the manufacture of SC and improve their efficiency. The energy of a photon is used to excite the electron from the valence band to the conduction band over a band gap in the semiconductor material used, leaving a hole caused by the absence of an electron behind, as illustrated in figure 2.1 [6]. A photon only needs more energy than that in the band gap to excite an electron from the valence band to the conduction band. A photon is absorbed, when its energy is given to an electron and "excites" it into the conduction band which leaves a hole. By collecting the holes and the electrons at the anode and the cathode and connecting the anode and cathode externally an electrical current will be generated.

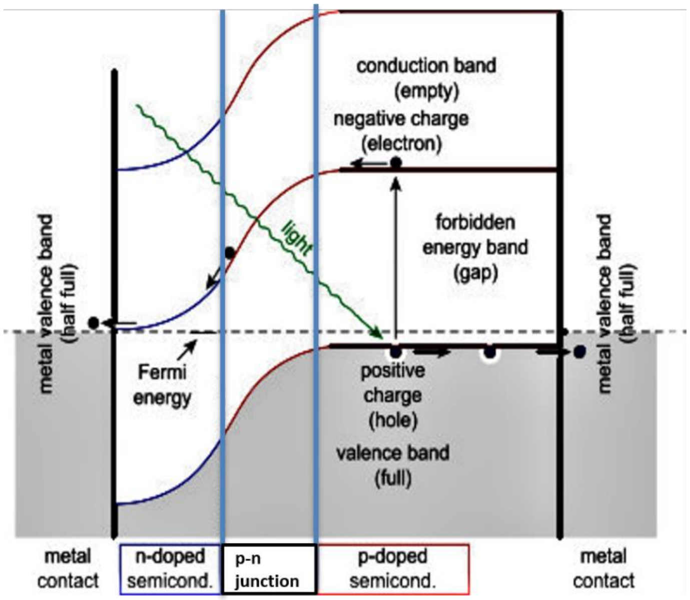

Figure 2.1: The process of absorption solar light and generating electrical current [6].

As the sunlight excites electrons in the region of the p-n junction, electrons with corresponding holes are seprerated. The free electrons are driven out by the electric field on the p-type side and hence move towards the p-type side as explained in figure 2.2. The region in which electrons and holes are scattered across the junction is called the depletion region because it practically does not contain mobile charge carriers.

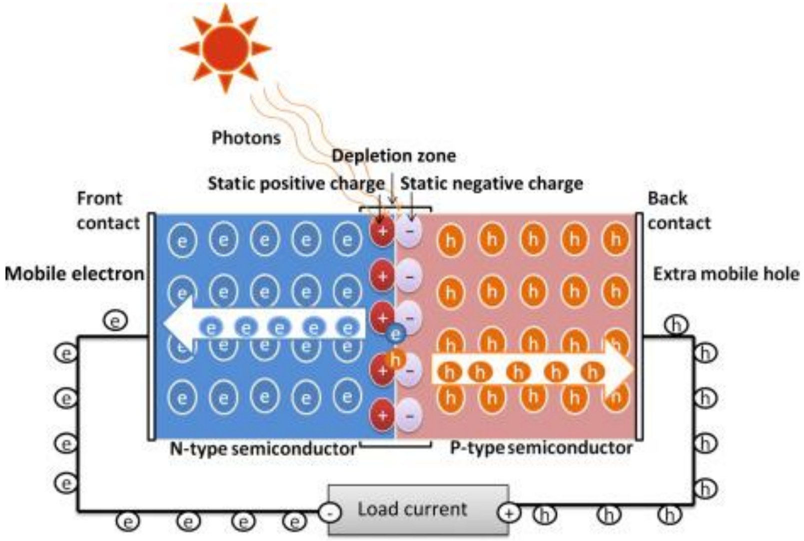

Figure 2.2: Schematic diagram showing the task of the P-N junction in the SC operation [7].

Much of the solar radiation that reaches the earth consists of photons with energies greater than the bandgap of Si that is mostly used in SCs. Normally the SC absorbs these high-energy photons, but unfortunately the difference in energy between these photons and the silicon bandgap is converted into heat (via lattice vibrations - called phonons) instead of being converted into usable electrical energy which is one of the reasons that limits the energy conversion effciency [6].

2.3 Solar cell conversion efficiency limits

The efficiency of SCs limits that part of the energy that comes from sunlight which the photovoltaic cells can convert into electricity. The maximum energy efficiency of a single-junction SC was already determined by Shockley and Queisser in the 1960s and is now referred to as the Shockley-Queisser limit (SQ) [8]. The calculated maximum theoretical efficiency of SC conversion is 86.8% for an array of an infinite number of cells, using incoming focused sunlight radiation, whereas the efficiency limit drops to 68.7% when the incoming radiation comes from an area in the sky the size of the sun [9]. The maximum conversion efficiency (η) of a SC is defined as the ratio of maximum power (P_m) generated by a SC to the incident power (P_{in}) [1]

$$\eta = \frac{P_m}{P_{in}} \qquad (2.1)$$

P_m is defined as the voltage at the point of maximum power (V_m) multiplied by the current at that point.

$$\eta = \frac{I_m V_m}{P_{in}} = \frac{I_{sc} V_{oc} FF}{P_{in}}, \qquad (2.2)$$

where J_{sc} and V_{oc} are the short-circuit current and open-circuit voltage, respectively. Low bandgap materials have high thermalization losses (giving low V_{oc} and V_m), whereas high bandgap materials have low I_m and I_{sc} due to their greater sub-bandgap losses [10]. FF is the fill factor describing the `squareness' of the IV curve. This factor is a measure of the quality of a SC [11].

$$FF = \frac{P_m}{V_{oc} I_{sc}} \quad (2.3)$$

The main reason for the low energy conversion efficiency is the mismatch between the energy distributions of photons in the incident solar spectrum, which reduces the spectral response of the Si SC [12]. Figure 2.3 represents the standard terrestrial solar spectrum and the fraction of the energy that is currently used by single-junction c-Si SCs. The regions that are not used and that are therefore available for conversion are also shown in the figure 2.3. Thus, SC efficiency can be improved by using spectral conversion, so we focus in the next paragraphs on this approach in more detail.

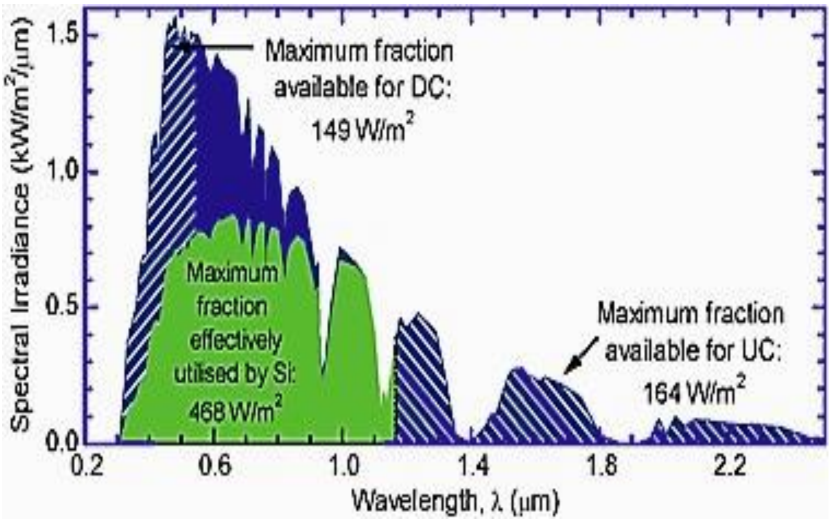

Figure 2.3: The terrestrial sunlight that is currently absorbed and effectively utilized by a thick crystalline silicon device and the additional regions of the spectrum that can contribute to up-or down conversion [1].

2.4 Photon conversion processes

The purpose of the photon conversion process is to adjust the solar spectrum to better match the absorption properties of the SC device by luminescence. As presented in figure 2.3 the solar spectrum consists of a wide range of photons with wavelengths varying between 300 to 2500 nm. Only photons with an energy equal to the bandgap of the SC can be used optimally in a single-junction photovoltaic device. As it is known, it is difficult to optimize the use of photons with higher and lower energy than the bandgap in the SC, so that the photons with higher energy lose a large part of their excess energy due to heat, while photons with lower energy than the bandgap are unable to create an electron-hole pair. To reduce spectral mismatch losses, the development of solar spectroscopic manipulation was urgently needed, thus the photon conversion processes are important options for application in such situations.

While down-shifting (DS) is a two-photon process, there are three-photon conversion processes, namely down-conversion (DC) and up-conversion (UC) shown in figure 2.4.

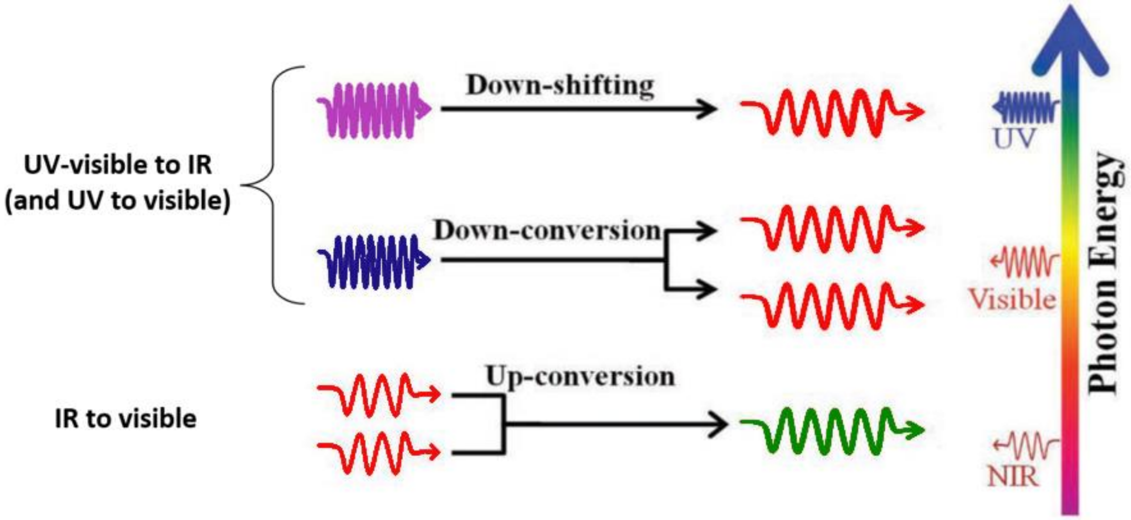

Figure 2.4: Schematic showing types of the photon conversion processes [13].

2.4.1 Down-shifting

The downshifting (DS) process is a direct optical method used to improve the short-wavelength response of a SC by converting a single photon of a higher energy into a single photon of lower energy. DS materials absorb the short-wavelength light, which is inefficiently absorbed by the photovoltaic material, and re-emit at a longer wavelength where the external quantum efficiency of the device is high, where it can be more efficiently absorbed by the SC. The ideal luminescent down-shifting material has a wide absorption band in the range of enhancement, high absorption coefficient, narrow emission band in the peak conversion efficiency region of the photoactive material, good separation between absorption and emission bands, and low cost [14]. In 1979, Hovel *et al.* [15] reported the first application of a DS layer on top of PV cells. Several research studies, both experimental and modeling, have been devoted to applying DS layers in different kinds of SCs. In a typical down-shifting process, upon excitation with a high-energy photon, nonradiative relaxation takes place followed by radiative relaxation, thereby resulting in the emission of a lower-energy photon. By properly adjusting the optical properties of the DS materials, it is possible to block UV radiation and convert it into radiation with a wavelength that spectrally matches the maximum of the external quantum efficiency of the device. This effect offers two benefits to the SC: first, the life of the device can be increased due to UV blocking or reduction, and second, the photo-generated current of the device is improved. Thus, because the short wavelength photons have lower spectral responses than the long wavelength photons, it is possible that DS offsets its lower quantum yield and enhances the efficiency of a solar cell [16]. Therefore, no change to the optimized electrical properties of the photovoltaic material is required. DS can give a marginal efficiency increase by shifting photons to a spectral region where the SC has higher efficiency, while DC and UC can raise the efficiency above the SQ limit [8]. In addition to the DS effect, DS layers strongly influence the front surface reflection. Hence, when designing DS layers, one takes into consideration the optical properties of the DS material so that it also acts as an anti-reflective coating.

2.4.2 Down-conversion

DC, also called quantum cutting (QC), is a luminescent conversion process that happens in a layer positioned on top of a SC. It occurs when a material is photoexcited at a shorter wavelength resulting in photoemission at a longer wavelength where a single photon gets absorbed to excite an electron to a higher energy level, and during the process for the system to return to the ground state two photons were emitted [17]. If the two photons could be absorbed by the SC and each produce electron-hole pairs, the quantum efficiency of short-wavelength light could nearly be doubled. Dexter [18] first proposed the theoretical possibility of DC in 1957. Experimentally, DC was first seen independently in 1974 by Piper *et al.* [19] and Somerdijk *et al.* [20] where the trivalent rare-earth praseodymium Pr^{3+} in a YF_3 host-material was used. For a typical industrial SC, photoluminescence would be useful if wavelengths shorter than approximately 500 nm could be converted into the 500-1000 nm range. Most of the systems that show DC consist of host materials doped with one or more active ions. For a silicon SC to benefit from DC, the following conditions should occur [21]:

- Excitation at wavelengths longer than 350 nm (high energy border of the solar-terrestrial spectrum).
- Excitation at wavelengths shorter than 550 nm for DC which 550 nm corresponds to twice the bandgap of silicon.
- Low excitation intensity (in the range of W/cm^2).
- Emission between 350 and 1100 nm.
- High quantum efficiency.

- Low absorption in the regions of the spectrum that will not be shifted or down-converted, since these wavelengths must be transmitted to the underlying SC.

Both DC and DS layers should be placed on top of a bifacial single-junction SC to convert the high energy photons to lower energy photons where the spectral response of the SC is high and also to minimize the thermalization loss [22]. Figure 2.5 shows the DC process where absorption of one high energy photon is “cut” into two lower energy photons. If the SC can absorb both lower energy photons, current doubling is achieved for the region of the solar spectrum [17].

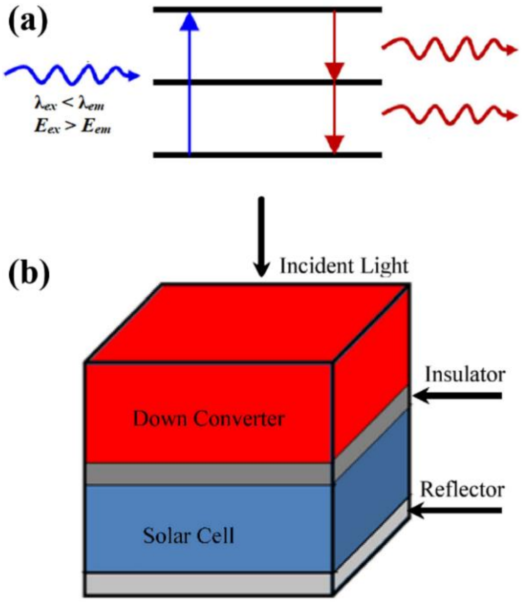

Figure 2.5: (a) Schematic showing the DC process and (b) schematic diagram of a solar cell with a down converter [23].

Different mechanisms that demonstrate NIR DC are illustrated in figure. 2.6. DC can occur with only one optically active center ion or with a combination of different ion centers. Figure 2.6(a) shows DC on a single ion A by the sequential emission of two visible photons, while figure 2.6(b-e) show the possibility of DC involving energy transfer (ET).

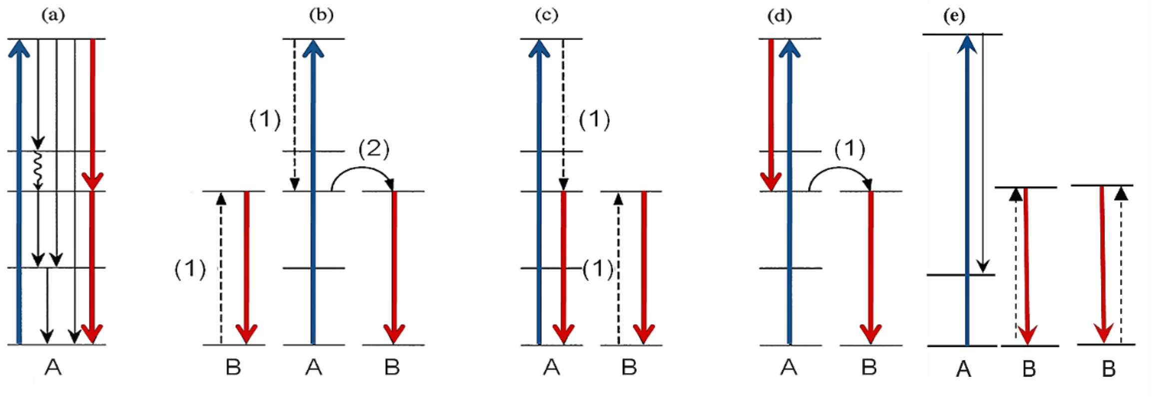

Figure 2.6: Schematic diagram of typical mechanisms of NIR DC. (a) DC on a single ion A by sequential emission of two photons. (b)-(d) DC by a pair of rare-earth ions via (partial) ET (resonant or not resonant) from ion A to ion B indicated by (1) and (2). (e) DC by single-step cooperative ET for ion A to 2 ions B (less efficient than sequential ET). Adapted from [1].

2.4.3 Up-conversion

UC occurs when a material is excited at a longer wavelength resulting in emission at a shorter wavelength. It refers to one higher energy photon being emitted for every two or more absorbed lower energy photons. The basic principle of UC is shown in figure 2.7. The sum of the energies of the absorbed photons must be greater or equal to the emitted photons energies. UC is an anti-Stokes process since Stokes law states that the wavelength of the emitted light should be longer than the wavelength of the exciting photon [1]. UC material could be placed behind a bi-facial SC to ‘up-convert sub-bandgap photons and then re-radiate these higher-energy photons back to the SC which they can be absorbed. The UC layer can be placed in the back of a SC and by converting a portion of the unabsorbed photons into absorbable wavelengths, it has a positive contribution to the efficiency [8]. Gibart et al. [24] reported the first application of UC on SCs in 1995. They applied a vitroceramic on a GaAs cell co-doped with trivalent erbium Er^{3+} and trivalent ytterbium Yb^{3+}. The first application of an up-converter into a silicon SC was reported by Shalav *et al.* [25] in 2003, where the trivalent rare-earth Er^{3+} in a $NaYF_4$ host material was used and was located on the rear side of a bifacial cell.

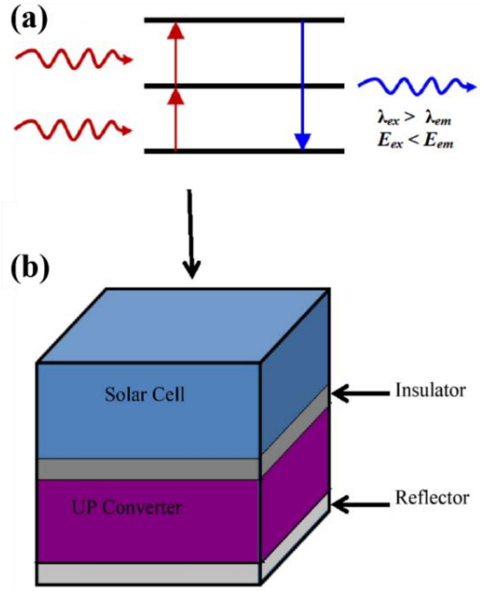

Figure 2.7: (a) Schematic showing the UC process and (b) schematic diagram of a solar cell with UP converter [23].

For a silicon SC to benefit from UC, the following conditions should occur [21]:

- High transmittance of the light that will excite up-conversion.
- The absorption range UC should be higher than 1100 nm ($E < 1.2$ eV, the band gap of silicon).
- Low excitation intensity (range of W/cm^2)
- The emission wavelength is shorter than 1100 nm.
- High UC efficiency.

The process of UC can occur through either a single or a combination of several mechanisms as shown in figure 2.8:

a) Excited-state absorption (ESA): Two low-energy photons excite an ion to a higher energy level and emit one high-energy photon when the ions transition to the ground state.
b) ET Upconversion (ETU): A transfer of energy between two rare-earth ions, culminating in the release of high-energy photons.
c) There are two mechanisms:

1. Photon Avalanche (PA): A combination of the previous two mechanisms culminating in the release of several high-energy photons. The PA is a scarce process due to the need for high pumping intensity. PA starts with the population of the intermediate excited state,

followed by the population of higher energy levels through resonant ESA. After the metastable level population is finished, cross-relaxation energy transfer occurs between the excited ion and a neighboring ground-state ion, resulting in both ions occupying the intermediate levels. Thus the higher energy levels could be populated considerably, resulting in bright UC emission through radiation.

2. Cooperative upconversion (CU): Two ions in their excited state simultaneously decay to their ground states, generating a higher energy photon. Similarly, in cooperative luminescence, two excited state ions transfer their energy to a neighboring ion in one elementary step.

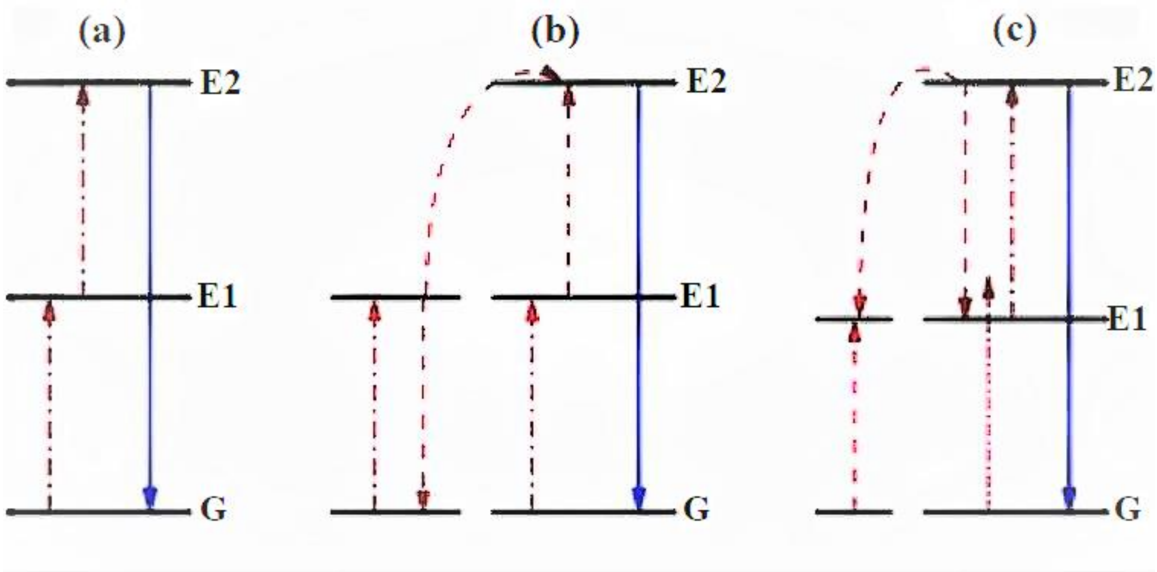

Figure 2.8: Schematic illustrating the different mechanisms for UC. (a) Excited-state absorption, (b) ET UC and (c) cooperative UC [4].

Spectral conversion design for PV applications involving (DS), DC, and (UC) luminescent materials are shown in figure 2.9. In a typical downshifting process, upon excitation with a high-energy photon, nonradiative relaxation takes place followed by radiative relaxation, thereby resulting in the emission of a lower-energy photon. In contrast, two-step radiative relaxation occurs in the DC process upon excitation with a high-energy photon, leading to the emission of two (or more) lower-energy photons. The UC process can convert two (or more) incident low-energy photons into a single higher-energy photon. Both DS and DC processes can make effective use of the high-energy portion of the solar spectrum, but with dramatically different quantum efficiency. Note that the DS and DC materials are generally placed on the front surface of a monofacial SC, allowing the downconverted photons to be absorbed by the SC. The UC material is typically placed in between a bifacial SC and a light-reflection layer to harvest the sub-bandgap spectrum of sunlight.

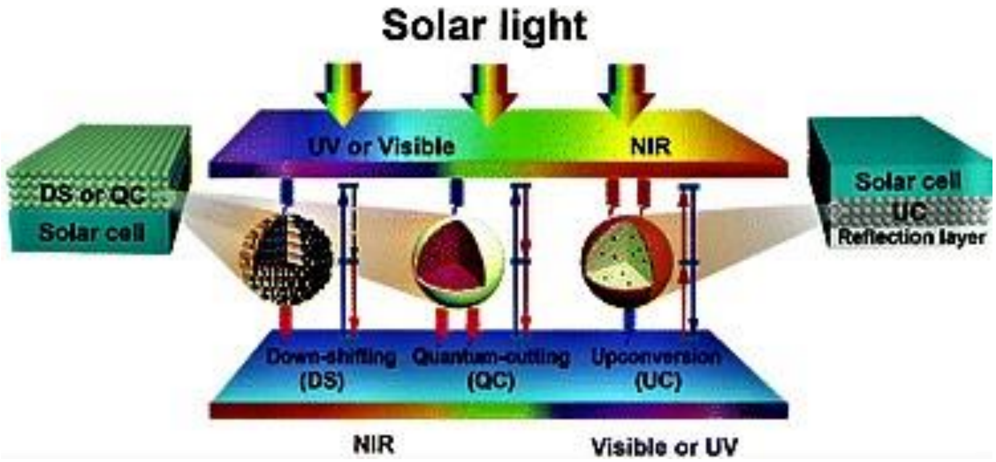

Figure 2.9: Spectral conversion design for PV applications including downshifting (DS), down-conversion (DC) and up-conversion (UC) luminescent materials [2].

2.5 Energy transfer

ET in phosphors involves the interaction between two luminescent centers, which is a process where the excitation energy is absorbed by a luminescent center (sensitizer) which is called a donor and then transferred to another luminescent center (activator) which is called an acceptor. To make the ET processes efficient, the donor (D) emission should overlap with the acceptor (A) absorption. When the overlap between them is absent, the cooperative ET (CET) may occur, in which a donor excites two acceptors simultaneously [26]. ET can play an important role to enhance the emission of phosphors by enhancing the luminescence efficiency. ET between a donor ion and an acceptor ion can be written as [27]:

$$D^* + A \rightarrow D + A^* \qquad (2.4)$$

where D and A represent the ground states of donor and acceptor respectively, while D* and A* represent their excited states. There are different mechanisms involved in the ET processes between two ions namely [28]:

- Resonant radiative transfer through the emission of the donor and reabsorption by the acceptor
- Non-radiative transfer associated with the resonance between the absorber and emitter
- Phonon-assisted ET
- Cross-relaxation between two identical ions.

The ET can be classified into two types [29]:

- Direct ET where the energy is transferred directly from the donor to the acceptor,
- Indirect ET which the energy is transferred to the acceptor after multistep diffusion among the donors.

The non-radiative ET process can be explained by two phenomena, namely Dexter exchange and Förster resonance.

Dexter ET: which is called the exchange interaction mechanism, relies on the overlap of the wave function and thus only exists over very short distances where the donor and acceptor orbitals must overlap with each other [30].

Förster ET: which called the multipolar interaction, depends on the strength of the optical transitions involved and can occur over relatively large distances, where energy from the donor is transferred to the acceptor through a long-range coloumbic interaction, typically a dipole-dipole interaction or more generally multipole interaction [31].

ET can only occur if the energy differences between the ground states and the excited states of D and A are equal and if there is an appropriate interaction (such as spectral or wavefunction overlap) between centers. The rate of ET from a donor to an acceptor is generally approximated as follows [32]:

$$W_{DA} = \frac{2\pi}{\hbar} |< DA^*|H_{DA}|D^*A >|^2 \int F_D(E)F_A(E)dE \qquad (2.5)$$

where DA^* is the final state, D^*A is the initial state, H_{DA} is the interaction Hamiltonian and the overlap integral reflects the requirement of energy conservation. The integral represents the spectral overlap between the donor (D) emission spectrum and the acceptor (A) absorption spectrum (see figure 2.10). The factors $F_D(E)$ and $F_A(E)$ represents the normalized shape of the donor's emission and acceptor's absorption spectra, respectively.

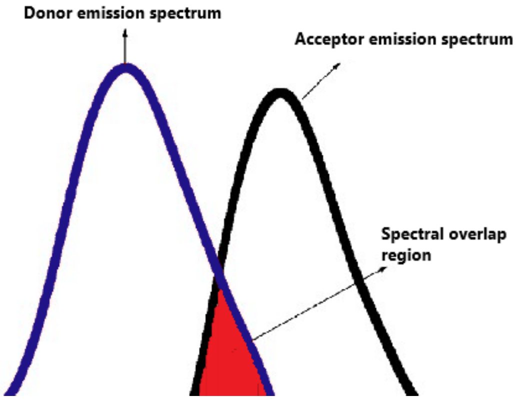

Figure 2.10: The spectral overlap between the donor (D) emission spectrum and the acceptor (A) absorption spectrum [33].

The square of the matrix element is expressed in Equation 2.5 in terms of the ET probability dependent on the distance between the donor and the acceptor. The dependence of the transfer rate on the distance varies with the type of reaction. The dependence of the transfer rate on the distance R depends on the type of interaction [3]. For electric multipolar interaction, the distance dependence is given by R^{-n} (n = 6, 8, …for electric-dipole electric-dipole interaction, electric-dipole electric quadrupole interaction, …). For the exchange interaction, the distance dependence is exponential, since it requires overlap of the wave functions.

2.6 Luminescent materials

Luminescence is the general term for light radiation (from ultraviolet to infrared) that is emitted from materials when exposed to an external energy excitation. So luminescent materials, also known as phosphors, can be defined as any material that will give or emit light (red, green and blue) when an external electromagnetic radiation excitation source is applied (photons, heat, etc.)

[34]. Luminescence can occur from inorganic or organic hosts. The inorganic hosts in some cases can emit due to some characteristics related to the host itself like the existence of vacancies or defects. Luminescence can be generated from different excitation sources, including photons, electromagnetic radiations, electric fields, X-rays, etc. The excitation source type can determine the type of the luminescence, which is generally indicated by a prefix, i.e. in the case of where the excitation source is photons, this luminescence is called photoluminescence (PL). The electron gets excited from its ground state (lowest energy level) to an excited state (higher energy level) when an excitation source is applied into a luminescent material. Then when it relaxes again to the ground state, it releases the energy absorbed (that caused it to become excited) in the form of a photon [12].

Luminescence is divided into two categories, namely fluorescence and phosphorescence, depending on the nature of the excited state and regarding the lifetimes, namely fluorescence and phosphorescence [33]. The emission rate of fluorescence is fast, typically 10^8 s^{-1}, so that a typical fluorescence lifetime is near 10 ns. Phosphorescence emission arises from triplet excitation states in which the electron in the excited state has the same spin orientation as the ground state electron. Such transitions are forbidden, and the emission rates are slow [1].

Generally, the luminescent materials (phosphors) maybe exists either in the form of a powder or a thin film with specific requirements on the particle size distribution and morphology [35]. The phosphors consist of one chemical compound referred to as a host lattice, and one or more activators (dopants), mostly rare-earth ions or transition metals, in amounts from parts per million to a few mole percent. These impurities are introduced intentionally in a host lattice to serve as luminescent (light-emitting) centers. If more than one activator is used during excitation, they are called co-activators or co-dopants, as one activator (sensitizer) tends to absorb energy from the primary excitation and transmits it to the other activator to enhance its luminescent intensity [34].

2.7 Host lattice

A host is regarded as the "home" of the optically active ions. The phosphor host or matrix is usually an insulator or a semiconductor, which should exhibit good optical, mechanical and thermal properties [33]. The host is necessary to optimize the distribution of the activators and prevent the occurrence of rapid non-radiative processes. The dopant ions substitutionally replace the host ions in the host lattice [37]. Many types of the host can be classified into several main types based on the anions such as simple oxides, chlorides, iodides, bromides and sulfides, or more complex hosts such as aluminates, fluorides, borates, silicates, etc [34]. Host materials can be categorized into three groups based on crystallinity: crystals, amorphous materials and hosts that incorporate the properties of both (glass-ceramics). In this project gadolinium oxide (Gd_2O_3) was used as a host matrix.

Recently trivalent rare earth oxides such as Gd_2O_3 has been the subject of intense research due to its optical properties, chemical and electronic characteristics resulting from the 4f electronic shell, where it works as a highly efficient optical transducer [38]. Like most rare earth oxides, it is an attractive candidate in optical applications due to its qualities such as high dielectric constant, good thermal stability and wide-band gaps of over 5 eV [39]. Further, has excellent physical and chemical properties, exhibiting optical properties typical of an insulator.

Some of the main properties of Gd_2O_3 are stated below [40]:

- The Gd_2O_3 powder appears white.
- Gd_2O_3 as a powder can be found in nano or micron form.
- It has high thermal conductivity (0.1 $Wcm^{-1}K^{-1}$) and a high dielectric constant (~ 16).
- The density of Gd_2O_3 is 7.407 g/cm^3.
- It is slightly hygroscopic.
- It is not soluble in water, but slightly soluble in strong mineral acids and produces the corresponding salt.
- The melting point of Gd_2O_3 powder is 2,420 °C.
- It has a wide bandgap of 5.2 eV [39].
- Although often grouped with the cubic rare earth oxides, Gd_2O_3 may also be found in the monoclinic or hexagonal phase under ambient conditions which the phase may depend on the synthesis conditions [39].

To date, different morphologies of various sizes, dimensions and structures such as nanoparticles, nanotubes, spheres, curved rods and plates of Gd_2O_3 have been fabricated by a variety of methods. Gd_2O_3 synthesis has been reported by many researchers due to potential applications of this material in several forms for example: solid-state reaction [38], combustion synthesis [42], sol–gel processes [43], co-precipitation [44], solvothermal reaction [45], hydrothermal routines [46], flame-spray pyrolysis [47], magnetron sputtering [48], spray pyrolysis [49], polyol [50], hydrogen flame pyrolysis, non-hydrolytic high temperature, aerosol routines, molten salts routes, chemical vapour deposition and pulsed laser deposition [51].

In this project, Gd_2O_3 phosphor powders were prepared using an urea-nitrate solution combustion synthesis (see chapter 3). Generally, Gd_2O_3 at room temperature up to 1200 °C will form as the cubic structure which is more stable. The phase change to the monoclinic structure takes place at 1200 °C. Above 2100 °C to the melting point at 2420 °C, a hexagonal phase dominates [52]. Our as-prepared Gd_2O_3 samples were annealed in air at various temperatures (800 to 1200 °C) for 2 h. The X-ray diffraction patterns indicated that a single-phase cubic crystal structure with the $Ia\overline{3}$ the space group was formed. In this study, it was drawn by using the Vesta program [53] as shown in figure 2.11. The cubic phase of Gd_2O_3 has two types of Gd sites, each with a coordination number of 6 but with different coordination geometries [54]. In the unit cell are 8 centrosymmetric sites with a S_6 symmetry which are octahedrally coordinated with six oxygen atoms and another 24 non-centrosymmetric sites with a C_2 symmetry which have four shorter and two longer bonds with O.

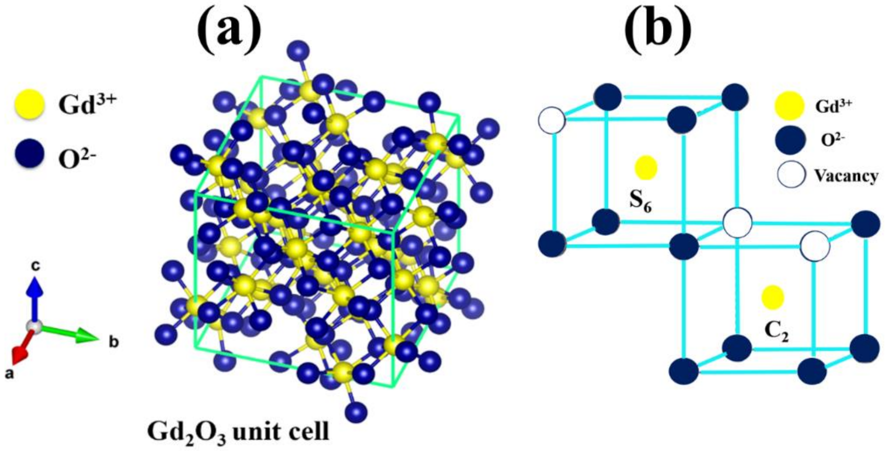

Figure. 2.11: (a) Crystal structure of unit cell of cubic phase Gd_2O_3. Gadolinium is represented by the blue color and oxygen with the yellow color spheres. (b) Crystallographic sites in the Gd_2O_3 crystal structure (C_2 site with non-inversion symmetry and S_6 site with inversion symmetry) are also shown.

Gd_2O_3 is suitable for rare earth oxide materials that emit UV regions up to NIR regions and has received considerable attention for different applications. Therefore, Gd_2O_3 is an excellent host matrix for luminescence material applications when doped with rare-earth ions used to produce DC or UC emissions, due to its ability to emit visible or ultraviolet light with subsequent excitation with near-infrared via the multiphoton process.

2.8 Activators (Luminescence centers)

An activator is a foreign ion added as a dopant to the crystal of the material to create the desired type of inhomogeneities or a structural defect that forms the heart of the phosphor material, which emits light when energy has been absorbed [32]. In inorganic phosphors, these inhomogeneities in the crystal structure are usually created by the addition of a trace amount as an optimal concentration of dopants incorporated intentionally into a host lattice. The wavelength emitted from the emission center depends on the atom itself, its electronic configuration and the surrounding crystal structure. The distribution of the activator in the crystal is also of great importance [33]. Ion diffusion can deplete the crystal from doping resulting in loss of efficiency. The luminescence process in the materials is due to the structure of the electronic band present in the crystals. The appropriate luminescent center can be selected according to the emission color, ionic valence, atomic radius and light output efficiency. There are many types of luminescent centers in inorganic phosphors such as:

- *Structural defects*: The defects in the inorganic phosphors contain vacancies, impurities, radical impurities, donor-acceptor pairs, etc which may create charge imbalances at the defect sites. The charge imbalances should be rectified by the localization of electrons and electron holes or give rise to impurity states within the bandgap. Therefore, the defect sites are apparently the precursors for various centers containing the emission center for defect-related luminescent materials and impart them with excellent photo-luminescent emission [55].
- *Transition metal ions*: a transition metal is an element whose atom has a partially filled d subshell, or which can give rise to cations with an incomplete d subshell. Some of the more well-known transitional metals include manganese (Mn^{2+}), copper (Cu^{2+}), chromium (Cr^{3+}).
- *Ions with an s^2 outer shell*: e.g. Thallium (Tl^{+}), lead (Pb^{2+}) and bismuth (Bi^{3+}).
- *Lanthanide ions:* e.g. ytterbium (Yb^{3+}), erbium (Er^{3+}) and europium (Eu^{3+}).

2.8.1 Ions with an s^2 outer shell

Several heavy metallic impurity ions in groups IIIB, IVB, and VB are multivalent ions, which act as luminescent centers in many materials [56]. The heavy metal 6p group is Tl, Pb, Bi and the 5p group is In, Sn, Sb. These ions in their ground states all have the outer electronic configuration of ns^2 and are therefore called ns^2 ions. These metallic impurities with an outer ns^2 configuration ground state may be excellent luminescence activators that are easily introduced in host materials to produce phosphors for different applications [57]. The Bi element is one of these elements with outermost $6s^2$ electrons, which was used in this research study as the luminescent center.

Bismuth (Bi) has an atomic number of 83 situated between the transition metals and metalloids. Bi belongs to the fifth major group of the periodic table and is the heaviest element in this group with an atomic weight of 208.98 amu, and it is also the most naturally diamagnetic element and has one of the lowest values of thermal conductivity among metals [58]. Bi is environmentally friendly since its toxicity is negligible as well as non-radioactive and it has a relatively low melting point of 271 °C and low mechanical strength: compared to the transition metals it is brittle or soft [59]. Bi atoms have an electronic configuration [Xe] $4f^{14}5d^{10}6s^{2}2p^{3}$ and have a large number of valence states (e.g. +3, +2, +1, 0, -2, etc.) in different materials [60]. Bi^{+} exhibit a broad emission in the near-infrared region. Bi^{2+} shows strong red-orange emission while Bi^{3+} emits strongly in the UV to green region depending on the surrounding structured environment [34]. The most stable state being the Bi^{3+} state and depending on its valance state bismuth may exhibit different luminescence properties. In this research study, the focus of investigations is the luminescence properties of Bi^{3+} doped Gd_2O_3 that can act as an activator or a sensitizer in phosphor materials. Bi^{3+} ions have been widely used as activators for various host materials including oxides, phosphates, aluminates and borates [27]. Bi^{3+} ions have a ground state electronic configuration of $6s^2$ corresponding to energy level $^1S_0$, while the excited 6s6p configuration is comprised of four levels: a triplet ($^3P_0$, $^3P_1$ and $^3P_2$) and singlet ($^1P_1$). Absorption bands of Bi^{3+} are usually attributed to $^1S_0 \rightarrow {}^3P_1$ and $^1S_0 \rightarrow {}^1P_1$ transitions, although the latter may often lie at very short inaccessible wavelengths. The position and the splitting of the emitting $^3P_1$ level are sensitive to the surrounding lattice, resulting in the band profile and peak wavelength of Bi^{3+} emission varying appreciably in different hosts. The emission from Bi^{3+} activated phosphors is usually ascribed to the $^3P_1 \rightarrow {}^1S_0$

transition. This is because of spin-orbit coupling between the $^1P_1$ and $^3P_1$ levels to make the lower energy transition $^1S_0 \leftrightarrow ^3P_1$ possible [34].

2.8.2 Lanthanides ions (Ln^{3+})

The lanthanides (Ln^{3+}) are a group of 15 chemical elements, with atomic numbers from La (Z = 57) to Lu (Z = 71). They are called lanthanides because they exhibit similar chemical properties to lanthanum, the first element in the group. They are called 4f elements because all the lanthanide series are the group of elements that have incompletely filled 4f subshells, which is important in the optical and magnetic properties of the lanthanides [61]. Trivalent RE ions emit almost as free ions, that is, they exhibit intense narrow-band intra−4f luminescence in a large variety of hosts. The $4f^n$ electrons are primarily responsible for the optical properties of the rare earth ions. The trivalent form of the lanthanide (Ln^{3+}) ions has an electronic configuration of $4f^n5s^25p^6$ where n is the number of electrons (from 0 to 14) as given in table 2.1.

Table 2.1: The ground-state electron configurations of the lanthanides.

Name of element	Symbol	Atomic number	Electron configuration		Valence
			The ground state electron configuration	Trivalent ion	
Lanthanum	La	57	$[Xe]5d^1 6s^2$	$4f^0$	3
Cerium	Ce	58	$[Xe]4f^1 5d^1 6s^2$	$4f^1$	3,4
Praseodymium	Pr	59	$[Xe]4f^3 6s^2$	$4f^2$	3
Neodymium	Nd	60	$[Xe]4f^4 6s^2$	$4f^3$	3
Promethium	Pm	61	$[Xe]4f^5 6s^2$	$4f^4$	3
Samarium	Sm	62	$[Xe]4f^6 6s^2$	$4f^5$	2,3
Europium	Eu	63	$[Xe]4f^7 6s^2$	$4f^6$	2,3
Gadolinium	Gd	64	$[Xe]4f^7 5d^1 6s^2$	$4f^7$	3
Terbium	Tb	65	$[Xe]4f^9 6s^2$	$4f^8$	2,3
Dysprosium	Dy	66	$[Xe]4f^{10} 6s^2$	$4f^9$	2,3
Holmium	Ho	67	$[Xe]4f^{11} 6s^2$	$4f^{10}$	3
Erbium	Er	68	$[Xe]4f^{12} 6s^2$	$4f^{11}$	3
Thulium	Tm	69	$[Xe]4f^{13} 6s^2$	$4f^{12}$	3
Ytterbium	Yb	70	$[Xe]4f^{14} 6s^2$	$4f^{13}$	2,3
Lutetium	Lu	71	$[Xe]4f^{14} 5d^1 6s^2$	$4f^{14}$	3

The portion of the Ln^{3+} configuration that is equivalent to the noble gas of the preceding period, is abbreviated as [Xe]. For atoms with many electrons, this notation can become lengthy and so an abbreviated notation is used. This is important as it is the valence electrons in the outermost shell that determine the chemical properties of the element. The ground-state electron configuration of the lanthanide elements is generally of the type [Xe] $4f^n6s^2$ [58]. La is outside this generalization but is included in the table for its uniform trivalency and other similarities. Among the lanthanides, exceptions to the $4f^n5d^06s^2$ pattern are found in three cases. In Ce, where the increase in effective nuclear charge after La is insufficient to stabilize the $4f^2$ $5d^0$ configuration compared to $4f^1$ $5d^1$. The nuclear charge is insufficient to hold 4f orbitals and reduce their energy below 5d. Also, Gd has the $4f^7$ $5d^1$ configuration, consistent with our expectation of a stabilized half-filled f shell. This means that the additional electron in Gd does not enter 4f-orbital but it goes to 5d level. This is because the 4f and 5d orbital in Gd are at about the same energy level and the Gd atom tends to retain the configuration with half-filled 4f-levels which are relatively more stable. Lu also has the $4f^{14}$ $5d^1$ configuration where the last electron is added beyond the capacity of the 4f shell. Dieke *et al.* [62] investigated the energy levels of 4f electrons of trivalent lanthanide ions. They showed their results in a diagram known as the Dieke diagram which is presented in figure 2.12 [63].

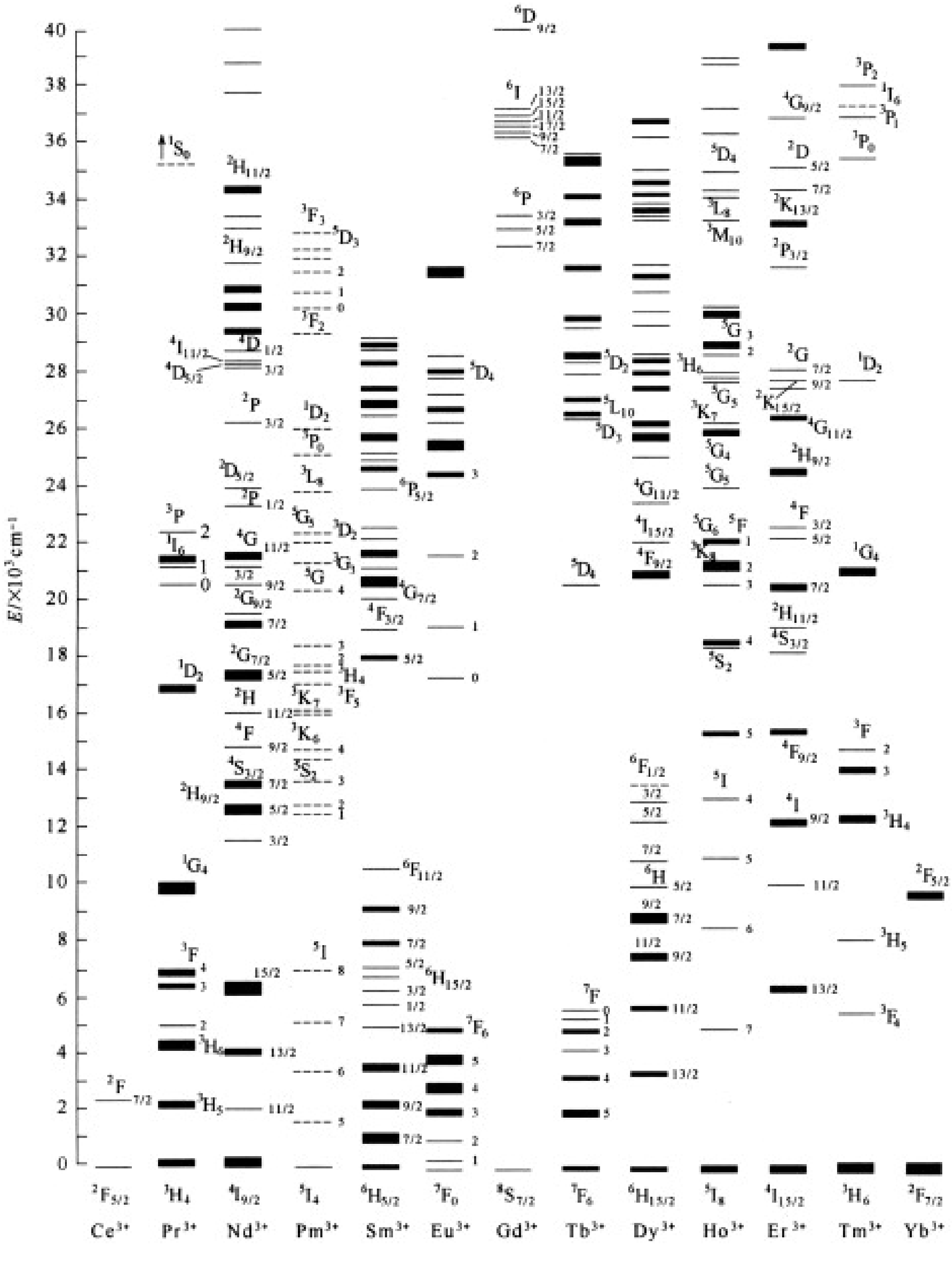

Figure 2.12: The Dieke diagram [63]

2.8.2.1 Ytterbium

Ytterbium (Yb) is a rare-earth chemical element with an atomic number of 70. It is the fourteenth and penultimate element in the lanthanide series, with an atomic weight of 173.045 amu [58]. With a melting point of 824 °C and a boiling point of 1196 °C, ytterbium has the smallest liquid range of all the metals [64]. Like other lanthanides, ytterbium is commonly found in the +3 state, and its salts in this oxidation state are nearly colorless [62]. Yb^{3+} has a closed-shell electron configuration ([Xe] $4f^{14}$ $6s^2$), which causes only the two 6s electrons to be available for metallic bonding (in contrast to the other lanthanides where three electrons are available) and increases ytterbium's metallic radius [61]. This means that Yb^{3+} has only two energy states: a $^2F_{7/2}$ ground state and a $^2F_{5/2}$ excited state where the two states are separated by approximately 10 000 cm^{-1} [55]. In contrast to other RE^{3+} ions with a narrow absorption band, the Yb^{3+} ions display a rather broad near-infrared absorption band between 870 nm to 1050 nm which makes it a highly efficient ion to improve the efficiency of silicon SCs [65]. Another well-known feature of Yb^{3+} is the simplicity of its energy level diagram, high quantum efficiency, high energy storage, and high doping ability [66]. Its simple energy level structure in principle prevents the existence of many de-excitation processes that can affect the dynamics of energy level groups as in other rare-earth ions with a more complex electronic structure, such as excited-state absorption, relaxation, or conversion within a system of active ions [67]. When Yb^{3+} ions are placed into the appropriate host lattice, the electrostatic interaction between the host lattice's crystal field and the ion causes a phenomenon known as Stark splitting. The Stark effect is the shifting and splitting of spectral lines of atoms and molecules due to the presence of an external electric field. The Stark splitting splits the ground state of Yb^{3+} into 4 sub-levels (Z_1, Z_2, Z_3, Z_4) and the excited state is split into 3 sub-levels (A_1, A_2, A_3) shown in figure 2.13 [68].

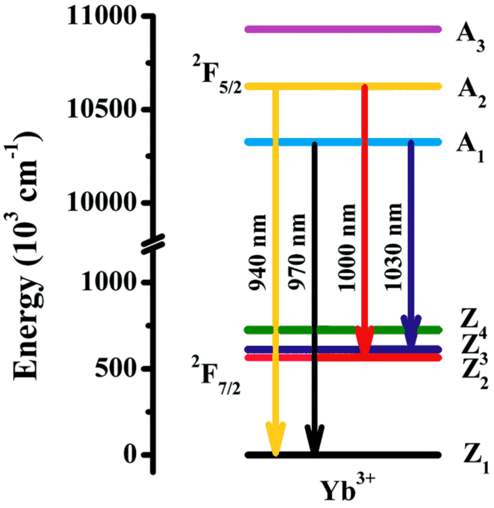

Figure 2.13: Energy level diagram of Yb^{3+} caused by the crystal field Stark splitting [68].

2.8.2.2 Erbium

Erbium (Er) is a rare-earth chemical element with an atomic number of 68. It is the twelfth element in the lanthanide series, with an atomic weight of 167.259 amu [58]. Er is one of the more abundant rare-earth elements with a melting point of 1529° C and a boiling point of 2868° C [64]. Because of erbium's narrow absorption band in the green region of visible light (at wavelengths of ~530 nm), erbium (III) salts are pink. When present in compounds, it exists mostly in the trivalent state, Er^{3+} [61]. The ground state electronic configuration of the neutral Er atom is [Xe] $4f^{12}$ $6s^2$. When Er is incorporated into a solid host, it loses two 6s electrons and one 4f electron, becoming the trivalent ion Er^{3+} and assuming the electronic configuration of [Xe]$4f^{11}$. The partially filled 4f electron shell lies within the closed $5s^25p^6$ shell (in the [Xe] configuration). Figure 2.14 showing the energy levels diagram of an Er^{3+} ion (a) in free space and (b) in solids. For free Er^{3+} ions, the first 12 energy levels starting from the ground state and continuing up to $^4G_{11/2}$. The ground state configuration of the single Er ion is divided into Stark levels owed to crystal field interactions. When Er ions are embedded in solids, the crystal field removes the degeneracy of the states in the Russell-Saunders (RS) terms $^{2S+1}L_J$, where S is the total spin, L is the total orbital momentum and J is the total angular momentum, which is known as the Stark splitting [58]. Each RS state splits into J+1/2 sublevels. For the first three lowest RS states $^4I_{15/2}$, $^4I_{13/2}$ and $^4I_{11/2}$, their sublevels are labeled by $Z_{1\sim8}$, $Y_{1\sim7}$ and $X_{1\sim6}$, respectively.

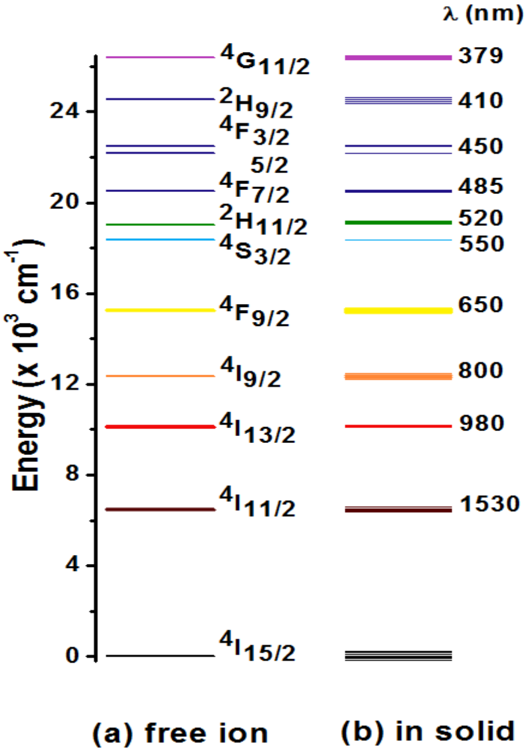

Figure 2.14: Energy levels diagram of an Er^{3+} ion (a) in free space and (b) in solid.

References

[1] X. Huang, S. Han, W. Huang and X. Liu. Enhancing solar cell efficiency: the search for luminescent materials as spectral converters. *Royal Society of Chemistry's leading reviews*, **42(1)** (2013) 173–201. doi:10.1039/c2cs35288e.

[2] M. Yagoub. Effect of broadband excitation ions in the luminescence of Ln^{3+} doped SrF_2 nanophosphor for solar cell application, PhD thesis, University of the Free State, (2015) 8–54.

[3] O. Morton. Solar energy: Silicon Valley sunrise. *Nature*, **443** (7107) (2006) 19–22. doi:10.1038/443019a.

[4] P. M. Ushasree and B. Bora, Chapter 1: Silicon Solar Cells, in Solar Energy Capture Materials. The Royal Society of Chemistry. Newcastle UK (2019) 55–260. ISBN: 978-1-78801-351-2.

[5] Y. Shang, S. Hao, C. Yang, G. Chen. Enhancing Solar Cell Efficiency Using Photon Upconversion Materials. *Nanomaterials*, **5(4)** (2015) 1782–1809. doi:10.3390/nano5041782.

[6] B. M.Van der Ende, L. Aarts and A. Meijerink. Lanthanide ions as spectral converters for solar cells. *Physical Chemistry Chemical Physics*, **11(47)**, (2009) 11081-11095. doi:10.1039/b913877c.

[7] O. K. Simya, P. Radhakrishnan and A. Ashok. Handbook of Nanomaterials for Industrial Applications || Engineered Nanomaterials for Energy Applications. *Micro and Nano Technologies*, **Chapter 41** (2018) 751–767. doi:10.1016/B978-0-12-813351-4.00043-2.

[8] J. de. Wild, R.E.I. Schropp, A. Meijerink, J.K. Rath and W.G.J.H.M. van Sark. Photon upconversion for thin film solar cells. Utrecht University Repository. PhD dissertation. (2010) 2–127. ISBN 978-90-393-5828-3.

[9] A. De Vos and H. Pauwels. On the Thermodynamic Limit of Photovoltaic Energy Conversion. *Applied Physics*, **25 (2)** (1981) 119–125. doi:10.1007/BF00901283.

[10] A. Shalav. Rare-Earth Doped Up-converting Phosphors For an Enhanced Silicon Solar Cell Response, University of New South Wales, PhD Thesis, (2006).p. 171-172.

[11] Jenny Nelson. The Physics of Solar Cells. Imperial College Press, UK (2003) 103-243. ISBN 978-1-86094-340-9.

[12] R. M. Jafer, Luminescence properties of Y_2O_3:Bi^{3+} as powder and thin film phosphor for solar cell application, PhD thesis, University of the Free State, (2015) 1-42.

[13] H. Wang, M. Batentschuk, A. Osvet, L. Pinna, C. J. Brabec. Rare-Earth Ion Doped Up-Conversion Materials for Photovoltaic Applications. *Advanced Materials*, **23(22-23)** (2011) 2675–2680. doi:10.1002/adma.201100511.

[14] Z. Hosseini, E. W. Diau, K. Mehrany, N. Taghavinia. Assessment of Luminescent Downshifting Layers for the Improvement of Light-Harvesting Efficiency in Dye-Sensitized Solar Cells. *ChemPhysChem*, **15(17)** (2014) 3791–3799. doi:10.1002/cphc.201402505.

[15] H. J. Hovel, R.T. Hodgson, J. M. Woodall. The effect of fluorescent wavelength shifting on solar cell spectral response. *Solar Energy Materials*, **2(1)** (1979) 19–29. doi:10.1016/0165-1633(79)90027-3.

[16] A. P. Perdomo, R. V. Fernandes, N. J. A. Cordeiro, F. Franchello, M. A. Toledo da Silva, J. Leonil Duarte, E. Laureto. Luminescent down-shifting film based on optimized mixture of organic dyes for improving the performance of P_3HT:$PC_{61}BM$ photovoltaic devices. *Applied Physics*, **128(3)** (2020) 035502–1–8. doi:10.1063/5.0003629.

[17] A. Ivaturi and H. Upadhyaya. Upconversion and Downconversion Processes for Photovoltaics. *A Comprehensive Guide to Solar Energy Systems*, **C (13)** (2018) 279–298. doi:10.1016/b978-0-12-811479-7.00013-0.

[18] D. L. Dexter. Possibility of Luminescent Quantum Yields Greater than Unity. *Physical Review*, **108(3)** (1957) 630–633. doi:10.1103/physrev.108.630.

[19] W.W. Piper; J.A. DeLuca; F.S. Ham. Cascade fluorescent decay in Pr^{3+}-doped fluorides: Achievement of a quantum yield greater than unity for emission of visible light. *Journal of Luminescence*, **8(4)** (1974) 344–348. doi:10.1016/0022-2313(74)90007-6.

[20] J. L. Sommerdijk; A. Bril; A.W. de Jager. Two photon luminescence with ultraviolet excitation of trivalent praseodymium. *Journal of Luminescence,* **8(4)** (1974) 341–343. doi:10.1016/0022-2313(74)90006-4.

[21] C. Strümpel; M. McCann; G. Beaucarne; V. Arkhipov; A. Slaoui; V. Švrček; C. del Cañizo; I. Tobias. Modifying the solar spectrum to enhance silicon solar cell efficiency—An overview of available materials. *Solar Energy Materials and Solar Cells,* **91(4)** (2007) 238–249. doi:10.1016/j.solmat.2006.09.003.

[22] B. Ahrens, Down- and Up-conversion in Fluorozirconate-Based Glasses and Glass Ceramics for Photovoltaic Application, University of Paderborn, PhD Thesis, (2009) 4–119.

[23] D. Verma, T. O. Saetre, Ole. Midtgard. Review on up/down conversion materials for solar cell application. 38th IEEE Photovoltaic Specialists Conference, (2012) 002608–002613. doi:10.1109/pvsc.2012.6318129.

[24] P. Gibart, F. Auzel, J.-C. Guillaume, K. Zahraman. Below band-gap IR response of substrate-free GaAs solar cells using two-photon up-conversion. *Japanese journal of applied physics*, **35.8R** (1996) 4401–4402. doi.org/10.1143/JJAP.35.4401.

[25] A. Shalav, B. S. Richards, T. Trupke, K. W. Krämer and H. U. Güdel. Application of $NaYF_4$:Er^{3+} up-converting phosphors for enhanced near-infrared silicon solar cell response. *Applied Physics Letters*, **86(1)** (2005) 0135051–0135053. doi:10.1063/1.1844592.

[26] D. Chen, Y. Wang, Y. Yu, P. Huang, F. Weng. Quantum cutting downconversion by cooperative energy transfer from Ce^{3+} to Yb^{3+} in borate glasses. *Applied Physics,* **104(11)** (2008) 116105–1/3. doi:10.1063/1.3040005.

[27] W. A. I. Tabaza, Synthesis, and characterization of $MgAl_2O_4$ and $(Mg_xZn_{1-x})Al_2O_4$ mixed spinel phosphors, Ph.D. thesis, University of the Free State, Bloemfontein, South Africa, (2014) 8–35.

[28] G. Liu and B. Jacquier, Spectroscopic Properties of Rare Earth in Optical Materials, Springer, China (2005) 60–167. ISBN 978-3-540-28209-9.

[29] H. C. Chow and Richard C. Powell. Models for energy transfer in solids. *Physical Review B*. **21(9)** (1980) 3785–3792. doi:10.1103/PhysRevB.21.3785.

[30] D. L. Dexter. A theory of sensitized luminescence in solids. *Chemical Physics,* **21** (1953) 836-850. doi.org/10.1063/1.1699044.

[31] T. Förster. Zwischenmolekulare Energiewanderung und Fluoreszenz. *Annals of Physics,* **437(1-2**) (1948) 55–75. doi:10.1002/andp.19484370105.

[32] G. Blasse. The luminescence of closed-shell transition-metal complexes. New developments. In: Luminescence and Energy Transfer. *Structure and Bonding*. **42(Chapter 1)** (1980) 1–41. doi:10.1007/3-540-10395-3_1.

[33] H. A. A. Seed Ahmed, Luminescence from lanthanide ions and the effect of co-doping in silica and other hosts, PhD thesis, University of the Free State, (2012) 1–15.

[34] M. H. M. Abdelrehman. Synthesis and characterization of bismuth doped strontium oxide powder and thin films, MSc thesis, University of the Free State, Bloemfontein, South Africa, (2019) 1–28.

[35] G. Blasse, B. C. Grabmaier. Luminescent Materials, Springer-Verlag, Berlin Heidelberg (1994) 5–142. ISBN: 978-3-540-58019-5, 978-3-642-79017-1. doi: 10.1007/978-3-642-79017-1.

[36] Ratnesh Tiwari, Vikas Dubey, Sanjay J. Dhoble, Emerging Synthesis Techniques for Luminescent Materials. Advances in Chemical and Materials Engineering (ACME). Publisher, IGI Global, Hershey PA. USA (2018) 56–525. ISBN: 1522551719, 9781522551713.

[37] A. Mohmmed, Luminescence properties of $Y_3(Al,Ga)_5O_{12}$:Tb thin films, Ph.D. thesis, University of the Free State, (2014) 1–21.

[38] R. K. Tamrakar, D. P. Bisen and N. Brahme. Comparison of photoluminescence properties of Gd_2O_3 phosphor synthesized by combustion and solid state reaction method. *Radiation Research and Applied Sciences*, **7(4)** (2014) 550–559. doi:10.1016/j.jrras.2014.09.005.

[39] X. Jiang, L. Yu, C. Yao, F. Zhang, J. Zhang and C. Li. Synthesis and Characterization of Gd_2O_3 Hollow Microspheres Using a Template-Directed Method. *Materials*, **9(5)** (2016) 3230-32311. doi:10.3390/ma9050323.

[40] Pradyot Patnaik. Handbook of Inorganic Chemicals. McGraw-Hill, (2002) 1–125. ISBN 0-07-049439-8.

[41] H. Jamnezhad and M. Jafari. Structure of Gd_2O_3 nanoparticles at high temperature. *Journal of Magnetism and Magnetic Materials*, **408,** (2016) 164–167. doi:10.1016/j.jmmm.2016.02.041.

[42] Y. Zou, L. Tang, J.-L. Cai, L.-T. Lin, L.-W. Cao and J.-X. Meng. Combustion synthesis and luminescence of monoclinic Gd_2O_3:Bi phosphors. *Journal of Luminescence*, **153** (2014) 210–214. doi:10.1016/j.jlumin.2014.03.026.

[43] Hai Guo; Yunfeng Li; Dianyuan Wang; Weiping Zhang; Min Yin; Liren Lou; Shangda Xia. Blue upconversion of cubic Gd_2O_3:Er produced by green laser. *Alloys and Compounds*, **376(1-2)** (2004) 0–27. doi:10.1016/j.jallcom.2003.12.020.

[44] G. Boopathi, S. G. Raj, G. R. Kumar, R. Mohan. A co-precipitation preparation, crystal structure and photoluminescent properties of Er5%: Gd_2O_3 nanorods. *Solid State Physics*, **1667** (2015) 050085-1-4. doi:10.1063/1.4917726.

[45] J. W. Chung, B. K. Moon, J. H. Jeong, J. H. Kim. Luminescence Properties of Bi^{3+} ions co-doped $Gd_2O_3:Eu^{3+},Tb^{3+}$ nanophosphors. [IEEE 2010 IEEE 3rd International Nanoelectronics Conference (INEC) - Hong Kong, China), **47(18)** (2010) 789–790. doi:10.1109/inec.2010.5425202.

[46] G. Liu, G. Hong, J. Wang, X. Dong. Hydrothermal synthesis of spherical and hollow $Gd_2O_3:Eu^{3+}$ phosphors. *J Alloys Compd*. **432(1-2)** (2007) 0-204. doi: 10.1016/j.jallcom.2006.05.127.

[47] F. Mangiarini, R. Naccache, A. Speghini, M. Bettinelli, F. Vetrone, J. A. Capobianco. Upconversion in Er^{3+}-doped Gd_2O_3 nanocrystals prepared by propellant synthesis and flame spray pyrolysis. *Materials Research Bulletin*. **45(8)**, 927–932. doi: 10.1016/j.materresbull.2010.04.016.

[48] Li. Yan-li, C. Nuo-fu, Z. Jian-ping, S. Shu-lin, L. Li-feng, Y. Zhi-gang, C. Chun-lin. Effect of the oxygen concentration on the properties of Gd_2O_3 thin films. *Crystal Growth.* **265(3-4)** (2004) 548–552. doi:10.1016/j.jcrysgro.2004.02.095.

[49] K. Y. Jung, J. H. Han, D. S. Kim, B. Choi and W. Kang. Aerosol Synthesis of Gd_2O_3:Eu/Bi Nanophosphor for Preparation of Photofunctional Pearl Pigment as Security Material. *The Korean Ceramic Society*. **55(5)** (2018) 461-472. dio: 10.4191/kcers.2018.55.5.09.

[50] A. Müller, O. Heim, M. Panneerselvam, M. Willert-Porada. Polyol method for the preparation of nanosized Gd_2O_3, boehmite and other oxides materials. *Materials Research Bulletin*. **40(12)**, 2153–2169. doi: 10.1016/j.materresbull.2005.07.006.

[51] Y. Liu, P. Yang, W. Wang, H. Dong, J. Lin. Fabrication and photoluminescence properties of hollow Gd_2O_3:Ln (Ln = Eu^{3+}, Sm^{3+}) spheres via a sacrificial template method. *CrystEngComm*, **12(11)** (2010) 3717-3723. doi:10.1039/C0CE00145G.

[52] A. F. Wells. Structural Inorganic Chemistry 5th edition. Oxford Science Publications (1984) 146–1424. ISBN 0-19-855370-6.

[53] K. Momma and F. Izumi, VESTA 3 for three-dimensional visualization of crystal, volumetric and morphology data. *Journal of Applied Crystallography,* **44(6)** (2011) 1272-1276. doi: 10.1107/s0021889811038970.

[54] B. Antic, A. Kremenovic, I. Draganic, P. Colomban, Vasiljevic-Radovic, D. Blanusa, J. Blanusa, M. Tadic and M. Mitric. Effects of O^{2+} ions beam irradiation on crystal structure of rare earth sesquioxides. *Applied Surface Science*, **255(17)** (2009) 7601–7604. doi:10.1016/j.apsusc.2009.04.035.

[55] C. Zhang, J. Lin. Defect-related luminescent materials: synthesis, emission properties and applications. *Chemical Society Reviews*, **41(23)** (2012) 7938-7961. doi:10.1039/C2CS35215J.

[56] M. H. Du. Chemical trends of electronic and optical properties of ns2 ions in halides. *Journal of Materials Chemistry C*, **2(24)** (2014) 4784-4791. doi:10.1039/c4tc00485j.

[57] P. Lecoq, A. Annenkov, A. Gektin, Inorganic Scintillators for Detector Systems, Springer-Verlag Berlin Heidelberg, (2006) 56–420. ISBN 978-3-319-45522-8.

[58] K. Sam. The Disappearing Spoon (and other true tales of madness, love, and the history of the world from the Periodic Table of Elements). New York/Boston: Back Bay Books. 158–160 (2011). ISBN 978-0-316-051637.

[59] A. Economou. Bismuth-film electrodes: Recent developments and potentialities for electroanalysis. *TrAC Trends in Analytical Chemistry*, **24(4)** (2005) 334–340. doi:10.1016/j.trac.2004.11.006.

[60] Fu. Jipeng, R. Pang, L. Jiang, Y. Jia, W. Sun, S. Zhang and C. Li, A novel dichromic self-referencing optical probe SrO:Bi^{3+},Eu^{3+} for temperature spatially and temporally imaging, *Dalton Transactions*, **45(34)** (2016) 13317–13323. doi: 10.1039/c6dt01552b.

[61] Arnold F. Holleman, Egon. Wiberg, Nils. Wiberg. "Die Lanthanoide". Lehrbuch der Anorganischen Chemie (in German) (91–100 ed.) (1985) pp. 1265–1279. Walter de Gruyter. ISBN 978-3-11-007511-3.

[62] G. H. Dieke, H. M. Crosswhite. The Spectra of the Doubly and Triply Ionized Rare Earths. *Applied optics*. **2(7)** (1963) 675-686. doi:10.1364/AO.2.000675

[63] C. Daqin, W. Yuansheng, H. Maochun. Lanthanide nanomaterials with photon management characteristics for photovoltaic application. *Nano Energy*, **1(1)** (2012) 0–90. doi:10.1016/j.nanoen.2011.10.004.

[64] C. R. Hammond. The Elements, in Handbook of Chemistry and Physics (81st ed.) (2000) 1265–2556. CRC press. ISBN 978-0-8493-0481-1.

[65] J. J. Eilers, D. Biner, J. T. Van Wijngaarden, K. Krämer; H. Güdel, A. Meijerink. Efficient visible to infrared quantum cutting through downconversion with the Er^{3+}–Yb^{3+} couple in $Cs_3Y_2Br_9$. *Applied physics letters*, **96(15)** (2010) 151106/1-151106/3. doi:10.1063/1.3377909.

[66] L. Zhang, T. Xue, D. He, M. Guzik, G. Boulon. Influence of Stark splitting levels on the lasing performance of Yb^{3+} in phosphate and fluorophosphate glasses. *Optics Express*, **23(2)** (2015) 1505-1511. doi:10.1364/oe.23.001505.

[67] O. Meza, L. A. Diaz-Torres, P. Salas, E. De la Rosa, C. Angeles-Chavez, D. Solis. Cooperative Pair Driven Quenching of Yb^{3+} Emission in Nanocrystalline ZrO_2:Yb^{3+}, *J. Journal of Nano Research*, **5** (2009) 121–134. doi:10.4028/www.scientific.net/JNanoR.5.121.

[68] Z. Fang, R. Cao, F. Zhang, Z. Ma, G. Dong, J. Qiu, Efficient spectral conversion from visible to near-infrared in transparent glass ceramics containing Ce^{3+} –Yb^{3+} codoped $Y_3Al_5O_{12}$ nanocrystals. *Journal of Materials Chemistry C*, **2(12)** (2014) 2204-2211. doi:10.1039/c3tc32231a.

Chapter 3

Experimental techniques

This chapter is divided into three main sections: Section 3.1 is allocated to a brief description of the techniques used to prepare the powder materials in this study. Section 3.2 is dedicated to a brief description of the PLD technique that was used for the thin film deposition. Then section 3.3 is devoted to a brief explanation of the basic principles on which the characterization techniques used in this study are based.

3.1 Powder preparation

In the phosphor field, the knowledge and the experience of what synthesis process is appropriate for the preparation of the samples under study, is very important. When the synthesis is performed with the best processing parameters, the best possible material properties will be obtained. In terms of efficiency, not all the preparation methodologies have an equipotential, each method has its own merits and demerits over the others. There are some points that must be considered when choosing the method of synthesis:

- Good saving energy, time, and production costs.
- Minimizing waste production as much as possible.
- Produce good materials for energy, environment, society and economy.

3.1.1 Combustion synthesis (CS)

The combustion synthesis (CS) method, commonly referred to as "burning" is a self-sustained thermal process. It was invented in the mid1980s [1]. CS is a low-cost method for production of various industrial materials where it allows for the synthesis of a variety of useful nanoscale materials, including oxides, sulfides, metals and alloys [2]. CS is good for a time/energy saving methodology for the preparation of a large variety of inorganic nano powders with high reactivity and tailored defects. Interaction occurs in a redox (i.e. reduction-oxidation) reaction which is an electron transfer process in which the oxidizer gains an electron and increase in its oxidation state and the reducer loses an electron and reduces in its oxidation state to form a sample product. The combustion method can be classified into several types as solution combustion synthesis (SCS), self-propagation high-temperature synthesis (SHS), emulsion combustion synthesis, sol-gel combustion synthesis, gel-combustion synthesis, low-temperature combustion synthesis (LTCS), solid-state combustion (SSC), etc [3]. In self-propagation high-temperature synthesis (SHS) the fire or furnace-less synthesis occurrs via high exothermic redox reactions between the metals and nonmetals with high reaction temperatures (226.85 – 3726.85 ºC) [4]. The main source of heat comes from the combustion reactions. It is a complex sequence of chemical reactions between an organic fuel (such as urea, glycine, carbohydrazide, etc.) and an oxidizer (such as metal nitrates or acetates) accompanied by the production of heat or both heat and light in the form of either a flame or a glow. The combustion synthesis can be represented by a simple chemical equation of the model:

$$mX + nY \rightarrow X_mY_n \qquad (3.1)$$

where X is a fuel (metal) and Y is the oxidizers (nonmetal) [5]. The fuel should be able to attain compositional homogeneity with the other constituents and should undergo combustion at low ignition temperature with the oxidizer. In general, good fuels should react non-violently, produce nontoxic gases, and act as chelating agents for metal cations. Urea is one of the best fuels because of its versatility in the combustion process by producing a large number of single phases and well crystallized multi-component oxides [6].

The typical steps involved in SCS that were employed in the synthesis of the Gd_2O_3 nanophosphors powder are shown in figure 3.1. The Gd_2O_3 powders were prepared by using an urea-nitrate solution combustion synthesis method. Gadolinium nitrate hexahydrate was used as the host precursor and urea for the fuel since this has been shown to produce cubic phase material [7], more detail will be given in Chapter 4. Equation 3.2 is an example of a host production by the SCS method, in which the precursor is incorporated stoichiometrically by dissolving in deionized water under stirring with a magnetic stirrer.

$$2\ Gd(NO_3)_3{\cdot}6H_2O + 5\ NH_2CONH_2 \rightarrow Gd_2O_3 + 5\ CO_2 + 22\ H_2O + 8\ N_2 \tag{3.2}$$

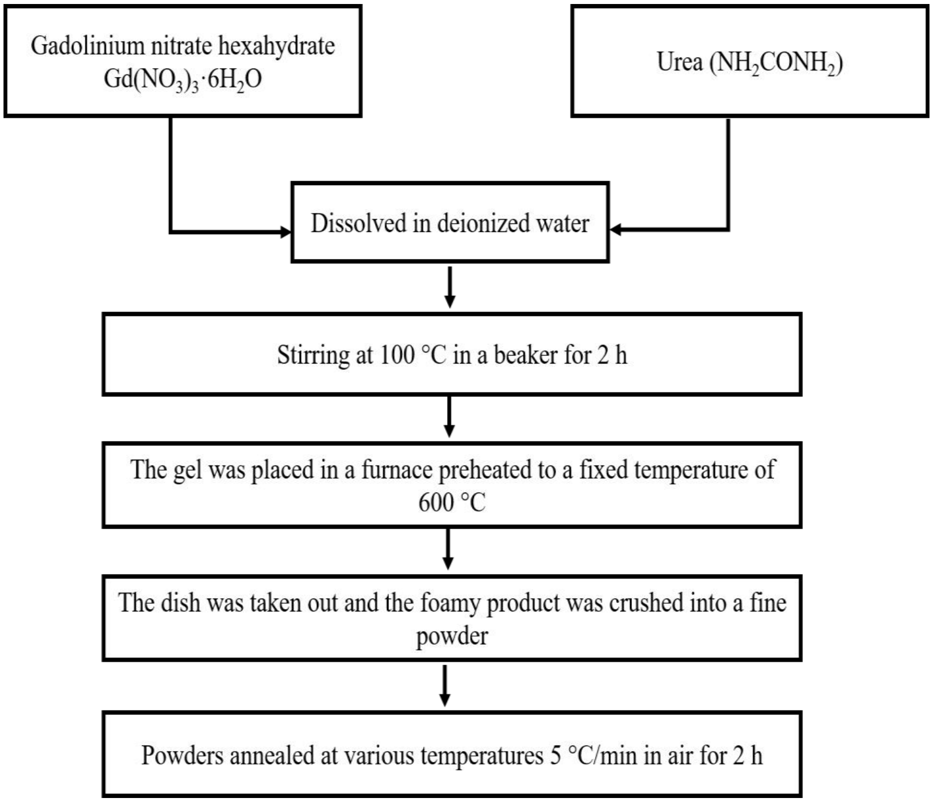

Figure 3.1: Schematic diagram for preparation of nanocrystalline Gd_2O_3 powder by combustion process.

3.2 Thin films preparation

3.2.1 Pulsed laser deposition (PLD) technique

Pulsed laser deposition (PLD) is a successful method for the fabrication of a large variety of thin films. Generally, in the PLD thin film deposition a source material is converted into the vapour form (atomic/molecular/ionic species) from the condensed phase (solid or liquid), which is transported to the substrate and then it is allowed to condense on the substrate surface to form the solid film [8]. The first reports of the use of pulses of laser radiation to remove or ablate material from the solid (or liquid) target followed closely after the first ruby lasers becoming available in the early 1960s [9]. Smith and Turner in 1965 used a pulsed ruby laser to deposit thin films in vacuum [5]. Then in 1987, Dijkkamp et al. [10] produced an $YBa_2Cu_3O_7$ laser film with high-quality using an alternative technique, which was the first real start to the production of thin films using the laser. Then the PLD was used to fabricate high-quality crystalline films, such as ceramic oxides, nitride films, metallic multilayers and various superlattices. Then that led to the rapid development of the laser technology in the 1990's such as lasers having a higher repetition rate and shorter pulse durations than the early ruby lasers [5].

The deposition techniques are broadly classified into two categories: physical methods and chemical methods, which depend on how the atoms/molecules/ions/clusters of species are created for the condensation process. The chemical method of thin films deposition includes the chemical bath deposition, chemical vapour deposition, and spray pyrolysis. The physical methods of thin-film preparation include the thermal evaporation, e-beam evaporation, radio frequency (rf) and direct current (dc) sputtering and PLD [11]. The principle of the PLD technique is based on physical processes that arise from the impact of high-power pulsed laser radiation on solid targets, where the laser is the source of energy in the form of monochromatic and coherent photons [12]. The high-energy laser pulses interact with the target material and the target material is removed by vaporization. Then the vaporization produces a plasma plume of particles that condense onto a heated substrate and a thin film is grown. The ablation process can occur in an ultra-high vacuum or in the presence of some background gas. The PLD system, is quite simple, consisting out of many parts that make up a complete PLD system. These parts each has its own specific purpose (see figure 3.2).

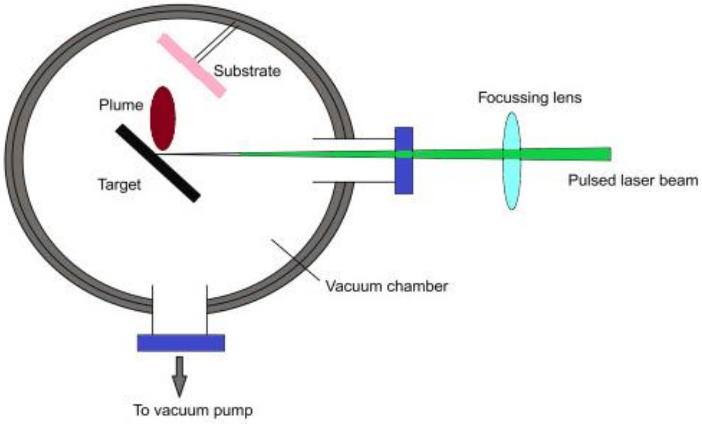

Figure 3.2: A general PLD system configuration.

3.2.1.1 The laser

The pulsed laser used in the PLD system must easily achieve the energies required for a material to transform into a plasma. Most thin film growth by PLD is done with a laser with a wavelength of between 200 nm and 400 nm. The primary purpose of using these wavelengths is the fact that most of the materials used for PLD have strong absorption in these ranges [13]. For the target material to be ablated the absorbed laser pulse energy must be greater than the binding energy of an atom to the surface which is the energy of vaporization per atom [12].

The laser beam is focused onto the surface of the target and all elements in the target are rapidly heated up to their evaporation temperature. The most accomplished work has been done with pulsed laser systems in the ultraviolet (UV) range, specifically neodymium-doped yttrium aluminium garnet (Nd^{3+}: YAG or Nd:YAG) or nanosecond excimer pulsed lasers. Nd:YAG lasers have a fundamental laser emission of 1064 nm with respectively a simple optical scheme and a high power flux density. To achieve other wavelengths (from 1st to 5th harmonics), nonlinear optics are used as a frequency doubler to 532 nm. Where the 532 nm output is mixed with the residual 1064 nm or frequency-doubled radiation to achieve the desired 3rd and 4th harmonics at the wavelength of 355 nm and 266 nm, most useable for PLD [12]. Excimer lasers, namely ArF (193 nm), KrF (248 nm) and XeCl (308 nm) have the flexibility in the repetition rate and high pulse energy in the ultraviolet range in contrast with the 4th and 5th harmonics of the Nd:YAG lasers. Among pulsed UV lasers, the excimer lasers extend the range of possible target materials that can be used, because it provides a variety of short wavelengths combined with energy levels that fit perfectly most PLD applications. The instantaneous ablation rate is dependent on the influence of the laser hitting the target. The intensity of the laser light penetrating the surface of the target in PLD is

$$I(x)=I(x_0)e^{-\alpha(x-x_0)} \qquad (3.3)$$

where $I(x)$ is $I(x)$ is the reduced intensity at an ablated-layer of thickness x below the surface of the target, $I(x_0)$ is the intensity just before the incident laser light hit the target material, and α is the absorption coefficient of the target material [14].

3.2.1.2 PLD Optics

The second part in the PLD system following the pulsed laser system is the optics (see figure 3.3). The simplest configuration of PLD optics consists of a focusing lens, mirrors and beam splitters and a deposition chamber windows as presented in figure 3.3, which assures the least amount of laser energy loss between the laser and target material. The task of the lenses is to focus the laser light and control the laser fluence. The most common lenses used in PLD is the spherical lens that magnifies in two planes and the projected laser energy is oriented as a point. When choosing the correct lens for a PLD system, one should consider the operating wavelength, laser beam size and energy when it passes through the lens. Also, the type of material the lens is composed of will determine if the lens has the characteristics that are needed for the system. Mirrors and beam splitters allow a PLD system to contain multiple deposition chambers. While allowing the redirection of the laser beam to multiple chambers for different PLD experiments, they also make it possible for the user to perform dual-beam PLD in a single chamber. The chamber windows are the simplest optical component of the PLD system. The simple chamber has two view windows and one laser window. A chamber used for dual beam PLD will have two laser windows. View windows are used to observe the plasma plume and aid in target alignment with the laser beam. When selecting the right view window, the requirements are the ability to see through them, handle the stress associated with the high vacuum or high gas pressure, and a high enough operating temperature to tolerate the radiated heat from the substrate heater.

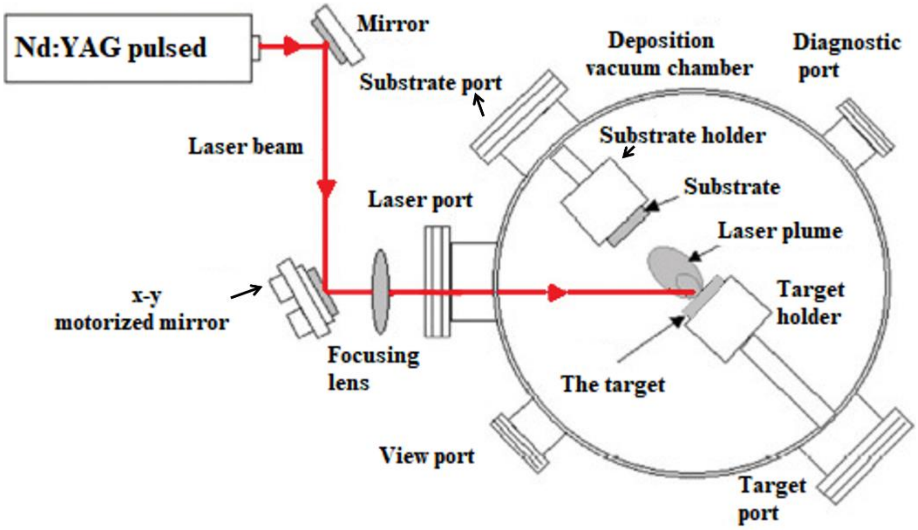

Figure 3.3: Typical pulsed laser deposition chamber.

3.2.1.3 Deposition Chamber

The deposition chamber consists of a central hub that is combined with vacuum pumps, gauges, gas flow, target and substrate holders (see figure 3.3). The background gas can be utilized to reduce the kinetic energy of the plume species and to increase the number of chemical reactions between the plume and gas [12]. A turbomolecular and rotary vane pump allow the deposition chamber to achieve a high vacuum. The two pumps work as one unit, the vane pump is used as a backing pump to bring the chamber pressure below 10^{-2} Torr and then the turbomolecular pump (TMP) is switched on to achieve high vacuum conditions. A single inlet allows a background gas to be introduced for deposition. The gas is regulated with the use of a mass flow controller [13]. There is a carousel capable of carrying up to six targets (25 mm in diameter) inside the vacuum chamber. The target holders can rotate in and out of the path of the laser that enables the deposition of multilayer films without having to open the deposition chamber between the deposition of layers. The target holder and the substrate holder are positioned in such a way that the plasma plume and the substrate are on the same axis, where the vapor (plume) is collected on a substrate place at a short distance, typically 2-10 cm, from the target.

There are many models for ablation [15]:

- For the first one, the laser is absorbed by the lattice of the material as heat before the bonds of the material are broken. The absorbed energy serves to heat the target, resulting in the melting of the target and subsequent material vaporization the so called photo-thermal ablation.
- In the second one, the laser is absorbed directly by the electronic bands, resulting in the immediate breaking of these bonds and is called photochemical ablation.
- In the third type, the processes in which the target surface melts forming small droplets of material, which causes a bulk material, particulates, or droplets to be ejected from the target. The particles are ejected in a liquid state and can be identified by their spherical shape and it is called hydro-dynamical ablation.

3.2.2 Advantages of pulsed laser deposition

PLD is a successful method for the fabrication of a large variety of thin films due to having the following advantages:

i. One of the simpler, cheaper and more versatile methods of depositing thin films, of a very wide range of materials (e.g. metals, carbon, and numerous more complex systems including oxides and other ceramics, ferroelectrics, high-Tc superconductors and materials exhibiting giant magnetoresistance), on a wide variety of substrates, at room temperature [9].

ii. It has a congruent transfer.

iii. Uniform thin films can be produced by PLD.

iv. Good crystallinity enhancement due to the highly energetic species [16].

v. High controllability of the composition of thin films and growth process with controllable gas partial pressure, such as ambient oxygen pressure [17].

vi. Clean deposition due to not needing an atmospheric gas.

vii. Virtually high-density arrival of species due to the pulsed process.

viii. Fast: high-quality sample can be grown reliably in 10 to 30 minutes [18].

ix. Simplicity and flexibility in engineering design.

3.2.3 Disadvantages of pulsed laser deposition

On the other hand, it has some disadvantages such as:

i. Difficult scale-up to large wafers, where the material flux is both directional and has a small radius [12].

ii. The deposition of droplets on the substrate surface due to the deposition process [16].

iii. Composition and thickness in PLD depend on deposition conditions such as wavelength, energy and shape of the laser pulse, process atmosphere, substrate temperature and other parameters [13].

3.3 Characterization techniques

3.3.1 X-ray diffraction (XRD)

XRD is an analytical technique that relies on the wave nature of X-rays to obtain information for phase identification of crystalline solid material of powders, thin films, polymers, fibers, ceramics, organics, metals, and electronic materials. The primary use of XRD is the identification and characterization of compounds based on constructive interference of monochromatic X-rays and a crystalline sample [19]. X-rays were accidentally discovered in 1895 by German physicist Wilhelm Conrad Roentgen while studying cathode rays in a high-voltage gas discharge tube, and the X-rays are located between ultraviolet and gamma radiation in the electromagnetic spectrum [20]. X-rays have extremely short wavelengths ranging from 10 to 0.1 nm. In 1912, Max von Laue discovered that crystalline substances act as three-dimensional diffraction gratings for X-ray wavelengths similar to the spacing of planes in a crystal lattice. X-ray diffraction has since becoming a common technique for the study of crystal structures and atomic spacing and it was further developed by Lawrence Bragg and his father William Henry Bragg in 1913 [19]. The International Center for Diffraction Data (ICDD) is currently responsible for general information about the structure of inorganic materials data in the powder diffraction files (PDF) [21]. Normally a diffractometer is consisting of an X-ray tube (generating monochromatic X-rays of known wavelength), a detector and sample holders (see figure 3.4).

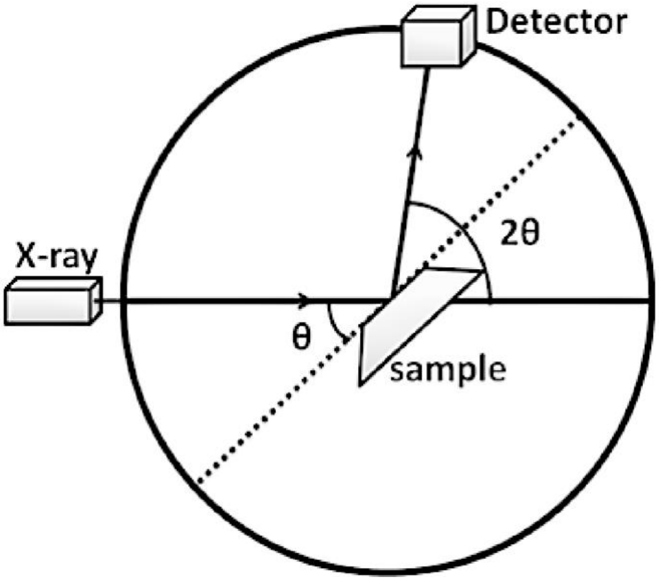

Figure 3.4: Schematic diagram of an X-ray diffractometer [22].

The interaction of an X-ray with the sample produces constructive interference when conditions satisfy Bragg's Law [19].

$$n\lambda = 2d \sin\theta \qquad (3.4)$$

where λ is the wavelength of the incident wave, *n* is a positive integer and θ is half of the scattering angle, which is the Bragg angle (see figure 3.5). When scanning the sample through a range of 2 θ angles, the possible peaks to *d*-spacings allow identification of the sample based on its unique *d*-spacings. Thus, measuring of the diffraction angles will allow for the inter-planar distance (*d*) to be calculated.

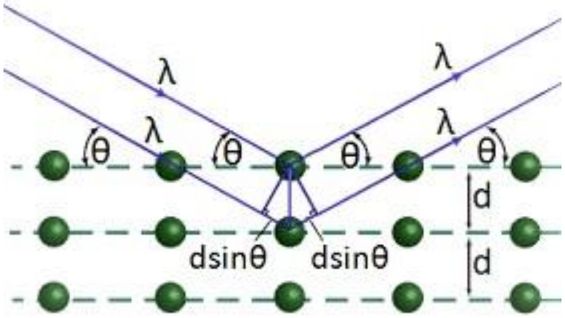

Figure 3.5: Bragg's diffraction scheme [21].

The lattice parameters usually related to the Miller indexes (hkl) of each reflection plane and inter-planar distance d_{hkl}. For cubic structures a lattice parameter a, can be formulated as [23]

$$a = d_{hkl}\sqrt{h^2 + k^2 + l^2} \qquad (3.5)$$

In 1918, Paul Scherrer first investigated the idea about the effect of limited particle size on X-ray diffraction patterns and since then it is known as the Scherrer equation [24]

$$D = \frac{k\,\lambda}{\beta\cos\theta} \qquad (3.6)$$

where D is the mean size of the crystallites, k is the shape factor (in this work taken as 0.9 [24]), β is the full width at half maximum (FWHM) of a diffraction line located at a diffraction angle θ.

In this study, a Bruker Advance D8 diffractometer (40 kV, 40 mA) with Cu Kα X-rays ($\lambda = 0.154$ nm) measured in the $\theta - 2\theta$ configuration in a step size of 0.0094° was used to obtained the XRD data.

3.3.2 Scanning Electron Microscopy (SEM)

Scanning Electron Microscopy (SEM) is used to provide information about the external morphology (texture), crystalline structure and orientation of materials making up the sample by producing images of the surface of the sample [25]. The SEM technique was invented in 1937 by a German Physicist Manfred von Ardenne [26]. A SEM image is a highly-magnified image obtained by scanning a focused energetic electron beam across the surface of a sample and detecting the signal that arises due to the interaction of the electron beam and the sample. Due to the method in which the image is created, SEM images have a characteristic three-dimensional appearance and are useful for judging the surface structure of the sample [25]. The principle of the SEM technique is based on the interaction of an incident electron beam and the solid sample. When an energetic electron beam is incident on a phosphor, hundreds of free electrons and free holes are produced along the path of the incident electron (primary electron) as illustrated in figure 3.6.

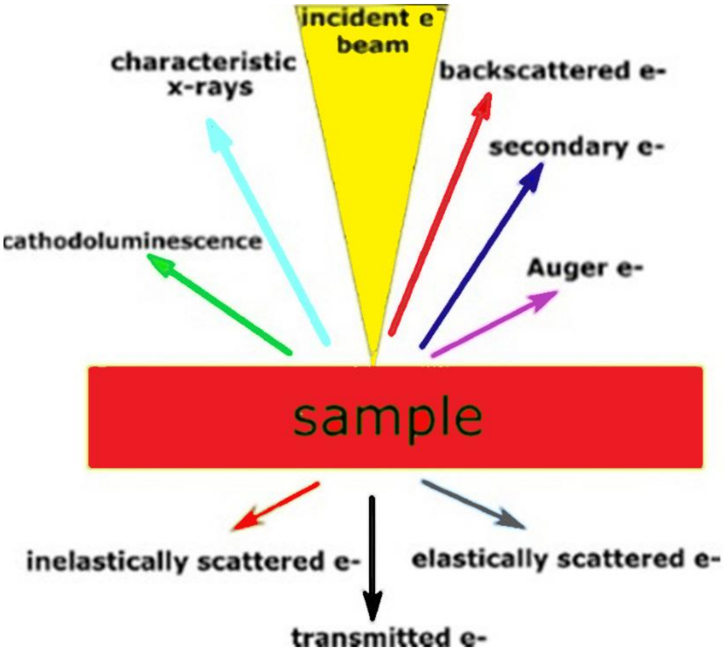

Figure 3.6: The energies produced from electron beam interaction with solid samples [27].

The characteristic X-rays gives the composition and abundance of elements in the sample. Energy-dispersive X-ray spectrometer (EDS) is used in SEM for detecting the characteristic X-rays that are generated and emitted from the sample [28]. Figure 3.7 shows the basic construction of a SEM. Usually, the SEM microscope operates at a high vacuum.

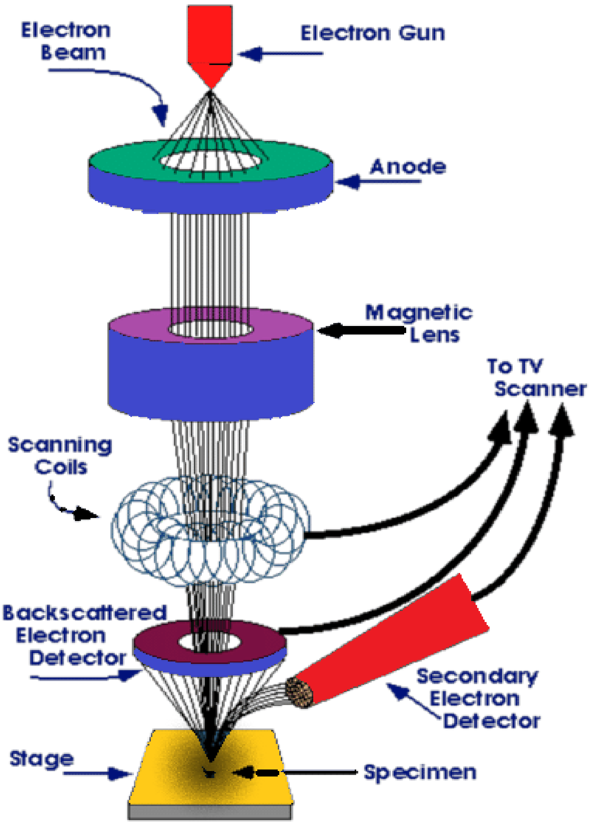

Figure 3.7: Schematic presentation of scanning electron microscope [29].

A beam of incident electrons is generated in a column above the sample chamber. The electrons are produced by a thermal emission source, such as a heated tungsten filament, or by a field emission cathode [12]. The electrons from the electron gun located at the top of the column flow into the metal plate as acting as the anode by applying a positive voltage. Then they pass through the lens to the specimen stage. After the beam hits the surface layers (100 nm) of a sample, electrons are ejected from the sample. Then the detector is used to detect the electrons emitted from the specimen. The output of the secondary electrons is converted to a voltage and amplified to produce an image and detected to transferred to the display unit where the specimen is observed at high magnification [30]. The magnification is controlled by the current supplied to the scanning coils, or voltage supplied to the deflector plates, and not by the power of the objective lens. The areas can be imaged in a scanning mode using the conventional SEM technique that enables high resolution observation of nano-materials up to 1,000,000X magnification with sub-1nm the spatial resolution [31]. The brightness of the signal depends on the number of secondary electrons reaching the detector. As the heavy elements (with a high atomic number) backscatter electrons more strongly than light elements (with a low atomic number), they appears brighter in the SEM images [5]. The SEM images of this study were collected by using a JEOL JSM-7800F high field emission scanning electron microscope (FE-SEM) equipped with an EDS.

3.3.3 Energy dispersive X-rays spectroscopy (EDS)

Energy Dispersive X-ray Spectroscopy (EDS, EDX, EDXS or XEDS), sometimes called energy dispersive X-ray analysis (EDXA) or energy-dispersive X-ray microanalysis (EDXMA), is a powerful analytical technique used for the elemental analysis or to determine the chemical composition of a sample. In EDS it is possible to determine which elements are present in the surface layer of the sample (at the depth in the micrometer range) or phases as small as 1 μm can be analyzed and for these elements can be presented in the mapping form [32]. Figure 3.8 shows that the electrons in the deeper electron shell can be ejected by primary electrons, resulting in an electron-hole [33], where the source of the electron beam is the electron gun of a scanning electron microscope.

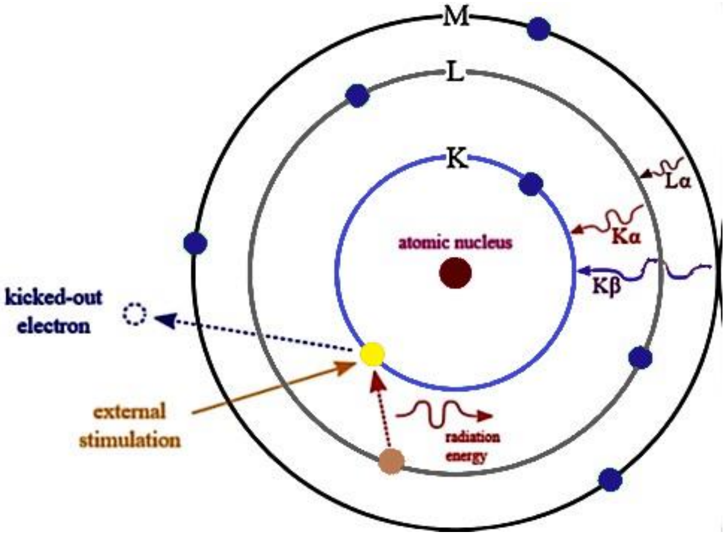

Figure 3.8: Schematic of emitted characteristic X-rays in an atom [32].

The lower-shell position is filled by an electron from the higher shell and the energy is released as an X-ray to balance the energy difference between the two states. These characteristic X-rays are used to identify the composition and measure the abundance of elements in the sample [32]. The spectrum of X-ray energy versus counts is evaluated to determine the elemental composition of the sampled size [32]. In this study, the EDS data was collected by using the Oxford Instruments X-MaxN-80 detector attached to the SEM.

3.3.4 Cathodoluminescence spectroscopy (CL)

Cathodoluminescence (CL) is defined as a process where the luminescence is stimulated by a collision between a beam of electrons (primary electrons) and solid luminescent material such as a phosphor that results in the emission of photons. The energy (color) of this photon and the probability that a photon will be emitted depends on the material, its purity and the defect states. CL occurs when a high energy electron beam impinges on luminescent materials, which will excite electrons from the valence band to the conduction band, leaving holes in the valence band [34]. Emission of photons occurs during recombination of the holes and electrons. Radiative recombination occurs when the e-h pairs diffuse through the phosphor and transfer their energy to activator ions and subsequently emit light. Also, e-h pairs recombine non-radiative by transferring their energy to killer centers (incidental impurities and inherent lattice defects) is possible. Thus, a thin dead (non-luminescent) layer sometimes may be formed on the surface [35]. Hundreds of free electrons and free holes are produced along the path of the incident electron (primary electron) and a number of physical processes take place including emission of secondary electrons, Auger electrons and back-scattered electrons as presented previously in Figure 3.6. In this study, the CL data were collected by two systems: a JEOL JSM-7800F high field emission scanning electron microscope (FE-SEM) equipped with a Gatan CL system and a 545 Auger system with an USB2000 spectrometer type using OOI Base 32 computer software.

In the first system (JEOL JSM-7800F) the measurements can be done in two different modes, namely, monochromatic (single wavelength) and panchromatic (all wavelengths of visible light). For the monochromatic mode, the focused e-beam is either scanned over the sample or positioned on the desired point. This mode enables the identification of different species according to their CL emission and their distribution. Additionally, the superimposed images (false-color overlay) deliver fast and efficient visual information. The light emitted from the sample, passing through the monochromator, result in a spectrum or it can create an image at a wavelength. In the panchromatic mode, complete light is directed at the detector and all the wavelengths emitted from the sample contribute to a panchromatic photon map resulting spectrums [6]. The second system (the PHI 545 Auger) the CL data was collected using the optical fiber with one end connected to the spectrometer and the other end positioned outside the chamber close to the sample. The powders were pressed into small holes of less than 1 mm that were drilled into a Cu sample holder. The holders and the Faraday cup were placed in the carousel. The Faraday cup function is to measure the electron beam size. A Faraday Cup enables accurate measurement of a focused beam of electrons or ions. It is basically an enclosed cavity with a small opening to collect charged particles which enter the cavity and feed the charge to a sensitive pico-ammeter. Therefore, the CL emission here is an optical and electrical phenomenon where a beam of electrons generated by an electron gun impacts on a phosphor causing it to emit visible light obtained by plotting an intensity against the wavelength of light, collected using a spectrometer and recorded by a computer.

3.3.5 Auger electron spectroscopy (AES) system

Auger electron spectroscopy (AES) represents a surface-sensitive analytical technique and it can determine the chemical composition of the surface layers of a sample with a shallow depth of about five monolayers from which data is taken. The Auger effect was discovered and deriving its name from the effect first observed by Pierre Auger in 1923 and AES was developed in the late 1960s [36]. Auger electrons are produced when an atom is probed by an electron beam (energy range 2 keV – 50 keV), and a secondary electron is generated. As a result, the Auger process starts with the removal of an inner shell atomic electron to form a vacancy. Several processes can produce the vacancy, but bombardment with an electron beam is the most common. The inner shell vacancy is filled by a second electron from an outer shell. The energy released kicks a third electron, the Auger electron, out of the atom, so that the atom will reorganize itself to a lower energy state [37]. So, if the energy is enough, the electron can be ejected from the surface and detected as an Auger secondary electron [37]. If the Auger electron is, however, released sufficiently close to the surface, it can escape the surface with little or no loss in energy and can be detected by an electron spectrometer. The process is shown in figure 3.9.

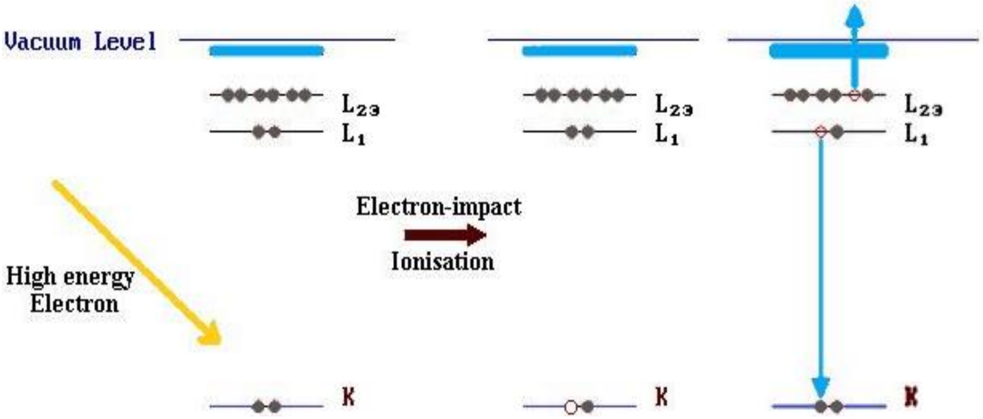

Figure 3.9: Relaxation of the ionized atom by the emission of a KL_1L_{23} Auger electron [38].

A secondary electron will be emitted from the core level, such as a K level. Then another electron falls from a higher level (L_1 in this case) to fill the vacancy in the K-shell. Thirdly the energy liberated in this process ($E_K – E_{L1}$) is simultaneously transferred to a second electron, for example in the $L_{2,3}$ shell. A fraction of this energy is required to overcome the binding energy of this second electron, and the remainder is retained by this emitted Auger electron as kinetic energy. The kinetic energy of the ejected Auger electron is given by [39]

$$E_{kin} = E_K - E_{L1} - E_{L2;3} - \phi \text{ ....}(3.7)$$

where the notation K is the initial state and L_1 and $L_{2;3}$ represent the final state transitions, ϕ is the work function of the analyzer. The changes in the chemical composition of the surface during degradation are also easily monitored with the AES. AES measurements must be performed under ultra-high vacuum conditions (pressures of 10^{-9} - 10^{-10} Torr) to prevent the effect of gases on the sample so that to prevent gasses from absorbing and scattering the very low energy Auger electrons, and to prevent the formation of a thin “gas layer” on the surface of the specimen degrading analytical performance [28]. In this study, we used the PHI model 545 Auger spectrometer. It was used for the measurement of the AES spectrum, CL emission spectrum and used for degradation of the elements and CL degradation. The phosphor was exposed to an electron beam voltage of energy 2 keV and beam current of 3.4 µA. The electron beam irradiation was prolonged for 100 h at a vacuum pressure of 1.3×10^{-9} Torr and with O_2 to a pressure of 1.1×10^{-7} Torr.

3.3.6 X-ray photoelectron spectroscopy (XPS)

X-ray photoelectron spectroscopy (XPS), first named electron spectroscopy for chemical analysis (ESCA), was developed by a Swedish scientist K. Siegbahn and his research group in 1954 at University of Uppsala (Nobel Prize 1981) [39]. XPS is an analytical technique that is widely used for the surface qualitative and quantitative study of the elemental composition, oxidation state, chemical and electronic states of elements in the surface region of a material [39]. Also, the XPS technique is routinely used to measure organic and inorganic compounds, elements, catalysts, ceramics, glasses, polymers, papers, inks, paints, woods, biomaterials, semiconductors, metal alloys, and many others. During XPS, the photoelectrons are ejected from the core-level after the sample is exposed to monochromatic X-rays with defined energy ($h\upsilon$). The energy of the emitted photoelectron is then analysed by the electron spectrometer and the data presented as a graph of intensity (usually expressed as counts or counts/s) versus electron binding energy (see figure 3.10). The photoelectric effect is used to investigate the binding energy (E_B) of the electrons in the sample that also has a work function (φ_A) [40]. If the X-ray's energy is high enough, ionization and emission of the core electrons, with kinetic energy (E_{kin}), occurs. The absorption of the photon and excitation of the electron, and the escape of the electron through the surface energy barrier will be carried out in a vacuum [41]. Often the energy source for XPS are Mg Kα radiation (1253.6 eV) or Al Kα radiation (1486.6 eV) [42].

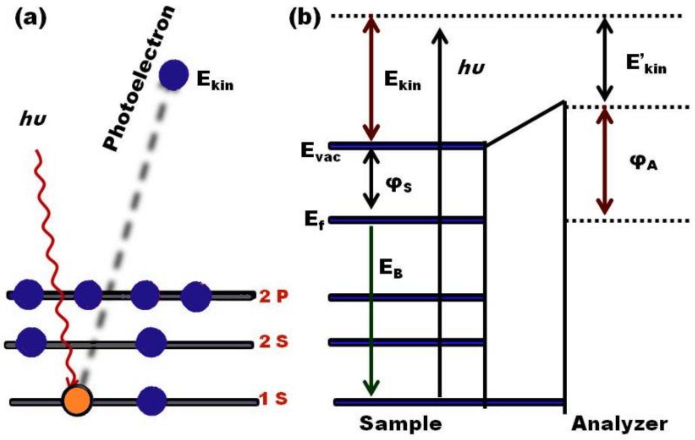

Figure 3.10: (a) Schematic diagram of the photoelectron emission effect and (b) the Fermi levels of both sides are aligned by electrical contact between the sample and the spectrometer [6].

From figure 3.10, the analyzer has a work function of φ_A while the electrons enter the analyzer with a kinetic energy of E'_{kin}. The kinetic energy of the ejected electrons is given by

$$E'_{kin} = h\upsilon - E_B - \varphi_A \qquad (3.8)$$

where E'_{kin} is the kinetic energy of the ejected electron, $h\upsilon$ is the energy of the photon, E_B is the binding energy of the state from which the electron is ejected, and φ is the sample's work-function. The Fermi levels of both sides are aligned by electrical contact between the sample and the spectrometer. If the work function of the spectrometer (φ_A) is a known value, due to the calibration of the spectrometer, the binding energy of the photoelectron emitted can be measured, without knowing the work function of the sample [6]. Since the binding energies of the core electrons are characteristic of the elements in a chemical environment, the XPS allows the determination of the atomic structures of the sample. One can obtain a depth profile of the sample by combining a sequence of ion gun etch cycles interleaved with XPS measurements from the current surface. The shifts in the binding energies also provide information regarding the chemical state of elements being analyzed. The characteristics of peaks detected by XPS correspond to the electron configuration of the electron within the atoms, e.g., 1s, 2s, 2p, 3s, 3p, 3d etc [32].

For collecting data in this study the PHI 5000 Scanning ESCA Microprobe system from the Department of Physics facilities at the University of the Free State was used. The VersaProbe PHI is operated by a patented high flux X-ray source providing a focused monochromatic X-ray beam that is scanned on the sample surface. In figure 3.11 a schematic diagram of the basic apparatus used in the PHI 5000 Versaprobe II Scanning XPS Microprobe is represented. An X-ray source uses a directed electron beam that is scanned at the Al anode to generate X-rays and a quartz crystal monochromator that focuses and scans the X-ray beam generated at the sample surface. Samples were irradiated by an X-ray source with a 100 μm diameter Al Kα monochromatic X-ray beam ($h\upsilon$ = 1486.6 eV) generated by an electron beam, in an ultra-high vacuum chamber (9×10^{-10} Torr). Multipack version 9 spectra analysis software is used to identify chemical compounds and their electronic states using Gaussian-Lorentz fits.

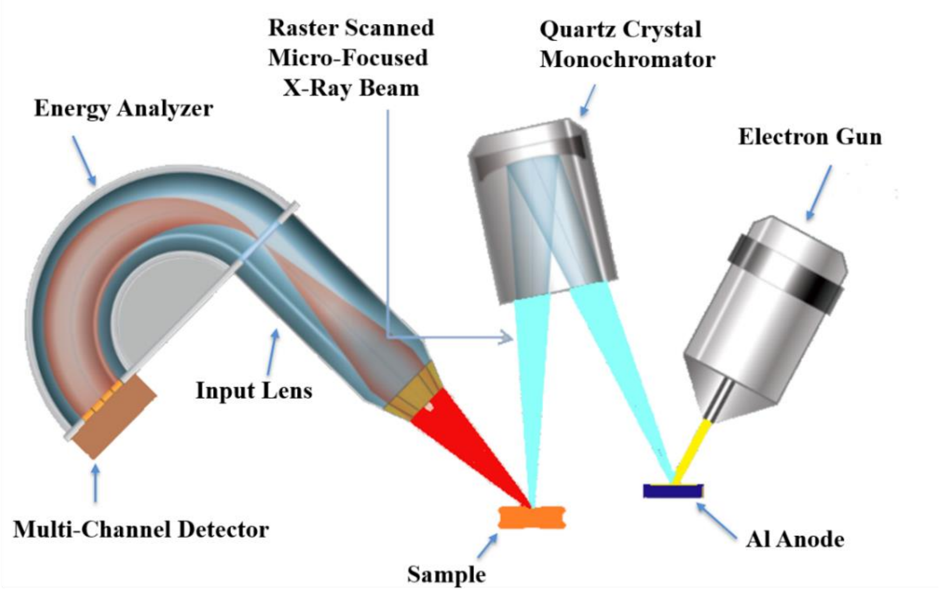

Figure 3.11: Schematic of the basic apparatus used in PHI 5000 Versaprobe II Scanning XPS Microprobe [43].

3.3.7 Thermoluminescence spectroscopy (TL)

Thermoluminescence (TL) is also a form of luminescence. The absorbed light is re-emitted upon heating of solid materials after the previous absorption of energy during irradiation. The basic effect leading to the production of TL is the trapping of charge carriers in the material (electrons and holes), produced during exposure to an external source at defect sites in the material on some minerals such as Gd_2O_3 which store energy when exposed to ultraviolet radiation [34]. In the TL process the radiation promotes electrons from the valence to the conduction band, resulting in free electrons and holes. A fraction of these is captured in traps at lattice sites due to imperfections and impurities. They are retained for a greater or lesser time depending on the physical characteristics of the trap. Some materials could retain the trapped charge for times of up to several million years at ambient temperatures [44]. But normally, after TL emission the material cannot be made to emit it again by simply cooling the specimen and reheating, where the material has to be re-exposed to radiation; raising the temperature will then result in TL emission again [45]. The TL measurement system is composed of a sample chamber, a temperature controller of the sample, heater, thermocouple, a photomultiplier and a recording part (computer) as presented in figure 3.12.

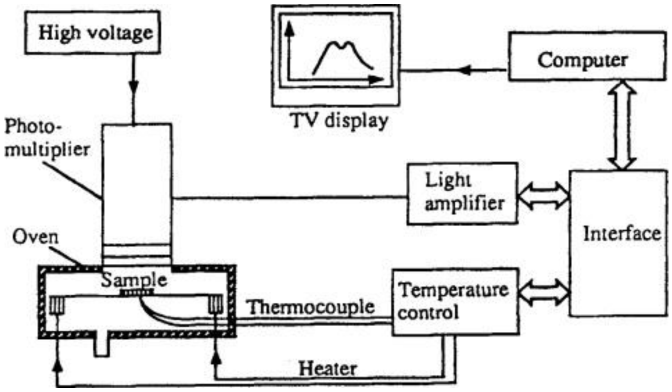

Figure 3.12: Schematic diagram of the measure thermo-luminescence system [46].

The intensity of the emitted radiation from the sample is measured as a function of the temperature of the sample during heating, and then a thermally stimulated luminescence glow curve will be plotted. The plot may exhibit one or many peaks depending on the number of electrons/holes traps with different trap depths, present in the lattice. The TL glow curve gives information about the luminescent centres present in the material. The minimum amount of sample required is tens of milligrams and the measurement temperature ranges from room temperature to 500 °C [45]. In this study, the TL data were collected by a TL 10091 NUCLEONIX spectrometer from the Department of Physics facilities at the University of the Free State.

3.3.8 UV-Vis spectroscopy

UV-Vis spectroscopy is a spectroscopic technique based on the measurement of the wavelength and the intensity of absorption of light in the ultraviolet (UV), visible (Vis) and near-infrared (NIR) regions after it passes through a sample or after reflection from a sample surface. It is a standard technique widely used to determine the absorption properties and the bandgap of phosphor powders [27]. Also, the transmission or absorption measurements in this technique are designed to measure the transmitted or absorbed light from liquid samples as the light passes through. For solid or powder samples, however, the diffuse reflectance is a more suitable technique. The basic parts of the spectrophotometer are a light source, a monochromator with diffraction grating to separate the different wavelengths of light where that only the light of a single wavelength is emitted at one time, a sample holder and a detector as shown in figure 3.13. A machine often has two lamps, a deuterium lamp for the UV region and a tungsten lamp for the visible region [27], with the transition usually set near 330 nm and controlled by the software.

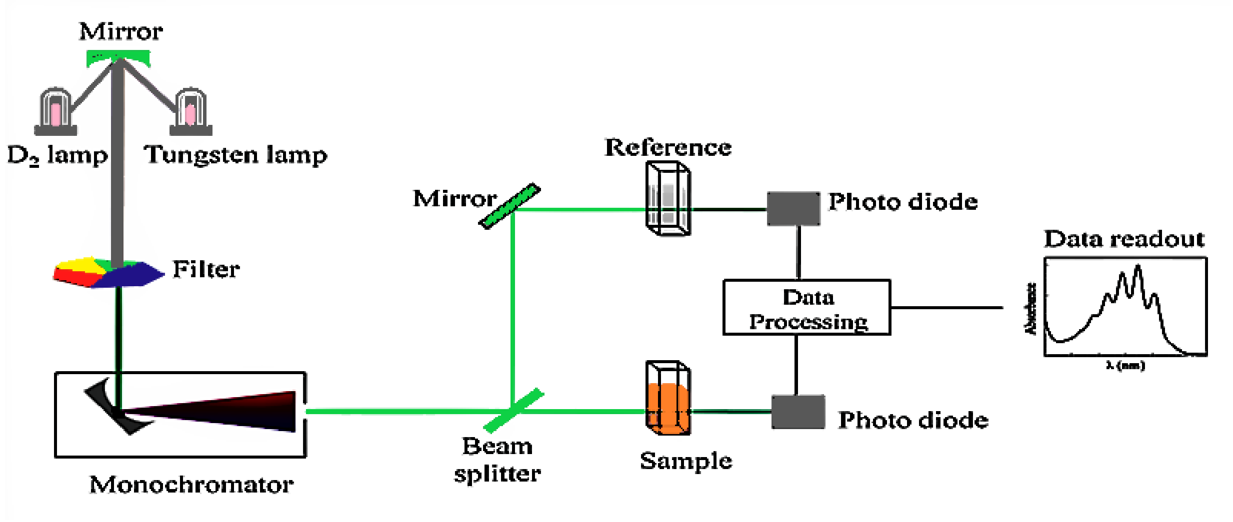

Figure 3.13: Schematic of a dual-beam UV-Visible spectrophotometer [43].

To determine the bandgap of the phosphor powder in the case of reflectance data, the reflectivity R_∞ must first be measured. A quantity proportional to the absorbance can be calculated by the Kubelka-Munk function, F(R) as follows:

$$F(R_\infty) = (1 - R_\infty)^2/(2R_\infty) = 2\alpha/S \qquad (3.9)$$

where $R_\infty = R_{sample}/R_{reference}$ and S is scattering coefficient [46]. Then optical band gap energy can be calculate using the well-known Tauc law relation [44]

$$\alpha h\nu = C(h\nu - E_g)^n \qquad (3.10)$$

where $h\nu$ is the incident photon energy, α is the absorption coefficient, C is constant, Eg is the optical gap energy and n which depends on the type of electronic transition responsible for absorption.

Assuming S is constant, using equations (3.9) and (3.10) can be combined as follows:

$$[F(R_\infty)*h\nu]^n = C_2\,(h\nu - E_g) \qquad (3.10)$$

To obtain E_g one can plot $[F(R_\infty)*hv]^n$ against hv and fit the linear region with a line and extend it to the energy axis.

In eq. 3.10, the value of the exponent n denotes the nature of the sample transition.

- For direct allowed transitions……………$n = 1/2$
- For direct forbidden transitions…………..$n = 3/2$
- For indirect allowed transitions…………...$n = 2$
- For indirect forbidden transitions………….$n = 3$

This is plotted on the y-axis and the energy (eV) is plotted on the x-axis.

In this study, the diffuse reflectance spectra were recorded with a Lambda 950 UV–Vis spectrophotometer with an integrating sphere using a Spectralon standard that exhibits reflectance close to 100% reflectance in the wavelength range from near UV to the near IR.

3.3.9 Photoluminescence spectroscopy

Photoluminescence (PL) is the luminescence of material after excitation by high energy photons in a process called photo-excitation (by absorbing a photon). PL spectroscopy has emerged as an important technique that is capable to study the optical properties such as emission and excitation as well as the luminescence lifetime of luminescent material and some electronic properties of solid-state materials suited for optoelectronic applications. The sample is excited by photons (generally in the UV range) from the ground electronic state to one of the various electronic excited states. The electron drops to the ground electronic state and will emit a photon during the process and can then be recorded for different modes, i.e. excitation and emission [38]. A schematic diagram of the PL technique is presented as visualized with the Jablonski diagram shown in figure 3.14.

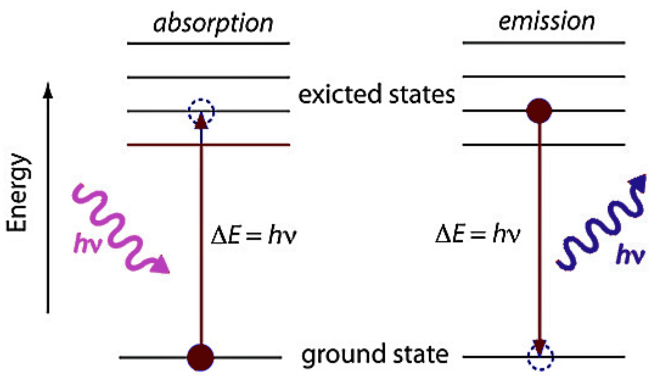

Figure 3.14: Simplified schematic energy diagram showing the excitation and emission involved in the photoluminescence process [3].

In the steady-state PL, the excitation source is kept on and information is normally extracted from the emission and the excitation spectra with respect to wavelength. In time-resolved measurements, the excitation source is pulsed and a decay curve is used to extract the lifetime. The basic set-up of a PL spectrometer comprises of two-wavelength selectors (monochromators). One wavelength selector selects the excitation wavelength from the light source and the other select the emission wavelength from the sample after excitation. The common excitation sources are Xe lamps or lasers with a monochromatic wavelength [14] as presented in the figure 3.15. Xenon lamps are useful because of their high intensity at all wavelengths ranging upward from 250 nm [47]. Normally the emitted light is analysed with a spectrometer and detected with a photomultiplier tube (PMT).

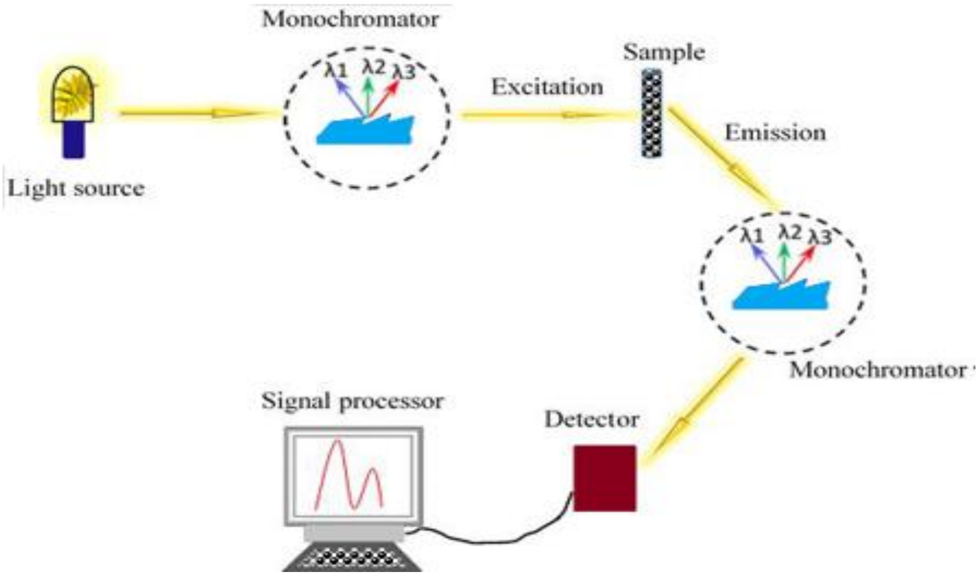

Figure 3.15: Schematic diagram of a photoluminescence spectrometer [14].

References

[1] A. Varma, A. S. Mukasyan, A. S. Rogachev, and K. V. Manukyan. *Solution Combustion Synthesis of Nanoscale Materials. Chemical Reviews*, **116(23)** (2016) 14493–14586. doi:10.1021/acs.chemrev.6b00279.

[2] S. T. Aruna and A. S. Mukasyan. Combustion synthesis and nanomaterials. *Current Opinion in Solid State and Materials Science*. **12(3-4)** (2008) 44–50. doi:10.1016/j.cossms.2008.12.002.

[3] M. Abdelrehman. Synthesis and characterization of bismuth doped strontium oxide powder and thin films. MSc. thesis, University of the Free State, (2019) 49-76.

[4] M. Lackner, Combustion synthesis: Novel routes to novel materials, Bentham Science Publishers, UAE (2009) a) p. 1, b) p. 2. ISBN: 978-1-60805-656-9.

[5] S. N. Ogugua, Tunable multicolor emission from dysprosium-doped mixed rare-earths oxyorthosilicate nanophosphors for application in ultraviolet-pumped multicolour and white light emitting diodes, MSc. thesis, University of the Free State, (2015) 19-37.

[6] R. M. Jafer. Luminescence properties of Y_2O_3:Bi^{3+} as powder and thin film phosphor for solar cell application, Ph.D. thesis, University of the Free State, (2015) 19-40.

[7] P. P. Fedorov, M. V. Nazarkin, and R. M. Zakalyukin. On polymorphism and morphotropism of rare earth sesquioxides. *Crystallography Reports*, **47(2)** (2002) 281–286. doi:10.1134/1.1466504.

[8] D. Bäuerle. Thin-Film Formation by Pulsed-Laser Deposition and Laser-Induced Evaporation. *Laser Processing and Chemistry*, **851** (2011) 489–531. doi:10.1007/978-3-642-17613-5_22.

[9] M. N. R. Ashfold, F. Claeyssens, G. M. Fuge and S. J. Henley. Pulsed laser ablation and deposition of thin films. *Chemical Society Reviews.* **33(1)** (2004) 23. doi:10.1039/b207644f.

[10] F. Ronci, P. Reale, B. Scrosati, S. Panero, V. Rossi Albertini Perfetti, P. Perfetti, V. Rossi Albertini, M. di Michiel and J. M. Merino. High-Resolution In-Situ Structural Measurements of the Li4/$_3$Ti$_{5/3}$O$_4$“Zero-Strain” Insertion Material. *Physical Chemistry B,* **106(12)** (2002) 3082–3086. doi:10.1021/jp013240p.

[11] R. Manoj. Characterisation of Transparent Conducting Thin Films Grown by PLD and RF Magnetron Sputtering. Department of Physics Cochin University of Science and Technology Cochin – 682 022, Kerala, India, (2006) 37-68.

[12] A. Mohmmed, Luminescence properties of $Y_3(Al,Ga)_5O_{12}$:Tb thin films, Ph.D. thesis, University of the Free State, (2014) 7-12.

[13] Garza. Ezra, "PLD of Thin Film Heterostructures". University of New Orleans Theses and Dissertations. (2011) Paper 459. http://scholarworks.uno.edu/td/459.

[14] O. S. Nnalue. Preparation and characterization of powders and pulsed laser deposited thin films of rare-earths doped oxyorthosilicates. PhD thesis, University of the Free State, (2017) 49-76.

[15] Robert Eason, Pulsed laser deposition of thin films: applications-led growth of functional materials. Edited by Wiley and Sons, New York (2007) 682 Pages. ISBN-13: 978-0-471-44709-2.

[16] T. Yoshitake, T. Hara and K. Nagayama. The influence of the repetition rate of laser pulses on the growth of diamond thin films by pulsed laser ablation of graphite. *Diamond and Related Materials*. **12(3-7)** (2003) 306–309. doi:10.1016/s0925-9635(02)00333-3.

[17] Y. Hsiu. Structure and properties of transparent conductive ZnO films grown by pulsed laser deposition (PLD). MS.c thesis The University of Birmingham, (2009) 19-23.

[18] A. Suzuki, T. Matsushita, Y. Sakamoto, N. Wada, T. Fukuda, H. Fujiwara and M. Okuda. Surface Flatness of Transparent Conducting ZnO:Ga Thin Films Grown by Pulsed Laser Deposition. *Jpn. J. Appl. Phys.* **35(Part 1, No. 10)** (1996) 5457–5461. doi:10.1143/jjap.35.5457.

[19] V. Pecharsky and P. Zavalij, Fundamentals of Powder Diffraction and Structural Characterization of Materials. 2nd Edition, Springer Science & Business Media, LLC (2009) 29-173. ISBN: 978-0-387-09578-3.

[20] H. A. Enge, M. R. Wehr and J. A. Richards. Introduction to Atomic physics. Addison-Wesley Publishing Company (1972) P 486. ISBN: 0201018799.

[21] B. D. Cullity, Element of x-ray diffraction, Addison-Wesley Publishing Company, Inc. 2nd Edition. Canada (1978) 77-73950. ISBN: 9780201011746.

[22] https://xrd.co/component-parts-x-ray-diffractometer/. (accessed November 2021).

[23] Harold P. Klug, Leroy E. Alexander. X-Ray Diffraction Procedures: For Polycrystalline and Amorphous Materials, 2nd Edition. John Wiley & Sons, New York, (1974) 960. ISBN: 978-0-471-49369-3.
[24] B. D. Cullity, Element of x-ray direction, Addison-Wesley Publishing Company, Inc. 2nd Edition. Canada (1978) 77-73950. ISBN: 0-201-01174-3.
[25] G. D. Danilatos. Foundations of Environmental Scanning Electron Microscopy. *Advances in Electronics and Electron Physics*. **71** (1988) 109–250. doi: 10.1016/s0065-2539(08)60902-6.
[26] M. von Ardenne. Improvements in electron microscopes. GB 511204, convention date (Germany) 18 February (1937) 538-572.

[27] https://www.azom.com/article.aspx?ArticleID=16256 (Accessed November 2021).

[28] J. R. Meyer-Arendt, Introduction to Classical and Modern Optics, 4th Ed., Prentice-Hall (Englewood Cliffs, 1995) P 431. ISBN: 9780131243569.

[29] S. S. Dlamini, Characterization of Y_3(AL,,Ga)$_5O_{12}$:Ce^{3+} phosphor thin films prepared by PLD, Bloemfontein, M.Sc thesis, University of the Free State, (2013) 26-38.

[30] D. K. Schroder. Semiconductor Material and Device Characterization, 3rd Edition, Wiley-VCH, Canada (2005) P 840. ISBN 0-471-73906-5.

[31] https://www.jeolbenelux.com/JEOL-BV-News/jeol-announces-a-new-field-emission-scanning-electron microscope-jsm-7800f . (Accessed November 2021).

[32] Pulane. Mokoena, Study of the structure, particle morphology and optical properties of mixed metal oxides, MSc thesis, University of the Free State, (2017) 15-38.

[33] https://www.mee-inc.com/hamm/energy-dispersive-x-ray-spectroscopyeds/. (Accessed October 2020).

[34] M. M. Biggs. Synthesis, characterization and luminescent mechanism of ZnS:Mn^{2+} nanophosphor, MSc. thesis, University of the Free State, (2009) 65-90.

[35] P.D. Nsimama, Characterization of $SrAl_2O_4$:Eu^{2+},Dy^{3+} Nano thin films prepared by pulsed laser deposition, PhD thesis, University of the Free State, (2010) 25-38.

[36] P. J. Potts, A Handbook of Silicate Rock, Springer Science & Business Media, US (1992). ISBN 10: 0216932092, ISBN 13: 9780216932098.

[37] M. Thompson. Auger electron spectroscopy. Wiley, Chemical analysis, London, (1985) 74. ISBN:047104377X, 9780471043775.

[38] M. Yagoub. Effect of broadband excitation ions in the luminescence of Ln^{3+} doped SrF_2 nanophosphor for solar cell application, PhD thesis, University of the Free State, (2015) 33-50.

[39] John F. Moulder. Handbook of X-ray Photoelectron Spectroscopy: A Reference Book of Standard Spectra for Identification and Interpretation of XPS Data. Editors, Jill Chastain, Roger C. King. Physical Electronics, (1995) 13-240. ISBN: 096481241X, 9780964812413.

[40] N. Zettili, Quantum Mechanics Concepts and Application, Wiley, Second Edition UK (2009) 79-155. ISBN: 978-0-470-02679-3.

[41] H. ezen and S. Suzer. XPS for chemical- and charge-sensitive analyses. *Thin Solid Films.* **534**, (2013) 1–11. doi:10.1016/j.tsf.2013.02.002.

[42] H. A. A. Seed Ahmed, Luminescence from lanthanide ions and the effect of co-doping in silica and other hosts. Ph.D. thesis, University of the Free State, (2012) IV-(1-30).

[43] https://www.irida.es/estudio-de-superficies/xps/phi-quantera-ii-scanning-xps-microprobe/ (Accessed November 2021).

[44] J. R. Prescott, P. J. Fox, R. A. Akber and H. E. Jensen. Thermoluminescence emission spectrometer. *Applied Optics*, **27(16)**, 3496 (1988). doi:10.1364/ao.27.003496.

[45] H. Uchikawa. Specialized Techniques. Handbook of Analytical Techniques in Concrete Science and Technology. **71** 820–934 (2001). doi:10.1016/b978-081551437-4.50023-0.

[46] S. Som and S. K. Sharma. Eu^{3+}/Tb^{3+}-codoped Y_2O_3 nanophosphors: Rietveld refinement, bandgap and photoluminescence optimization. *J. Phys. D*. **45(41)** (2012) 415102. doi:10.1088/0022-3727/45/41/415102.

[47] W. A. I. Tabaza, Synthesis, and characterization of $MgAl_2O_4$ and $(MgxZn_{1-x})Al_2O_4$ mixed spinel phosphors, Ph.D. thesis, University of the Free State, (2014) 36-63.

Chapter 4

Photoluminescence, thermoluminescence and cathodoluminescence of optimized cubic Gd_2O_3:Bi phosphor powder

In this chapter, the luminescence properties of Bi doped Gd_2O_3 powders were investigated for samples having different doping concentrations and different annealing temperatures. The cathodoluminescence degradation and the surface elemental composition of the phosphor was also investigated.

4.1 Introduction

Rare earth oxides have proved to be excellent host materials for many luminescent activator ions as they have outstanding optical, mechanical, chemical and electronic properties [1]. Phosphors based on these materials can be used in devices such as white light emitting diodes, cathode ray tubes, high definition televisions, medical diagnostic equipment, catalysts, night glowing panels guiding highway traffic and to enhance the efficiency of solar cells [2]. Amongst suitable rare earth oxide hosts having the cubic crystal structure, Gd_2O_3 has the largest cation radius [3], even though the ionic radius of VI-coordinated Gd^{3+} (93.8 pm) is still slightly less than that of Bi^{3+} (103 pm) [4]. Gd_2O_3 has received considerable attention for optoelectronics, data storage, sensors and display applications [5]. It has a high thermal conductivity (0.1 $Wcm^{-1}K^{-1}$) [6]. Since the phonon energies of cubic rare earth oxides decrease as the lattice constant increase [7], Gd_2O_3 also has lower phonon energies than other cubic rare earth oxide hosts, which reduces the probability of detrimental phonon-assisted non-radiative transitions. Although often grouped with the cubic rare earth oxides, Gd_2O_3 may also be found in the monoclinic phase under ambient conditions [8]. Its phase may depend on the synthesis conditions, e.g. the type of fuel used during combustion synthesis [9]. This is because Gd_2O_3 lies near the controversial transition between the cubic rare earth oxides and those with larger ionic radii having monoclinic structure (or, for even greater ionic radii, hexagonal structure) [10,11]. Figure 4.1 shows the crystal structure of cubic Gd_2O_3 as drawn using the VESTA program [12]. The cubic phase of Gd_2O_3 has a space group $Ia\bar{3}$ and forms crystals with two types of Gd sites, each with a coordination number of 6 but with different coordination geometries [13]. In the unit cell are 8 sites which are octahedrally coordinated with six oxygen atoms and another 24 sites which have four shorter and two longer bonds with O.

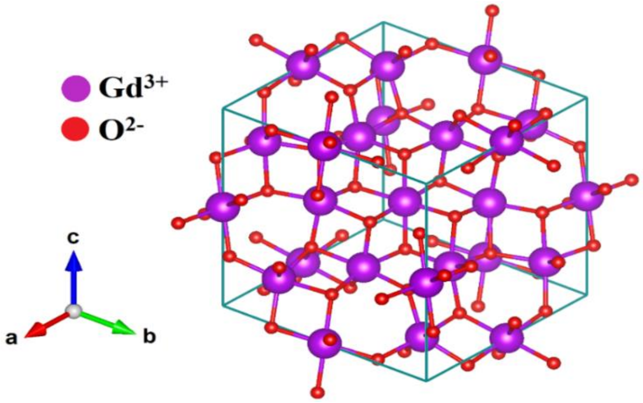

Figure 4.1: The unit cell of cubic Gd_2O_3.

Emission from undoped Gd_2O_3 is not usually reported, although Zatsepin *et al.* [14] attributed emission at 315 nm to Gd^{3+} ions associated with intrinsic defects, while numerous peaks in the ultraviolet and visible range have been recorded in isolated studies [9]. Following some pioneering work [15,16,17], there has been renewed interest in Bi doped Gd_2O_3 over the past decade. Some of the current interest originates from the prospect of using Bi as a co-dopant to improve the luminescence of other activators in Gd_2O_3, e.g. Sm^{3+} [18], Tb^{3+} [19], Eu^{3+} [19,20], Nd^{3+} [21,22] and Yb^{3+} [23], although there is also significant interest in the luminescence from the Bi^{3+} ions themselves. The luminescence from Bi^{3+} ions is highly dependent on the host and also depends on the coordination characteristics of the activator site [24]. Bi^{3+} ions have a ground state electronic configuration of $6s^2$ corresponding to one level (singlet $^1S_0$), while the excited 6s6p configuration is comprised of four levels: a triplet ($^3P_0$, $^3P_1$ and $^3P_2$) and singlet ($^1P_1$) [25]. Absorption bands of Bi^{3+} are usually attributed to $^1S_0 \rightarrow {}^3P_1$ and $^1S_0 \rightarrow {}^1P_1$ transitions [25], although the latter may often lie at very short inaccessible wavelengths. The position and the splitting of the emitting $^3P_1$ level is sensitive to the surrounding lattice, resulting in the band profile and peak wavelength of Bi^{3+} emission varying appreciably in different hosts. The luminescence of Bi^{3+} in cubic Gd_2O_3 thin films has been reported to consist of a blue emission band peaked at 420 nm when excited at 372 nm and a wide blue-green emission band with maximum at 502 nm when excited at 328 nm [26].

Broad emissions covering both these bands were observed from electroluminescent devices fabricated with Gd_2O_3:Bi thin film emitting layers [26]. Cubic Gd_2O_3 features two types of Gd^{3+} sites, both with coordination number of 6 but with different coordination geometries, i.e. where two O^{2-} ions are missing either along the body (S_6) or a face (C_2) diagonal of a cube surrounding a Gd^{3+} ion. When Bi^{3+} occupies a S_6 site having inversion symmetry in cubic Y_2O_3, its Stokes shift is less compared to when it occupies a less symmetric C_2 site having more neighbouring ions to one side than the other [27] and the same effect is apparent for Gd_2O_3 [23]. The peak position for the blue-green emission has also been reported at slightly longer wavelengths of 515 nm [20], 520 nm [23] and 542 nm [21]. The luminescence of Bi^{3+} ions in monoclinic Gd_2O_3 was investigated by Zou *et al.* [5] and was found to consist of a single emission peak, which varied only slightly from 449 – 458 nm although the excitation was varied considerably between 319 – 370 nm. Recently, Zhang *et al.* [28] identified superbroad near-infrared luminescence between 800 – 1400 nm from mixed phase bismuth doped Gd_2O_3 (predominantly monoclinic) which had been reduced, in addition to visible blue luminescence at 478 nm. Although infrared emissions have been established to occur for bismuth ions reduced to lower oxidation states than Bi^{3+} [29], it was instead suggested that the infrared emission originated from Bi^{3+} ions substituting Gd^{3+} ions in monoclinic Gd_2O_3 for which the coordination environment had been affected by oxygen vacancies. Thermoluminescence (TL) is a technique for studying the defects in both insulators and semiconductor materials: when a sample is exposed to an ionizing source such as ultraviolet radiation or electron, proton, neutron, gamma and ion beam radiation, the generated free electrons and holes can be trapped by defects in the material. The consequent heating of the material can release some of these trapped carriers and recombination may then produce a TL signal [30].

Electron beam degradation studies have been reported for bismuth doped oxide hosts such as SrO [25] and La_2O_3 [31] that demonstrated stability during electron irradiation. Also, electron beam degradation has been reported by Swart *et al.* [32] for Gd_2O_2S:Tb^{3+} thin films, demonstrating that during prolonged electron bombardment some Gd_2O_3 phase was formed on the surface that helped to stabilise the cathodoluminescence (CL). In this context, further study of Gd_2O_3:Bi to include its CL and electron beam stability would be useful. In this work the photoluminescence (PL), TL and CL of the optimized cubic Gd_2O_3:Bi produced using the combustion method is presented and its CL degradation investigated.

4.2 Experimental

4.2.1 Sample preparation

Powder samples of the host Gd_2O_3 as well as doped $Gd_{2-x}O_3:Bi_x$ (x = 0.0005, 0.0009, 0.002, 0.003, 0.004 and 0.006) phosphor were prepared by using urea-nitrate solution combustion synthesis. Gadolinium nitrate hexahydrate was used as the host precursor and urea for the fuel, since this has been shown to produce cubic phase material [10]. All chemicals were purchased from Sigma Aldrich and used as received. To produce the host, the precursors were combined stoichiometrically according to the reaction

$$2\ Gd(NO_3)_3{\cdot}6H_2O + 5\ NH_2CONH_2 \rightarrow Gd_2O_3 + 5\ CO_2 + 22\ H_2O + 8\ N_2 \qquad (4.1)$$

by dissolving 0.01 mol of $Gd(NO_3)_3{\cdot}6H_2O$ and 0.025 mol of H_2CONH_2 in 50 ml of deionized water under stirring using a magnetic agitator. Bismuth nitrate pentahydrate was substituted for some gadolinium nitrate hexahydrate to produce doped samples. The solution was heated at 100 °C in a beaker for 2 h to obtain a mixed aqueous homogeneous solution with no suspended particles. As the water content decreased, the solution gradually changed into a transparent gel. The gel was placed in a furnace preheated to a fixed temperature of 600 °C to undergo combustion and produce the desired material. The authentic temperature of a combustion reaction is generally much lower than the calculated theoretical as a result of various factors including the heat evolution of a large amount of gas, incomplete combustion of fuels, and loss of heat by radiation. It took about 5 min for the combustion process to complete, resulting in foam-like crispy end products. The products were allowed to cool to room temperature and were gently ground into fine powders using an agate mortar and pestle. Such as in many cases of combustion, synthesis needs to be followed by a calcination step to remove excess organic impurities from the as-synthesised powders. Portions of these as-prepared samples were also annealed in air at various temperatures for 2 h with an initial increasing heating rate of 5 °C/min starting from room temperature up to the required temperature for each sample being formed. The combustion process and the temperature was used is affected by the chemical composition of the mixture and also maybe the number of concentrations of the dopant. A possible reason could be a stronger bond between transition metal oxides and the fuel depending on the chemical compositions, stronger or weaker metal-to-fuel interactions are present in the combustion mixture, leading to a stronger or weaker redox reaction between the fuel and the oxidant. Therefore, the combustion procedure must be adapted according to the chemical composition of the product and to the concentration of the constituents, to avoid a too high ignition temperature and a too intense/slow combustion. In our samples Eq. (4.1), stoichiometric composition mixture was calculated in a way that the total oxidizing and reducing valencies of the oxidizer and fuel were balanced and the release of energy was maximized for each reaction.

4.2.2 Characterization

The $Gd_{2-x}O_3$:Bi_x powders were characterized using a Bruker D8 Advance powder diffractometer, a JEOL JSM-7800F scanning electron microscope (SEM), a Lambda 950 UV-vis diffuse reflectance (DR) spectrophotometer with a spectralon integrating sphere accessory. An Edinburgh Instruments FS5 spectrophotometer with a 150 W CW ozone-free xenon lamp as an excitation source was used for PL measurements. TL glow curves of the samples excited with 254 nm UV radiation for 10 min were recorded at a heating rate of 5 K/s using a TL 10091 NUCLEONIX instrument. The CL spectra were measured using both a Gatan MonoCL4 accessory fitted to the JEOL JSM-7800F system as well as in a PHI 549 Auger electron spectrometer using an Ocean Optics PC2000 spectrometer. Auger electron spectroscopy (AES) was performed simultaneously with CL measurements to monitor the relationship between CL degradation and surface reactions during prolonged electron bombardment.

4.3 Results and discussion

4.3.1 Structure and morphology

Figure 4.2(a) shows the XRD patterns of $Gd_{2-x}O_3$:$Bi_{x=0.002}$ annealed at various temperatures between 800 to 1200 °C. The XRD patterns are in agreement with the JCPDS standard #43-1014 of the cubic phase of Gd_2O_3. The structure of cubic Gd_2O_3 has been formed at the lowest annealing temperature and has not changed with the increasing temperature. No monoclinic Gd_2O_3 or extra phases were observed and no shift occurred in the diffraction angles, which means that there was no change in the structure with the increasing annealing temperatures of the Gd_2O_3 matrix. The average crystallite size was calculated by the Scherrer equation by using the 2θ full width at half maximum of the high-intensity diffraction peak [33]. The calculated average crystallite sizes and the results are tabulated in table 4.1.

Table 4.1 Crystallite size D of $Gd_{2-x}O_3:Bi_{x=0.002}$ after it was annealed at different temperatures

Sample	**Crystallite size *D* (nm)**
800 °C	46
900 °C	47
1000 °C	49
1100 °C	53
1200 °C	54

A slight increase in the average crystallite size with increasing annealing temperature was observed. Figure 4.2(b) shows the XRD patterns of $Gd_{2-x}O_3:Bi_x$ powders with x varying from 0 to 0.006 annealed at 1000 °C. The addition of Bi in the Gd_2O_3 matrix did not change the structure, as might be expected due to the similar ionic radii of Bi^{3+} and Gd^{3+} given earlier. A decrease in crystallite size with an increase in the Bi concentration was observed, which the results are tabulated in table 4.2.

Table 4.2. $Gd_{2-x}O_3:Bi_x$ for different doping concentrations after annealing at 1000 °C.

Sample	**Crystallite size *D* (nm)**
Gd_2O_3	52
$Gd_{2-x}O_3:Bi_{x=0.0005}$	51
$Gd_{2-x}O_3:Bi_{x=0.0009}$	50
$Gd_{2-x}O_3:Bi_{x=0.002}$	49
$Gd_{2-x}O_3:Bi_{x=0.003}$	49
$Gd_{2-x}O_3:Bi_{x=0.004}$	48
$Gd_{2-x}O_3:Bi_{x=0.006}$	47

51.6 nm for the un-doped sample, 51.2 nm for x = 0.0005, 50.3 nm for x = 0.0009, 49.3 nm for x = 0.002, 49.1 nm for x = 0.003, 48.7 nm for x = 0.004 and 47.8 nm for x = 0.006. The slight difference in the size of the radii may have caused a strain field or stress that disturbed the grain growth process or some of the dopant might have formed a diffusion barrier at the grain boundaries.

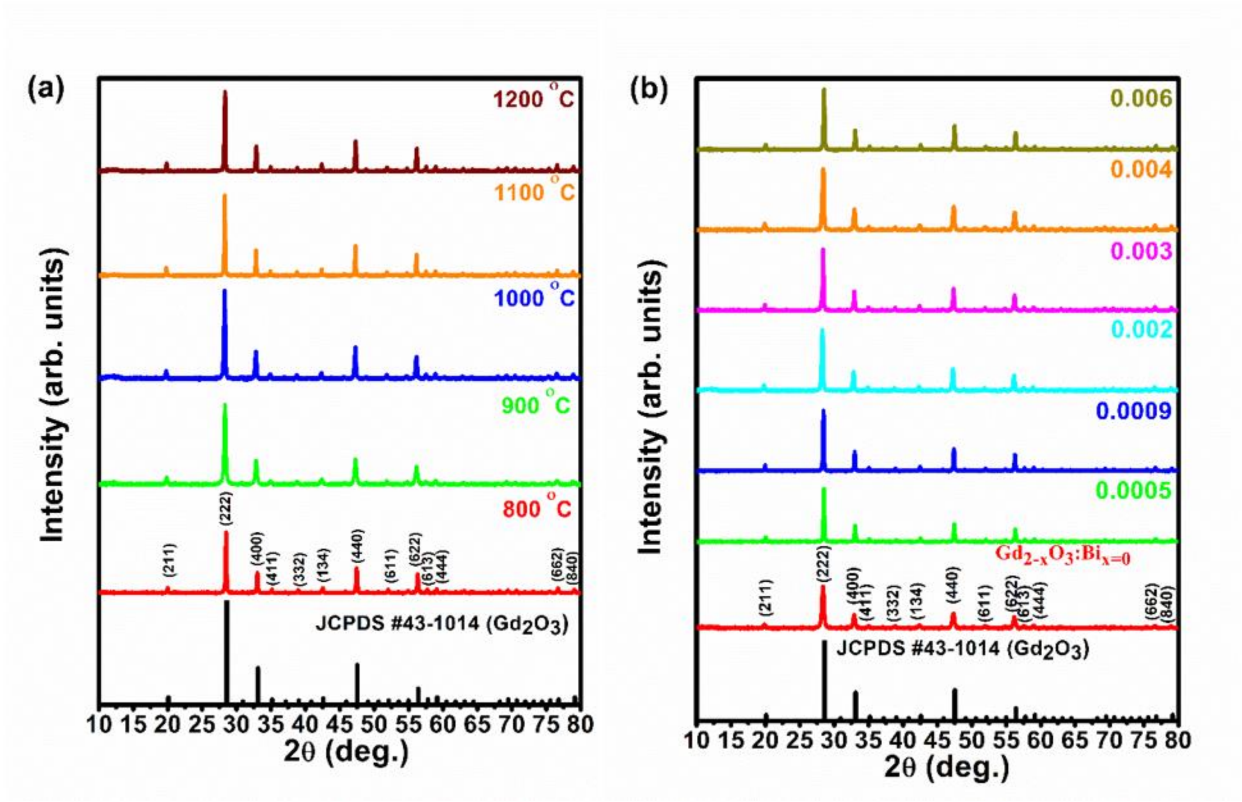

Figure 4.2: XRD patterns of (a) $Gd_{2-x}O_3$:$Bi_{x=0.002}$ after it was annealed at different temperatures. (b) $Gd_{2-x}O_3$:Bi_x for different doping concentrations after annealing at 1000 °C.

Figure 4.3 shows SEM images of the $Gd_{2-x}O_3$:$Bi_{x=0.002}$ phosphor after annealed at various temperatures. Figure 4.3(a) shows that the sample annealed at 800 °C has a non-uniform morphology of flake-like particles. Then when annealed at 900 °C, irregular microstructures were observed as in figure 4.3(b). For an annealing temperature of 1000 °C, figure 4.3(c) shows a homogeneous microstructure has formed with small grains that were highly agglomerated with an open porosity, where diffusion and growth as well as agglomeration to form bigger particles with size greater than 100 nm has occurred. When the temperature was increased to 1100 °C, figure 4.3(d) displays irregular crystallites formed with larger particles having spherical and more longitudinal shapes. The sample annealed at the highest temperature of 1200 °C shown in figure 4.3(e) has bigger spherical particles grown by diffusion with diameter close to 400 nm. These changes in the morphology of the cubic Gd_2O_3 annealed at different temperatures prepared by solid-state reaction were also reported by Tamrakar *et al.* [6] who observed the increase in agglomeration of the smaller nanoparticles into bigger particles with increasing temperature.

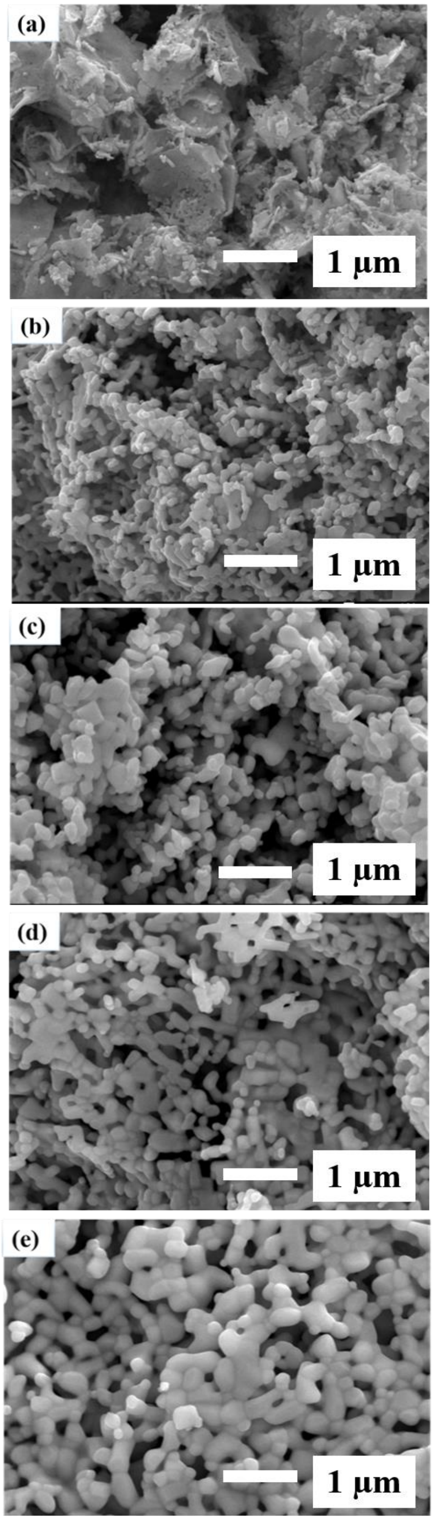

Figure 4.3: SEM images of the Gd$_{2\text{-}x}$O$_3$:Bi$_{x=0.002}$ samples after annealed at the different temperatures for (a) 800 °C, (b) 900 °C, (c) 1000 °C, (d) 1100 °C and (e) 1200 °C.

Figure 4.4 shows the SEM images for the samples of $Gd_{2-x}O_3:Bi_x$ doped at different concentrations, after annealing at 1000 °C. There is no systematic change in the morphology.

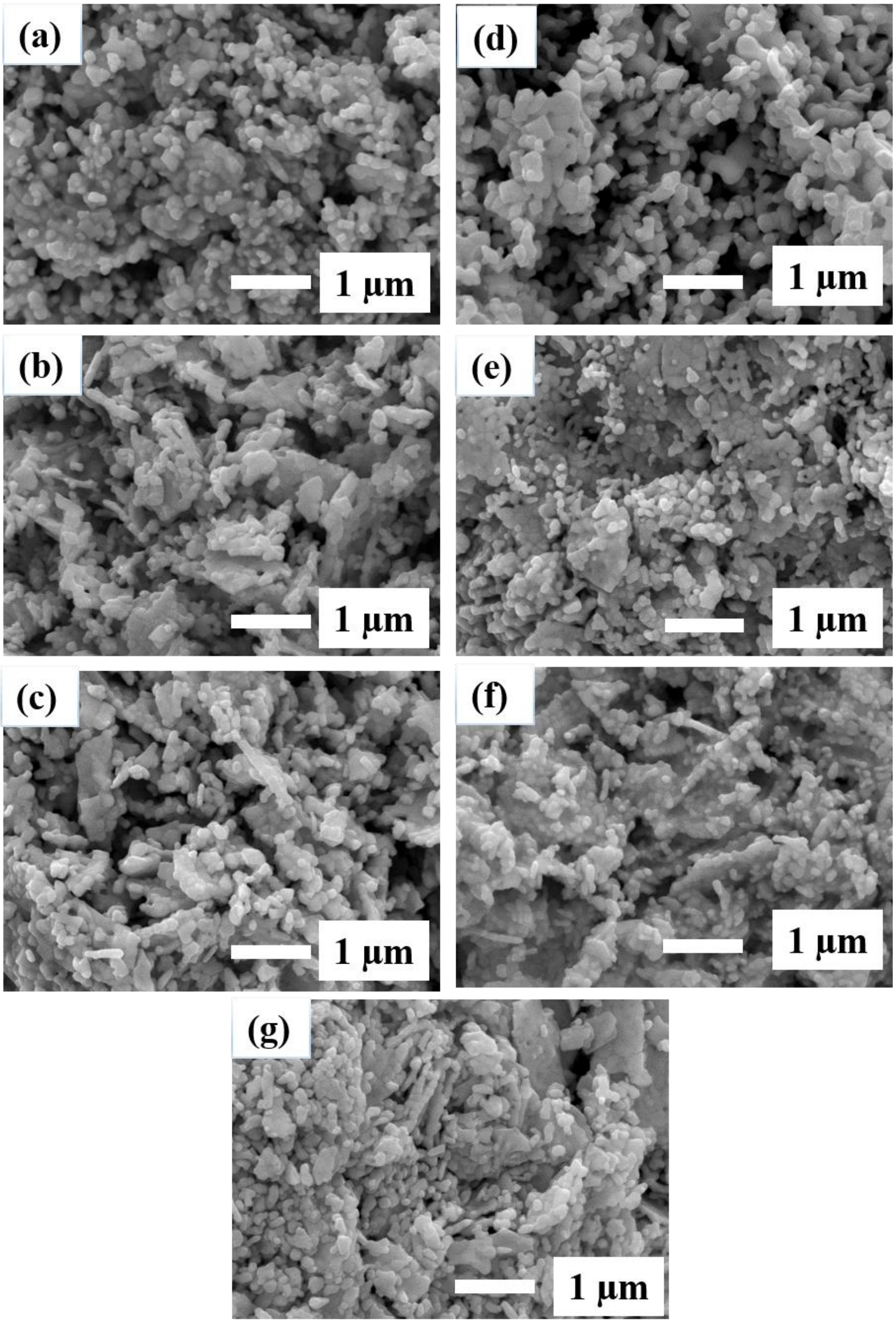

Figure 4.4: SEM images of $Gd_{2-x}O_3:Bi_x$ samples doped with different concentrations of Bi^{3+} (x) (a) 0, (b) 0.0005, (c) 0.0009, (d) 0.002, (e) 0.003, (f) 0.004 and (g) 0.006, were annealed at 1000 °C for 2 hours in air.

4.3.2 Diffuse reflection spectra and band gap calculations

Figure 4.5(a) shows the DR measurements for the Gd_2O_3 host sample, as prepared and annealed at 800 and 1000 °C. The spectra contain several absorption bands in the near UV region. The strong band at about 227 nm corresponds to inter-band transitions of the Gd_2O_3 matrix [34]. The absorption bands at 275 and 315 nm can be attributed to the 4f-4f optical transitions of the Gd^{3+} ion from the ground $^8S_{7/2}$ to the excited ^6I_J and ^6P_J states, respectively [35]. The weak absorption band near 250 nm is probably due to another 4f-4f transition of the Gd^{3+} ion from $^8S_{7/2}$ to ^6D_J, which is similar to that observed in other rare-earth doped Gd_2O_3 systems [36,37]. The DR data (R_∞) can be transformed into values proportional to absorbance by using the Kubelka–Munk equation [38]

$$F(R_\infty) = (1 - R_\infty)^2/(2R_\infty). \qquad (4.2)$$

The optical band gap energy was then calculated using the well-known Tauc law relation [39]

$$\alpha hv = C(hv - E_g)^m \qquad (4.3)$$

where $F(R_\infty)$ was substituted for the absorption coefficient (α), $h\nu$ is the incident photon energy, C is a constant, E_g is the optical band gap energy and m = ½ for a direct bandgap material such as Gd_2O_3. Plotting $[F(R_\infty)hv]^2$ against hv and extending a linear fit to the energy axis as shown by figure 4.5(b) allowed the determination of E_g as 5.09 for the as prepared sample and 5.15 eV and 5.18 eV for the samples annealed at 800 and 1000 °C, respectively. The optical band gap increased when the annealing temperature increased and was similar to the value of 5.09 eV from the literature [35]. The decrease in the band gap may be due to a variety of crystal defects in the structures of the lower annealing samples, which may lead to intermediate energy levels merging with the conduction band, and lowering the band gap.

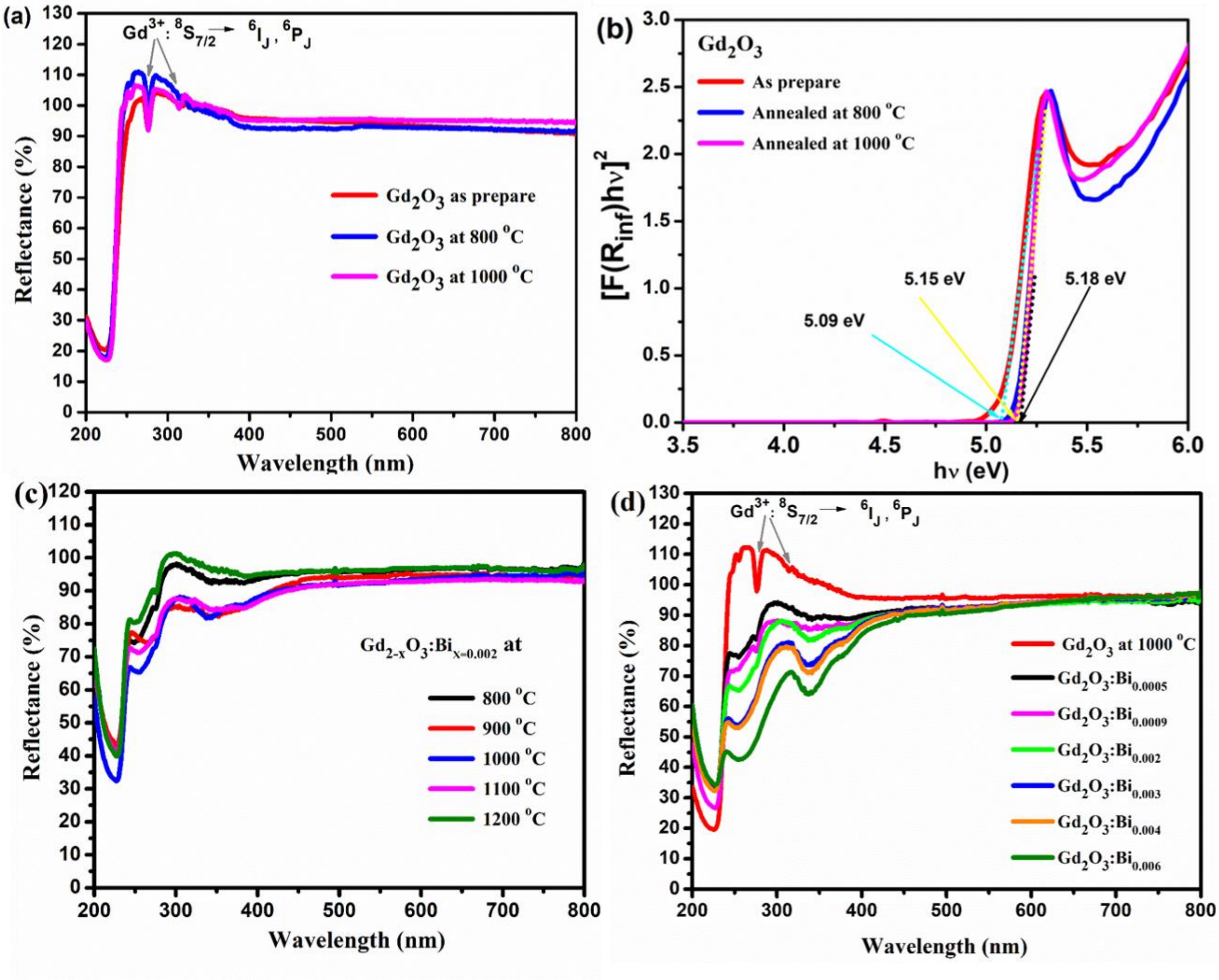

Figure 4.5: DR spectra of (a) Gd_2O_3 and (b) Tauc plot to determine the bandgap. (c) DR spectra of $Gd_{2-x}O_3:Bi_{x=0.002}$ after different annealing temperatures, and (d) DR spectra of $Gd_{2-x}O_3:Bi_x$ samples annealed at 1000 °C.

Figure 4.5(c) shows the DR spectra of doped samples (x = 0.002) annealed at various temperatures. All the samples showed an absorption edge around 227 nm, which corresponds to the optical band gap of Gd_2O_3. There are another three bands, located around 260, 335 and 375 nm, which were the same as the maximum PL luminescence excitation wavelengths as shown in the next section; therefore these bands are due to the excitation transitions of Bi^{3+} ions. The strength of these absorption bands increased when the temperature was increased to 1100 °C and then decreased at a higher temperature, to become almost similar to the host. This may be due to a loss in Bi^{3+} as volatile species at the higher annealing temperatures. Figure 4.5(d) shows the DR measurements for the various doped samples. The same four absorption band edges were observed and those associated with Bi^{3+} increased with the doping concentration as expected. The presence of enhanced light absorption peaks could be attributed to the possible introduction of more defects within the bandgap, which may accelerate the production of electron–hole pairs, thus improve the photocatalytic performance.

4.3.3 Photoluminescence properties

Figure 4.6(a) shows the effect of the annealing temperature on the PL excitation and emission spectra for $Gd_{2-x}O_3:Bi_{x=0.002}$ samples annealed at various temperatures. The spectra show the luminescence excited at 375 nm with the emission in the blue range centred at 418 nm. The PL intensity increased with the annealing temperature up to 1000 °C and then decreased, as shown by the inset. The reason for the intensity increase up to 1000 °C may be the increased crystallinity of the samples. Since the Bi^{3+} ions are very sensitive to the surrounding environment, therefore any defect such as (surface defects, grain boundaries, dislocations, impurity atoms, stacking faults, strain, ... etc) affects in principle emission of Bi^{3+} by changing the emission energy or by destroying all luminescence properties. Thus the luminescence intensity may be expected to increase with annealing temperature due to improvement of the crystalline quality and elimination of defects. Zou *et al.* [5] reported that the emission intensity of monoclinic Gd_2O_3:Bi phosphors was greatly enhanced by calcination at higher temperatures. The decrease in the intensity above 1000 °C may be due to the high volatility of Bi which causes it to vaporize and therefore leave the sample surface. Jafer *et al.* [39] reported that the emission intensity of the luminescence of Y_2O_3:Bi phosphor was strongly affected by the reaction temperatures and that a decrease in the luminescence intensity occurred due to the fact that the majority of the Bi ions evaporated from the sample surfaces as volatile species.

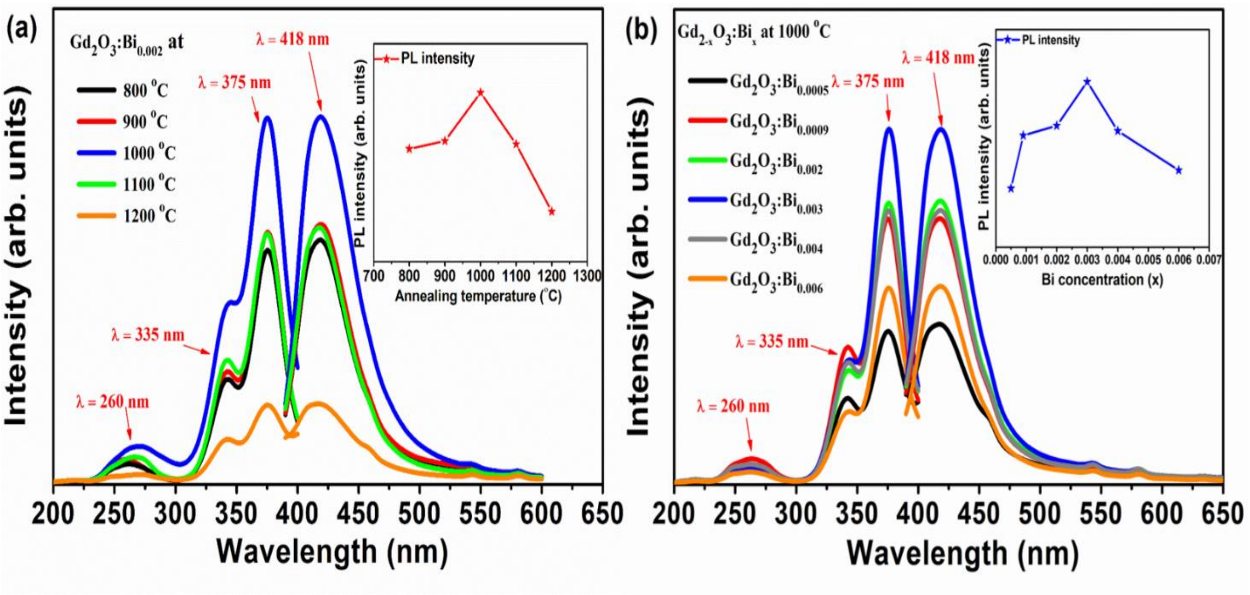

Figure 4.6: PL excitation and emission spectra of (a) $Gd_{2-x}O_3$:$Bi_{x=0.002}$ produced using different annealing temperatures. The inset shows the maximum PL intensity of 418 nm as a function of annealing temperature, (b) $Gd_{2-x}O_3$:Bi_x phosphor for different concentrations of Bi^{3+} annealed at 1000 °C. The inset shows the maximum PL intensity (at 418 nm) as a function of Bi^{3+} concentration.

The effect of the Bi^{3+} concentration on the emission of the $Gd_{2-x}O_3$:Bi_x phosphors annealed at 1000 °C was also investigated. The PL excitation and emission for x = 0.0005, 0.0009, 0.002, 0.003, 0.004 and 0.006 are shown in figure 4.6(b). The spectra show the emission in the blue range centred at 418 nm when excited at 375 nm. For our samples, figure 4.6(b) shows that the PL intensity of the sample having x = 0.003 was the maximum.

Bi^{3+} has excited states of $^3P_0$, $^3P_1$, $^3P_2$, and $^1P_1$ in sequence of increasing energy, while the ground state electronic configuration [Xe] $4f^{14}5d^{10}6s^2$ has a single level $^1S_0$. Excitation peaks can occur for transitions from $^1S_0$ to $^3P_1$, $^3P_2$ and $^1P_1$ which are usually denoted as A, B and C, respectively [26]. The transitions $^1S_0\rightarrow{}^3P_0$ and $^1S_0\rightarrow{}^3P_2$ are spin forbidden, while spin-orbit coupling of the $^1P_1$ and $^3P_1$ levels means that the $^1S_0\rightarrow{}^3P_1$ transition is generally observed [26]. Fukada *et al*. [26] reported that intense blue PL emissions were observed from all Bi-activated Gd_2O_3 cubic phosphor thin films post annealed at a high temperature. The PL emission from the optimum $Gd_{2-x}O_3$:$Bi_{x=0.003}$ phosphor powder annealed at 1000 °C was evaluated under 260, 335 and 375 nm excitation as shown in figure 4.7(a), which were also the wavelengths of the absorption bands noted earlier for DR spectra of the Bi^{3+} doped samples. Either blue emission with a single broad peak at around 418 nm or blue-green emission consisting of broad peaks from 400 to 600 nm was observed when exciting at 375 and 335 nm, respectively. For green emission at 505 nm two excitation bands were observed in the 200 - 400 nm range, with maxima at 260 and 335 nm. For blue emission at 418 nm three excitation bands were observed in the 200 – 400 nm range with the maxima at 260, 335 and 375 nm. When excited by 375 nm the only emission was the blue emission at 418 nm, while when excited by 260 nm the same blue peak at 418 was observed with a low intensity. If excited at 335 nm UV light, a similar emission was obtained as a shoulder with another extra broad green emission centred around 505 nm [26]. The excitation band centred at 335 nm is a result of the excitation of the Bi^{3+} ion in the C_2 site, while the band centred at 375 nm is a result of the excitation of the Bi^{3+} ion in the S_6 site [22]. The luminescence is similar to that of Y_2O_3:Bi reported by Zou *et al.* [22]. Due to the high sensitivity of the Bi to its environment, the emission spectra are dependent on the position of the Bi^{3+} in the Gd_2O_3 matrix. The blue and green emissions are ascribed to the Bi^{3+} occupying S_6 and C_2 symmetry, respectively. The energy level schemes of free Bi^{3+} ions and the split energy levels under S_6 and C_2 symmetry are shown in figure 4.7(b). The emission band at 418 nm can be assigned to the transition $^3E_u \rightarrow {}^1A_g$ of Bi^{3+} at the S_6 site [23, 40]. These transitions match well the results reported before for this material (see e.g. [23,24, 27,39]) and reveal two PL bands due to two nonequivalent cation sites in Gd_2O_3 (or Y_2O_3). Thus, the excitation bands of the blue emission centred at 260 and 375 nm can be assigned to the transitions $^1A_g \rightarrow {}^3A_u$ and $^1A_g \rightarrow {}^3E_u$ of Bi^{3+} ion at the S_6 site, respectively. The green emission band centred at 505 nm can be ascribed to the $^3B \rightarrow {}^1A$ transition of Bi^{3+} at the C_2 site, while the transitions $^1A \rightarrow {}^3A$ and $^1A \rightarrow {}^3B$ of the Bi^{3+} ion under C_2 symmetry are responsible for the excitation bands at 330–345 nm monitored at the green emission of 505 nm. We therefore interpret the short wavelength shoulder of the broad Gd_2O_3:Bi emission excited at 335 nm in figure 4.7(a) as originating from the upper $^3A \rightarrow {}^1A$ transition of Bi^{3+} at the C_2 site, with the emission at 505 nm (reported at 542 nm by Awater and Dorenbos [40]) therefore being associated not with a charge transfer emission, but originating from the $^3B \rightarrow {}^1A$ transition of Bi^{3+} at the C_2 site. Some overlap of the excitation bands of Bi^{3+} at the S_6 and C_2 sites may also allow a partial contribution of emission at 418 nm from Bi^{3+} at the S_6 site to the shoulder observed in the emission excited at 335 nm. Lee *et al.* [41] report that the PL spectrum of cubic Y_2O_3:Bi which was very similar to our emissions spectra from cubic Gd_2O_3:Bi with a slight difference in wavelength positions with the same S_6 and C_2 symmetry in the structure. The report revealed two Bi^{3+} emission bands, a narrow band centred at 409 nm and a broad band centred at 490 nm, originating from S_6 and C_2 sites that Bi^{3+} ions may occupy within the Y_2O_3 host lattice. The emission at 409 nm showed two excitation bands, one centred at 330 nm and another at 390 nm. For the 490 nm emission, two excitation bands were also observed centred at 330 nm and 345 nm. Scarangella *et al.* [42] reported that the PL spectrum of cubic Y_2O_3:Bi thin films have wavelength positions with S_6 and C_2 symmetry in the structure. When the emission wavelength is fixed at 406 nm the two excitation peaks at 334 nm and 368 nm which associated to the $^1S_0 \rightarrow {}^3P_1$ transition, where the $^3P_1$ excited state splits in the doublet [^3A_u, ^3E_u] typical of Bi^{3+} in the S_6 site. Therefore under 368 nm, corresponding to the $^1S_0 \rightarrow {}^3P_1$ (^3E_u) transition of Bi^{3+} in S_6 site, the sharp blue emission at 406 nm is observed. When the emission wavelength is fixed at 500 nm, the broad and asymmetric excitation band peaked at 330 nm it can be ascribed to the same transition $^1S_0 \rightarrow {}^3P_1$, where $^3P_1$ splits in the triplet [^3A, ^3B, ^3B] owing to the presence of the crystalline field and the occurrence of spin-orbit coupling when Bi^{3+} is in the C_2 site. The location of the cation within the host material is very important as it determines the optical and physical properties of the final material. But Y_2O_3 and Gd_2O_3 have similar crystal structures and therefore Bi^{3+} doped in them has the same energy level structure for PL although they have different wavelengths of the excitation/emission bands. Thus the cause for the changes in the emission intensity may be due to changes in the surrounding environment of Bi^{3+} when introduced into the host material due to lattice distortions caused by the difference in ionic radius between the Y^{3+} ion (90 pm), Gd^{3+} ion (93.8 pm) and the Bi^{3+} ion (103 pm) [29], because Bi^{3+} ions are very sensitive to the surrounding environment, resulting in the different peaks wavelength of Bi^{3+} emissions in different hosts. The tabulation of Bi^{3+} emissions in different hosts by Awater and Dorenbos [40] includes that of Gd_2O_3:Bi (considering the C_2 site) excited at 347 nm has emission bands at 425 and 542 nm which they attributed to the A band and charge transfer (CT) emission, respectively, with a similar scheme for the other Bi^{3+} doped cubic oxides Y_2O_3, Lu_2O_3 and Sc_2O_3. In contrast, Scarangella *et al.* [43] used temperature dependent measurements of Bi^{3+} doped Y_2O_3 excited at 325 nm to motivate that the two observed emission wavelengths, 430 nm and 500 nm, originated from the upper and lower levels of the crystal field split $^3P_1$ energy level of Bi^{3+} ions at the C_2 symmetry site.

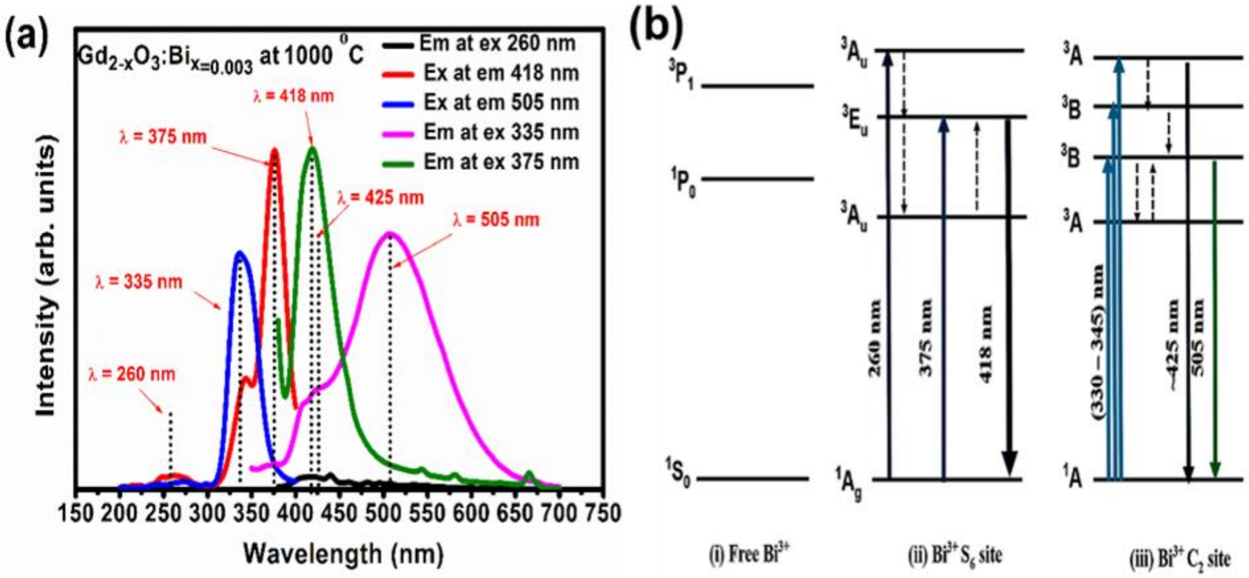

Figure 4.7: (a) Emission and excitation spectra of optimized sample. (b) The energy level schemes of Bi^{3+} ion. (i) Free Bi^{3+} ion. (ii) The split energy levels under S_6 symmetry. (iii) The split energy levels under C_2 symmetry.

The Commission Internationale de l'Eclairage (CIE) chromaticity diagram [44] was used to illustrate the colour of the $Gd_{2-x}O_3:Bi_{x=0.003}$ phosphor under excitation at 260, 335 and 375 nm and is shown in figure 4.8. The colour coordinates for the emitting phosphor are situated in the blue-green region and have significant variation with excitation wavelength. This is in contrast to monoclinic Gd_2O_3:Bi which shows little variation of its emission wavelength when the excitation wavelength is varied [5].

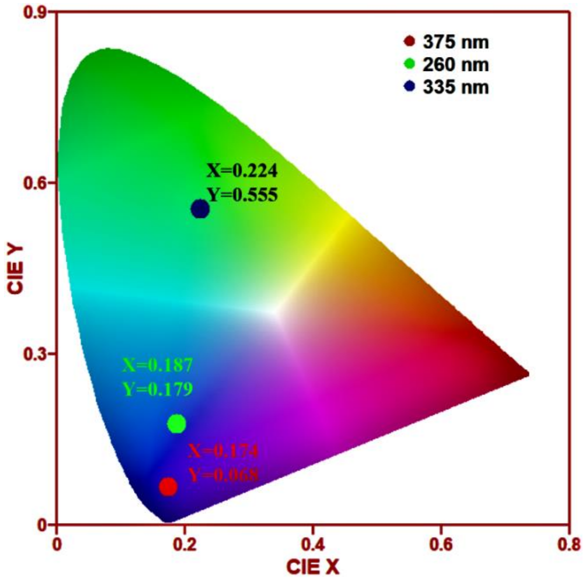

Figure 4.8: CIE coordinates for emission of optimized sample at different excitation wavelengths 375 nm, 260 nm and 335 nm.

4.3.4 Thermoluminescence studies

TL measurements are used to investigate the defect levels in the bandgap of insulating or semiconducting materials. The trap levels react differently to different heating rates, due to the different characteristics of trapped charge carriers [32]. Glow curves giving the intensity of light as a function of time or temperature may be used to determine the traps created or activated in an emitting material that has been exposed to ionizing radiation. TL glow peak temperature and intensity depend on various parameters such as the nature and structure of the sample, including the impurity content and crystallinity. Some factors influenced the measurements, such as heat treatment given to the sample before irradiation, the nature of the ionizing radiation, the amount of irradiation (dose), temperature at which the TL measurements are made, the time interval between the measurements, the environment condition of the sample during TL measurements, the type of detector and the heating rate [45].

Figure 4.9(a) shows the TL glow curves of $Gd_{2-x}O_3:Bi_{x=0.002}$ which had been annealed at various temperatures, after exposure to UV radiation for 15 min. The TL was recorded at a heating rate of 5 Ks^{-1}. Two broad peaks with maxima at about 365 K and 443 K were obtained for all the samples. These peaks are due to the presence of V^{-} centres and oxygen vacancies [46] and no shift in the maximum peak temperatures was observed. The presence of oxygen vacancies causes some electronic states to appear above and below the Fermi level in the case of the bulk electronic structure for the cubic Gd_2O_3 phases. So, maybe Bi^{3+} make strong distortions of the periodic distribution of the electronic densities of states, because of the localized point-defects of the crystalline lattice. However, as shown in figure 4.9(a), the structure of the TL glow curves is strongly affected by the annealing temperature. The maximum intensity was obtained for the sample annealed at 800 °C. With an increase of the annealing temperature to 900 °C, the height of the low and main temperature peaks started to decrease, which may be attributed to the existence of trapping levels at different energies below the conduction band [47]. Then at 1000 °C, the height of the main peak increased again which may be attributed to the dissolution of the defect complexes. Then when the annealing temperature was increased at 1100 and 1200 °C the height of the low and main temperature peaks starts to decrease which may be attributed to the increasing effect on the sensitivity of lower concentration of Bi in the Gd_2O_3 matrixes as a result of volatilization at high temperatures. The inset of figure 4.9(a) shows the variation of the TL glow peak intensity at 364 K as a function of annealing temperatures. It presented an irregular arrangement of the TL glow peak intensity with annealing temperature, which means there is a correlation between the TL area and the amount of energy released during the combustion (heat of combustion).

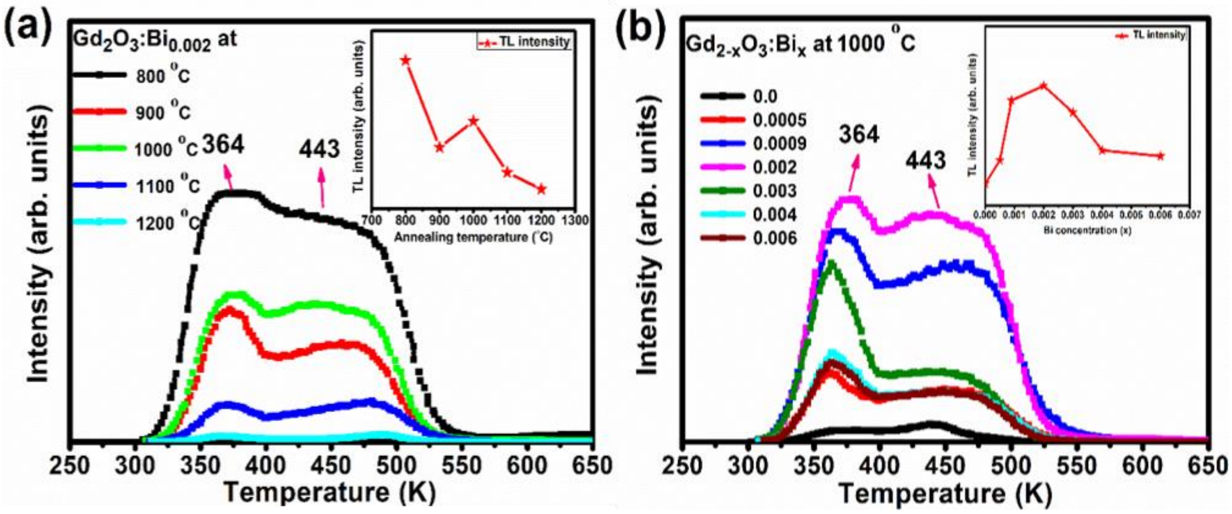

Figure 4.9: (a) TL glow curves of $Gd_{2-x}O_3$:$Bi_{x=0.002}$ after different annealing temperatures. The inset shows the variation of the TL glow peak intensity at 364 K as a function of annealing temperature. (b) TL glow curves of $Gd_{2-x}O_3$:Bi_x for different concentrations of Bi^{3+} annealed at 1000 °C. The inset shows the variation of the TL glow peak intensity at 364 K as a function of Bi^{3+} concentration.

TL glow curves of undoped Gd_2O_3 and $Gd_{2-x}O_3$:Bi_x (x = 0.0005, 0.0009, 0.002, 0.003, 0.004 and 0.006) annealed at 1000 °C and exposed to UV rays for 10 min are shown in figure 4.9(b). For the undoped sample the TL intensity was very small, but it increased with Bi^{3+} concentration and reached a maximum at x = 0.002. It then decreased after further increasing of Bi^{3+} concentration, as shown in the inset of figure 4.9(b). When the Bi concentration was increased it caused an increase in the concentration of the recombination centres. Yousif *et al.* [30] and Lyu and Dorenbos [48] reported that Bi^{3+} may act as both an electron and hole trap and Bi^{3+} also can act as a deep electron trapping centre in Y_2O_3 and YPO_4. The increasing the Bi concentration may be lead to a restructuring of traps in the Gd_2O_3 host crystal lattice was caused by the incorporation of Bi ions into the host lattice. This resulted into deeper traps, which suggest that the incorporation of Bi^{3+} ions was responsible for the creation of additional electron traps [30].

To understand the TL glow curve behaviour of the $Gd_{2-x}O_3$:Bi_x it is important to evaluate the kinetic parameters. A glow-curve deconvolution procedure (GCD) was applied to the data analysis using the TLAnal program [49]. The TL light intensities for the first, second and general order kinetic processes have been given by Randall-Wilkins, Garlick-Gibson and May Partridge [50] respectively and are expressed as

$$\mathrm{I(t)} = nse^{-E/kT} \qquad (4.4)$$

$$\mathrm{I(t)} = (n^2/N)\, se^{-E/kT} \qquad (4.5)$$

$$\mathrm{I(t)} = n^{b\,s}\; e^{-E/kT} \qquad (4.6)$$

where E is the activation energy for the TL process or trap depth, k is the Boltzmann constant, t the time, T the absolute temperature, s a constant pre-exponential frequency factor (or attempt to escape frequency), n the concentration of trapped electrons at time t, b the kinetic order with values typically between 1 and 2 and N the total trap concentration. The integration of equations (4.4), (4.5) and (4.6) for a linear heating rate β, are respectively [50,51]

$$\mathrm{I(t)} = n_0 s \exp(-E/kT) \exp\left[-s/\beta \int_{T_0}^{T} \exp\left(-\frac{E}{kT'}\right) dT'\right] \qquad (4.7)$$

$$\mathrm{I(t)} = n_0^2 s' \exp(-E/kT) \exp\left[-s/\beta \int_{T_0}^{T} \exp\left(-\frac{E}{kT'}\right) dT'\right] \qquad (4.8)$$

$$\mathrm{I(t)} = s'' n_0^2 \exp(-E/kT) \exp\left[1 + s''(b-1)/\beta \int_{T_0}^{T} \exp\left(-\frac{E}{kT'}\right) dT'\right]^{(-b/(b-1))} \qquad (4.9)$$

where β is the heating rate, T_0 is the initial temperature, n_0 is the initial number of filled traps and the parameter $s'' = s' \ n_0^{(b-1)}$ [52]. Two samples with Bi concentrations x = 0.002 and 0.003 annealed at 1000 °C were chosen since these have the maximum TL intensity and optimum PL emission and the results are presented in figure 4.10 and Table 4.3. The samples showed two broad glow peaks and each glow peak consisted of more than one peak, five peaks for both samples x = 0.002 and 0.003, peaks located at 356, 380, 417, 447 and 480 K were fitted into the TL glow curve for both samples, which indicated that more than one trap was responsible for each glow peak. The determined TL peaks that corresponded to the order of kinetics, trap depth (activation energy) values are tabulated in Table 4.3. The similarity of certain peaks in the nanopowder samples suggests that the defects responsible for the traps may be similar, while the slightly different energy depths may be below the conduction band due to synthesis conditions and/or structural disorder. In Table 4.3 it is noticed that the strong intensity peaks were attributed to the second-order kinetics which indicated that the retrapping probability was greater [30]. The calculated frequency factors for all deconvoluted peaks are tabulated in Table 4.3. The obtained values are closed to the normal lattice vibration in the materials [53]. The densities of traps were found to be a maximum for peak 5 for samples (0.002) and peak 1 for sample (0.002). From these results, it was concluded that the trap depth and frequency factors are reasonably good for Gd_2O_3:Bi under UV exposure and the high trap density peak may be suitable for dosimeter studies.

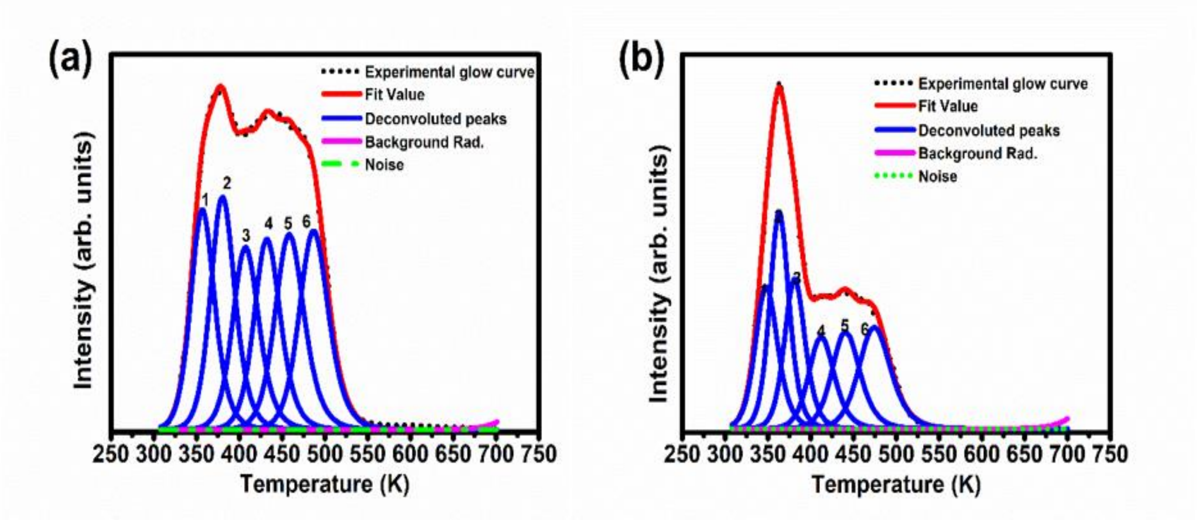

Figure 4.10. Glow curve deconvolution of (a) $Gd_{2-x}O_3:Bi_{x=0.002}$ and (b) $Gd_{2-x}O_3:Bi_{x=0.003}$ annealed at 1000 °C.

Table 4.3 Trapping parameters obtained from the TL glow curves of the $Gd_{2-x}O_3:Bi_{x=0.002}$ and the $Gd_{2-x}O_3:Bi_{x=0.003}$ samples.

Sample	**Peak**	**Peak position (K)**	**Order of kinetics**	**Activation energy (eV)**	**Frequency factor (s^{-1})**	**Trap density (arb. units)**
$Gd_{2-x}O_3:Bi_{x=0.002}$	1	356	2	1.1	6.4×10^{8}	3.3×10^{6}
	2	380	2	1.2	5.7×10^{8}	3.8×10^{6}
	3	417	2	1.3	1.3×10^{9}	3.4×10^{6}
	4	447	2	1.3	3.9×10^{9}	3.6×10^{6}
	5	480	2	1.5	8.8×10^{9}	4.5×10^{6}
$Gd_{2-x}O_3:Bi_{x=0.003}$	1	356	2	1.1	6.6×10^{8}	2.1×10^{6}
	2	380	2	1.2	1.3×10^{9}	2.2×10^{5}
	3	417	2	1.3	5.9×10^{9}	9.4×10^{5}
	4	447	2	1.4	4.2×10^{9}	1.2×10^{6}
	5	480	2	1.5	2.9×10^{9}	1.3×10^{6}

4.3.5 Cathodoluminescence properties

Figure 4.11 shows the CL spectra for the samples measured with the Gatan system connected to the SEM for an electron energy of 5 keV in a vacuum of the order of 10^{-5}–10^{-6} Torr. Figure 4.11(a) shows the CL spectra of $Gd_{2-x}O_3$:$Bi_{x=0.002}$ annealed at various temperatures. Similar to the PL emission, the intensity first increased for the samples annealed up to 1000 °C and then decreased, as shown by the inset of figure 4.11(a). The effect of doping concentration on the CL of $Gd_{2-x}O_3$:Bi_x phosphors annealed at 1000 °C is given in figure 4.11(b). The inset shows the variation of intensity as a function of Bi concentration and the sample doped with x = 0.003 has the highest CL intensity, as for the PL emission. The CL consists of two emission bands: a blue band centred at 418 nm and a green band centred at 505 nm were observed for all the samples. As indicated in PL studies the blue and green emissions are ascribed to Bi^{3+} under S_6 and C_2 symmetry, respectively, suggesting that the electron beam did not change the electron energy level configuration or transitions of the activator ion in the phosphor. The broadening at longer wavelengths in the CL emission may be due to the large energy difference as well as the different mechanisms for the excitation. High energy electrons would excite the Bi^{3+} ions at both sites in the host lattice. Abdelrehman *et al.* [25] reported that CL excitation sources energy have the ability to excite Bi^{3+} ions as well as the host lattice. Scarangella *et al.* [41] reported that CL excitation sources for Y_2O_3:Bi thin films under electrical pumping have the ability to excite Bi^{3+} ions at both lattice sites C_2 and S_6 excitation energy. There was no shift in the main peak position at 418 nm between the PL and CL maximum intensity positions in the samples which is due to no change the electron energy level configuration of the Bi^{3+} ion in the phosphor. In Y_2O_3:Bi thin films a slight redshift (<10 nm) in the peak position between the PL and CL was reported [41], which was attributed to the presence of charge effects and local oxidation mechanisms in the Bi^{3+} since the energy position of Bi is strongly dependent on the ion environment.

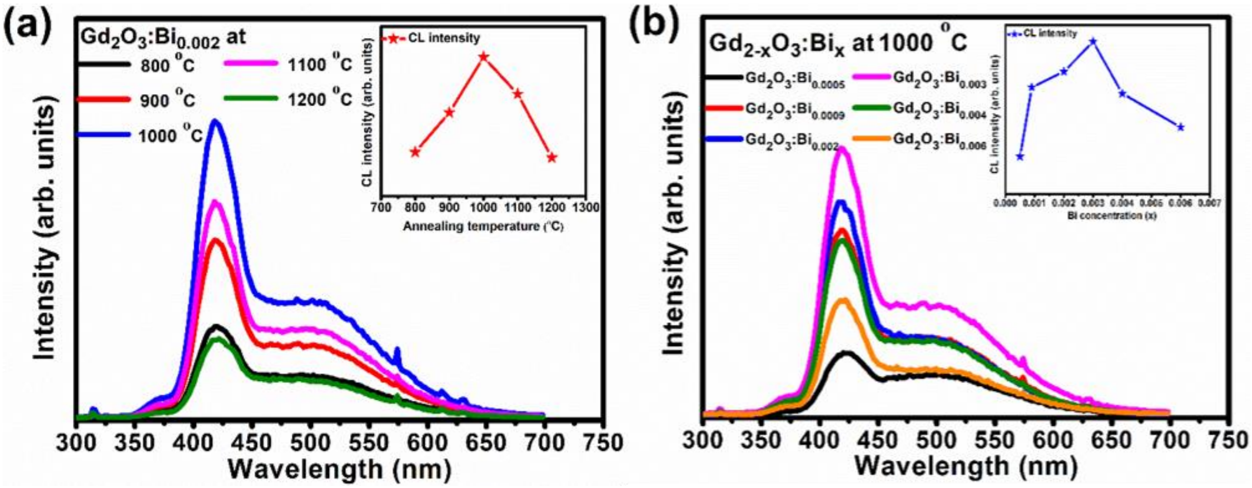

Figure 4.11: CL emission spectra for (a) $Gd_{2-x}O_3$:$Bi_{x=0.002}$ obtained after annealing at different temperatures. The inset shows the maximum CL intensity as a function of annealing temperatures. (b) $Gd_{2-x}O_3$:Bi_x phosphor for different concentrations of Bi^{3+} annealed at 1000 °C. The inset shows the maximum CL intensity as a function of Bi^{3+} concentration.

4.3.6 Surface analysis and CL degradation

Figure 4.12 shows the CL peak intensities of the $Gd_{2-x}O_3$:$Bi_{x=0.003}$ sample annealed at 1000 °C at 418 and 505 nm as a function of electron dose in (a) a vacuum with a base pressure of 1.3×10^{-8} Torr for around 100 h and (b) an oxygen partial pressure of 1.1×10^{-7} Torr for around 40 h, excited using an electron beam of 2.5 keV energy in the Auger system. The CL spectra are shown by the insets before and after the degradation process. The intensity of the peak at 505 nm is higher than that at 418 nm, which differs from the spectra recorded for the same sample using the Gatan system in the SEM at 5 keV. Since both these electron energies are orders of magnitude above the bandgap of the host material, it seems improbable to consider the differences in the CL spectra as due to different excitation processes or the interaction volume. However, there are very large differences in the beam currents and diameters which may influence the excitation dynamics and the relative abundance of phonons for the sample excited by the two systems. Further investigation of this for $Gd_{2-x}O_3$:Bi_x and other Bi-doped oxide phosphors is planned. By simultaneously monitoring the CL intensity and Auger peak-to-peak heights (APPHs) over time for 100 h in a vacuum and 33 h in O_2, the CL degradation and surface chemical changes of the phosphor could be directly correlated. For vacuum figure 4.12(a), the CL intensity for the peak at 418 nm reduced at around 150 C/cm^2

]

and stabilized thereafter, while the peak at 505 nm has slightly reduced up to an irradiation of about 450 C/cm^2 and then stabilized. With O_2 in figure 4.12(b), taking into account the smaller values of electron dose on the horizontal scale it is clear that the degradation rate was slightly faster, where the CL intensity for the peak at 418 nm reduced up to 50 C/cm^2 and then stabilized, while the peak at 505 nm slightly reduced up to an irradiation of about 150 C/cm^2 and then stabilized. A non-luminescent surface layer, which formed due to the electron-stimulated surface chemical reactions (ESSCRs) after removal of the C and Cl from the surface maybe was responsible for the CL degradation. So this layer it could be a layer with high defect density quenching luminescence, or maybe the surface layer becomes depleted of Bi or the Bi forms clusters in this layer which in either case would reduce the Bi^{3+} emission. The peak positions at 418 and 505 nm and the shape of the CL spectra remained the same before and after degradation, with only a small decrease in the intensity, especially in the vacuum where it decreased more than in O_2. The CL intensity in O_2 decreased more quickly in the beginning and then it settled continuously so that at the end of the measurements it was only about 70% of the initial value.

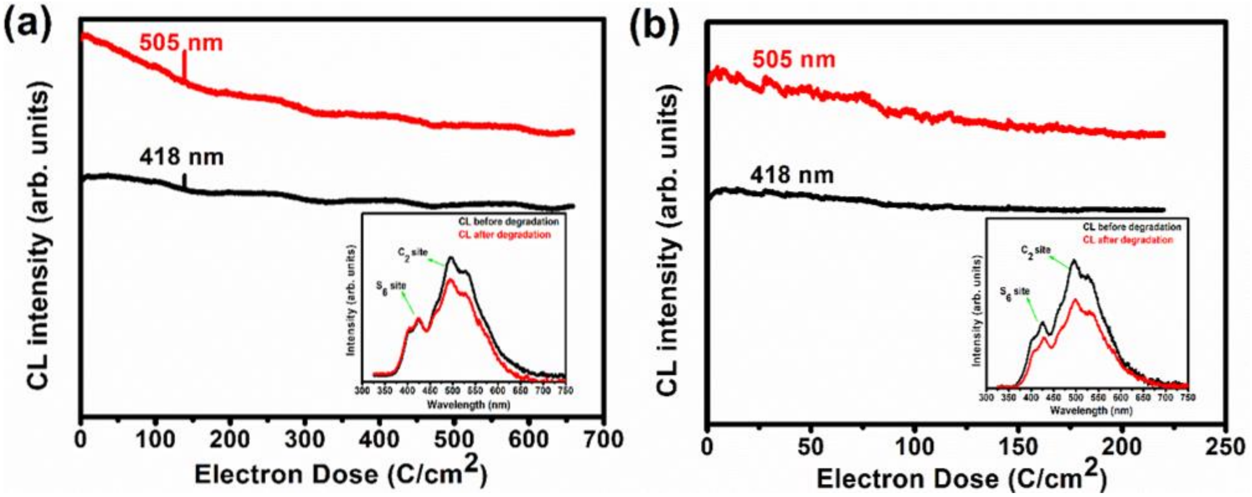

Figure 4.12: CL intensity as a function of electron dose exposure in (a) vacuum and (b) backfilled with oxygen. The insets represent the CL spectra before and after degradation.

Figure 4.13(a,b) show the Auger spectra of the $Gd_{2-x}O_3:Bi_{x=0.003}$ sample annealed at 1000 °C before and after electron beam exposure in (a) vacuum and (b) backfilled with oxygen. The presence of the elements of Gd_2O_3, namely Gd at the lower energy range 50–170 eV and O at 510 eV [54] were confirmed, but Bi was not observed due to its low concentration. Cl and C were detected (at

188 and 272 eV, respectively) before degradation and were attributed to adventitious impurity species on the surface due to handling and exposure to atmospheric pressure. The corresponding Auger peak-to-peak heights (APPHs) as a function of electron dose are presented in figure 4.13(c,d). During the period of electron beam exposure, the C and Cl Auger signals decreased or were almost eliminated as these elements were converted to volatile species (such as CO and CO_2) [55], which indicated that the contaminants were only present on the sample surface. In general, electron-stimulated surface chemical reactions (ESSCRs) occur when the electron beam dissociates the molecular O_2 and other residual gases that adsorb on the surface from molecular species to atomic/ionic species that will than react with C and Cl to form volatile compounds (CO_x, CH_4, etc.) [56]. The surface impurities (Cl and C) reduced at a faster rate in the O_2 atmosphere compared to the vacuum base pressure because the reaction of the O_2 with the adventitious species occurred at a higher rate to form volatile compounds for the irradiated sample [57]. Swart *et al.* [58] reported that the removal of carbonates from the surface of phosphors during degradation may occur due to ESSCRs. After 300 C/cm^2, no further degradation reactions occurred because the APPH signals remained constant after the ESSCR mechanism removed the Cl and C completely as shown in figure 4.13. The Auger signals associated with the host elements (Gd and O) are expected to increase when the C was removed from the surface, as reported for the degradation of oxides component such as SrO:Bi [25], ZnO [55,58] and La_2O_3:Bi [31]. Figure 4.13(c) for vacuum shows an increase in the APPH of Gd and O after an electron dose of about 30 C/cm^2, when most of the Cl and C contaminations have been removed from the surface. Figure 4.13(d) APPH in O_2, showing an increase in the decay rates of the Gd and O peaks very fast during oxygen uptake after an electron dose of about 30 C/cm^2 indicating oxygen-induced more segregation of Gd which maybe was then creating derivatives of Gd_2O_3. Swart *et al.* [57] reported that during the degradation of ZnS, the Zn increased during oxygen uptake, indicated oxygen-induced segregation of Zn which was then converted into either ZnO or $ZnSO_4$. Also, Swart *et al.* [59] reported that a thin SrO surface layer formed during electron bombardment of $SrAl_2O_4$:Eu^{2+},Dy^{3+} in oxygen pressure. The CL degradation can also be explained by the ESSCRs as reported by Swart *et al.* [59], Hasabeldaim *et al.* [58], Abdelrahman *et al.* [25] and Jaffar *et al.* [31]. Abdelrehman *et al.* [25] reported that some changes in the surface character and the presence of defects played a crucial role in the CL emission and degradation of SrO:Bi. The presence of surface contamination such as C and Cl initially severely affected the CL degradation. Which causes the CL emission

intensity degrades due the formation and possibly diffusion of point defects during electron beam irradiation. The sample became stable after some initial effects when the C and Cl were removed under long term electron bombardment, which makes it an excellent candidate for application in field emission displays.

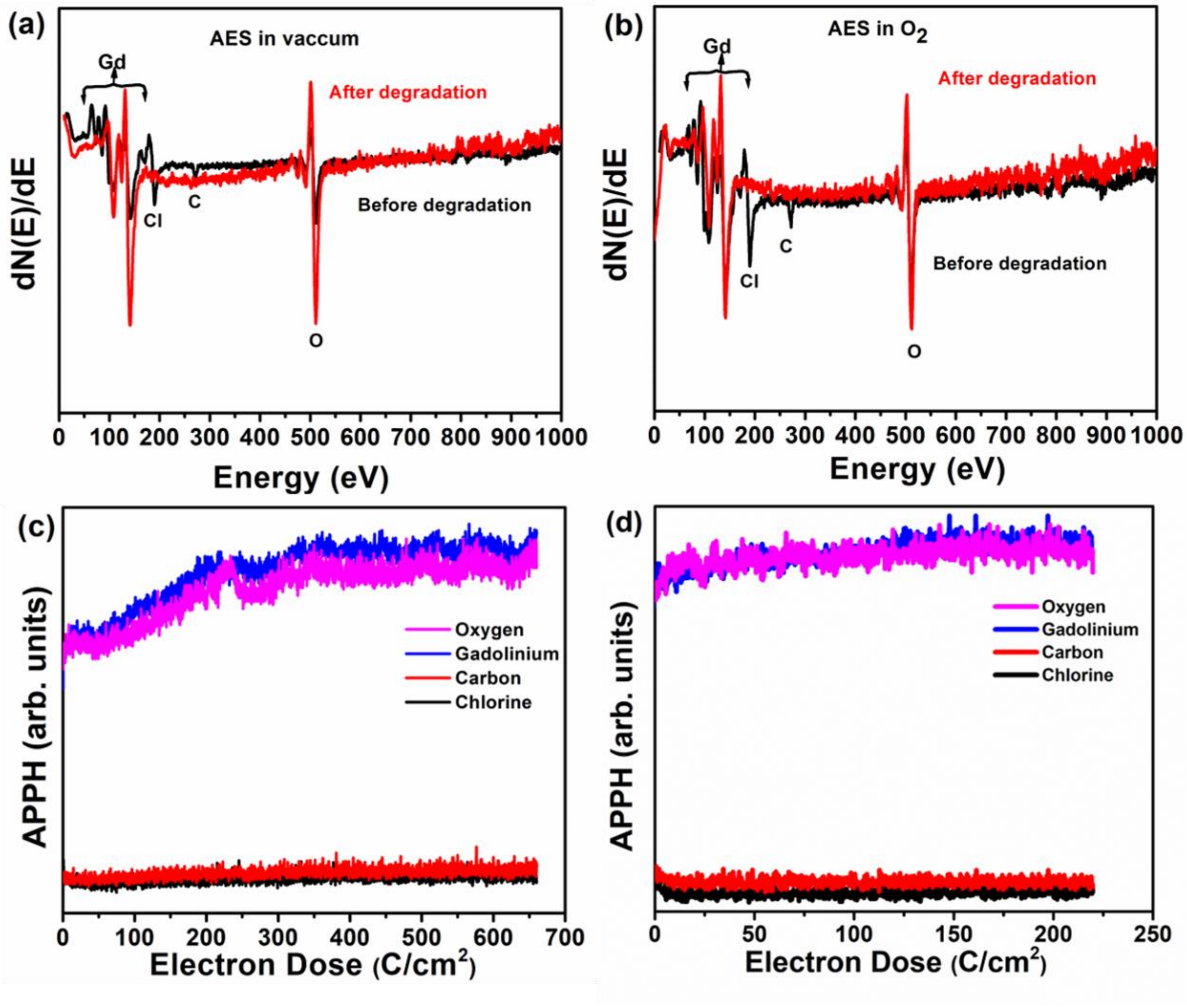

Figure 4.13: $Gd_{2-x}O_3$:$Bi_{x=0.003}$ powder before and after electron-beam bombardment: AES spectra in (a) vacuum and (b) backfilled with oxygen, APPHs in (c) vacuum and (d) backfilled with oxygen.

4.4 Conclusion

$Gd_{2-x}O_3:Bi_x$ powders were successfully synthesized and characterized. The XRD results showed that the samples were successfully prepared by the combustion method and that the single cubic crystal structure phase with an $Ia\overline{3}$ space group was formed for the different annealing temperatures and different concentrations of Bi^{3+}. The average crystallite size and bandgap increased slightly with increasing annealing temperature, while there was a decrease in crystallite size with an increase in the Bi doping concentration. The DR spectra for the undoped sample showed two bands located around 275 and 315 nm which were attributed to the 4f-4f optical transitions of Gd^{3+}, while for the doped samples three bands located around 260, 335 and 375 nm were observed due to the excitation transitions of Bi^{3+} ions into the different sites (C_2 and S_6). The optimum annealing temperature for the maximum PL and CL intensity of the $Gd_{2-x}O_3:Bi_x$ was 1000 °C. The intensity first increased due to increased crystallinity of samples and then decreased for the highest annealing temperatures of 1100 and 1200 °C due to a decrease in the dopant concentration due to the formation of volatile species. The optimum Bi^{3+} concentration for the maximum PL intensity of $Gd_{2-x}O_3:Bi_x$ was found to be at $x = 0.003$, while for the higher Bi^{3+} doping levels concentration quenching occurred for the PL intensity. The PL and CL results showed that the phosphor has two emission bands centred at 418 nm for blue emission and a third band centred at 505 nm for the green emission. The excitation spectra showed 3 bands that correspond to the $^1S_0 \rightarrow {}^3P^1$ transitions in the Bi^{3+} ion in the two different sites (S_6 and C_2). The excitation to the two main levels at 335 and 375 nm resulted in blue emission for the S_2 site and only broad green emission for the C_2 site. TL glow curves of the UV-irradiated $Gd_2O_3:Bi$ samples exhibited second-order kinetics. Two broad peaks with maxima at about 365 K and 443 K in the TL intensities for the different temperature's dopants in the Gd_2O_3 was observed. The TL kinetic parameters were calculated using the glow curve shape method. The CL intensity for both the blue and green peaks only slightly reduced during prolonged electron bombardment. A non-luminescent surface layer, which formed due to the ESSCR after removal of the C and Cl from the surface was responsible for the CL degradation. Except for the initial degradation, $Gd_2O_3:Bi$ powder was found to be stable under electron irradiation in both the base vacuum and back-filled O_2 environments. From these results it can be inferred that the phosphor is an excellent candidate for application in field emission displays and quite suitable for applications in high radiation environments.

References

[1] H. Guo, Y. Li, D. Wang, W. Zhang, M. Yin, L. Lou and S. Xia. Blue upconversion of cubic Gd_2O_3:Er produced by green laser. *Journal of Alloys and Compounds*, **376(1-2)** (2004) 23–27. doi:10.1016/j.jallcom.2003.12.020 .

[2] S. K. Singh, K. Kumar and S. B. Rai. Optical properties and switching behavior in $Gd_2O_3:Er^{3+}$ nanophosphor. *Journal of Applied Physics*, **106(9)** (2009) 093520. doi:10.1063/1.3259370.

[3] E. Antic-Fidancev, J. Hölsä and M. Lastusaari. Crystal field strength in C-type cubic rare earth oxides. *Journal of Alloys and Compounds*, **341(1-2)** (2002) 82–86. doi:10.1016/s0925-8388(02)00073-7.

[4] R. D. Shannon, Revised Effective Ionic Radii and Systematic Studies of Interatomic Distances in Halides and Chalcogenides, *Acta Crystallographica Section A*, **A(32)** (1976) 751-767. doi: 10.1107/s0567739476001551.

[5] Y. Zou, L. Tang, J.-L. Cai, L.-T. Lin, L.-W. Cao and J.-X. Meng. Combustion synthesis and luminescence of monoclinic Gd_2O_3:Bi phosphors. *Journal of Luminescence*, **153** (2014) 210–214. doi:10.1016/j.jlumin.2014.03.026.

[6] R. K. Tamrakar, D. P. Bisen and N. Brahme. Comparison of photoluminescence properties of Gd_2O_3 phosphor synthesized by combustion and solid state reaction method. *Journal of Radiation Research and Applied Sciences*, **7(4)** (2014) 550–559. doi:10.1016/j.jrras.2014.09.005.

[7] M. V. Abrashev, N. D. Todorov and J. Geshev. Raman spectra of R_2O_3 (R—rare earth) sesquioxides with C-type bixbyite crystal structure: A comparative study. *Journal of Applied Physics*, **116(10)** (2014) 103508. doi:10.1063/1.4894775.

[8] H. Jamnezhad and M. Jafari. Structure of Gd_2O_3 nanoparticles at high temperature. *Journal of Magnetism and Magnetic Materials*, **408** (2016) 164–167. doi:10.1016/j.jmmm.2016.02.041.

[9] N. Dhananjaya, H. Nagabhushana, B. M. Nagabhushana, B. Rudraswamy, S. C. Sharma, D. V. Sunitha, C. Shivakumara R. P. S. Chakradhar. Effect of different fuels on structural, thermo and photoluminescent properties of Gd_2O_3 nanoparticles. *Spectrochimica Acta Part A: Molecular and Biomolecular Spectroscopy*, **96** (2012) 532–540. doi:10.1016/j.saa.2012.04.067.

[10] P. P. Fedorov, M. V. Nazarkin, and R. M. Zakalyukin. On polymorphism and morphotropism of rare earth sesquioxides. *Crystallography Reports*, **47(2)** (2002) 281–286. doi:10.1134/1.1466504.

[11] M. Zinkevich. Thermodynamics of rare earth sesquioxides. *Progress in Materials Science*, **52(4)** (2007) 597–647. doi:10.1016/j.pmatsci.2006.09.002.

[12] K. Momma and F. Izumi, VESTA 3 for three-dimensional visualization of crystal, volumetric and morphology data, *Journal of Applied Crystallography*. **44(6)** (2011) 1272-1276. doi: 10.1107/s0021889811038970.

[13] B. Antic, A. Kremenovic, I. Draganic, P. Colomban, Vasiljevic-Radovic, D. Blanusa, J. Blanusa, M. Tadic and M. Mitric. Effects of O^{2+} ions beam irradiation on crystal structure of rare earth sesquioxides. *Applied Surface Science*, **255(17)** (2009) 7601–7604. doi:10.1016/j.apsusc.2009.04.035.

[14] D. A. Zatsepin, D. W. Boukhvalov, A. F. Zatsepin, Y. A. Kuznetsova, M. A. Mashkovtsev, V. N. Rychkov, V. Ya. Shur, A. A. Esin, E. Z. Kurmaev. Electronic structure, charge transfer, and intrinsic luminescence of gadolinium oxide nanoparticles: Experiment and theory. *Journal of applied surface science*, **436** (2018) 697–707. doi:10.1016/j.apsusc.2017.12.086.

[15] R. K. Datta. Luminescent behavior of bismuth in rare-earth oxides. *Journal of the electrochemical Society*, **114(11)** (1967) 1137. doi:10.1149/1.2426433.

[16] S. Z. Toma and D. T. Palumbo. Luminescence of Some Bismuth-Activated Oxides. *Journal of the electrochemical society*, **116(2)** (1969) 274. doi:10.1149/1.2411813.

[17] G. Boulon. Processus de photoluminescence dans les oxydes et les orthovanadates de terres rares polycristallins activés par l'ion Bi^{3+}. *Journal de Physique*, **32(4)** (1971) 333–347. doi:10.1051/jphys:01971003204033300.

[18] G. Liu, Y. Zhang, J. Yin and W. F. Zhang. Enhanced photoluminescence of Sm^{3+}/Bi^{3+} co-doped Gd_2O_3 phosphors by combustion synthesis. *Journal of Luminescence*, **128(12)** (2008) 2008–2012. doi:10.1016/j.jlumin.2008.06.013.

[19] J. W. Chung, B. K. Moon, J. H. Jeong and J. H. Kim. Luminescence properties of Bi^{3+} ions co-doped $Gd_2O_3:Eu^{3+}$, Tb^{3+} nanophosphors. *2010 3rd International Nanoelectronics Conference (INEC).* (2010) 789-790. doi:10.1109/inec.2010.5425202.

[20] K.Y. Jung, J. H. Han, D. S. Kim, Byung-Ki. Choi, Wkang-Jung. Kang. Aerosol Synthesis of Gd_2O_3:Eu/Bi nanophosphor for preparation of photofunctional pearl pigment as security material. *Journal of the Korean ceramic society*, **55(5)** (2018) 461-472. doi:10.4191/kcers.2018.55.5.09.

[21] G.-X. Liu, R. Zhang, Q.-L. Xiao, S.-Y. Zou, W.-F. Peng, L.-W. Cao and J.-X. Meng. Efficient $Bi^{3+}\rightarrow Nd^{3+}$ energy transfer in $Gd_2O_3:Bi^{3+},Nd^{3+}$. *Optical Materials*, **34(1)** (2011) 313–316. doi:10.1016/j.optmat.2011.09.003.

[22] Y. Zou, J.-L.Cai, L.-T. Lin, L.Tang and J.-X. Meng. Combustion Preparation and Near-infrared Phosphors of $Gd_2O_3:Bi^{3+},Nd^{3+}$. *Chinese Journal of Luminescence*, **35(5)** (2014) 531-535. doi: 10.3788/fgxb20143505.0531.

[23] Ya. Zhydachevskyya, V. Tsiumraa, M. Baranc, L. Lipińskac, P. Sybilskia and A. Suchockia. Quantum efficiency of the down-conversion process in Bi^{3+}–Yb^{3+} co-doped Gd_2O_3. *Journal of Luminescence*, **196** (2018) 169–173. doi:10.1016/j.jlumin.2017.12.042.

[24] L. G. Jacobsohn, M. W. Blair, S. C. Tornga, L. O. Brown, B. L. Bennett and R. E. Muenchausen.Y_2O_3:Bi nanophosphor: Solution combustion synthesis, structure, and luminescence, *Journal of Applied Physics*, **104(12)** (2008) 124303. doi:10.1063/1.3042223.

[25] M. H. M. Abdelrehman, R. E. Kroon, A. Yousif, H. A. A. Seed Ahmed and H. C. Swart. Luminescence properties and cathodoluminescence degradation of Bi doped SrO powder. *Journal of Vacuum Science & Technology B*, **37(1)** (2019) 011206. doi:10.1116/1.5075492.

[26] H. Fukada, K. Ueda, J. Ishino, T. Miyata and T. Minami. Blue PL and EL emissions from Bi-activated binary oxide thin-film phosphors. *Thin Solid Films*, **518(11**) (2010) 3067–3070. doi:10.1016/j.tsf.2009.08.014.

[27] A. M. Van de Craats and G. Blasse. The quenching of bismuth (III) luminescence in yttrium oxide (Y_2O_3). *Chemical Physics Letters*, **243(5-6)** (1995) 559–563. doi:10.1016/0009-2614(95)00897-d.

[28] K. Zhang, J.-S. Hou, B.-M. Liu, Y. Zhou, Z.-J. Yong, L.-N. Li, Sun. Hong-Tao and Y.-Z. Fang. Superbroad near-infrared photoluminescence covering the second biological window achieved by bismuth-doped oxygen-deficient gadolinium oxide. *Journal of the royal society of chemistry advances*, **6(82)** (2016) 78396–78402. doi:10.1039/c6ra14389j.

[29] H. C. Swart and R. E. Kroon. Ultraviolet and visible luminescence from bismuth doped materials. *Optical Materials*: X, **2** (2019) 100025. doi:10.1016/j.omx.2019.100025.

[30] A. Yousif, B. H. Abas, S. Som, N. J. Shivaramu and H. C. Swart. Structural and luminescence properties of Y_2O_3:Eu^{3+} red phosphor by incorporation of Ga^{3+} and Bi^{3+} ions. *Materials Research Bulletin*, **114** (2019) 110752. doi:10.1016/j.materresbull.2019.110752.

[31] B. M. Jaffar, H. C. Swart, H. A. A. Seed Ahmed, A., Yousif and R. E. Kroon. Cathodoluminescence degradation of Bi doped La_2O_3 and La_2O_2S phosphor powders. *Physica B: Condensed Matter*, **574** (2019) 411659. doi:10.1016/j.physb.2019.411659

[32] H. C. Swart, E. Coetsee, J. J. Terblans, O. M. Ntwaeaborwa, P. D. Nsimama, F. B. Dejene, and J. J. Dolo. Cathodoluminescence degradation of PLD thin films. *Applied Physics A*, **101(4)** (2010) 633–638. doi:10.1007/s00339-010-5915-6.

[33] P. Kumar, H.K. Malik, A. Ghosh, R. Thangavel and K. Asokan. Doped zinc oxide window layers for dye sensitized solar cells, *Journal of Applied Physics*, **102** (2013) 221903–5. doi:10.1063/1.4824363.

[34] M. C. Ferrara, D. Altamura, M. Schioppa, L. Tapfer, E. Nichelatti, L. Pilloni and M. Montecchi. Growth, characterization and optical properties of nanocrystalline gadolinia thin films prepared by sol–gel dip coating. *Journal of Physics D: Applied Physics*, **41(22)** (2008) 225408. doi:10.1088/0022-3727/41/22/225408.

[35] Y. A. Kuznetsova and A. F. Zatsepin. Optical properties and energy parameters of Gd_2O_3 and Gd_2O_3:Er nanoparticles. *Journal of Physics: Conference Series*, **917** (2017) 062001. doi:10.1088/1742-6596/917/6/062001.

[36] Y. A. Kuznetsova, A. F. Zatsepin, R. A. Tselybeev, V. N. Rychkov and V. A. Pustovarov. Luminescence of rare-earth ions and intrinsic defects in Gd_2O_3 matrix. *Journal of Physics: Conference Series*, **741** (2016) 012089. doi:10.1088/1742-6596/741/1/012089.

[37] T. Selvalakshmi, S. Sellaiyan, A. Uedono and A. Chandra Bose. Investigation of defect related photoluminescence property of multicolour emitting Gd_2O_3:Dy^{3+} phosphor. *Journal of the royal society of chemistry advances*, **4(65)** (2014) 34257. doi:10.1039/c4ra07094a.

[38] S. Som and S. K. Sharma. Eu^{3+}/Tb^{3+}-codoped Y_2O_3 nanophosphors: Rietveld refinement, bandgap and photoluminescence optimization. *Journal of Physics D: Applied Physics*, **45(41)** (2012) 415102. doi:10.1088/0022-3727/45/41/415102.

[39] R. M. Jafer, A. Yousif, Vinod Kumar, H. C. Swart and E. Coetsee. The effect of annealing temperature on the luminescence properties of Y_2O_3 phosphor powders doped with a high concentration of Bi^{3+}, *Journal of Luminescence*, **180** (2016) 198–203. doi: 10.1016/j.jlumin.2016.08.042.

[40] R. H. P. Awater and P. Dorenbos. The Bi^{3+} 6s and 6p electron binding energies in relation to the chemical environment of inorganic compounds. *Journal of Luminescence*, **184** (2017) 221–231. doi:10.1016/j.jlumin.2016.12.021.

[41] E. Lee, J. J. Terblans and H. C. Swart. The effect of pH on the luminescence properties of Y_2O_3:Bi phosphor powders synthesised using co-precipitation. *Vacuum*, **157** (2018) 237–242. doi:10.1016/j.vacuum.2018.08.060.

[42] A. Scarangella, F. Fabbri, R. Reitano, F. Rossi, F. Priolo and M. Miritello. Visible emission from bismuth doped yttrium oxide thin films for lighting and display applications. *Scientific Reports*, **7** (2017) 17325. doi:10.1038/s41598-017-17567-9.

[43] A. Scarangella, R. Reitano, F. Prioloa and M. Miritello. Bismuth doping of silicon compatible thin films for telecommunications and visible light emitting devices. *Materials Science in Semiconductor Processing*, **92** (2019) 47–57. doi: 10.1016/j.mssp.2018.04.017.

[44] A. D. Broadbent. A critical review of the development of the CIE1931 RGB color-matching functions. *Color Research & Application*, **29(4)** (2004) 267–272. doi:10.1002/col.20020.

[45] P. B. Vidyasagar, S. Thomas, M. Banerjee, U. Hegde and A. D. Shaligram. Determination of peak parameters for thermoluminescence glow curves obtained from spinach thylakoid preparations, using mathematical models based on general order kinetics. *Journal of Photochemistry and Photobiology B: Biology*, **19(2)** (1993) 125–128. doi:10.1016/1011-1344(93)87106-w.

[46] N. J. Shivaramu, B. N. Lakshminarasappa, K. R. Nagabhushana, F. Singh and H. C. Swart. Synthesis, thermoluminescence and defect centres in Eu^{3+} doped Y_2O_3 nanophosphor for gamma dosimetry applications. *Materials Research Express*, **4(11)** (2017) 115033. doi:10.1088/2053-1591/aa99ec.

[47] A. Yahyaabadi, F. Torkzadeh, D. Rezaei Ochbelagh and S. M. Hosseini Pooya. Effect of annealing temperature and dopant concentration on the thermoluminescence sensitivity in LiF:Mg,Cu,Ag material. *Luminescence*, **33(5)** (2018) 891–896. doi:10.1002/bio.3487.

[48] T. Lyu and P. Dorenbos. Bi^{3+} acting both as an electron and as a hole trap in La-, Y-, and $LuPO_4$. *Journal of Materials Chemistry C*, **6(23)** (2018) 6240–6249. doi:10.1039/c8tc01020j.

[49] K. S. Chung, H. S. Choe, J. I. Lee, J. L. Kim and S. Y. Chang. A computer program for the deconvolution of thermoluminescence glow curves. *Radiation Protection Dosimetry*, **115(1-4)** (2005) 343–349. doi:10.1093/rpd/nci073.

[50] V. Pagonis, G. Kitis, C. Furetta, Numerical, Practical Exercises in Thermoluminescence, Springer Science Business Media Inc., USA, 2006. ISBN: 978-0-387-30090-0.

[51] A. J. J. Bos. Theory of thermoluminescence. *Radiation Measurements*, **41** (2006) S45–S56. doi:10.1016/j.radmeas.2007.01.003.

[52] V. Pagonis and G. Kitis. On the Possibility of using Commercial Software Packages for Thermoluminescence Glow Curve Deconvolution Analysis. *Radiation Protection Dosimetry*, **101(1)** (2002) 93–98. doi:10.1093/oxfordjournals.rpd.a006067.

[53] R. Berman. Thermal Conduction in Solids. Clarendon Press, Oxford, UK, 1976. ISBN: 0198514298.

[54] Lawrence E. Davis, Noel C. Mac Donald, Paul W. Palmberg, Gerald E. Riach and Roland E. Weber. Handbook of Auger Electron Spectroscopy. 2nd Edition. Published by Physical Electronics Division of Perkin-Elmer. Minnesota (1976) 19-249. ISBN: 9788578110796.

[55] E. Hasabeldaim, O. M. Ntwaeaborwa, R. E. Kroon, V. Craciun, E. Coetsee, H. C. Swart. Surface characterization and cathodoluminescence degradation of ZnO thin films. *Applied Surface Science*, **424** (2016) 412-420. doi.org/10.1016/j.apsusc.2016.11.178.

[56] A. Yousif, H. C. Swart and O. M. Ntwaeaborwa, Surface state of $Y_3(Al,Ga)_5O_{12}$:Tb phosphor under electron beam bombardment. *Applied Surface Science*, **258(17)** (2012) 6495–6503258. doi:10.1016/j.apsusc.2012.03.066.

[57] H. C. Swart, J. S. Sebastian, T. A. Trottier, S. L. Jones and P. H. Holloway, Degradation of zinc sulfide phosphors under electron bombardment. *Journal of Vacuum Science & Technology A*, **14(3)** (1996) 1697–1703. doi: 10.1116/1.580322.

[58] Emad Hasabeldaim, Odireleng M. Ntwaeaborwa, Robin E. Kroon, Hendrik C. Swart. Surface analysis and cathodoluminescence degradation of undoped ZnO and ZnO:Zn phosphors. *Journal of Vacuum Science & Technology B*, **34(4)** (2016) 041221. doi:10.1116/1.4953561.

[59] B. M. Jaffar, H. C. Swart, H. A. A. Seed Ahmed, A. Yousif and R. E. Kroon. Cathodoluminescence degradation of Bi doped La_2O_3 and La_2O_2S phosphor powders. *Physica B: Condensed Matter*, **574** (2019) 411659. doi:10.1016/j.physb.2019.411659.

[60] H. C. Swart, J. J. Terblans, O. M. Ntwaeaborwa, R. E. Kroon and B. M. Mothudi, PL and CL degradation and characteristics of $SrAl_2O_4:Eu^{2+},Dy^{3+}$ phosphors. *Physica B: Condensed Matter*, **407(10)** (2012) 1664–1667. doi: 10.1016/j.physb.2011.09.112.

Chapter 5

Photoluminescence, cathodoluminescence degradation and surface analysis of Gd_2O_3:Bi pulsed laser deposition thin films

In this chapter $Gd_{2-x}O_3:Bi_{x=0.003}$ *thin films were successfully deposited on Si (100) substrates in vacuum and an oxygen atmosphere at different substrate temperatures using the pulsed laser deposition technique. The microstructure, surface topography, chemical composition analysis and luminescent properties of the samples were studied. The influence of prolonged electron beam exposure on the surface state, chemical and cathodoluminescence (CL) stability of the samples was investigated.*

5.I Introduction

Recently, several studies have been conducted on rare earth element oxide phosphors to enhance their properties for potential applications in light-emitting appliances, flat-screen televisions, cell phone displays, diagnostic medicine and chemical catalysts. Rare earth oxide thin films have been investigated extensively for use in alternative energy applications and in various optical applications of phosphors. This includes the improvement of the luminous color purity, emission intensity, quantum efficiency and radiation conversion systems. The rare earth oxides are attractive candidates in optical applications due to their high quality, based on the thermodynamic energy considerations due to their exhibiting high dielectric constants, good thermal stability and wide band gaps of over 2 eV, which is large compared to Si [1]. Gadolinium oxide (Gd_2O_3) has received much attention among the rare earth element oxides from the scientific and research community, but has been reported on primarily in the powder form [2]. This oxide has excellent physical and chemical properties and is an insulator with a wide bandgap of 5.2 eV [3]. It has a thermal conductivity of more than 0.1 $Wcm^{-1}K^{-1}$ and a high dielectric constant (~ 16) [4]. Gd_2O_3 may occur in three different structures: cubic, monoclinic and hexagonal. The high quality of the Gd_2O_3 thin films with excellent surface morphologies, good optical properties and thermal stability have made it attractive as one of the best rare earth oxide materials to be used in different optical applications [5]. Because of the useful electrical properties of Gd_2O_3 and the ability for it to be used as efficient electrolytes in solid oxide fuel cells, it may be applied as a dielectric material [6]. These properties, along with the ability to incorporate a large amount of luminescent center ions, have made Gd_2O_3 excellent host arrays for potential use in many luminescence applications.

Broadly tunable emissions occur from Bi^{3+} ions when doped in different oxide hosts. The Bi^{3+} ion has significant interaction with the host lattice, thereby affecting its optical transitions. Ultraviolet (UV) light used as excitation is efficiently converted to longer wavelengths. In the past decade, some pioneering luminescence reports have focused on Bi doped Gd_2O_3 [5] [7] [8]. In different hosts, absorption of the Bi^{3+} ion occurs in the UV region [9]. Absorption bands of Bi^{3+} are commonly ascribed to two transitions, namely the allowed $^1S_0 – ^1P_1$ transition and the $^1S_0 – ^3P_1$ transition that becomes allowed due to spin-orbit coupling. The energy of the $^3P_1$ excited state is less than that of the $^1P_1$ excited state and provides emission usually in a single broad band due to the $^3P_1–^1S_0$ transition [10]. However, in Gd_2O_3 the $^3P_1$ level is split into two (^3A_u and ^3E_u) and three (^3A, ^3B and ^3B) levels at the S_6 and C_2 symmetry sites, respectively. According to the report published previously, it has been revealed that the luminescence of Bi^{3+} in the cubic Gd_2O_3 powder has two unresolved emission bands concentered at 418 nm for the blue emission and a third band centered at 505 nm for the green emission [3]. The excitation spectra of Bi^{3+} exhibited three bands that were attributed to the $^1S_0 \rightarrow ^3P_1$ transitions of the Bi^{3+} ion at the S_6 and C_2 sites of the cubic Gd_2O_3. The excitation to the two main levels at 335 and 375 nm allocated to the transitions $^1A_g \rightarrow ^3A_u$ and $^1A_g \rightarrow ^3E_u$ resulted in blue emission for the S_2 site and only broad green emission for the C_2 site was attributed to the $^3B \rightarrow ^1A$ transition of Bi^{3+} [3]. Also, the optical properties emissions of Bi^{3+} in the cubic Gd_2O_3 thin films were previously studied as consisting of a blue emission and a wide blue-green emission band that peaked at 420 nm when excited at 372 nm and a maximum at 505 nm when excited at 328 nm [10]. Many research studies have been conducted about the growth and characterization of Gd_2O_3:Bi phosphor thin films by reason of the potential use for different optical applications [11].

Recently, a lot of attention has been given to the preparation of blue phosphors using various chemical and physical methods. Thin film phosphors have considerable advantages over common powder forms, for instance comparatively greater thermal stability, better structural densities, better coalescence with the basic substrates and effective heat conduction for high power operation [12], but they still lack high efficiency light output. It has been demonstrated that

Gd_2O_3:Bi thin film phosphors fabricated by the radio frequency magnetron sputtering method are advantageous for use in high luminance blue emitting oxide thin film electroluminescence device applications [12,13]. Various techniques may be applied to fabricate Gd_2O_3 thin films such as electron-beam evaporation [14], sputtering [6], atomic layer deposition [15], H_2O-assisted atomic layer deposition [16], metal-organic chemical vapor deposition [17], sol-gel method [18], molecular beam epitaxy [19] and pulsed laser deposition (PLD) [20]. Each of these techniques has its advantages and disadvantages, depending largely on the quality of the chemical material, crystallization of phosphor material, its luminescence properties, stability, etc., as well as the field of film applications. It was recently demonstrated that the PLD method is an appealing technique for making and developing thin films to be used in a wide diversity of implementations. The PLD technique is broadly used to fabricate thin films which are more suitable compared to others and is an efficient technique that enables the control of the optical and structural properties of the films [21]. The low substrate temperature used in the PLD techniques is balanced by the high energy of the ablated particles in the laser-produced plasma plume [22]. The PLD films have some special advantages for fabricating a film consisting of the same material as the target. The film is affected by the grain growth operation and the different types of ionization in the laser-produced plasma, that potentially allows the produced thin films to have high quality at room temperature and higher temperatures. It is recognized that the PLD system is an important technique to produce different oxide thin films, but there are several factors and experimental conditions of PLD that control the quality of the films produced. Therefore it is significant to evolve the best comprehension of the kinetics for the Gd_2O_3:Bi film formation, where these further differ for various PLD growth conditions. Detailed analysis with regard to the stability for Gd_2O_3 thin film luminescence under electron beam irradiation has not been reported. Hence, it is expected that by using PLD technique it is possible to obtain high quality thin films with good optical, luminescence, electrical and chemically stable properties.

In this study, Gd_2O_3:Bi^{3+} phosphor thin films for possible application in favorable for solar cells applications were deposited on Si (111) substrates using the PLD technique. In our previous work, Bi-doped cubic Gd_2O_3 phosphor powders were prepared via a combustion method, exhibited good luminescence properties and excellent stability under electron beam irradiation [3]. The aim of this article is firstly to study the properties of the Gd_2O_3:Bi thin films as amorphous and crystalline films that were successfully prepared using the PLD technique in different background atmospheres, namely in a vacuum and oxygen. Therefore, the influence of the background atmosphere and substrate temperature on the structural, morphological and optical properties of Gd_2O_3:Bi thin films were explored. Thin films have been deposited by keeping some experimental parameters constant, such as working pressure, target to substrate distance and deposition times, but changing the substrate temperature. Secondly the cathodoluminescence (CL) degradation behavior and luminescence stability of the optimized Gd_2O_3:Bi thin film during prolonged electron beam exposure was also investigated for display applications. Auger electron spectroscopy (AES) was used to examine the surface composition and chemical stability under the same electron beam while simultaneously monitoring the CL emission during prolonged electron beam irradiation in vacuum and an O_2 partial pressure. AES and X-ray photoelectron spectroscopy (XPS) techniques were used to assess the changes of the elemental composition and oxidation state of cations on the surface of the powder and thin films prior and after electron beam irradiation.

5.2 Experimental

5.2.1 Sample preparation

$Gd_{2-x}O_3$:Bi_x phosphor powders with cubic crystal structure were previously successfully prepared using a solution combustion method and the influence of the dopant concentration and heat treatment were investigated [3]. The optimum powder sample was found for $Gd_{2-x}O_3$:$Bi_{x=0.003}$ that was annealed at 1000 °C [3]. In this study 8 g of this powder was compressed at 75 tons for 4 h after mixing it with ethanol as a binder to prepare an ablation target pellet for PLD. Afterwards, the target was sintered for 8 h at a temperature of 1260 °C to ensure that all impurities and incidental water and binder could be eliminated. Then the target was placed inside a holder in the PLD system chamber at the carrousel target holder, which can be moved by rotating as well as forward and backward movement. Pieces of a Si (100) orientation wafer were used as substrates after cut into pieces of ~ 3 x 2 cm and then they had been cleaned in an ultrasonic bath using acetone, ethanol and finally a distilled water bath consecutively for 15 min each, and then dried by blowing N_2 gas over the surfaces. The PLD deposition chamber was pumped down until the pressure reached 3.4×10^{-5} mbar. The target was ablated at the base pressure (vacuum) or after backfilling the chamber with O_2 working atmosphere at a pressure of 2.7×10^{-2} mbar. The Nd:YAG laser (60 mJ/pulse) emitting at 266 nm was used for the target ablation. The target-to-substrate distance within the deposition chamber was fixed to a setting of 4.5 cm. The substrate temperature was varied for different runs and values of 30, 100, 200, 350 or 500 °C were used. The deposition time, laser pulse frequency and fluency were kept at 11 min, 10 Hz and 0.77 J/cm^2 per pulse for all samples.

5.2.2 Characterization

A Bruker D8 Advance X-ray diffractometer (XRD) with Cu Kα X-rays (0.154 nm) generated at a voltage and current of 40 kV and 40 mA was used to characterize the structure of the thin films. The surface morphological features were studied using a JEOL JSM-7800 F scanning electron microscope (SEM). The PL spectra were collected at room temperature using a 325 nm He-Cd laser system with a PMT detector. The CL spectra were measured using a PHI 549 Auger electron spectrometer using an Ocean Optics PC2000 spectrometer interfaced with OOI Base32 computer software. AES was performed simultaneously with CL measurements to monitor CL degradation and to determine if there was any relation between the degradation and surface chemical compositional changes during prolonged electron bombardment. XPS analysis was performed before and after degradation to evaluate the differences and changes of the surface chemical composition. MultiPak software was utilized to analyze the spectra to determine the chemical compounds and their electronic states using Gaussian–Lorentz fits.

5.3 Results and discussion

5.3.1 Structure analysis

Figure 5.1 displays the XRD patterns of thin films grown in various atmospheres as well as the $Gd_{2-x}O_3:Bi_{x=0.003}$ powder that was utilized to create the PLD target. The pattern of the powder follows the JCPDS standard #43-1014 for cubic phase Gd_2O_3 [3]. In Figure 5.1(a) the XRD patterns of the films prepared in vacuum at 50 and 100 °C exhibited an amorphous state because no peaks were observed. It is known that the PLD thin film crystallinity will depend on the deposition conditions and many parameters of the material, e.g. the surrounding gas pressure, besides the temperature and physicochemical properties of the substrate [21]. The thin films prepared at the 200 °C substrate temperature exhibited diffraction peaks at 20.7° and 28.3° assigned to the Gd_2O_3 cubic phase with a preferential growth on the (211) and (222) planes. Chang *et al.* [22] reported the crystallinity of grown cubic Gd_2O_3 films came gradually upon increasing the substrate temperature when they deposited the films on $LaAlO_3$ by using the PLD technique at various substrate temperatures. The films fabricated at 350 and 500 °C showed diffraction peaks at 28.4° and 22.8° that are attributed to $Gd_2Si_2O_7$ (112) and (212) planes of the orthorhombic phase, that are a result of Si diffusion from the substrate to the films. Yamamoto *et al.* [23] have done a study on Y_2O_3 and La_2O_3 thin films, where it was indicated that they were converted to YSi_xO_y and $LaSi_xO_y$ structures as a result of Si interaction from the substrate and the films when calcination was performed at high temperatures. Also, Yousif *et al.* [24] stated that $Y_{2-x}O_3$:$Bi_{x=0.005}$ thin films deposited on Si substrates using a spin coating technique changed into $Y_2Si_2O_7$:Bi after being annealed at high temperatures. Since the 222 peak of Gd_2O_3 and the 112 peak of $Gd_2Si_2O_7$ coincide, the relative peak heights of the sample fabricated at 350 °C suggests a mixture of these materials.

In Figure 5.1(b) the XRD patterns of the films deposited in O_2 at 30 °C and 100 °C also showed an amorphous state. A crystalline film growth evidenced by a diffraction peak centered at 28.2° corresponding to the Gd_2O_3 cubic phase with preferred 222 orientation occurred in the film fabricated at 200 °C and continued growing at the 350 °C substrate temperature. The peaks which are tagged with an asterisk (*) are related to diffusion from the Si substrate. The thin film prepared at 500 °C substrate temperature displayed all diffraction peaks matched with the cubic phase Gd_2O_3 powder. Although these peak positions may also appear to coincide with some peaks from the Si substrate, they can be differentiated because they are significantly broader. It is documented that the PLD mechanism may be a credible technique for fabricating oxide thin films. The appropriate outcomes of PLD do not occur under all experimental environments with the same parameters [25]. Parameters such as the substrate temperature, distance between the target and substrate and the presence of a background gas composition and the type and pressure of the gas present, as well as the kinetic energy of the plume particles, play an important role in the deposition of the films, which allow adequate control of film growth and properties [26]. The thin films, in Figure 5.1(b), deposited in O_2 indicated that crystallinity of the thin films was improved with an increase in the substrate temperature, transforming from an amorphous state to a cubic structure.

Sato *et al.* [27] have reported that the increase of the substrate temperature assisted chemical reactions, leading to an increase of nucleation density on the substrate. Also, Ghorannevis *et al.* [28] reported that the degree of crystallinity of a deposited thin film is strongly depended on the substrate temperature. Generally, the crystallization and microstructure of the films depend upon the deposition parameters within the chamber. For vacuum, comparatively little collisions of the emitted particles occur, leading to a greatly directional deposition and increased mobility of the deposited species on the substrate that constitutes difficulty in controlling the film depositing mechanism. Thus the new phase at high substrate temperature possibly resulted from the destruction of the deposited film due to re-sputtering by the fast-moving plume particles and their interaction with the substrate. But during PLD in a reacting gas atmosphere like oxygen, the hydrodynamic interaction between the plume and the background gas helps to achieve the same composition as that of the target. Thus the adatom mobility is expected to become higher at higher temperatures, which leads to an increased probability of finding active nucleation sites on the substrate [23]. Dolo *et al.* [29] reported that the crystallinity of $Gd_2O_2S:Tb^{3+}$ thin films produced using PLD was enhanced by increasing the oxygen pressure. Under O_2 gas pressure in the chamber, extra collisions occur between the ablated substance particles and the gas. Accordingly, the particles are given enough time to form. When the amount of the ablated substance particles was enhanced, the directionality reduced, and the kinetic energy of the atoms colliding with the substrate was decreased, with a direct result of the growth of larger particles that occurred before reaching the substrate.

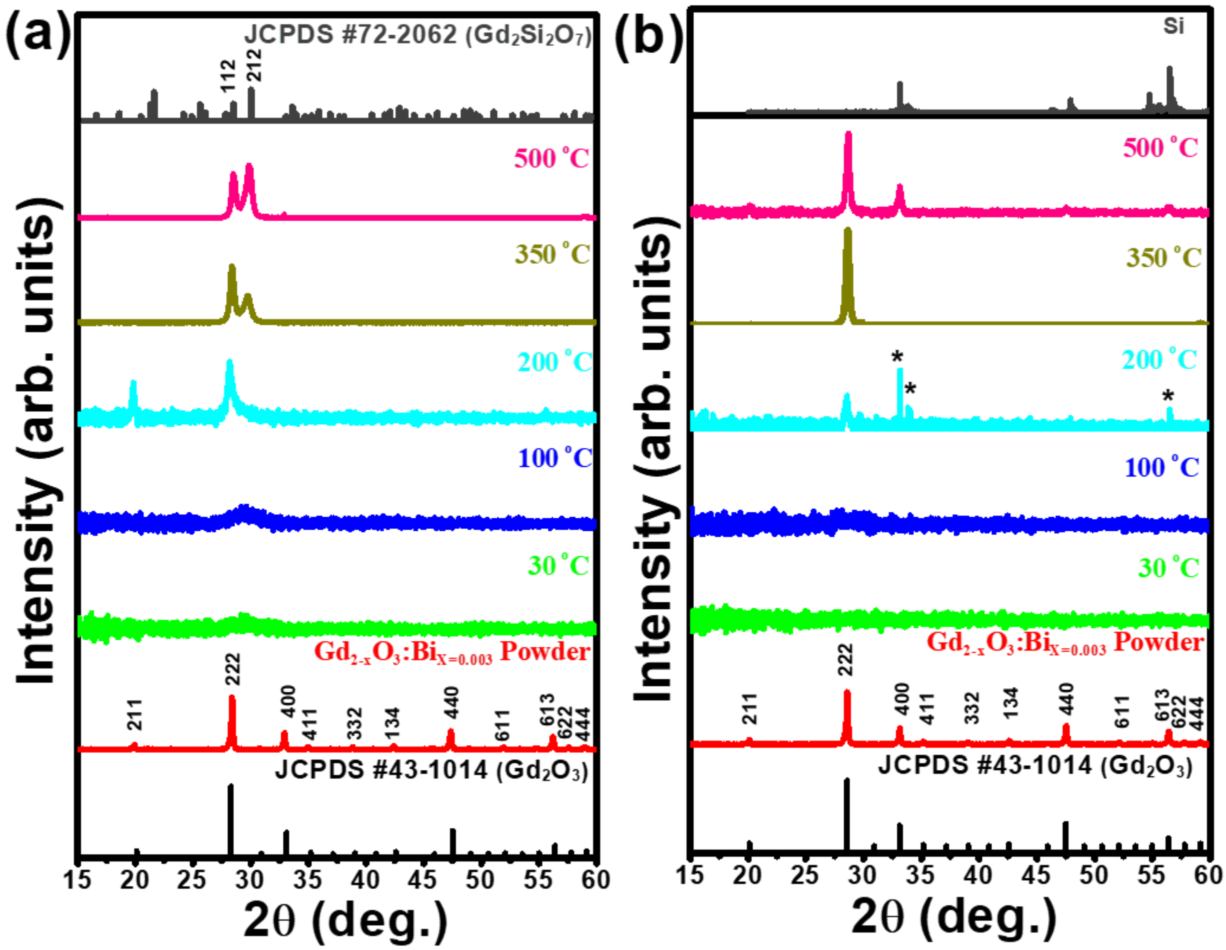

Figure 5.1: XRD spectra of $Gd_{2-x}O_3:Bi_{x=0.003}$ powder besides thin films grown in (a) base pressure and (b) in an O_2, for various substrate temperatures at 30, 100, 200, 350 and 500 °C, respectively. The peaks marked with an asterisk (*) were from the Si substrate.

The crystallite sizes of the thin films for substrate temperatures of 200 °C, 350 °C and 500 °C in O_2 were estimated using the full width at half maxima (FWHM) of the 222 peak using Scherrer's formula [30]

$$D = \frac{k\lambda}{\beta \cos\theta} \qquad (5.1)$$

where D is the crystallite size, k is a constant correlation factor taken as 0.94, λ is the wavelength of the X-rays (0.154 nm), β is the FWHM in radians and θ is Bragg's diffraction angle of the 222 peak. The crystallite sizes were obtained using Eq. (5.1) at substrate temperatures of 200 °C, 350 °C and 500 °C in O_2 were 23, 25 and 29 nm, respectively. The crystallite size of the thin films varied depending on the substrate temperature and increased with an increase in temperature. This was possibly as a result of the boost in the crystallinity of the film deposited at the higher substrate temperature [31]. Deposition at a higher temperature resulted in a higher adatom mobility, leading to a higher probability for finding active nucleation sites on the substrate [32].

5.3.2 Surface morphology

Figure 5.2 shows SEM micrographs for the thin films deposited at various substrate temperatures from 30 °C to 500 °C, with (a-e) in vacuum and (f-j) in O_2. All SEM images show smooth surfaces with a small presence of spherical particles of various sizes that appear highly independent of the substrate temperature. The film fabricated in vacuum features a smooth surface with small spherical particles. In a vacuum, the ablated substance particles move from the target to the substrate with their original kinetic energy and very high speed. Due to their high energy, once the particles arrive at the substrate, the chance of these particles to bond on the surface of the substrate is low and there is a high possibility of re-sputtering some of the material. Thus, the film fabricated in vacuum has a smooth surface with small spherical and irregular particles of varying size with poor crystallinity as also appeared in the XRD results, figure 5.1(a). If the samples deposited in O_2 are compared, the number of bigger particles deposited onto the surface of the films decreased as the substrate temperature increased. During the PLD deposition process, large particulates will have formed on the film surface originating from small droplets blasted from the molten target which solidify to spheres by the time they reach the substrate. Then particulates are relocated through ablated substance particles to the substrate and become integrated into the developing film [21].

In any thin film application, after properly forming the film and selecting the wavelength, the thickness of the film will greatly affect its performance characteristics. The characteristics of the film deposition process show great influences on the optical properties of the films, especially for the thinner films [34]. Undoubtedly, the thin film cross-section is interesting as a direct measure of its thickness. It can also be used to monitor boundaries between the film and substrate, the boundaries between multiple thin-film layers and the graininess within the layers. Cross-sectional observation can also be described as an important observation technique with respect to inspection of adhesion and diffusivity between thin films of different types [35]. Figure 5.3 shows the cross-sections for all the thin films. The cross-sectional images were similar, which clearly revealed the presence of spherical particles in the morphology. Figures 5.3 (a - e) of samples deposited in vacuum show that the thickness of the films was around 150–200 nm. The thickness of the sample (e) fabricated at the substrate temperatures of 500 °C decreased to around 100 nm, which may be due to the presence of the silicate phase as presented in the XRD results of figure 5.1(a). For the sample deposited in room temperature in O_2 (Figure 5.3 (f)), it was perceived that the thickness of the film was about a micron in size, which might be due to direct ejection from melted ablated substance particles from the target during the laser ablation since, as shown in figure 5.2 (f), the large particulates have a similar size. Also, when depositing at low substrate temperatures in O_2, it might have led to a reduction in the surface diffusion coefficient of the species reaching the surface of the substrate which limited significantly their reactivity with the substrate, which may be the reason for the thicker film. The thicknesses of the other films (g – j) deposited at higher temperatures were relatively constant at around 100 nm. There is a slight discrepancy between the thicknesses obtained by using the SEM cross-sections due to the surface roughness. Since the film thicknesses were relatively constant, it is clear that the thickness of the film was not appreciably affected by the substrate temperature, although the film thickness was slightly affected by the deposition atmosphere. From the cross-section images, it is clear that the features which appear spherical in the top view (Figure 5.2) are actually truncated or deformed spheres, although it is not clear to what extent they penetrate into the thin film (i.e. extend below the upper surface).

Figure 5.2: SEM photographs for films deposited (a - e) in vacuum base pressure (f - j) in O_2 for various substrate temperatures at 30 °C, 100 °C, 200 °C, 350 °C and 500 °C.

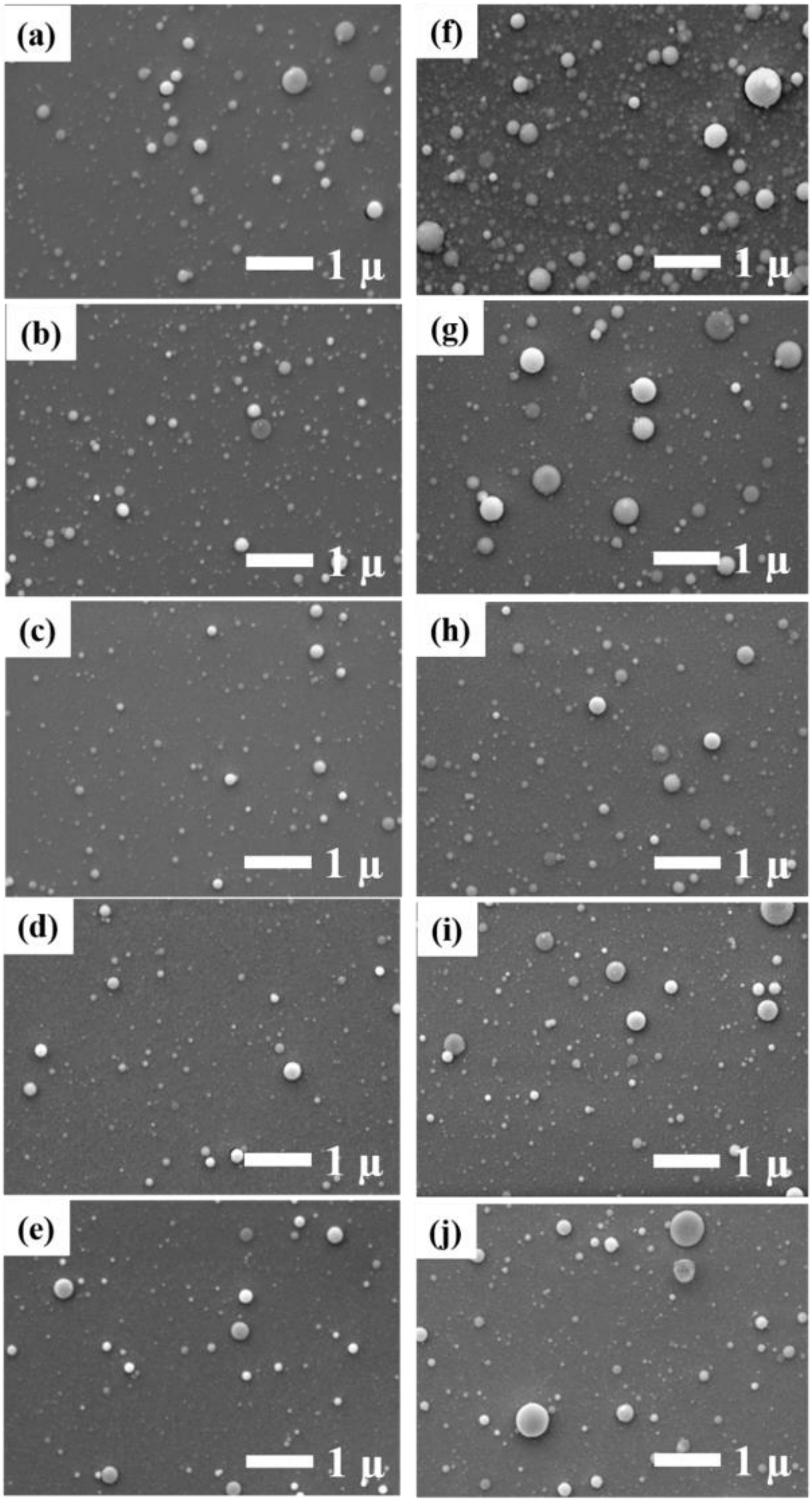

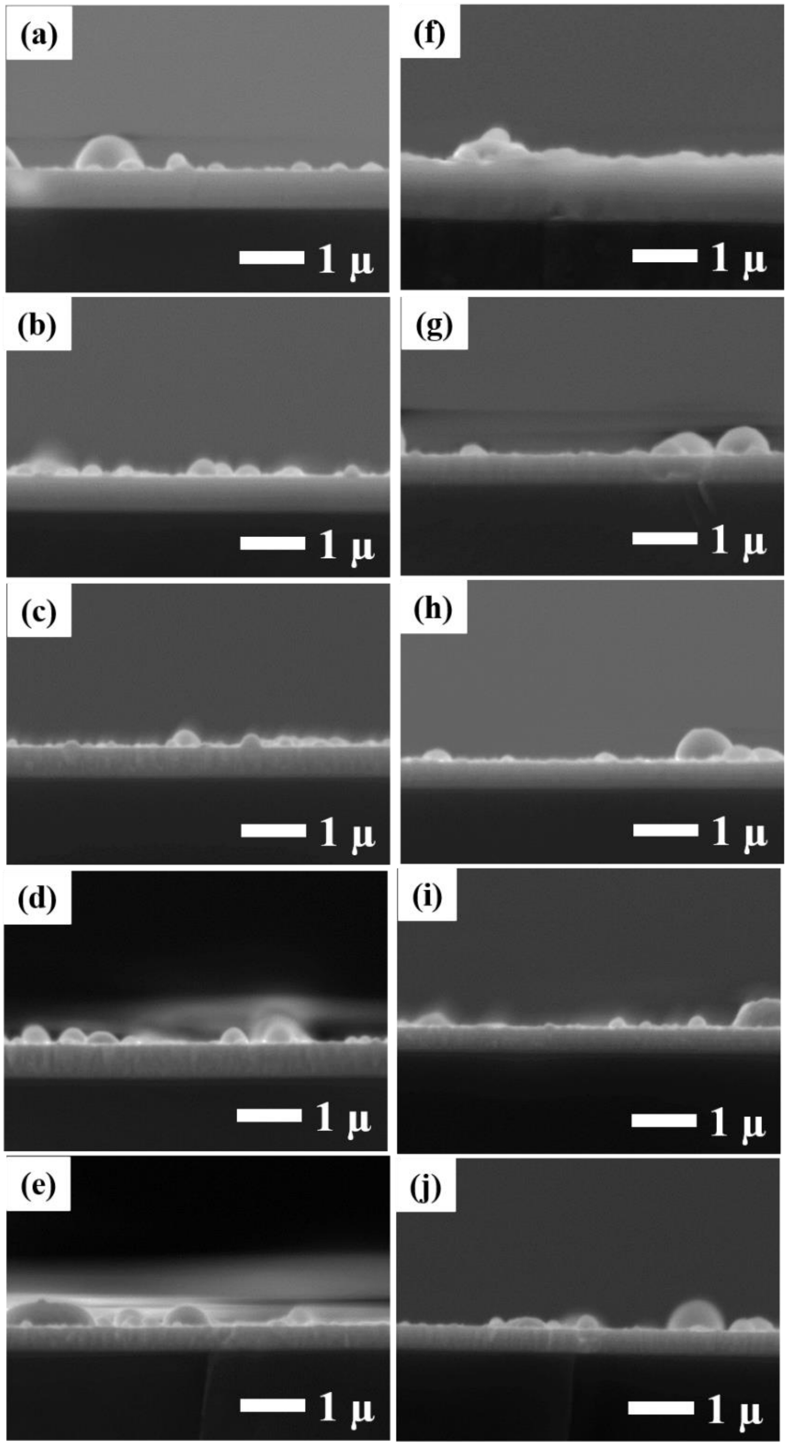

Figure 5.3: Cross-sectional SEM photographs for the films deposited (a - e) in vacuum base pressure (f - j) in O_2 for various substrate temperatures at 30 °C, 100 °C, 200 °C, 350 °C and 500 °C.

5.3.3 Photoluminescence analysis

Figure 5.4(a) displays the room temperature PL emission spectra of the $Gd_{2-x}O_3:Bi_{x=0.003}$ powder sample excited with the 325 nm He-Cd laser. The PL emissions were already reported previously [3] but we summarize the results for comparison with the thin films. The luminescence spectra revealed in figure 5.4(a) show two blue emission bands centered at 360 and 418 nm, and another green emission band at around 505 nm. The emissions are ascribed to the Bi^{3+} in the S_6 and C_2 symmetry sites. Bi^{3+} ions can be excited from the ground state to states $^3P_1$ (A band) or $^1P_1$ (C band) with a convenient wavelength of light in the UV range. The blue emission bands which peaked at 360 and 418 nm could be designated by the Bi^{3+} transitions of $^3A_u \rightarrow {}^1A_g$ and $^3E_u \rightarrow {}^1A_g$ at the S_6 site, respectively, while the wide blue-green emission band centered at 505 nm could be ascribed to the $^3B \rightarrow {}^1A$ transition of Bi^{3+} at the C_2 site [3]. Figure 5.4(b) and (c) show the PL emission spectra of the thin films prepared at different substrate temperatures of 50 °C, 100 °C, 200 °C, 350 °C and 500 °C excited by the 325 nm He-Cd laser at room temperature, that were fabricated in (b) vacuum and (c) O_2. A broad emission band from all the PLD thin film samples was observed, in contrast to the double peak observed for the powder. They showed a broad band of blue-green luminescence emission that extended from 370 to 650 nm, centered at 502 nm. Fukada *et al.* [11] reported that the thin films of Gd_2O_3:Bi cubic phosphor annealed at a high temperature give some broad peaks that are composed of blue and green emissions in the wavelength range from about 400 to 600 nm when excited by UV light at a wavelength of about 325 nm. In figures 5.4(b) and (c) the position of the main PL emission peak of the thin films showed a small shift to shorter wavelengths compared with the PL maximum intensity positions for the powder [3]. This shift can be associated with the alteration of the environment of the Bi^{3+} ions, as a result of the varying in the crystal field, where the binding energy of the atoms and molecules in the thin film forms on average, much less compared to that in bulk powder [11]. Yousif *et al.* [36] reported that each one of the phosphor hosts activated with Bi^{3+} ions showed significant changes in their luminescence properties thanks to their outer electrons which are not shielded from the surrounding environment. Also, Abdelrehman *et al.* [21] have measured a slight shift in the wavelength of the PL spectra for the $SrO:Bi^{3+}$ PLD thin films due to a change in the crystal field.

Figure 5.4(d) shows that for the thin films deposited in vacuum the PL intensity increased with the increase of the substrate temperatures up to 200 °C and then decreased with a further increase of temperature to 350 °C and 500 °C. The increase in PL intensity at 200 °C may be attributed to the improved film crystallinity, as the samples at 30 and 100 °C showed an amorphous state (see figure 5.1 (a)). The lower luminescence intensity of the samples prepared at the higher substrate temperatures of 350 and 500 °C may be as a result of the change of the environment of the Bi^{3+} ions from cubic Gd_2O_3 to orthorhombic $Gd_2Si_2O_7$ (see figure 5.1 (a)). The Si diffusion was responsible for the change in the structure of the Bi^{3+} doped Gd_2O_3 phosphor material to Bi^{3+} doped gadolinium silicate phosphor. Also, in samples prepared with substrate temperatures of 350 °C and 500 °C a new small intensity peak was observed on the high wavelength side around 700 nm, which might be because of a change in the surrounding of the Bi^{3+} ions due to the presence of the $Gd_2Si_2O_7$ phase. The second peak at 700 nm was due to the contributing presence of the silicate as well as the oxide. Because of outer electrons of Bi^{3+} which are not shielded from the surrounding environment, all phosphor hosts activated with Bi^{3+} ions show significant changes in their luminescence properties [37]. Figure 5.4(d) demonstrates that for the thin films deposited in O_2 the PL intensity increased with the increase of the substrate temperatures up to 350 °C and then decreased with a further increase in temperatures to 500 °C. The increase in PL intensities may also be due to the increased crystallinity of the films (see figure 5.1(b)) [21]. The crystallinity of the films may be enhanced by increasing the substrate temperature [33], which may have caused the improvement in the emission. Abdelrehman *et al.* [21] reported that when studying $SrO:Bi^{3+}$ (0.2 mol%) phosphor thin films prepared by PLD in the presence of O_2 gas at higher substrate temperatures, the increased PL intensities were due to the improvement of the films' crystallinity. Also, Jafer *et al.* [25] reported that the increase in PL intensities of the $Y_2O_3:Bi^{3+}$ phosphor thin films prepared by PLD in the presence of O_2 gas were due to the increased crystallinity and were related to the decrease in the surface roughness of the thin films. On the other hand, the lower luminescence intensity of the sample prepared at 500 °C may be due to the subsequent loss in Bi^{3+} due to volatile species as a result of the increased substrate temperature. The XRD results indicated that the high growth temperature can improve the crystallization of the Gd_2O_3 PLD thin film in the O_2 atmosphere. The sample prepared at 500 °C in O_2 had the best crystallinity, but the film deposited at a substrate temperature of 350 °C had the best emission intensity and good morphology. Therefore, it is evident that the PL data did not fully correspond with the XRD data when viewed from the perspective of crystallization. Thus, it is suggested that the PL intensity depends not only on the crystallization of the material but also on stoichiometry and the presence of the dopants in the crystal [38]. In the sample prepared above 350 °C at 500 °C, the species of Bi^{3+} may be volatilized in large quantities causing a decrease in luminescence intensity. To obtain the best films when the substrate temperature and background gas pressure are balanced, this determines the best stoichiometric measurement of the material. Therefore, in our case, the optimum sample was at the substrate temperature of 350 °C in O_2.

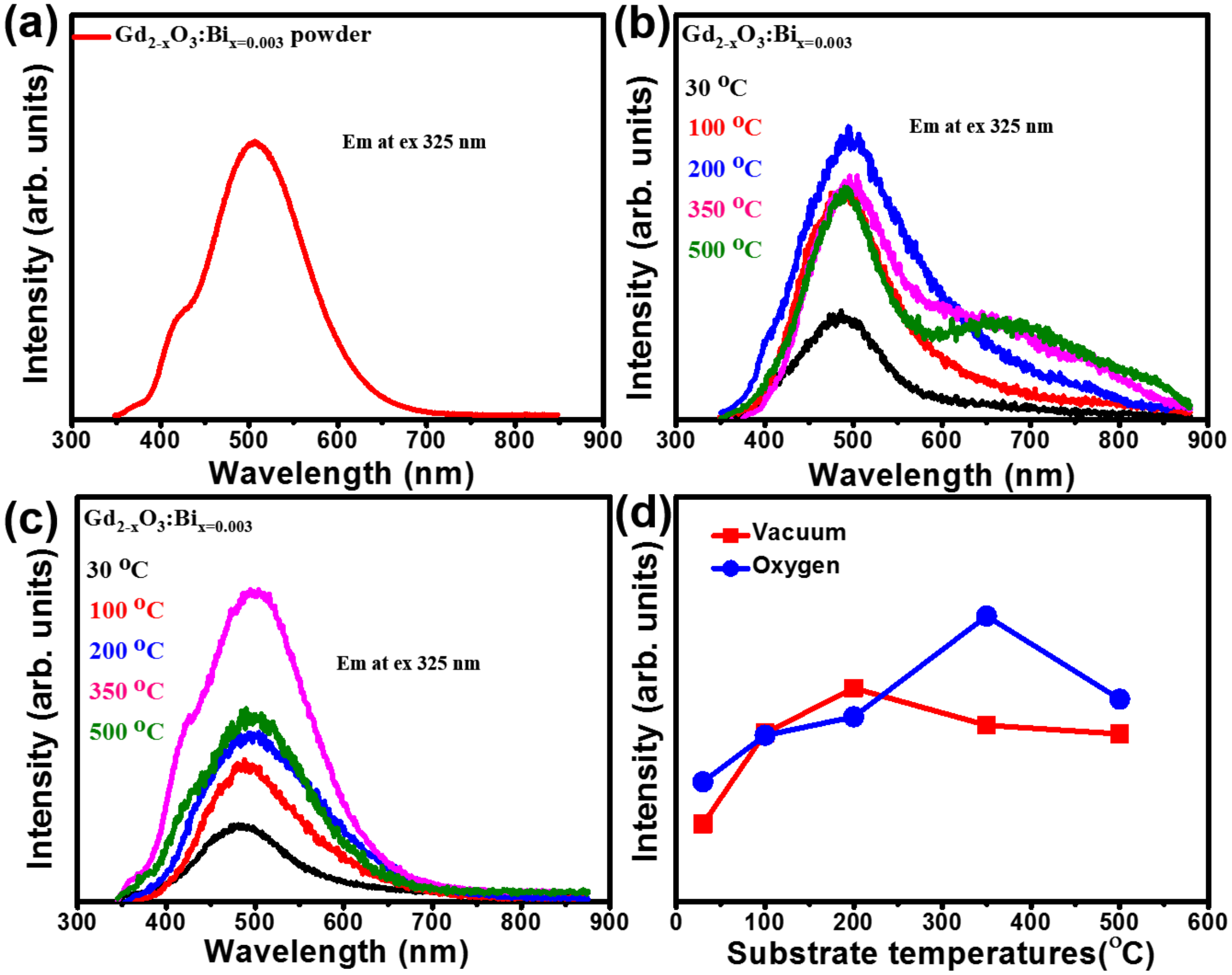

Figure 5.4: PL emission of the $Gd_{2-x}O_3:Bi_{x=0.003}$ under a 325 nm He-Cd laser excitation for (a) the powder and PLD thin films prepared in (b) vacuum, (c) O_2 deposited at various substrate temperatures, (d) the variation of maximum PL intensity as a function for substrate temperature.

Figure 5.5 illustrates the color coordinates of the PL emissions of the $Gd_{2-x}O_3:Bi_{x=0.003}$ as powder and deposited thin films which were obtained using the Commission Internationale de I'Eclairage (CIE) coordinate system [39]. The color coordinates in figure 5.5 were obtained for the thin films samples prepared in O_2 and vacuum with maximum emission intensities, which were found to be (0.21, 0.53) and (0.54, 0.53) for the films fabricated at 200 °C in a vacuum and 350 °C in O_2, as compared to (0.22, 0.55), for the powder sample. The colors emitted by the thin films were almost the same with the color coordinates for the powder in the blue-green region.

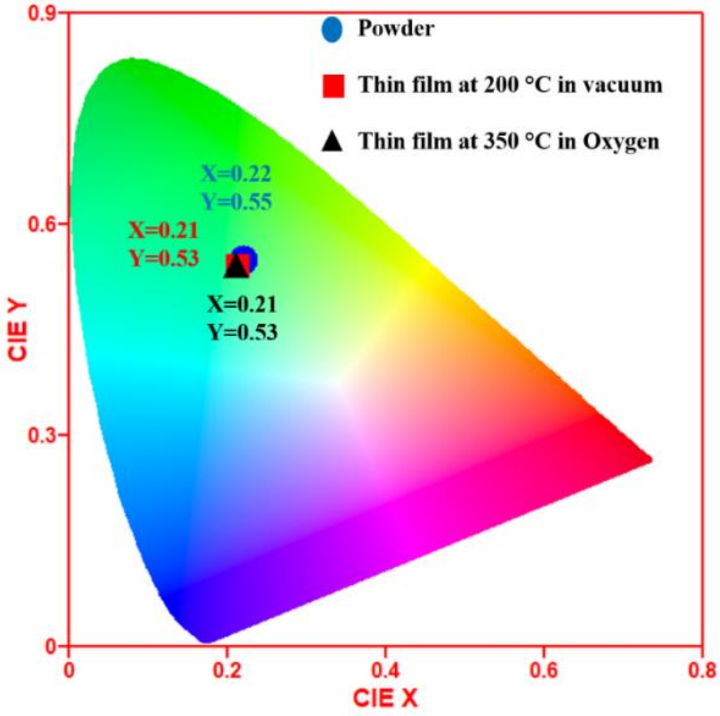

Figure 5.5: The calculated chromaticity coordinates for the emission for the $Gd_{2-x}O_3:Bi_{x=0.003}$ powder and optimized thin film samples prepared at 200 °C in vacuum and 350 °C in O_2.

5.3.4 Surface analysis and CL degradation

Figure 5.6 displays the EDS spectrum for the $Gd_{2-x}O_3:Bi_{x=0.003}$ for (a) the powder and (b) the 350 °C in O_2 thin film, which was the optimized thin film sample. Carbon (C) probably came from contamination by atmospheric hydrocarbons that were introduced to the sample during synthesis and due to atmospheric handling, also probably came from the carbon tape on which the samples were mounted. Gd and O were observed in the samples as expected. No Bi peaks were observed in the spectra as they would be expected to be detected at 2.4, 2.7 and 3.4 keV [40], probably due to its low concentration in the samples. Silicon (Si) around 1.7 keV is associated with the diffusion of Si from the substrate. In addition to the EDS spectrum, an elemental map displaying the dispensation of the elements that were also detected on the surface of the material has also been shown. From the map, it can be seen that all the elements existent within the phosphor material were uniformly distributed over the sample.

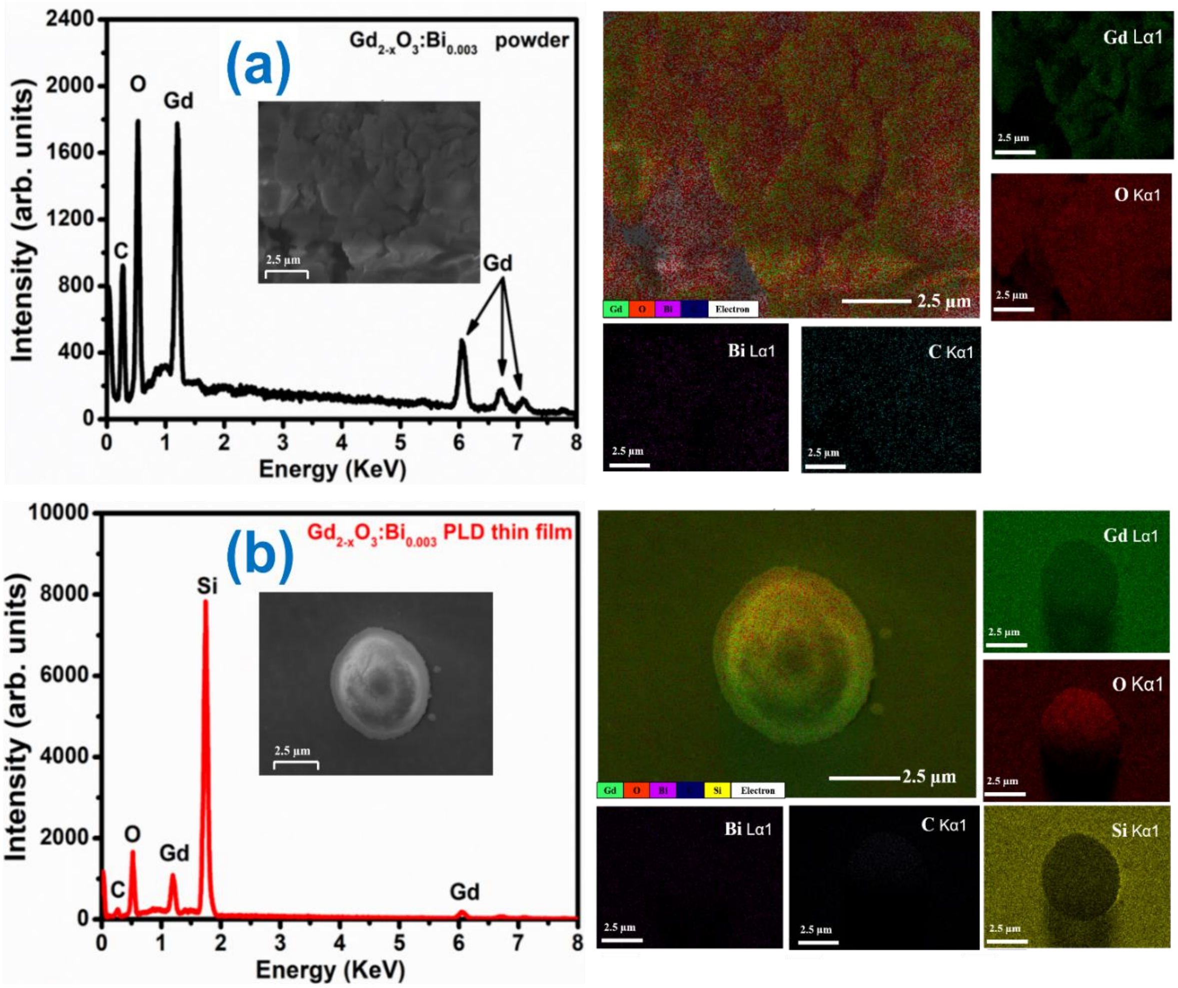

Figure 5.6: (Color online) EDS spectra and elemental mapping of the $Gd_{2-x}O_3:Bi_{x=0.003}$ (a) powder and (b) thin film prepared at the substrate temperature of 350 °C in O_2.

Figure 5.7 (a,b) displays Auger survey spectra prior and post to electron irradiation, for electron beam exposure using a beam current of 6.2 µA (current density of 1.27 mA cm^{-2}) and beam energy of 2.5 keV in (a) vacuum and (b) O_2 for the thin film sample deposited at 350 °C in O_2. The principal elements of the Gd_2O_3 material are present, namely Gd in the 50–170 and 255 -

260 eV energy range and O at 510 eV [41], indicating that a compound of Gd_2O_3 was formed for the films as compared to the powder [3]. Bi was not detected because of its low concentration. Additionally, AES is only sensitive for the upper few surface layers, so there were also adventitious Cl and C on the surface detected with peaks around 188 and 272 eV, respectively, before degradation. The species of occasional impurities are present on the surface layers because of exposure to the atmosphere [3]. It is evident that the surface contaminations of the Cl and C were approximately removed during the prolonged electron irradiation process. Thus, the O and the Gd peaks became more prominent after the removal of the contaminants Cl and C, as vaporized species [3]. The variation of element/oxygen Auger peak-to-peak heights (APPHs) as a function of the electron dose is illustrated in figure 5.6 (c) in a vacuum at a base pressure of 1.3×10^{-8} Torr and (d) backfilled to an oxygen atmosphere partial pressure of 1.1×10^{-7} Torr for around 24 h. It is clearly seen that Cl and C peaks were reduced whereas the Gd and O peaks were growing slightly concurrently. Some of the Gd and O atoms were also covered initially by C atoms. Then with C removed from the upper layers of the phosphor when irradiated, this increased the AES intensity of the elements. The primary growth in the Gd and O intensity accompanied by the decrease of C and Cl were spotted up to the rate of degradation of 20 C/cm^2 in vacuum, figure 5.6(c), and then stabilized after that. The removal of the contaminants such as C and Cl from the surface in the course of degradation has been well explained by the electron stimulated surface chemical reaction (ESSCR) model as reported by Swart *et al.* [42]. The electron beam separates O_2 and other gases absorbing on the surface from molecular species to atomic/ionic species that will then interact with C and Cl to form volatile compounds [43]. Similarly, when degraded in O_2, figure 5.6(d), initially the growing intensity for Gd and O was caused by loss of the adventitious C and Cl from the surface. It must be pointed out that more C was present at the spot of the film used for the O_2 degradation. There was an instability in the C, Gd and O intensities up to around 100 C/ cm^2. The C components on the surface were exhausted during the initial phase of exposure from 0 to 125 C/cm^2 and concurrently the Gd grew at first, then reduced and stabilized during further electron exposure. The C was entirely eliminated from the surface after a dose of about 150 C/cm^2. There might have been a much higher rate of interaction between the components in the oxygen atmosphere, causing changes to the sample surface chemistry [43].

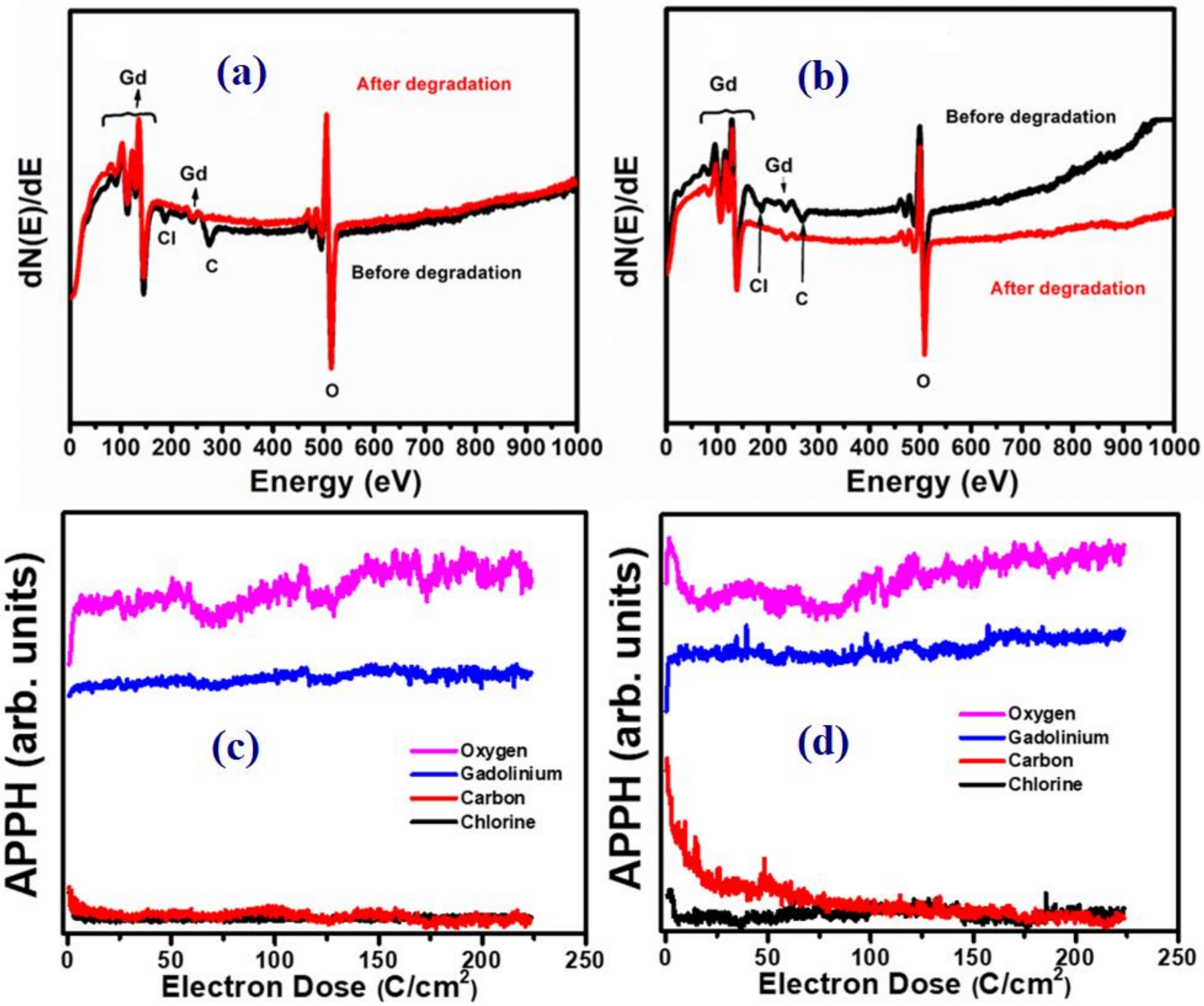

Figure 5.7: $Gd_{2-x}O_3:Bi_{x=0.003}$ thin film deposited at 350 °C in O_2 prior and post-irradiation: AES spectra in (a) vacuum and (b) backfilled with oxygen, APPHs in (c) vacuum and (d) backfilled with oxygen.

Figure 5.8 displays the CL peak intensities at 505 nm of the thin film deposited at 350 °C in O_2 as a function of electron beam exposure in (a) vacuum with a base pressure of 1.3×10^{-8} Torr and (b) backfilled to oxygen up to the pressure of 1.1×10^{-7} Torr for around 24 h, excited using an electron beam of 2.5 keV energy in the Auger system. The CL spectra are displayed by the insets prior and post to degradation by the electron beam irradiation process. In we earlier work [3] we reported that the CL degradation and surface chemical changes of the $Gd_{2-x}O_3:Bi_{x=0.003}$ phosphor powder directly correlated. In this case, the initial degradation of the CL intensity may also have been related to the presence of contamination elements on the surface, figure 5.7. For the vacuum case shown in figure 5.8(a) the CL intensity showed an initial substantial reduction beginning up to 15 C/cm^2 dose and subsequently a 10–20% slight increase until the finish of the CL intensity measurements. The CL intensity at the end of data collection was about 75% of the initial value, but it never returned to its initial value. The CL first decreased and then increased due to the formation of some non-luminescent surface layer which formed due to the ESSCR as C and Cl are removed from the thin film surface, or perhaps the surface layer became exhausted of Bi or the Bi formed clusters during this layer, which in both cases would reduce the emission from Bi^{3+}. Therefore the recently formed surface layer has an effect on the charging of the surface with a direct effect on the intensity of the CL system. There was no change in the shape and peak position of the CL spectra prior to and after the degradation. For the degradation in the oxygen atmosphere shown in figure 5.8(b), the sample showed a different degradation behavior than in vacuum. The CL intensity initially increased up to a dose of 90 C/cm^2 and then stabilized. During the initial irradiation, the change of the CL was inhibited until the C was eliminated entirely from the surface as presented in figure 5.7(b).

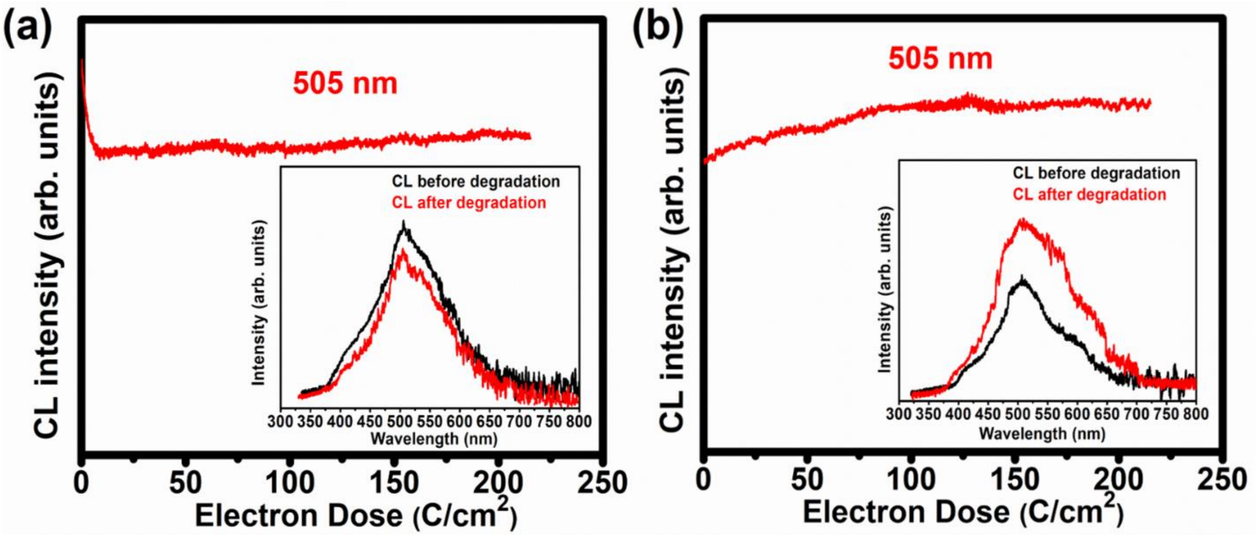

Figure 5.8: CL intensity of $Gd_{2-x}O_3:Bi_{x=0.003}$ thin film deposited at 350 °C in O_2 as a function of electron dose exposure in (a) vacuum and (b) backfilled with oxygen. The insets represent the CL spectra prior and after degradation.

To determine the electronic state and oxidation of the constituent elements on the phosphor surface before and after the electron exposure of the thin film sample, XPS measurements were made for the un-degraded sample and the samples degraded in vacuum and oxygen. Figure 5.9

displays the XPS survey spectra obtained from the $Gd_{2-x}O_3:Bi_{x=0.003}$ undegraded powder and thin film and the electron beam irradiated thin film samples. The surveys confirm that Gd and O were the major components on the surface of these materials, while Bi also was observed. In addition, adventitious C and Cl were also present. The C and Cl impurity species is attributed to occasional hydrocarbons and was present only on the surface layer in view of handling and exposure to the atmospheric environment. It was completely removed post-irradiation as earlier determined by AES, thus indicating that the synthesized $Gd_{2-x}O_3:Bi_{x=0.003}$ films have good pureness and that the observed C was not occurring from the incorporation of precursor impurities during PLD deposition. As concerning the elemental composition of $Gd_{2-x}O_3:Bi_{x=0.003}$ thin films prior and post to degradation experiments performed in different environments of vacuum and oxygen, only C, Cl, O, Gd and Bi peaks were detected at the sample surface. No peaks from silicon were detected, indicating complete substrate coverage. XPS spectra for all binding energies were corrected by using the C─C bond of the C 1s peak (binding energy 284.5 eV) as a standard, to compensate for the effect of charging on the material in the course of analysis. The above is achieved since C is present as an adsorbed carbon in any XPS sample also its binding energy normally remains constant, regardless of the sample's chemical state. In the peak fit procedure, all the peaks were postulated to have a mixed Gaussian-Lorentzian shape [44].

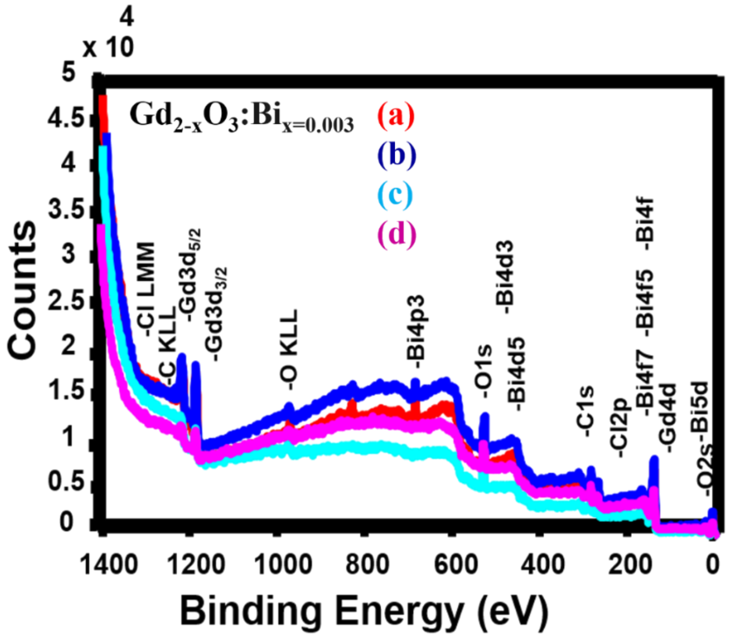

Figure 5.9: XPS survey spectra for $Gd_{2-x}O_3:Bi_{x=0.003}$ after 60 s of Ar^+ sputtering (a) powder and thin film deposited at 350 °C in O_2 (b) un-degraded and after degradation (c) in vacuum and (d) backfilled with oxygen.

XPS measurements can be used to determine the different bonding states for Gd 4d, O 1s and Bi 4f. There are two different sites for the Bi^{3+} ions in the Gd_2O_3 crystal structure that correspond to the C_2 and S_6 sites of Gd^{3+}. Figure 5.10 displays the XPS high-resolution spectra of the Gd 4d and Bi 4f energy region (measured after 60 s Ar^+ ion beam sputter cleaning) from the un-degraded powder and thin film and the degraded thin film samples in vacuum and backfilled with oxygen. A complex multiplet structure of the Gd 4d peak was observed, arising from electrostatic interactions between the 4d hole and 4f electrons, very large in the current state because of the same basic quantum number of the two shells [45]. Figure 5.10 (a) of the un-degraded powder sample exhibits four characteristic deconvoluted peaks at binding energies present in the lower energy positions at 139.8 and 142.4 eV and 144.4 and 146.7 eV which are due to Gd $4d_{5/2}$ and Gd $4d_{3/2}$, originating from the 4d shells of the ions in the two different Gd^{3+} sites [46]. There were two main peaks of Bi 4f centered at 157.9 eV and 163.2 eV, each of which can be deconvoluted into two shoulder peaks which indicate that Bi was at two site. The lower binding energy values are allocated at the 156.7 and 162.3 eV of the Bi $4f_{7/2}$ peaks at the two possible sires, while the other pair's at higher binding energy values at 158.6 eV and 163.8 eV are due to the Bi $4f_{5/2}$ levels. In Figure 5.10 (b) the un-degraded thin film sample consisted of eight peaks caused by Gd $4d_{5/2}$ and Gd $4d_{3/2}$ and the same four peaks of Bi $4f_{7/2}$ and Bi $4f_{5/2}$ levels as for the un-degraded powder sample. Figure 5.10 (c and d) show the electron beam irradiated thin film samples in base pressure and backfilled with oxygen. The same peaks of Gd $4d_{5/2}$ and Gd $4d_{3/2}$ were observed for the un-degraded thin film sample with increasing peak intensity. The removal of the C from the surface after the degradation process resulted in the peak intensities of Gd increased (which was also observed in the AES results, figure 6.7). The same Bi 4f peaks were observed for the degraded thin film samples as for the un-degraded thin film sample with a decrease in the peak intensities, showing that the Bi concentration on the surface was reduced during CL degradation.

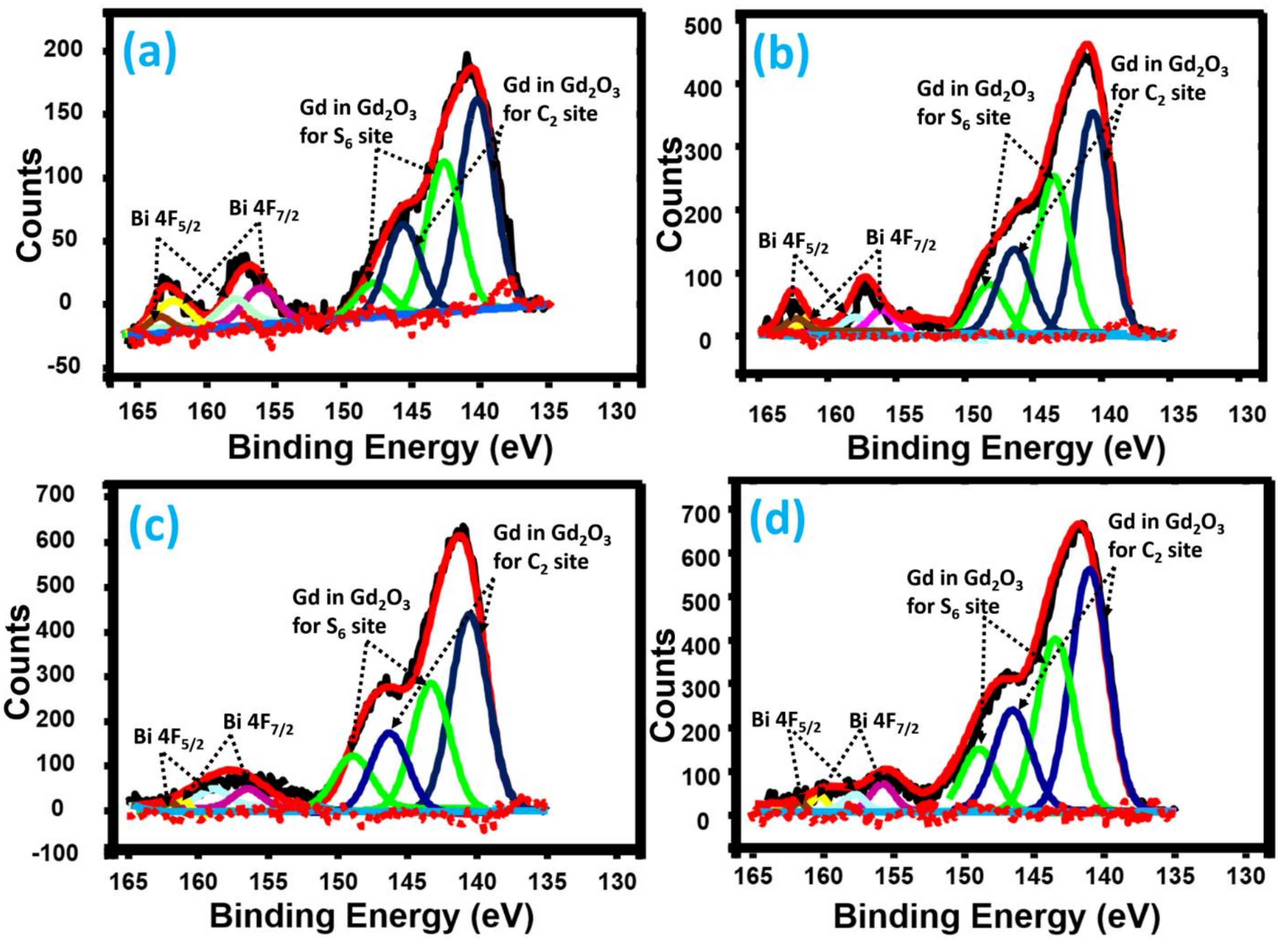

Figure 5.10: High-resolution XPS spectra of deconvoluted Gd 4d and Bi 4f in $Gd_{2-x}O_3$:$Bi_{x=0.003}$ after 60 s of Ar^+ sputtering (a) powder, and thin film deposited at 350 °C in O_2 (b) un-degraded and after degradation (c) in vacuum and (d) backfilled with oxygen.

Figure 5.11 shows a deconvolution of the O1s XPS spectra for the un-degraded powder and thin film and the electron beam irradiated thin film samples in vacuum and backfilled with oxygen. The O 1s peak is very broad with an asymmetrical shape. This suggested the O^{2-} ions are occupying more than one site in the crystal structure and that there is more than one bonding state. In Figure 5.11(a) the un-degraded powder sample revealed that the O 1s peak is comprised of six components. The peak located at 529.0 eV was attributed to the standard binding energy of O^{2-} in Gd_2O_3 while the peak at 530.9 was attributed to adsorbed -OH groups and carbonates [45, 47]. The peak positioned at ~531 eV is correlating to the loss of oxygen from the sample as well as the O^{2-} ions in the oxygen-deficient regions [48]. The peak at 531.1 eV was assigned to the O^{2-} ions related to Bi_2O_3 as the XPS handbook reference Bi_2O_3 to be at 528.5-531.5 eV [44]. The O 1s peak at 531.7 eV can be ascribed to oxygen associated with carbonates [44]. The attributed presence of hydroxyl groups and carbonates/bicarbonates is due to the sample being exposed to air. The O 1s associated with carbonates and hydroxyl groups was removed after electron degradation, which was due to the removal of the surface contamination. The highest peak around 532.1 eV is attributed to absorbed O^{2-} chemically adsorbed oxygen (O^{Chem}) on the surface [49]. In Figure 5.11 (b) of the un-degraded thin film sample spectrum revealed that the O 1s peak consisted of five sub-peaks. Figure 5.11 (c) and (d) present the O 1s peak spectra after electron beam irradiation of the sample in vacuum and backfilled with oxygen, respectively. As presented in AES results it seems that all peaks related by contaminations components such as hydroxyl groups and carbonates/bicarbonates were removed after degradations in both cases at vacuum and backfilled with oxygen, because the peaks at 529.0 eV and 531.1 eV were allocated to O^{2-} ions situated of the Gd_2O_3 host and Bi_2O_3. There were a variation in the intensities between the peaks at 531.1 and 532.1 eV were associated with Bi_2O_3 and O^{chem} in figure 5.11 (c,d). This may be due to the different binding energies of the electrons in the Bi_2O_3 structure due to screening and charge density exchange between the layers in different degradation environments. It was found that the different bonding states measured by XPS for O 1s, Gd 4d and Bi 4f indicate two different Bi^{3+} ion sites in the Gd_2O_3 crystal structure and that the energy modes correlate well with the theory and results from the C_2 and S_6 sites as reported in the literature. Therefore, have been established the presence of the contaminant species absorbed at the surface of the sample according to the XPS results, and then removed in the course of irradiation to form volatile species during ESSCRs, which is consistent with the AES and EDS results.

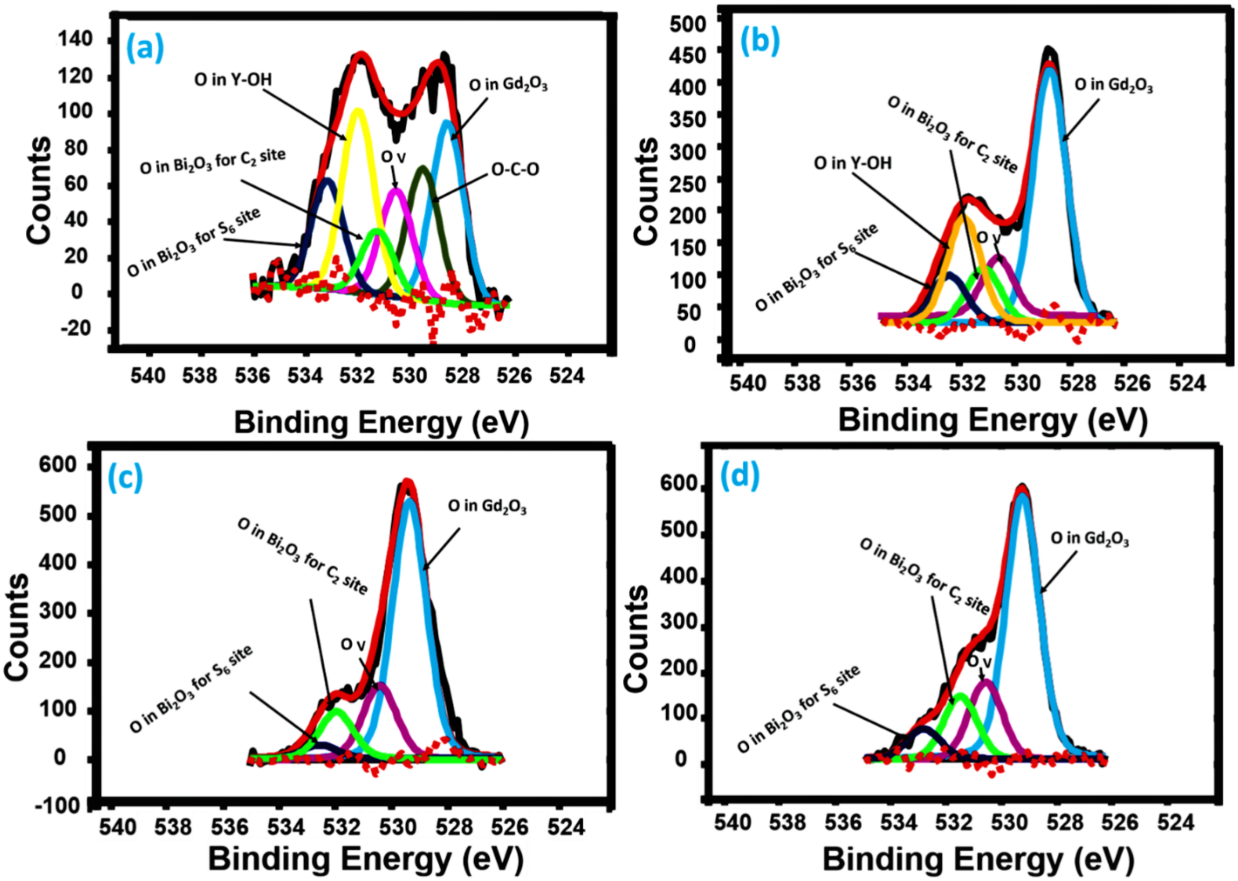

Figure 5.11: High-resolution XPS spectra of deconvoluted O 1s peak in $Gd_{2-x}O_3:Bi_{x=0.003}$ after 60 s of Ar^+ sputtering (a) powder and thin film deposited at 350 °C in O_2 (b) un-degraded and after degradation (c) in vacuum and (d) backfilled with oxygen.

5.4 Conclusion

$Gd_{2-x}O_3:Bi_{x=0.003}$ thin films were successfully deposited on silicon (100) substrates in vacuum and an oxygen atmosphere at different substrate temperatures using the PLD technique. The thin films fabricated in vacuum exhibited an amorphous structure at the lower substrate temperature and then a strong preferential growth on the (211) and (222) planes of the cubic phase at substrate temperatures up to 200 °C. The XRD for samples at higher substrate temperatures of 350 and 500 °C exhibited preferred orientation Miller indices on the (211) and (222) planes attributed to the orthorhombic phase of $Gd_2Si_2O_7$ as a result of Si diffusion. The thin films fabricated in O_2 displayed a crystallinity improvement with an increase in the substrate temperature, changing from an amorphous to a cubic structure with a strong (222) preferential orientation. The SEM cross-section film thickness was relatively constant, that meant the film thickness was not significantly affected by the substrate temperature. All thin films samples showed a broad PL emission from 380 - 650 nm, centered at 502 nm, which was ascribed of the Bi^{3+} ions substituting Gd^{3+} ions at sites of S_6 and C_2 symmetry. PL emission peak exhibit a minor blue shift in the location of the maximum peak intensity of the thin films compared to powder, because the peak intensity wavelength and FWHM of the Bi^{3+} ions activated oxide phosphors are greatly affected as result of the relative positions of the formation coordinate curves of the excited states are very sensitive to the surrounding bonds. The improvement in the crystallinity of the films fabricated in vacuum led first to an enhancement in PL emission intensities with increasing substrate temperature, and then to a reduction with the appearance of another peak at 700 nm at the highest substrate temperatures due to the formation of orthorhombic $Gd_2Si_2O_7$. The improved crystallinity of the films prepared in O_2 resulted first in an increase in PL emission intensities, and then a decrease for the highest substrate temperatures. From the XRD results, the films deposited at the substrate temperature of 500 °C in O_2 have the best crystallinity which matched the powder crystalline structure, but the film deposited at a substrate temperature of 350 °C had better emission intensity and good morphology. The intensity for the green CL peak decreased slightly during exposure to prolonged electron bombardment in vacuum only, while it slightly increased during prolonged electron bombardment exposure in back-filled O_2. Except for the initial change under degradation resulting from the elimination of C of the sample surface, the $Gd_{2-x}O_3$:$Bi_{x=0.003}$ thin film was found to be relatively stable when exposed to the electron beam in both the base vacuum and back-filled O_2 environments. Using the AES, EDS and XPS techniques, it has been confirmed that the main elements of the Gd_2O_3 material were obtained with no changes in the chemical composition. The high-resolution XPS results show the Bi 4f peaks close to the Gd 4d energy range. There were no additional chemical alterations detected from the XPS results of the thin films before and after degradation compared with the powder. Therefore, this thin film phosphor is favorable for field emission display applications.

References

[1] X. Jiang, L. Yu, C. Yao, F. Zhang, J. Zhang and C. Li. Synthesis and Characterization of Gd_2O_3 Hollow Microspheres Using a Template-Directed Method. *Materials*, **9(5)** (2016) 323. doi:10.3390/ma9050323.

[2] R. K. Tamrakar, D. P. Bisen and N. Brahme. Comparison of photoluminescence properties of Gd_2O_3 phosphor synthesized by combustion and solid state reaction method. *Journal of Radiation Research and Applied Sciences*, **7(4)** (2014) 550–559. doi:10.1016/j.jrras.2014.09.005.

[3] M. H. M. Abdelrehman, R. E. Kroon, A. Yousif, H. A. A. Seed Ahmed and H. C. Swart. Photoluminescence, thermoluminescence, and cathodoluminescence of optimized cubic Gd_2O_3:Bi phosphor powder. *Journal of Vacuum Science & Technology A.* **A 38,** (2020) 063207. doi:10.1116/6.0000567.

[4] M. F. Wasiq, M. Y. Nadeem, F. Chollet and S. Atiq. Substrate Temperature Effect on Optical Constants of Gd_2O_3 Thin Films. *Key Engineering Materials,* **442,** (2010) 96–101. doi:10.4028/www.scientific.net/kem.442.96.

[5] R. K. Datta. Luminescent behavior of bismuth in rare-earth oxides. *Journal of the electrochemical Society*, **114(11)** (1967) 1137. doi:10.1149/1.2426433.

[6] M. Mishra, P. Kuppusami, S. Ramya, V. Ganesan, A. Singh, R. Thirumurugesan and E. Mohandas. Microstructure and optical properties of Gd_2O_3 thin films prepared by pulsed laser deposition. *Surface and Coatings Technology*, **262**, (2015) 56–63. doi:10.1016/j.surfcoat.2014.12.012.

[7] S. Z. Toma and D. T. Palumbo. Luminescence of Some Bismuth-Activated Oxides. *Journal of the electrochemical society,* **116(2)** (1969) 274. doi:10.1149/1.2411813.

[8] G. Boulon. Processus de photoluminescence dans les oxydes et les orthovanadates de terres rares polycristallins activés par l'ion Bi^{3+}. *Journal de Physique*, **32(4)** (1971) 333–347. doi:10.1051/jphys:01971003204033300.

[9] A. Yousif, Vinod Kumar, H. A. A. Seed Ahmed, S. Som, L. L. Noto, O. M. Ntwaeaborwa and H. C. Swart, Effect of Ga^{3+} Doping on the Photoluminescence Properties of $Y_3Al_{5-x}Ga_xO_{12}$:Bi^{3+} Phosphor *ECS J. Solid State Sci. Technol*. **3 (11)** (2014) 222. doi: 10.1149/2.0021412jss.

[10] R. H. P. Awater and P. Dorenbos. The Bi^{3+}6s and 6p electron binding energies in relation to the chemical environment of inorganic compounds. *J. Lumin*, **184,** (2017) 221–231. doi: 10.1016/j.jlumin.2016.12.021.

[11] H. Fukada, K. Ueda, J. Ishino, T. Miyata and T. Minami. Blue PL and EL emissions from Bi-activated binary oxide thin-film phosphors. *Thin Solid Films,* **518(11**) (2010) 3067–3070. doi:10.1016/j.tsf.2009.08.014.

[12] A. Yousif, H. C. Swart, O. M. Ntwaeaborwa and E. Coetsee. Conversion of $Y_3(Al,Ga)_5O_{12}$:Tb^{3+} to $Y_2Si_2O_7$:Tb^{3+} thin film by annealing at higher temperatures. *Applied Surface Science*, **270,** (2013) 331–339. doi:10.1016/j.apsusc.2013.01.025.

[13] T. Minami, T. Miyata, J. Ishino and K. Sahara. Luminescent characteristics in blue-emitting Bi-activated multicomponent oxide phosphor thin films. *Journal of Vacuum Science & Technology B, Nanotechnology and*

Microelectronics: Materials, Processing, Measurement, and Phenomena, **28(2)** (2010) C2B56–C2B61. doi:10.1116/1.3363942.

[14] C. Ohshima, I. Kashiwag, S.-I. Ohmi and H. Iwai. Electrical Characteristics of Gd_2O_3 Thin Film Deposited on Si Substrate. *32nd European Solid-State Device Research Conference*, (2002) 215-418. doi:10.1109/essderc.2002.194956.

[15] A. Molle, S. Spiga, M. N. K. Bhuiyan, G. Tallarida, M. Perego, C. Wiemer and M. Fanciulli. Atomic oxygen-assisted molecular beam deposition of Gd_2O_3 films for ultra-scaled Ge-based electronic devices. *Materials Science in Semiconductor Processing,* **11(5-6)** (2008) 236–240. doi:10.1016/j.mssp.2008.10.002.

[16] R. Ranjith, A. Laha, E. Bugiel, H. J. Osten, K. Xu, A. P. Milanov and A. Devi. Downscaling of defect-passivated Gd_2O_3 thin films on p-Si(0 0 1) wafers grown by H_2O-assisted atomic layer deposition. *Semiconductor Science and Technology,* **25(10)** (2010) 105001. doi:10.1088/0268-1242/25/10/105001.

[17] D. Barreca, A. Gasparotto, A. Milanov, E. Tondello, A. Devi and R. A. Fischer. Gd_2O_3 Nanostructured Thin Films Analyzed by XPS. *Surface Science Spectra*, **14(1)** (2007) 60–67. doi:10.1116/11.20080703.

[18] H. Guo, X. Yang, T. Xiao, W. Zhang, L. Lou and J. Mugnier. Structure and optical properties of sol–gel derived Gd_2O_3 waveguide films. *Applied Surface Science,* **230(1-4)** (2004) 215–221. doi:10.1016/j.apsusc.2004.02.032.

[19] G. Niu, B. Vilquin, N. Baboux, C. Plossu, L. Becerra, G. Saint-Grions and G. Hollinger. Growth temperature dependence of epitaxial Gd_2O_3 films on Si(111). *Microelectronic Engineering,* **86(7-9)** (2009) 1700–1702. doi:10.1016/j.mee.2009.03.107.

[20] K.-S. Chang, L.-Z. Hsieh, S.-K. Huang, C.-Y. Lee and Y.-S. Chiu. Characteristics of high dielectric cubic Gd_2O_3 thin films deposited on cubic $LaAlO_3$ by pulsed laser deposition. *Journal of Crystal Growth,* **310(7-9)** (2008) 1961–1965. doi:10.1016/j.jcrysgro.2007.11.221.

[21] M. H. M. Abdelrehman, V. Craciun, R. E. Kroon, A. Yousif, H. A. A. Seed Ahmed and H. C. Swart. Effect of background atmosphere and substrate temperature on SrO:Bi^{3+}(0.2 mol%) thin films produced using pulsed laser deposition with different lasers. *Physica B: Condensed Matter,* **(851)** (2020) 411757. doi:10.1016/j.physb.2019.411757.

[22] A. Yousif, R. M. Jafer, J. J. Terblans, O. M. Ntwaeaborwa, M. M. Duvenhage, V. Kumar and H. C. Swart. TOF SIMS induced artificial topographical effects on the $Y_2(Al,Ga)_5O_{12}:Tb^{3+}$ thin films deposited on Si substrates by the pulsed laser deposition technique. *Applied Surface Science*, **313,** (2014) 524–531. doi:10.1016/j.apsusc.2014.06.016.

[23] T. Yamamoto, Y. Izumi, H. Hashimoto, M. Oosawa and Y. Sugita. Structural Changes of Y_2O_3 and La_2O_3 Films by Heat Treatment. *Japanese Journal of Applied Physics*, **45(8A)** (2006) 6196–6202. doi:10.1143/jjap.45.6196.

[24] A. Yousif, R. M. Jafer, S. Som, M. M. Duvenhage, E. Coetsee and H. C. Swart. The effect of different annealing temperatures on the structure and luminescence properties of Y_2O_3:Bi^{3+} thin films fabricated by spin coating. *Applied Surface Science,* **365,** (2016) 93–98. doi:10.1016/j.apsusc.2016.01.013.

[25] R. M. Jafer, H. C. Swart, A. Yousif and E. Coetsee. The effect of different substrate temperatures on the structure and luminescence properties of Y_2O_3:Bi^{3+} thin films. *Solid State Sci*, **53**, (2016) 30–36. doi:10.1016/j.solidstatesciences.2016.01.005.

[26] V. Kumar, H. C. Swart, S. Som, V. Kumar, A. Yousif, A. Pandey and O. M. Ntwaeaborwa. The role of growth atmosphere on the structural and optical quality of defect-free ZnO films for strong ultraviolet emission. *Laser Phys*. **24(10)** (2014) 105704 (1-9). doi:10.1088/1054-660x/24/10/105704.

[27] Y. Sato, M. Taketomo, N. Ito and Y. Shigesato. Study on early stages of film growth for Sn doped In_2O_3 films deposited at various substrate temperatures. *Thin Solid Films*, **516(17)** (2008) 5868–5871. doi:10.1016/j.tsf.2007.10.044.

[28] Z. Ghorannevis, M. T. Hosseinnejad, M. Habibi and P. Golmahdi. Effect of substrate temperature on structural, morphological and optical properties of deposited Al/ZnO films. *J Theor Appl Phys.* **9** (2015) 33–38. doi.org/10.1007/s40094-014-0157-1.

[29] J. J. Dolo, O. M. Ntwaeaborwa, J. J. Terblans, E. Coetsee, B. F. Dejene, M.-M. Biggs and H. C. Swart. The effect of oxygen pressure on the structure, morphology and photoluminescence intensity of pulsed laser deposited Gd_2O_2S:Tb^{3+} thin film phosphor. *Applied Physics A*, **101(4)** (2010) 655–659. doi:10.1007/s00339-010-5919-2.

[30] R. E. Kroon, Nanoscience and the scherrer equation versus the “Scherrer–Gottingen equation”, S. Afr. J. Sci. **109 (5/6)** (2013) Art. #a0019 (2 pages). doi:10.1590/sajs.2013/ a0019.

[31] A. Kennedy, K. Viswanathan and K. Pradeev raj. Study of the influence of substrate temperature on structural, optical, and electrical properties of Zn-doped $MnIn_2S_4$ thin films prepared by chemical spray pyrolysis. *Phys Letts A.* **380(36)** (2016) 2842–2848. doi:10.1016/j.physleta.2016.06.043.

[32] V. Vrakatseli, A. Kalarakis, A. Kalampounias, E. Amanatides and D. Mataras. Glancing Angle Deposition Effect on Structure and Light-Induced Wettability of RF-Sputtered TiO_2 Thin Films. Micromachines, **9(8)** (2018) 389. doi:10.3390/mi9080389.

[33] E. Hasabeldaim, O. M. Ntwaeaborwa, R. E. Kroon, E. Coetsee and H. C. Swart, “Effect of substrate temperature and post annealing temperature on ZnO:Zn PLD thin film properties,” *Opt. Mater. (Amst)*. **74**, (2017) 139–149. doi:10.1016/j.optmat.2017.03.027.

[34] P. Whiteside, J. Chininis and H. Hunt. Techniques and Challenges for Characterizing Metal Thin Films with Applications in Photonics. *Coatings,* **6(3)** (2016) 35. doi:10.3390/coatings6030035.

[35] E. Felder, S. Roy and E. Darque-Ceretti. Characterization of the adhesion of thin film by Cross-Sectional Nanoindentation. *Comptes Rendus Mécanique*, **339(7-8)** (2011) 443–457. doi:10.1016/j.crme.2011.05.003.

[36] A. Yousif, R. M. Jafer, S. Som, M. M. Duvenhage, E. Coetsee, H. C. Swart, Ultrabroadband luminescent from a Bi-doped CaO matrix, *RSC Adv*. **5 (67)** (2015) 54115–54122. doi.org/10.1039/c5ra09246a.

[37] A.Yousif, R. E. Kroon, E. Coetsee, O. M. Ntwaeaborwa, H. A. A. Seed Ahmed, H. C. Swart. Luminescence and electron degradation properties of Bi doped CaO phosphor. *Applied Surface Science*. **356**, (2015)1064–1069. doi:10.1016/j.apsusc.2015.08.210.

[38] B. L. Zhu, X. H. Sun, X. Z. Zhao, F. H. Su, G. H. Li, X. G. Wu, J. Wu, R. Wu, J. Liu. The effects of substrate temperature on the structure and properties of ZnO films prepared by pulsed laser deposition. *Vacuum*, **82(5)** (2008) 495–500. doi:10.1016/j.vacuum.2007.07.059.

[39] A. D. Broadbent. A critical review of the development of the CIE1931 RGB color-matching functions. *Color Research & Application*, **29(4)** (2004) 267–272. doi:10.1002/col.20020.

[40] P. Ju, P. Wang, B. Li, H. Fan, S. Ai, D. Zhang and Y. Wang. A novel calcined Bi_2WO_6/$BiVO_4$ heterojunction photocatalyst with highly enhanced photocatalytic activity. *Chemical Engineering Journal*, **236**, (2014) 430–437. doi:10.1016/j.cej.2013.10.001.

[41] E. D. Lawrence, C. M. Donald, W. P. Paul, E. R. Gerald and E. W. Roland. Handbook of Auger Electron Spectroscopy. 2nd Edition. Published by Physical Electronics Division of Perkin-Elmer. Minnesota (1976) 19-249. ISBN: 9788578110796.

[42] H. C. Swart, J. S. Sebastian, T. A. Trottier, S. L. Jones and P. H. Holloway, Degradation of zinc sulfide phosphors under electron bombardment. *Journal of Vacuum Science & Technology A,* **14(3)** (1996) 1697–1703. doi: 10.1116/1.580322.

[43] A. Yousif, H. C. Swart and O. M. Ntwaeaborwa, Surface state of $Y_3(Al,Ga)_5O_{12}$:Tb phosphor under electron beam bombardment. *Applied Surface Science,* **258(17)** (2012) 6495–6503258. doi:10.1016/j.apsusc.2012.03.066.

[44] J. F. Moulder, Handbook of X-ray Photoelectron Spectroscopy: a Reference Book of Standard Spectra for Identification and Interpretation of XPS Data, Physical Electronics, Chicago, (1995) 13-240. ISBN: 096481241X 9780964812413.

[45] Barreca, Davide; Gasparotto, Alberto; Milanov, Andrian; Tondello, Eugenio; Devi, Anjana; Fischer, Roland A.. Gd_2O_3 Nanostructured Thin Films Analyzed by XPS. *Surface Science Spectra.* **14(1)** (2007) 60–0. doi:10.1116/11.20080703.

[46] A. Saha, S. C. Mohanta, K. Deka, P. Deb, P. S Devi. Surface-Engineered Multifunctional Eu:Gd_2O_3 Nanoplates for Targeted and pH-Responsive Drug Delivery and Imaging Applications. *ACS Applied Materials & Interfaces*, **9(4)** (2017) 4126–4141. doi:10.1021/acsami.6b12804.

[47] S. Yang, H. Gao, Y. Wang, S. Xin, Y. He, Y. Wang, W. Zeng. A simple way to synthesize well-dispersed Gd_2O_3 nanoparticles onto reduced graphene oxide sheets. *Materials Research Bulletin.* **48(1)**, (2013) 37–40. doi:10.1016/j.materresbull.2012.09.065.

[48] S. K.S. Patel, P. Dhak, M. Kim, J. Lee, M. Kim, S. Kim. Structural and magnetic properties of Co-doped Gd_2O_3 nanorods. *Journal of Magnetism and Magnetic Materials.* **403**, (2016)155–160. doi:10.1016/j.jmmm.2015.11.093.

[49] M. Mukesh, K. K. Thejas, V. R. Akshay, B. Arun, M. Vasundhara. Effect of annealing conditions on particle size, magnetic and optical properties of Gd_2O_3 nanoparticles. *AIP Conference Proceedings*, **2162**, (2019) 020091–. doi:10.1063/1.5130301.

Chapter 6

Luminescence properties of Yb^{3+} and Er^{3+} co-doped into $Gd_2O_3:Bi^{3+}$ phosphor powder

This chapter reports on the DC and UC investigations of Yb^{3+} *and* Er^{3+} *co-doped* $Gd_2O_3:Bi$ *phosphor powders for SC enhancement as well as the energy transfer mechanism. Results obtained in this chapter showed that the* Gd_2O_3 *materials based on the* Bi^{3+}–Yb^{3+} *and* Bi^{3+}–Er^{3+} *couples are appropriate candidate phosphors for improving photovoltaic conversion efficiency via spectral modification utilizing the DC and UC processes.*

6.1 Introduction

The amount of energy that comes from the sun to the earth is more energy than we can consume, therefore photovoltaic (PV) technology used in solar cells (SCs) was developed to take advantage of the sun's radiation to combat the energy crises we face today. The most commonly used SCs are based on c-Si crystalline Si. Silicon PV devices are able to convert only a portion of the solar spectrum to electricity. Therefore, researchers and developers are still conducting a lot of research and experiments to develop SCs and to improve their efficiency by the photons conversion process. Luminescence materials have played an important role in the fabrication of PV and electronic applications and some of them can also be used to improve the efficiency of (SC) [1]. Recently, more attention has been on the research of modifying the solar spectrum for using in SC applications in order to decrease the dependence on non-renewable and unclean energy resources, to invest in a greener planet by producing sustainable green energy [2]. After the sunlight is absorbed by the solar cells, some of the energy is dissipated, but the high-energy photons are not used effectively and the low-energy photons are not absorbed, resulting in a lot of energy lost in converting solar energy into electrical energy, which is usually called spectral mismatch.

To reduce the amount of energy loss caused by spectral mismatch, both down-conversion (DC) or shifting (DS) and up-conversion (UC) are usually used as available options that can be effectively applied to increase the efficient use of the solar spectrum [3]. Those effects can enhance visible and infra-red lights response and improve SC performances. The effect is largely studied numerically and theoretically in solar cells based on silicon, silicon carbide and GaAs [4]. Currently, DC is reliably considered as a good way to modulate the solar spectrum and thus improve the efficiency of silicon SC [5]. The DC is the process of cutting one high-energy photon into two or more low-energy photons, which results in photon emission at a longer wavelength. The DC of UV photons to NIR photons occurs by a process of the transfer of energy between two lanthanide (Ln^{3+}) ions [6]. The UC process can be defined as the process in which two or more photons of low energy are converted into photons of higher energy, these two photons are absorbed as a result of exciting a phosphor material through a higher wavelength that leads to the emission of light with a wavelength shorter than the excitation wavelength [7]. Ln^{3+} are among the best elements that can be used as optical centers in materials for energy conversion because of the narrow emission bands and long radiation emission lifetimes, as well as the structure of their energy levels [8]. One of the most important advantages of Ln^{3+}-doped luminescence materials are the extremely effective conversion of NIR photons to visible/ultraviolet photons and vice-versa, depending on the energy levels. Emissions from the Ln^{3+}-doped materials originate from the $4f \rightarrow 4f$ transitions, which are shielded by the 5s and 5p outer orbitals, thus leading to their narrow emissions bands [9]. Ytterbium (Yb^{3+}) has only two energy states, the ${}^2F_{7/2}$ ground state and the ${}^2F_{5/2}$ excited state, separated by around 10,000 cm^{-1}, which translates to emission at approximately 1000 nm [10], potentially enabling the Yb^{3+} emission to be efficiently absorbed by c-Si SC, and make it ideal for application in SC [11]. The luminescent quantum efficiency of Yb^{3+} is approaching 100% and its unique emission from 900 to 1100 nm corresponds considerably with the bandgap of c-Si. Since the Yb^{3+} ion has NIR emission close to 1000 nm, it is promising to enhance the efficiency of silicon SC without significant thermalization losses [12]. Regrettably, Yb^{3+} has weak absorbance of photons in the UV to blue regions, which could cause weak NIR emission of Yb^{3+} limiting the possibility of SC applications [9]. Recently, it has been demonstrated that the luminescence of Ln^{3+} could be significantly improved via energy transfer from Bi^{3+} to the Ln^{3+} ions [2]. The combination of the Bi^{3+} and the Yb^{3+} ion is promising to enhance the NIR emission of the Yb^{3+} ions [13]. On the other hand, recently, significant progress has been achieved on the luminescence properties of trivalent erbium Er^{3+} in various material hosts that were well suited for UC studies [14]. Since the $4f^n$ electron levels of Er^{3+} ions have readily accessible intermediate levels upon excitation by NIR, they are therefore strong candidates for the UC processes. Er^{3+} has branched energy levels capable of pumping infrared radiation that nicely correspond to the most attractive wavelength of 980 nm making it an excellent the most efficient ions for UC luminescence. Since Er^{3+} has dense energy levels existing in an extensive range of infrared wavelengths, most of the UC research has been concentrated on excitation by an infrared laser [15]. The excited state ($^4I_{11/2}$) of Er^{3+} with a longer lifetime can be easily populated stepwise after 980 nm infrared excitation [16]. Er^{3+} ions generally show three strong blue-green fluorescence transitions and a weak red emission in the visible region [17].

Recently trivalent rare earth oxides such as gadolinium oxide (Gd_2O_3) have been the subject of great interest in optical properties and energy transfer studies. Gd_2O_3 is a stable compound and has a 4f electron shell which makes its optical, chemical and electronic properties have high potential, which is suitable to work as a host of highly efficient optical transfer materials [18]. The best materials for DC and UC hosts must not only have excellent optical aspects but also be simple to synthesize and have high chemical and thermal stability [19]. Among the rare earth oxides, crystalline Gd_2O_3 has very favourable optical properties as well as stable physical and chemical properties, which makes Gd_2O_3 considered as exceedingly appropriate for coating of SC [20]. It is known that Gd_2O_3 is a low-phonon energy host, making it is an excellent host for luminescent rare-earth ions that contribute to DC or UC materials, which strongly enhance radiative transitions by reducing non-radiative relaxation [21]. Gd_2O_3 has three confirmed polymorphic structural forms, namely cubic, monoclinic and hexagonal, depending on the preparation conditions [22]. The cubic structure of Gd_2O_3 is located in the space group $Ia\bar{3}$, with two dissimilar Gd lattice sites and a variety of 6 surrounding geometries for oxygen [23]. In a unit cell, there are eight octahedral coordinated sites with six oxygen atoms that will have the S_6 symmetry. In addition, there are another 24 sites where two oxygen vacancies are located on a cube of the C_2 symmetry where the vacancies are located on a face diagonal [24]. It has been observed that energy transfer from Bi^{3+} to Ln^{3+} ions can significantly improve the fluorescence of the Ln^{3+} ions which enhances the efficiency of SCs [2,25]. As reported in the literature the luminescence of Yb^{3+} [26], Nd^{+3} [27], Er^{3+} [17], Eu^{3+} Dy^{3+}, Ho^{3+} and Sm^{3+} [28] as DC and UC emissions can be greatly enhanced through resonant energy transfer from Bi^{3+} to these ions.

Bi^{3+} ions can act and be used as an excellent sensitizer ion to enhance lanthanide, as it can significantly absorb ultraviolet light and transfer energy to other luminescent centers [16]. The ground state of free Bi^{3+} ions has a $6s^2$ electronic configuration in the $^1S_0$ state and the excited configuration is 6s6p. In general the emission spectra observed from the Bi^{3+}-activated phosphor are attributable to the transition from the 6s6p (which has four levels, the triplet ($^3P_0$, $^3P_1$, and $^3P_2$) and singlet ($^1P_1$)) to the $6s^2$ [29]. The emission of the Bi^{3+} ions in Gd_2O_3 are from two different sites (C_2 and S_6). For the C_2 site it takes place mainly around 505 nm by reason of the $^3P_1 \rightarrow {}^1S_0$ transition of Bi^{3+} [24]. The energy responsible for the transition of the $^3P_1 \rightarrow {}^1S_0$ of Bi^{3+} in the C_2 site is almost twice that of the $^2F_{7/2} \rightarrow {}^2F_{5/2}$ transition for the Yb^{3+} ions. This enables the efficient use of Bi^{3+} ions in the efficient cooperative energy transfer process from Bi^{3+} to Yb^{3+}, for use in increasing the efficiency of silicon SC when co-doped with Bi^{3+} in the Gd_2O_3 as a host [2]. On the other hand, due to the broadening of the excitation and emission range of the Bi^{3+} doped various hosts, there was a large energy overlap between the Bi^{3+} emission band and the Er^{3+} excitation band which makes them candidates for highly efficient energy transfer from Bi^{3+} ions to Er^{3+} ions [17]. Several kinds of research using Bi^{3+} as a sensitizer for the luminescent center of Yb^{3+} and Er^{3+} in the Gd_2O_3 matrix that could greatly improve the transfer of the resonance energy from Bi^{3+} to Yb^{3+} and Er^{3+} have been reported [2, 14]. Here the effects on the luminescence properties of different Yb^{3+} and Er^{3+} concentrations of co-doped $Gd_2O_3:Bi^{3+}$ phosphors prepared using the combustion method were studied, for the possibility of being used in the thin-film form as the luminescent DC and UC layers in front of c-Si SC to improve the efficiency of the SC. The luminescence results obtained in this chapter showed that the Gd_2O_3 materials based on the Bi^{3+}–Yb^{3+} and Bi^{3+}–Er^{3+} couples are appropriate candidate phosphors for improving photovoltaic conversion efficiency via spectral modification utilizing the DC and UC processes.

6.2 Experimental setup

6.2.1 Material preparation

Gd_2O_3 and $Gd_{2-x}O_3:Bi_x^{3+}$ phosphor powders have been prepared by using the combustion method and the influence of various calcining temperatures and dopant concentration were investigated [24]. The optimum luminescent intensity was found for the $Gd_{2-x}O_3:Bi_{x=0.003}^{3+}$ sample annealed at 1000 °C for 2 h. Thus $Gd_{1.997-x}O_3$: $Bi_{x=0.003}^{3+}$ co-doped by Yb and Er were also fabricated by using the combustion method. For a typical preparation, $Gd(NO_3)_3 \cdot 6H_2O$ and H_2CONH_2 were used as the starting materials according to the reaction [24].

$$2\ Gd(NO_3)_3 \cdot 6H_2O + 5\ NH_2CONH_2 \rightarrow Gd_2O_3 + 5\ CO_2 + 22\ H_2O + 8\ N_2 \qquad (6.1)$$

These weighed components were then dissolved in deionized water under stirring using a magnetic stirrer for about 2 h at 100 °C in a beaker until the material was converted into a transparent precursor liquid. $Bi(NO_3)_3 \cdot 5H_2O$ was substituted for some $Gd(NO_3)_3 \cdot 6H_2O$ to produce the doped samples. The co-doped $Gd_{1.997\text{-}x}O_3$: $Bi_{x=0.003}^{3+}$, Yb_x^{3+} and Er_x^{3+} (x=0.005, 0.010, 0.015, 0.020, 0.025 and 0.030) samples were fabricated by the same manner with only introducing ytterbium (III) nitrate $Yb(NO_3)_3$ and Erbium(III) nitrate pentahydrate $Er(NO_3)_3 \cdot 5H_2O$ as part of the starting materials. All chemicals used were bought from Sigma Aldrich. The solution was placed in a furnace that was already heated to a temperature of 600 °C. Within 5 min, successful combustion occurred with crunchy, foamy end products. To obtain the final formation of the required samples, they were annealed at a temperature of 1000 °C for 2 h in an air atmosphere.

6.2.2 Characterization

The phosphor samples synthesized were characterized by X-ray diffraction (XRD) using a Bruker Advance D8 diffractometer (40 kV, 40 mA) with Cu Kα X-rays ($\lambda = 0.154$ nm) to determine the structure of the powder. Scanning electron microscope (SEM) images were captured by using a JEOL JSM-7800F SEM. UV–visible absorptions by diffuse reflectance measurements were collected by the Lambda 950 UV–Vis spectrophotometer with the reflectivity relative to Spectralon standard. Photoluminescence (PL) spectra were recorded using an Edinburgh Instruments FS5 spectrophotometer with a 150 W steady state ozone-free xenon lamp as an excitation source. The visible emission spectra and NIR luminescence spectra for co-doped samples were collected using a Kimmon IK Series He-Cd Laser (325 nm) as the excitation source. The NIR emission was dispersed by a Horiba iHR 320 monochromator and detected by a solid-state DSS-IGA020T detector. The cathodoluminescence (CL) spectra were collected using a Gatan MonoCL4 accessory fitted to the JEOL JSM-7800F system connected to the SEM for an electron energy of 5 keV in a vacuum of the order of 10^{-5}–10^{-6} Torr. All measurements were performed at room temperature.

6.3 Results and discussion

6.3.1 Structure and morphology

Figure 6.1(a) and (b) display the representative XRD patterns for the obtained pure Gd_2O_3 host samples, the single doped $Gd_{1.997}O_3$: $Bi_{x=0.003}^{3+}$ and $Gd_{1.997-x}O_3$: $Bi_{x=0.003}^{3+}$ co-doped by Yb_x^{3+} and Er_x^{3+}. All observed diffraction peaks of the XRD patterns indicated the formation of the cubic type crystalline single-phase Gd_2O_3. The obtained lattice parameters were $a = b = c = 10.813$ Å and $\alpha = \beta = \gamma = 90°$ according to the JCPDS card #43-1014 with a space group $Ia\bar{3}$. No change on the Gd_2O_3 phase structure was observed except for a small shift when adding the Bi^{3+} ions, which could be as a consequence of the difference in the ionic radius of the Bi^{3+} (103 pm) and the Gd^{3+} (93.8 pm) [24]. With an increase in the Yb^{3+} and Er^{3+} ions concentration, also no other phase was also observed. However, a slight shift in the XRD reflections to higher Bragg angles were observed. These shifts might be caused by lattice deformations as a result for the slight variation in the ionic radius of the Gd^{3+} host ion and the Yb^{3+} (86.8 pm) and Er^{3+} (89.0 pm) dopants ions [29]. Such phenomenon can be attributed to the substitution of Gd^{3+} by Yb^{3+} and Er^{3+} ions with smaller ionic radius, which resulted in the contraction of the crystal lattice [30]. Therefore, it was ascertained that the incorporation of the sensitizer Bi^{3+} ion and the activators Yb^{3+}, Er^{3+} ions did not affect the crystal structure of the Gd_2O_3 matrix, which means that these ions were well dispersed in the Gd_2O_3 host sites by substitution for the Gd^{3+}.

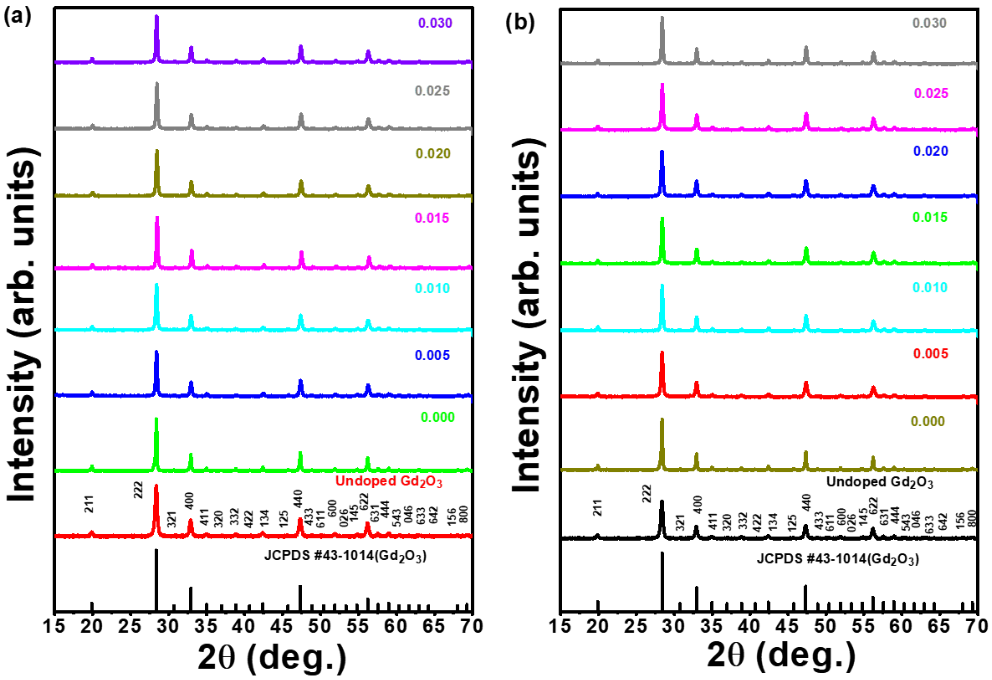

Figure 6.1: (a) XRD pattern for $Gd_{1.997-x}O_3$: $Bi_{x=0.003}^{3+}$, Yb_x^{3+}phosphor synthesised at varying Yb^{3+} concentration. (b) XRD pattern for $Gd_{1.997-x}O_3$: $Bi_{x=0.003}^{3+}$, Er_x^{3+} phosphor synthesised at varying Er^{3+} concentration while keeping the Bi^{3+} concentration constant.

The Rietveld method was applied mainly for the purpose of evaluating the detailed crystal structure information of the samples. For the Rietveld refinement, the software known as Material Analysis Using Diffraction (or MAUD for short) was used for the Gd_2O_3 host as well as the higher concentration samples [32]. Figure 6.2 shows the Rietveld refinement of (a) the Gd_2O_3 host (b) $Gd_{1.997-x}O_3$:$Bi_{0.003}$, $Yb_{x=0.030}$ and (c) $Gd_{1.997-x}O_3$:$Bi_{0.003}$, $Er_{x=0.030}$. The refinement of all the Gd_2O_3 samples were started using the crystal structure model of the C-form of Gd_2O_3 as mentioned earlier in that from JCPDS card #43-1014 with a space group $Ia\overline{3}$, $a = b = c = 10.813$ Å and $\alpha = \beta = \gamma = 90°$, atomic positions for Gd1 in *8b*, Gd2 in *24d* with x = -0.03243, and O in 48*e* with $x = 0.391$, $y = 0.1518$, and $z = 0.37545$ and isotropic atom displacement $B = 0.25$ (Gd1), $B = 0.21$ (Gd2), and $B = 0.5$ (O) [33]. The refinement was performed for unit cell, FWHM parameters and atom position. The atom displacements were with the values found in literature. Finally the Rietveld refinement parameters are summarized in Table 6.1, where V is the cell volume R_p profile R-factor, R_{wp} the weighted profile R-factor, R_{exp} the expected factor and S goodness of fit [34]. The structure refinement results are indicating that the atom positions, fraction factors, and temperature factors of the samples agree well with the reflection conditions.

Table 6.1 Rietveld refinement factors

Parameters	**Gd_2O_3**	**$Gd_{1.997-x}O_3$:$Bi_{0.003}$, $Yb_{x=0.030}$**	**$Gd_{1.997-x}O_3$:$Bi_{0.003}$, $Er_{x=0.030}$**
$a = b = c$ (Å)	10.8	10.8	10.8
V (Å)^3	1256.2	1256.2	1256.2
R_p (%)	17.8	19.8	18.1
R_{wp} (%)	20.3	26.2	23.1
R_{exp} (%)	14.5	22.7	20.8
$S = R_{wp}/R_{exp}$	1.4	1.2	1.1

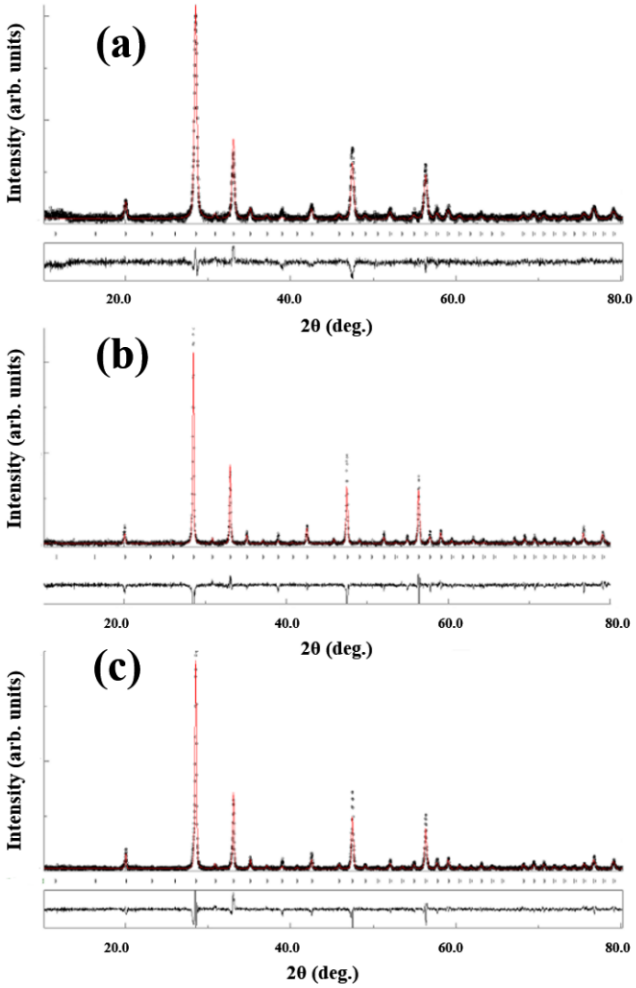

Figure 6.2: Graphical results of the Rietveld refinement of the XRD patterns of the (a) Gd_2O_3 (b) $Gd_{1.997-x}O_3$: $Bi_{x=0.003}^{3+}$, $Yb_{x=0.030}^{3+}$ and (c) $Gd_{1.997-x}O_3$: $Bi_{x=0.003}^{3+}$, $Er_{x=0.030}^{3+}$. The upper traces illustrates the observed data as dots, and the calculated pattern as solid line; the lower solid trace is a plot of the difference, observed intensity minus calculated one. The vertical markers show positions calculated for Bragg reflection.

The crystallite size and microstrain were obtained using the Williamson-Hall plot (equation 6.1), shown in figure 6.3, and the results are tabulated in table 6.2.

$$B \cos \theta = K\lambda / D + 4\varepsilon \sin \theta, \qquad (6.1)$$

where β is the 2θ-FWHM (in radians) for the diffraction peaks at the angle θ, K is the shape factor (assumed to be 0.9), λ is the X-ray wavelength (0.154 nm), D is the crystallite size and ε is the microstrain [35]. The crystal size D of the samples is estimated by calculating the inverse of the y-intercept and the strain ε from the slope of the straight-line exhibited in figure 6.3. The crystallite size of all samples are between 43.1 nm and 51.7 nm. There was a variation of the microstrain with adding Yb^{3+} and Er^{3+} ions which may be as a result of the changes in the lattice parameter of the Gd_2O_3 with increasing Yb^{3+} and Er^{3+} concentration [10]. It is well-known that the synthesis parameters and calcination conditions play a very important role in tuning the microstrain present in nanoparticles [36]. Additionally, using dopants with a similar ionic radius to that of the host cation may further reduce the stresses and strain within the host lattice. Thus the variation on the microstrain is probably due to the effect of dopants as well the environmental condition during the annealing process. The XRD peak broadening, depends on the non-uniform lattice distortions and grain surface relaxation which in turn depend on the nature of the sample such as solid solution homogeneity, and temperature factors. Therefore an irregular microstrain value for the sample x=0.015 was probably as a result of the effect of the environment during the preparation process. Figure 6.4 displays the SEM micrographs for the (a) Gd_2O_3 and $Gd_{1.997}O_3$: $Bi_{x=0.003}^{3+}$ and (b) the histogram of the particle sizes distribution. Figure 6.4(a) shows that the shape was nearly spherical with small cubic particles, such that a group of small highly agglomerated grains formed homogeneous microstructures. The histogram of the particle size distribution and the average particle size calculations for the samples were made through the ImageJ program. The resulting values were plotted in a histogram and fitted with a Gaussian function with an average size greater than 100 nm. Both the undoped and Gd_2O_3:Bi^{3+} samples showed that the 100 nm particles were of high density but are not closely agglomerated). For the other samples, the non-uniform character of the structure shows that the surfaces were rough and spongy, which makes it difficult to do the same process to identify the sizes of the crystals as a result of the aggregation. The alteration in morphology upon addition of Bi^{3+} is negligible except for a small difference in clustered particle sizes. This indicates that the doping of Bi^{3+} ions had a slight influence on the shape and size of the resulting powder. Figure 6.5 displays the SEM micrographs for the (a) $Gd_{1.997-x}O_3$: $Bi_{x=0.003}^{3+}$, Yb_x^{3+} and (b) $Gd_{1.997-x}O_3$: $Bi_{x=0.003}^{3+}$, Er_x^{3+} powders. In figure 6.5(a) after added Yb^{3+} the particle morphology changed with the irregular formation of large clusters of flakes and particles. The non-uniform character of the structure shows that the surface became rough and spongy, which makes it difficult to identify the sizes of the crystals as a result of the aggregation, so that the number of grains and the possibility of determining their sizes decrease with the increase in the size of the grains and their agglomeration [37]. In figure 5.5(b) after the Er^{3+} was added, the particle morphology shows a mixture of different non-uniform particle shapes due to the addition of Er^{3+} in the matrix, which indicates that doping of Er^{3+} ions had some slight effect on the shape and size of the resulting phosphors. The results suggest that the surface morphology of the resulting phosphor depends on the Er^{3+} doping concentration from nearly spherical with small cubic particles to a mixture of different non-uniform particle shapes.

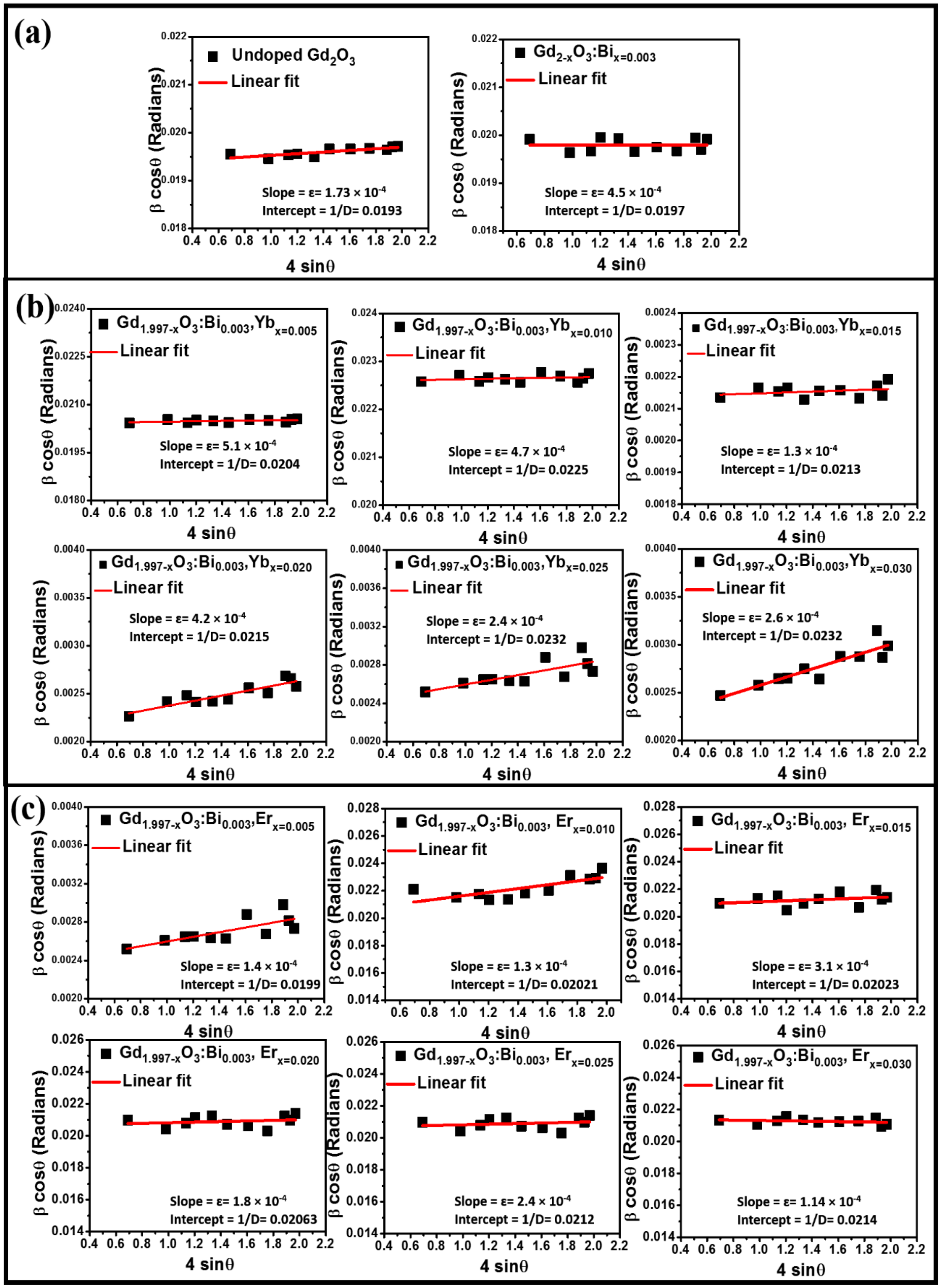

Figure 6.3: Williamson-Hall plot of (a) Gd_2O_3 and $Gd_{2-x}O_3$: $Bi_{x=0.003}^{3+}$, (b) $Gd_{1.997-x}O_3$: $Bi_{x=0.003}^{3+}$, Yb_x^{3+} (x = 0.005, 0.010, 0.015, 0.020, 0.025, 0.030) and (c) $Gd_{1.997-x}O_3$: $Bi_{x=0.003}^{3+}$, Er_x^{3+} (x = 0.005, 0.010, 0.015, 0.020, 0.025, 0.030) powder.

Table 6.2. Structural parameters crystallite size *D* and micro-strain *ε* of both the undoped and doped phosphors.

Sample	**Crystallite size *D* (nm)**		**Micro-strain *ε* (x 10^{-4})**	
Undoped Gd_2O_3	52		1.7	
$Gd_{2-x}O_3$:$Bi_{0.003}$	51		4.5	
Co-doped samples	Yb	Er	Yb	Er
x = 0.005	49	50	5.1	1.4
x = 0.010	44	49.5	4.7	1.3
x = 0.015	47	49	1.3	3.1
x = 0.020	47	48	4.2	1.8
x = 0.025	43	47	2.4	2.4
x = 0.030	47	47	2.6	1.14

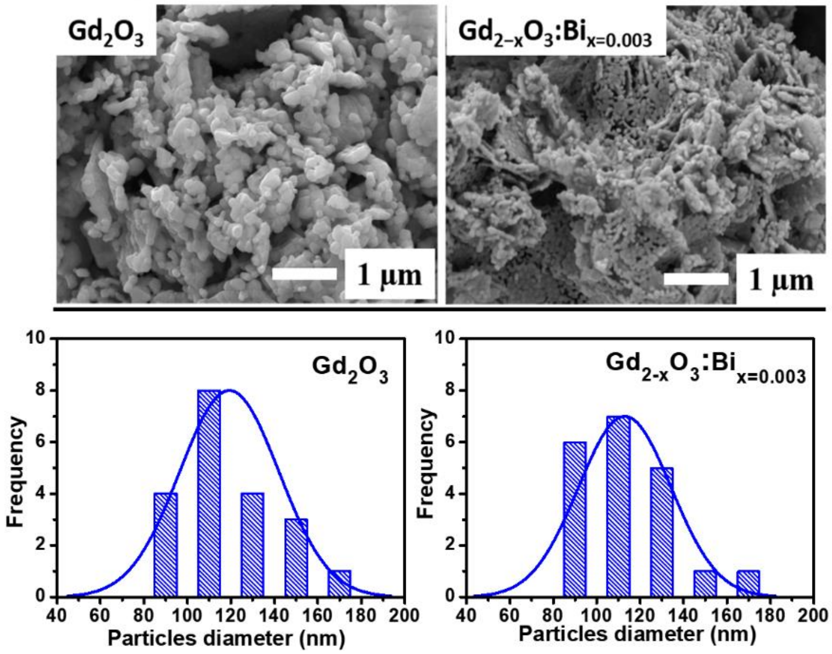

Figure 6.4: displays the SEM micrographs for the (a) Gd_2O_3 and $Gd_{1.997}O_3$: $Bi_{x=0.003}^{3+}$and (b) the histogram of the particle sizes distribution.

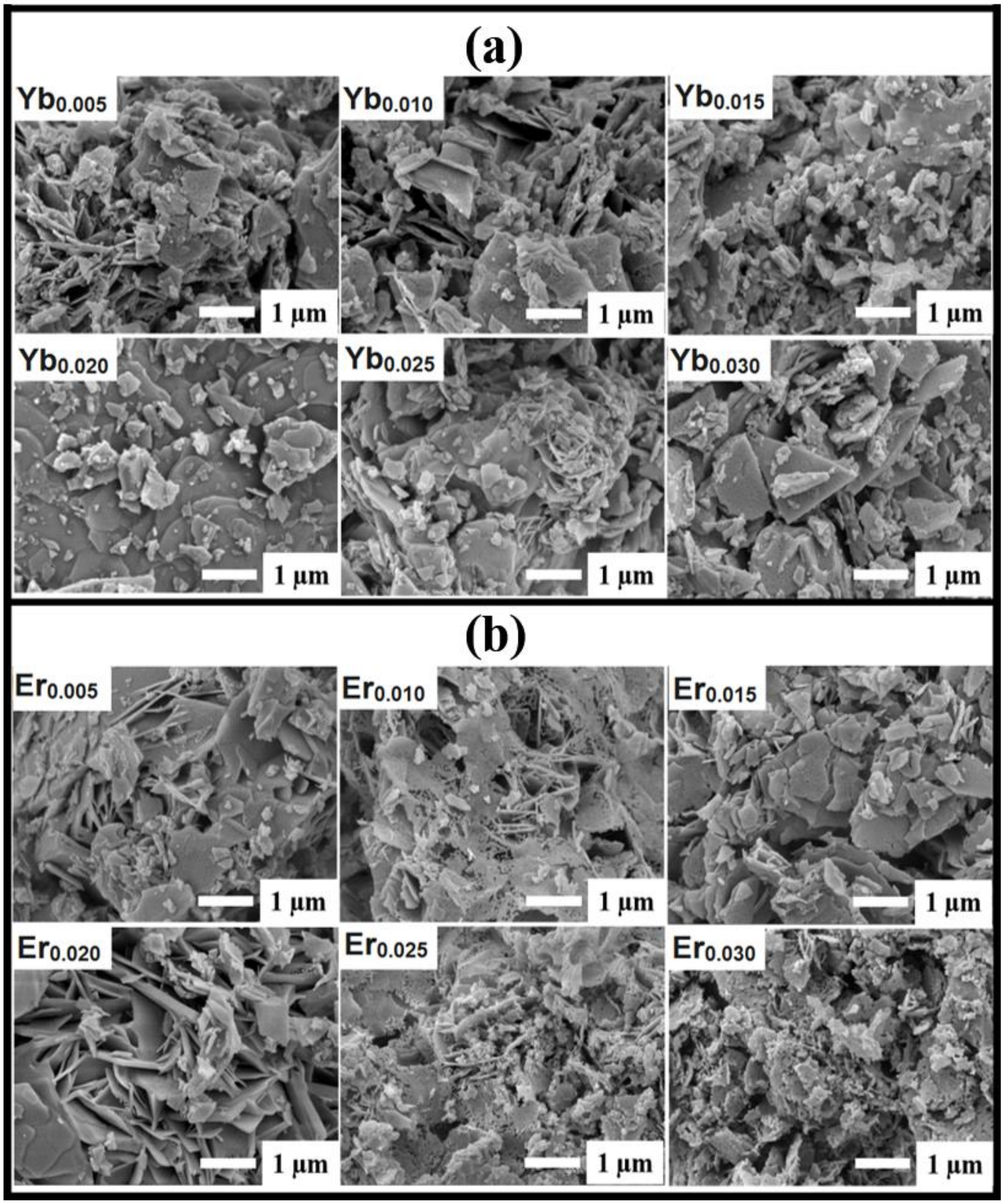

Figure 6.5: SEM micrographs for the (a) Gd_2O_3 and $Gd_{1-.997}O_3$: $Bi_{x=0.003}^{3+}$, (b) $Gd_{1.997-x}O_3$: $Bi_{x=0.003}^{3+}$, Yb_x^{3+} and (c) $Gd_{1.997-x}O_3$: $Bi_{x=0.003}^{3+}$, Er_x^{3+} powders.

6.3.2 Diffuse reflectance (DR) spectrum

Figure 6.6(a) and (b) display the diffuse reflectance measurements for the host, $Gd_{1.997}O_3$: $Bi_{x=0.003}^{3+}$ and (a) $Gd_{1.997-x}O_3$: $Bi_{x=0.003}^{3+}$, Yb_x^{3+} and (b) $Gd_{1.997-x}O_3$: $Bi_{x=0.003}^{3+}$, Er_x^{3+} samples, with various Yb^{3+} and Er^{3+} concentrations. The spectra consist of various absorption bands in the near UV region. All samples exhibited strong absorption at a wavelength of about 227 nm, which was due to the inter-band transitions of the Gd_2O_3 [38]. The absorption bands at 275, 315 nm and 250 nm have been ascribed to the 4f-4f optical transitions of the Gd^{3+} ion from the ground $^8S_{7/2}$ to the excited ^6I_J, ^6P_J and ^6D_J state, respectively [39]. It is noticeable that the reflectance value for the undoped Gd_2O_3 phosphors slightly exceeds 100%. For these measurements, a Spectralon standard was used. At short UV wavelengths, the reflectivity of the Spectralon is slightly less than perfect and hence the measured reflectance of the sample can be above 100% if the sample is more reflective than the standard. The UV spectra of the single-doped Bi^{3+} and co-doped Yb^{3+}, Er^{3+} revealed the same absorption band peaked at 227 nm and the other absorption peaks were observed located at around 260, 335 and 375 nm are due to the excitation transitions of the Bi^{3+} ions [24]. Thus, the absorption bands at 260 and 375 nm were assigned to the transitions $^1A_g \rightarrow {}^3A_u$ and $^1A_g \rightarrow {}^3E_u$ of the Bi^{3+} ion at the S_6 site, while the absorption band at 335 was attributed to the transitions $^1A \rightarrow {}^3A$ and $^1A \rightarrow {}^3B$ of the Bi^{3+} ion in the C_2 symmetry site. With the addition of Yb^{3+} and Er^{3+} in the $Gd_{1.997}O_3$: $Bi_{x=0.003}^{3+}$matrix, the same four absorption peaks were found to be related to the Bi^{3+} with a slight increased with concentrations of Yb^{3+} and Er^{3+}. In order to determine whether there were absorption by Yb^{3+} and Er^{3+} ions in the Gd_2O_3:Bi^{3+}, two samples were prepared with a high concentration at (0.3 and 0.2 of Yb^{3+} and Er^{3+} ions) that are shown in figure 6.6(c). In the sample $Gd_{1.997-x}O_3$:$Bi_{0.003}$, $Yb_{x=0.030}^{3+}$, in addition to the previous Bi^{3+} bands, an intense broad absorption band was also observed at 880-1050 nm, which corresponds to the $^2F_{7/2} \rightarrow {}^2F_{5/2}$ transition of the Yb^{3+} ion [40, 41], while in the $Gd_{1.997-x}O_3$: $Bi_{x=0.003}^{3+}$, $Er_{x=0.2}^{3+}$ sample there were absorption bands observed around 520, 655 and 802 nm, which can be attributed to the optical transitions in Er^{3+} ions from the ground $^4I_{15/2}$ to the excited $^2H_{11/2}$, $^4F_{9/2}$ and $^4I_{9/2}$ energy levels, respectively [42]. The DR data (R_∞) can be analysed by using the Kubelka–Munk equation [43]

$$F(R_\infty) \propto (1 - R_\infty)^2/(2R_\infty). \qquad (6.2)$$

The optical band gap energy was then calculated using the well-known Tauc law relation [44]

$$\alpha(h\nu) = C(h\nu - E_g)^m \qquad (6.3)$$

where $F(R_\infty)$ was substituted for the diffuse reflection coefficient (α), $h\nu$ is the incident photon energy, C is a constant and E_g refers to the bandgap energy. As Gd_2O_3 has a direct bandgap, the value $m = ½$ was used. The E_g was estimated by using the plotted graphs of $[F(R_\infty)h\nu]^2$ versus $h\nu$ and extending a linear fit to the energy axis as shown by figure 6.6(d) from which the bandgap was found to be 5.18, 5.20, 5.22 and 5.21 eV for the undoped Gd_2O_3, $Gd_{1.997}O_3$: $Bi_{x=0.003}^{3+}$, $Gd_{1.997-x}O_3$: $Bi_{x=0.003}^{3+}$, $Yb_{0.030}$ and $Gd_{1.997-x}O_3$: $Bi_{x=0.003}^{3+}$, $Er_{0.030}$ samples with highest concentrations of Yb^{3+} and Er^{3+} used, respectively. The slight increase in the optical band gap could be related to the distortion due to the high absorption of the Bi^{3+} ion. The high absorption of Bi^{3+} might be leading to hybridization with the existing orbitals and result in a change in energy levels which means that more energy is needed to excite an electron from the valence band to the conduction band. Kuznetsova *et al.* [45] have reported that the bandgap of Gd_2O_3 increasing under the activation by Er^{3+} ions due to shifting within the edge of the valence and conduction band. Accordingly, the bandgap may be increased due to the shift of the Fermi level to the conduction band and hence occupation of some of the bottom states in the conduction band.

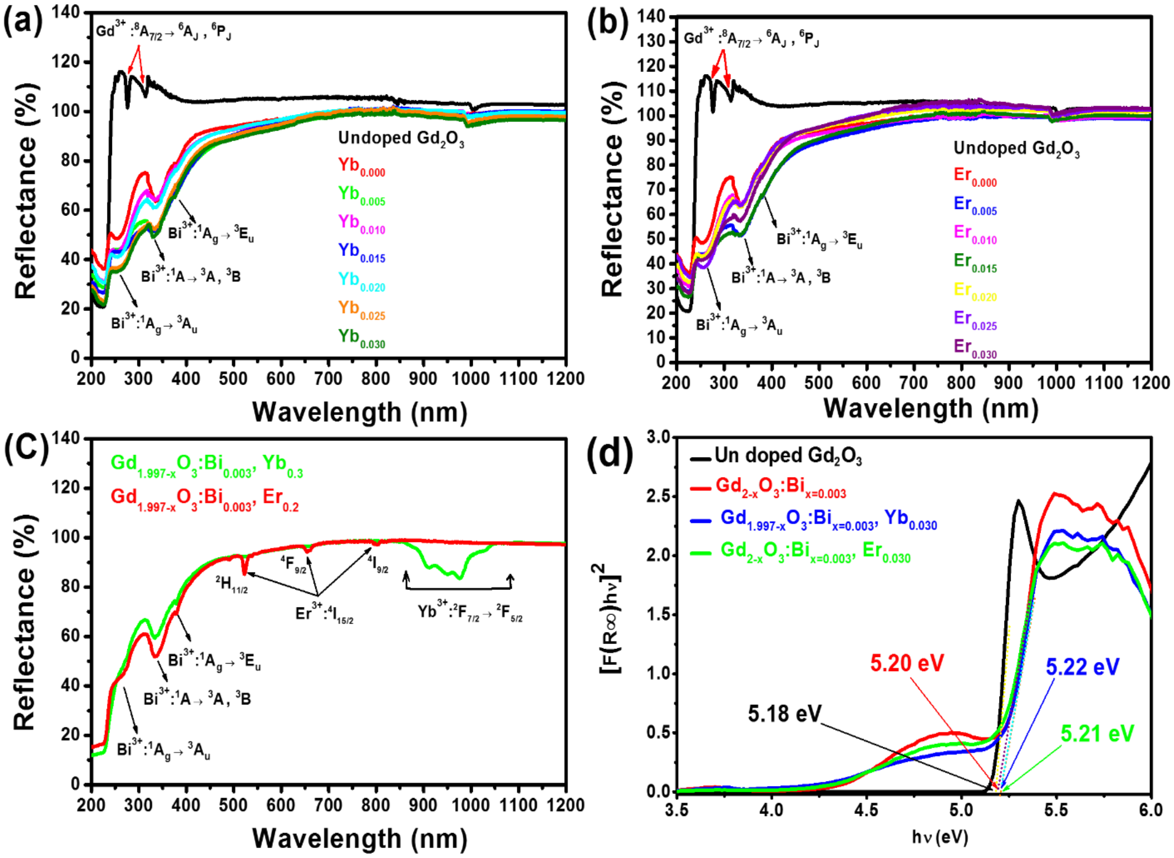

Figure 6.6: DR spectra of (a) Gd_2O_3 host and $Gd_{1.997-x}O_3$: $Bi_{x=0.003}^{3+}$, Yb_x^{3+}, (b) Gd_2O_3 host and $Gd_{1.997-x}O_3$: $Bi_{x=0.003}^{3+}$, Er_x^{3+}, (c) $Gd_{1.997-x}O_3$: $Bi_{x=0.003}^{3+}$, $Yb_{0.3}$ and $Gd_{1.997-x}O_3$: $Bi_{x=0.003}^{3+}$, $Er_{0.2}$, and (d) Estimation of the optical bandgap by a Tauc plot.

6.3.3 Luminescence properties

The PL excitation and emission spectra of the $Gd_{1.997-x}O_3$: $Bi_{x=0.003}^{3+}$, Yb_x^{3+}phosphor are shown in figure 6.7(a). The PL emission was evaluated under 260, 335 and 375 nm excitation. When using an excitation wavelength λ_{ex} = 375 nm there was a blue emission at λ_{em} = 418 nm, and when the excitation was carried out at λ_{ex} = 260 nm a blue peak was also observed at λ_{em} = 418 nm but with less intensity. This peak corresponds to the excitation of the Bi^{3+} ion at the S_6 symmetry site [24]. When excited by UV light at λ_{ex} = 335 nm, the same blue emission was obtained with an additional broad green emission centered at λ_{em} = 505 nm, caused by the excitation of the Bi^{3+} ion in the C_2 site [24]. The cubic Gd_2O_3 features two types of Gd^{3+} sites, both with coordination number of 6 but with different coordination geometries, i.e. where two O^{2-} ions are missing either along the body (S_6) or a face (C_2) diagonal of a cube surrounding a Gd^{3+} ion. Thus, when Bi^{3+} occupies a S_6 site having inversion symmetry as in cubic Y_2O_3, its Stokes shift is less compared to when it occupies a less symmetric C_2 site having more neighboring ions to one side than the other and the same effect is apparent for Gd_2O_3. As discussed in the literature [46], the $^1S_0 \rightarrow {}^3P_1$ and $^3P_1 \rightarrow {}^1S_0$ of the Bi^{3+} ions mostly are responsible for the excitation and emission in the different hosts. Figure 6.7(b) shows the room temperature PL emission of the $Gd_{1.997-x}O_3$: $Bi_{x=0.003}{}^{3+}$, $Yb_x{}^{3+}$ powder with a fixed Bi^{3+} ion concentration but varied Yb^{3+} concentration under the 325 nm He-Cd laser excitation. The spectra display a broad band of blue and green fluorescence emission that extended from 350 to 700 nm centered at 360, 418 and 505 nm. The emissions are ascribed of the Bi^{3+} in the S_6 and C_2 symmetry. It well known that, Bi^{3+} ion's luminescence are highly sensitive to the coordination of the donor site. Therefore, any changes in the structure around the Bi^{3+} ion can result in a change in the PL peaks' positions. Accordingly, upon excitation at 325 nm to stimulate the observed emission wavelengths, the emissions originates from the upper and lower levels of the crystal field split $^3P_1$ energy level of Bi^{3+} ions at the C_2 symmetry site [24]. The luminescence is similar to that for Bi^{3+}–Yb^{3+} co-doped Gd_2O_3 reported by Zhydachevskyya *et al.* [5]. It was seen that the $^3P_1$ level splits into several sublevels due to the crystal field effect and was dependent on the position of the Bi^{3+} ion in the Gd_2O_3 host matrix. In the C_2 symmetry site, the $^3P_1$ level splits into three sublevels (^3A, ^3B and ^3B) while the S_6 splits into two sublevels (^3A_u and ^3E_u). Therefore upon excitation at different wavelengths, absorption occurs by those different sublevels of $^3P_1$ level splits. The wide bluish-green emission extending from 350 to 650 nm is assigned to the $^3P_1 \rightarrow {}^1S_0$ transitions from the Bi^{3+} ions. The inset of figure 6.7(b) represents the maximum PL intensity at 505 nm as a function of Yb^{3+} concentration. A reduction in the PL emission intensity resulting from the Bi^{3+} was observed with an increase in Yb^{3+} ion concentration. The energy transfer (ET) between the activator Bi^{3+} and the Yb^{3+} ions might cause the reduction of the Bi^{3+} emission. Lee *et al.* [10] report that the visible PL emission spectrum of Y_2O_3:Bi^{3+}, Yb^{3+} reduced with an increase in Yb^{3+} ion concentration due to the ET from the Bi^{3+} to the Yb^{3+} ions. Less efficient energy transfer from the sensitizer to the activator with increasing concentration of sensitizer may be attributed to the critical concentration of Yb^{3+} with the host or dipole-quadrupole interaction amongst the Yb^{3+} ions.

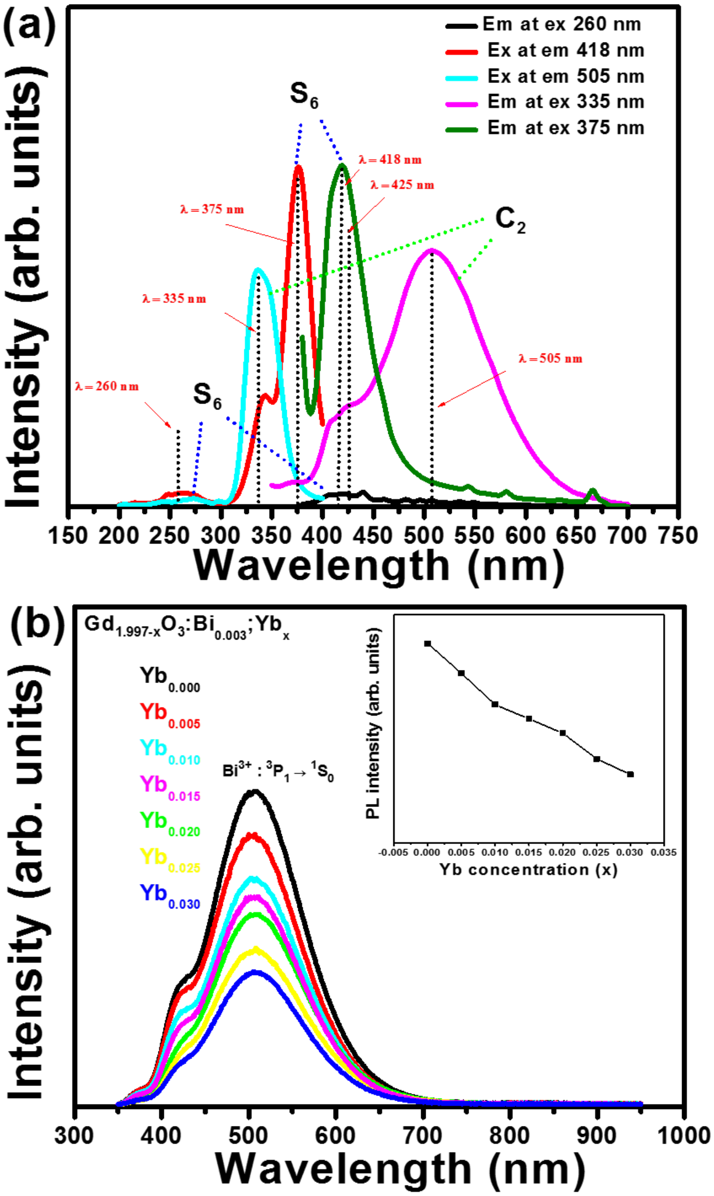

Figure 6.7: (a) PL excitation and emission spectra of Gd$_{1.997}$O$_3$: Bi$_{x=0.003}^{3+}$ powder measured with the FS5 spectrophotometer. (b) PL spectra of the Gd$_{1.997-x}$O$_3$: Bi$_{x=0.003}^{3+}$, Yb$_x^{3+}$ as a function of Yb concentration measured using a 325 nm He-Cd laser.

Figure 6.8(a) shows the NIR emission spectra of Gd$_{1.997-x}$O$_3$: Bi$_{x=0.003}^{3+}$, Yb$_x^{3+}$ displaying a wide infrared emission range originating from the $^2F_{5/2} \rightarrow {}^2F_{7/2}$ transition of Yb^{3+}, given that the Bi^{3+} ions have no contribution to the NIR emission [2]. The Yb^{3+} emission consists of a narrow series of peaks centered at 976 nm and less intense peaks centered around 950 nm, 1025 nm and 1065 nm caused by the crystal field Stark splitting of the $^2F_{5/2}$ and $^2F_{7/2}$ energy levels. The inset of figure 6.8(a) shows the variation of the NIR emission intensity as a function of Yb^{3+} concentration. The

NIR emission intensity increased as a result of an increase in the Yb^{3+} concentration, while the emission of the Bi^{3+} ions at 505 nm has been decreasing monotonically. Huang *et al.* [2] reported that energy transfer occurred when the Bi/Yb were doped into Gd_2O_3 phosphor. They observed an enhancement in the NIR emission (980 nm) of Yb^{3+} ions when exciting the sample in the UV range. They attributed the result to the transfer of Bi^{3+} $^3P_1$ energy to two Yb^{3+} ions via the DC process. To determine if Bi^{3+} aids in enhancing the infrared emission of Yb^{3+}, two samples were prepared, one with and the other without the presence of Bi^{3+}. The NIR emission spectra of the $Gd_{1.997-x}O_3$: $Bi_{x=0.003}^{3+}$, $Yb_{x=0.030}^{3+}$ and the $Gd_{2-x}O_3$: $Bi_{x=0.00}^{3+}$, $Yb_{x=0.030}^{3+}$ which were obtained under the same conditions, using a He-Cd laser with 325 nm excitation are shown in figure 6.8(b). There was a strong increase in the NIR emission by adding of the Bi^{3+} ions compared with the sample doped by a Yb^{3+} ion only, indicating that Bi^{3+} efficiently transferred the initial excitation energy to the Yb^{3+} ion. These results revealed that the broad UV-Vis energy excitation photons were successfully converted into NIR photons which may correspond well with the energy of the bandgap of Si. Xiao *et al.* [47] also found similar results in $Gd_{2-x-y}O_3$:Bi_x^{3+}, Yb_y^{3+} phosphors when excited by UV photons varying in wavelengths from 320–390 nm due to the transitions between the Bi^{3+}:$^3P_1$ level to the rare-earths Yb^{3+}: $^2F_{5/2}$ level. The intensity of Yb^{3+} in the 900 –1100 nm region can be significantly enhanced by doping with Bi^{3+}.

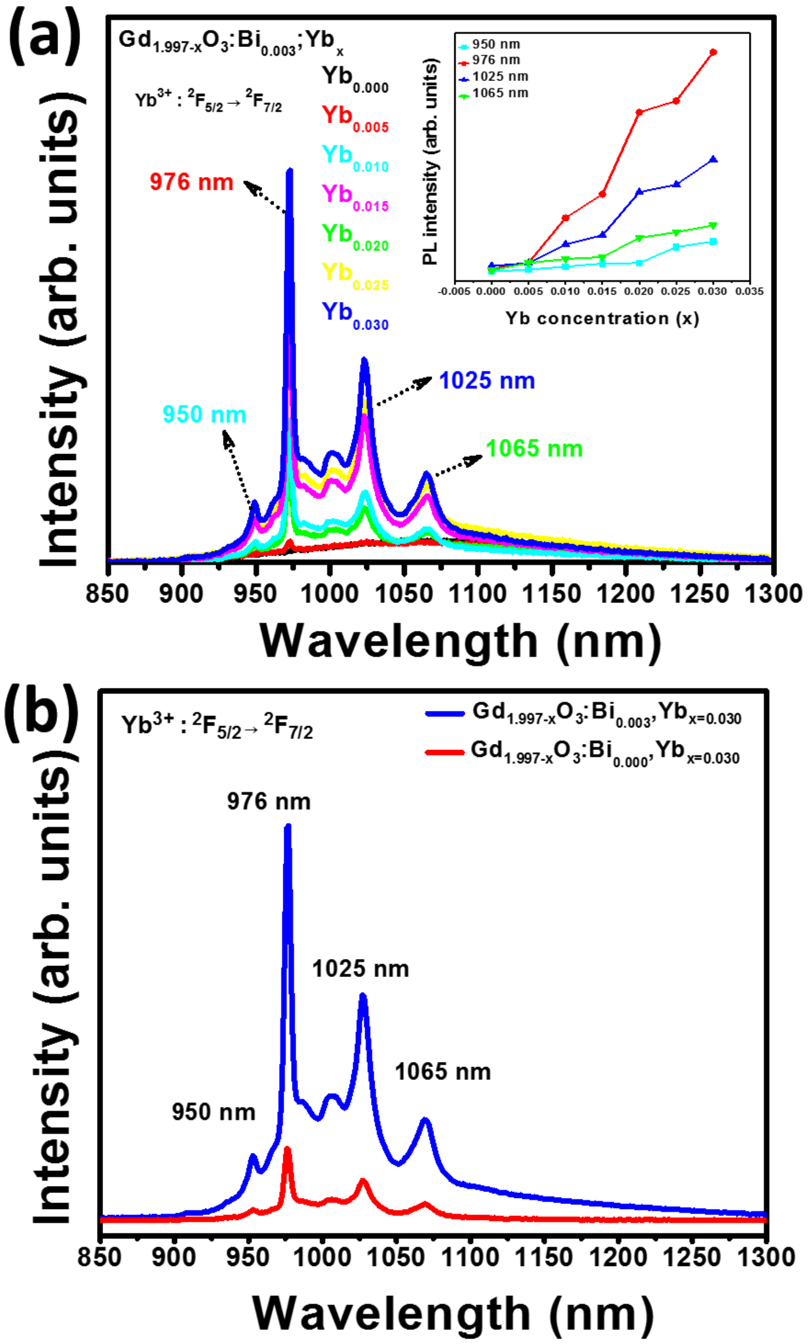

Figure 6.8: (a) NIR emission of Gd$_{1.997-x}$O$_3$: Bi$_{x=0.003}^{3+}$, Yb$_x^{3+}$. The inset shows the maximum PL emission intensity of the different peaks as a function of Yb^{3+} concentration. (b) NIR emission of Gd$_{1.997-x}$O$_3$: Bi$_{x=0.003}^{3+}$, Yb$_{x=0.030}^{3+}$ and Gd$_{2-x}$O$_3$: Bi$_{x=0.003}^{3+}$, Yb$_{x=0.030}^{3+}$. All measured under a 325 nm He-Cd laser.

Figure 6.9(a) displays a schematic diagram of the energy levels for the Bi^{3+} → Yb^{3+} ET process in the Gd$_{1.997-x}$O$_3$: Bi$_{x=0.003}^{3+}$, Yb$_x^{3+}$ phosphors. The Bi^{3+}: $^3P_1$ level is located at just about double the energy of the Yb^{3+}: $^2F_{5/2}$ level and Yb^{3+} has no further levels reaching the UV region, so the cooperative energy transfer (CET) process of Bi^{3+}: $^3P_1 \rightarrow Yb^{3+}$: $^2F_{5/2}$ could be responsible for enhancing the Yb^{3+} NIR emission. The Bi^{3+} ion absorbs the UV photon energy and then it will be excited from the ground state ($6s^2$) to the excited state (6s6p). The excited state will relax to the ground state by emitting a blue-green photon and NIR emissions. The CET Bi^{3+}: $^3P_1 \rightarrow Yb^{3+}$: $^2F_{5/2}$ is the only possible relaxation route to achieving the Yb^{3+} NIR emission since the Yb^{3+} has no other energy states up to the UV region. Thus, in this case, upon excitation in the $^3P_1$ level by 325 nm, Bi^{3+} emission occurs in the region of 350–600 nm (shown in Figure 6.7(b)), which can be assigned to the $^3P_1 \rightarrow {}^1S_0$ transition. The broad blue-green emission band was recorded at ~505 nm with an additional small peak at the blue region ~425 nm. The peak at ~425 nm upon excitation at 325 nm originated from the upper and lower levels of the crystal field split $^3P_1$ of Bi^{3+} ions at the C_2 symmetry site [24]. Meanwhile, two NIR photons corresponding to the Yb^{3+}: $^2F_{5/2} \rightarrow {}^2F_{7/2}$ transitions are obtained after absorption of a single UV photon, since the Bi^{3+} ion does not emit in the emission of in the region at 900 -1100 nm.

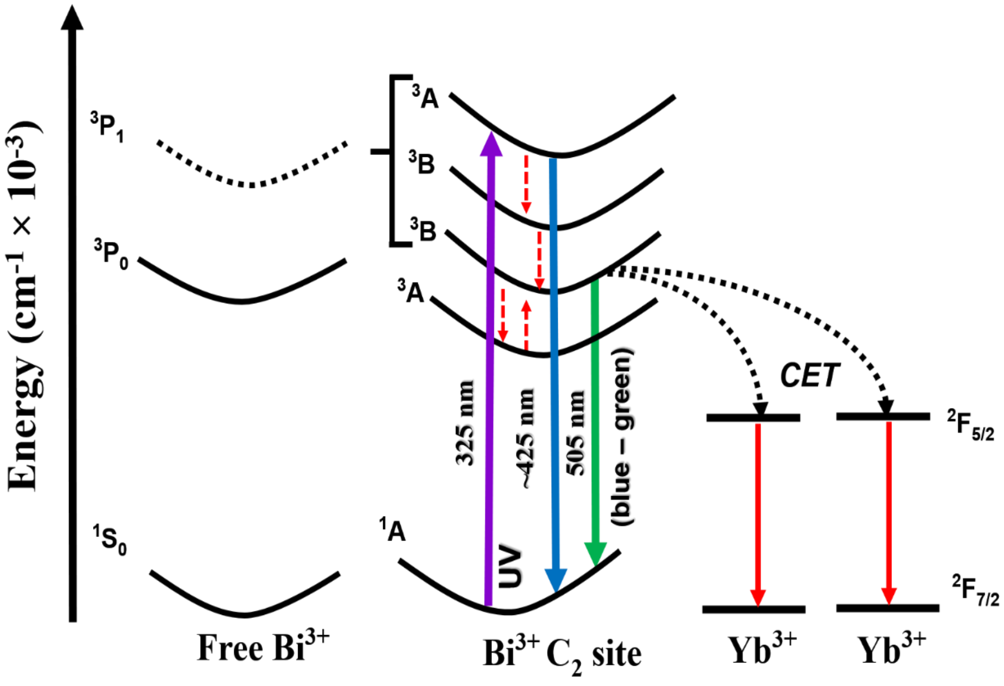

Figure 6.9: (Colour online) Schematic energy level diagram of Bi^{3+} and Yb^{3+} in the Gd_2O_3 phosphors, showing the CET mechanism for the NIR-DC luminescence under UV excitation.

As reported in the literature by a large number of authors [48, 49, 8] the energy transfers efficiency η_{ET} from Bi^{3+} to Yb^{3+} in Gd_2O_3 can be calculated using the following equation

$$\eta_{ET} = 1- \frac{I_s}{I_{s0}} \qquad (6.4)$$

where I_s and I_{s0} are the luminescence intensities of the sensitizer (Bi^{3+}) in the absence and the presence of the activator (Yb^{3+}) respectively. Figure 6.10 shows the η_{ET} trend for the Bi^{3+} → Yb^{3+} system, from which it is evident that the energy transfer efficiency increased with increasing Yb^3 concentration. The maximum value of about 88% was calculated for the $Yb_{0.030}$ sample.

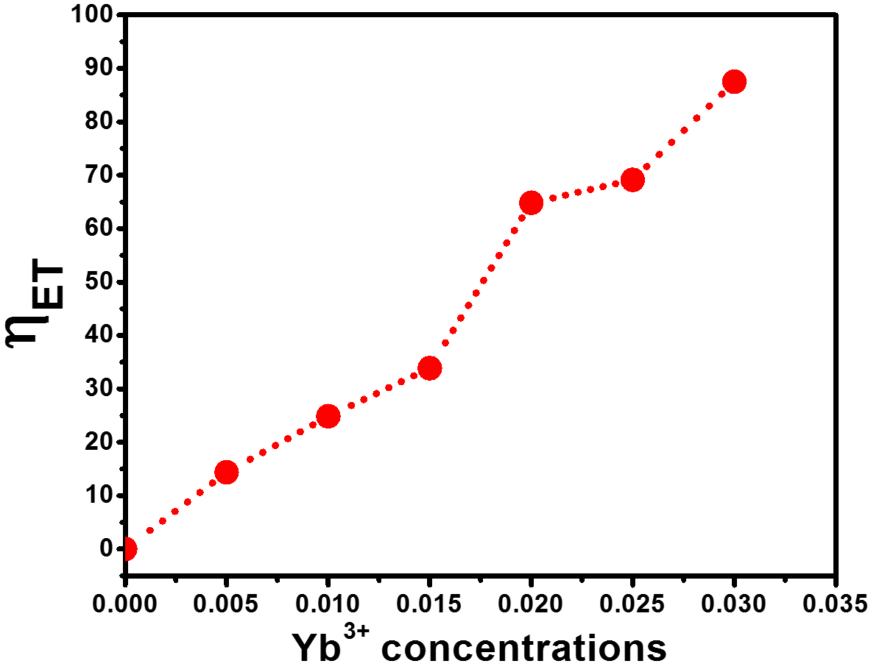

Figure 6.10: Energy transfer efficiency versus Yb^{3+} content.

Figure 6.11(a) shows the room temperature upconversion emission of the $Gd_{1.997-x}O_3$: $Bi_{x=0.003}^{3+}$, Er_x^{3+} powders with a fixed Bi^{3+} and varied Er^{3+} concentration under 980 nm infrared excitation. The spectra show sharp emission peaks. Green emission bands in the range (520 to 560 nm) and red emission in the range (645 to 685 nm) were observed for all the Er^{3+} co-doped samples. The luminescence spectrum was not related to the Bi^{3+} emission as it has an emission center at 505 nm and it is shown that there was no emission peak from the single doped sample. Therefore, when excited under infrared by 980 nm the PL spectra of the $Gd_{1.997-x}O_3$: $Bi_{x=0.003}^{3+}$, Er_x^{3+}samples exhibited sharp emission peaks centered at 520, 560 and 670 nm, that coincided with $^2H_{11/2}$, $^4S_{3/2}$, and $^4F_{9/2}$ to $^4I_{15/2}$ transitions of the Er^{3+} ions, in view of the fact of no emission contribution from Bi^{3+} ions occurs in this range [7]. No apparent shift in the emission peaks was observed. Obvious Stark-splitting can be observed in all samples co-doped with Er^{3+}. The phosphor has a maximum of three main emission bands at 520 nm (green), 560 nm (green), and 670 nm (red). Upon 980 nm excitation, Er^{3+} underwent excitation to higher energy levels through ground-state absorption. Thus, the emissions bands peaking around 520, 537, 550 and 670 nm and are assigned to $^4F_{5/2} \rightarrow {}^4I_{15/2}$, $^2H_{11/2} \rightarrow {}^4I_{15/2}$, $^4S_{3/2} \rightarrow {}^4I_{15/2}$, and $^4F_{9/2} \rightarrow {}^4I_{15/2}$ transitions of the Er^{3+} ion, respectively [50]. As indicated by the peaks in the UC emissions available in green and red belong only to the 4f-4f transitions characteristic of Er^{3+} ions, so that no peak related to the Bi^{3+} ion was observed. The inset of figure 6.11(a) shows the variation of the 560 and 670 nm emission PL intensity as a function of Er^{3+} concentration. The UC process is concentration-dependent. There was an enhancement in the emission intensity of the 560 nm with increasing Er^{3+} concentration up to x = 0.015 wt% and then the intensity reduced as a result of concentration quenching effects. The 670 nm emission intensity reached a maximum value at 0.025 wt%. Above that concentration the emission intensity became weak, which might also occur due to the concentration quenching effect. As a result of a wide range energy levels of Er^{3+} ions, the color of the UC materials doped by Er^{3+} will easily be influenced by several things such as the type of excitation used, wavelength used for excitation and concentration of rare ionic doping etc. [51]. In general, the PL emission intensity of Er^{3+} distribution is related to the difference in the concentration of the Er^{3+} ions in the various excitation states [52]. Since the concentration of the Bi^{3+} ions was constant, changes in the emissions depend on the concentration of the Er^{3+}. It is important to note that the grain size of the samples also may influence the intensity of UC because the relative intensity of the higher conversion emissions varies with the quenching effect of the surface concentration [53]. This increases the energy transfer from the high-energy excited state clusters of Er^{3+} ions, which leads to an enhancement in the intensity of the near-infrared emission. This is possibly due to the probability of the electron in the $^4I_{11/2}$ state that gets promoted to the $^4F_{7/2}$ states via an energy-transfer UC process, which is much higher than that of the non-radiative relaxation to the $^4I_{13/2}$ states (see figure 6.12). To determine whether Bi^{3+} helps to enhance the visible UC emission of Er^{3+}, two samples were prepared, one with and the other without Bi^{3+}. Figure 6.11(b) shows the room temperature PL emission spectra of $Gd_{1.997-x}O_3$: $Bi_{x=0.003}{}^{3+}$, $Er_{x=0.015}{}^{3+}$ and $Gd_{2-x}O_3$: $Bi_{x=0.00}{}^{3+}$, $Er_{x=0.015}{}^{3+}$ powders which were both prepared and measured under the same conditions, under 980 nm infrared excitation. The range of the spectrum was 500 up to 950 nm, which has the green emission in the range 520 to 560 nm and the red emission bands in the range 645 to 685 nm as mentioned earlier, and an extra red emission band in the range 825 to 925 nm corresponding to the $^4I_{9/2} \rightarrow {}^4I_{15/2}$ transitions of the Er^{3+} ion [54]. Figure 6.11(b) shows there was an increase in the green-orange-red emissions with the addition of Bi^{3+} in the Er^{3+} sample compare to the sample only doped with Er^{3+} ions. It is worth mentioning that the doping of Bi^{3+} ions did not have an obvious effect on the characteristics of the emission peaks in terms of position and the shape of the emission peaks of the Er^{3+} ions [55]. However, a significant enhancement of the emission intensities of Er^{3+} ions was observed after Bi^{3+} doping. There may be several reasons for an increase in the emission of the intensity of Er^{3+} ion in the phosphor sample. The initial reason for this enhancement in the UC emission might be attributed to the modification of the local crystal field around Er^{3+}. Substitution of Bi^{3+} for Gd^{3+} can modify the crystal field symmetry in the lattice and enhance the radiative transition rate in favor of enhancing the UC emission intensity. Yang *et al.* [56] studied the effect of adding the Bi^{3+} ions to an Er^{3+} doped Y_2O_3 host and similarly found that the presence of the Bi^{3+} ions increased the intensity of the Er^{3+} emission. Also, the enhancement in the UC emission might be attributed to the slight modification in the crystallinity of the phosphor sample when the two ions are combined together in a single matrix. The effect of Bi^{3+} ion concentration on the crystallinity of the phosphor has been studied by Choudhary *et al.* [57] and they have found an enhancement in the emission intensity of the dopant ions due to improvement in crystallinity. Doping with a variety of dopants with rare-earth ions might change the band structure of the matrix and cause bandgap changes, affecting the center of gravity of the 5d electrons of Gd^{3+} and other doped ions in the matrix, crystal field splitting energy and electron-phonon interaction. The optical band might be reduced in the presence of a Bi^{3+} ion, which leads to promoting a large number of excited ions in the upper energy levels, thereby emitting large photoluminescence intensity [40]. It has been also reported that the presence of Bi^{3+} ion increases the lifetime of the emitting levels, which supports the larger photoluminescence intensity for the phosphor samples. Thus, in this case, there might be an enhancement in the emission intensity in the presence of Bi^{3+} ion due to one or all of these combined effects.

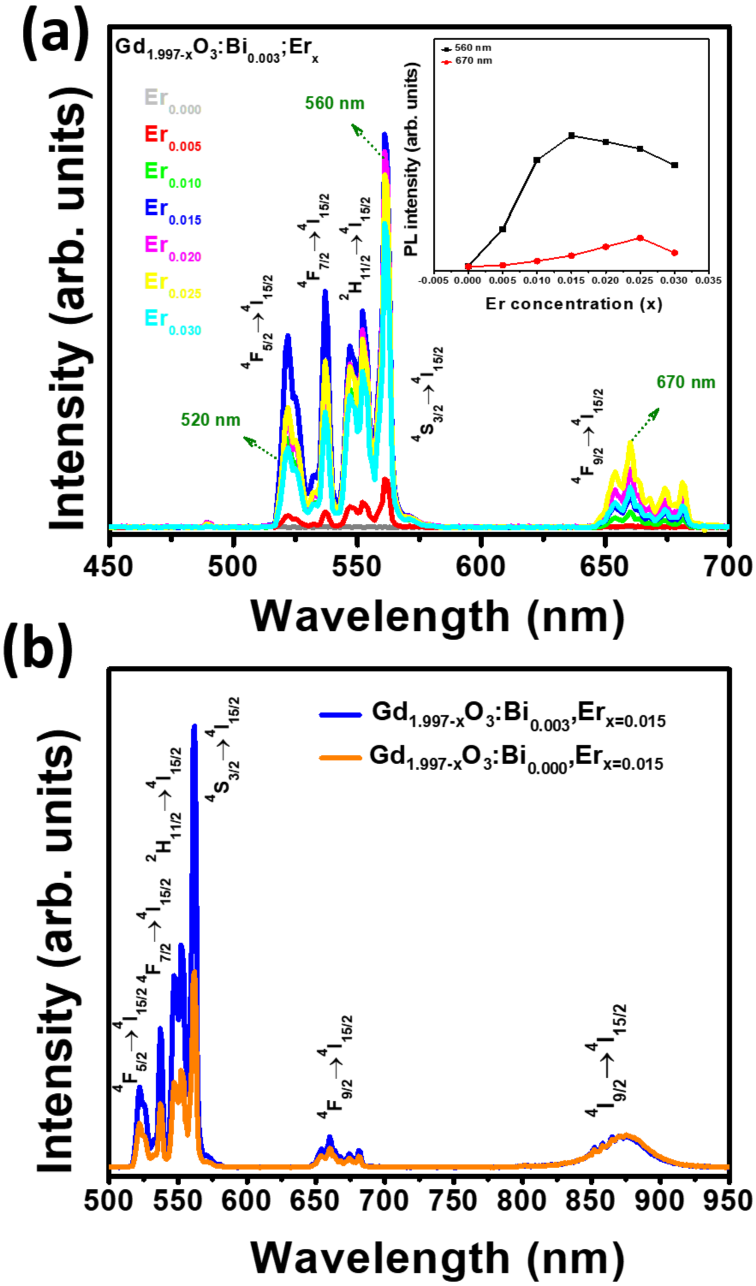

Figure 6.11: (a) UC visible emission spectra of $Gd_{1.997\text{-}x}O_3$: $Bi_{x=0.003}^{3+}$, Er_x^{3+} for different Er^{3+} concentration under 980 nm infrared excitation. (b) UC visible emission spectra of $Gd_{1.997\text{-}x}O_3$: $Bi_{x=0.003}^{3+}$, $Er_{x=0.015}^{3+}$ and $Gd_{2\text{-}x}O_3$: $Bi_{x=0.00}^{3+}$, $Er_{x=0.015}^{3+}$ under 980 nm infrared excitation.

Figure 6.12 shows the schematic diagram proposed for the red emission mechanism of the Er^{3+} ET process of the UC of the $Gd_{1.997\text{-}x}O_3$: $Bi_{x=0.003}^{3+}$, Er_x^{3+}phosphors. Under the excitation of 980 nm, a first photon directly excites the Er^{3+} ion from the ground state $^4I_{15/2}$ to the first excited state $^4I_{11/2}$. Usually, portions of the subsequently excited Er^{3+} ions relax non-radiatively from the $^4I_{11/2}$ state to the $^4I_{13/2}$ level [58]. Then the excitation potential gradually increases from the $^4I_{13/2}$ level to the red emission level. After that, the photons at the $^4I_{11/2}$ level further absorbed a second photon and get excited in the second excited state $^4F_{5/2}$. There is a big probability of filling the $^4F_{5/2}$ level as a result of the interaction between two excited states of the Er^{3+} ions produced by the process of the energy transfer process in the $^4I_{11/2}$ state. Then a non-radiative relaxation may occur from the $^4F_{5/2}$ level to the $^4F_{7/2}$ or $^2H_{11/2}$ or $^4S_{3/2}$ level, of which the Er^{3+} ions can either return to the ground state at which green light is emitted or relax non-radiatively to the $^4F_{9/2}$ level which in turn tends to return to the ground state, that causes red light to be emitted. Firstly the green emission around 520 nm occur due to transition $^4F_{5/2} \rightarrow {}^4I_{15/2}$. Then, the excited ions at $^4F_{5/2}$ undergo a transition to the $^4F_{7/2}$ $^2H_{11/2}$, $^4S_{3/2}$, $^4F_{9/2}$ levels by non-radiative relaxation, and they also display green emission around 550 and 560 nm ($^2H_{11/2}$, $^4S_{3/2} \rightarrow {}^4I_{15/2}$) and red emission around 670 and 830 nm ($^4F_{9/2}$, $^4I_{9/2} \rightarrow {}^4I_{15/2}$) by relaxation to the ground state. As can be seen from figure 6.11(a and b), the green Er^{3+} emission intensity is greatly enhanced compared to the emission of the other infrared (670 nm) and near-infrared (830 nm) emissions.

This is probably because the electron in the $^4I_{11/2}$ state can be upgraded to $^4F_{5/2}$ states through the UC energy transfer process, which is far greater than that of nonradiative relaxation to the $^4I_{13/2}$ (for 670 nm emission) and $^4I_{9/2}$ (for 830 nm emission) states.

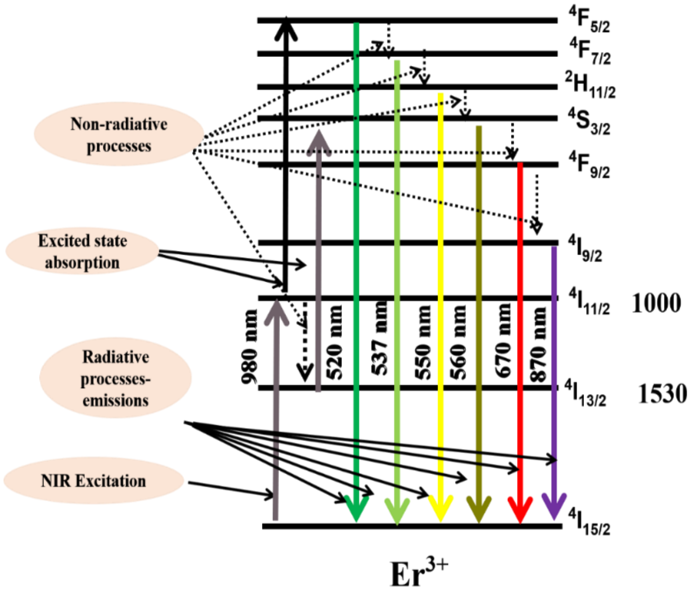

Figure 6.12: Schematic energy level diagrams upon excitation energy (980 nm, up arrow), proposed the possible UC processes for the green and red mechanism of Er^{3+} co-doped $Gd_{1.997-x}O_3$:$Bi_{0.003}$, Er_x^{3+} phosphors.

6.3.4 Cathodoluminescence properties

Figure 6.13 shows the CL spectra of (a) $Gd_{1.997}O_3$: $Bi_{x=0.003}^{3+}$and $Gd_{1.997-x}O_3$: $Bi_{x=0.003}^{3+}$, Yb_x^{3+} and (b) $Gd_{1.997-x}O_3$: $Bi_{x=0.003}^{3+}$, Er_x^{3+} samples. In figure 6.13 (a) it is clear that the CL spectra of all samples fall in the broad emission range from 300 to 700 nm. There were three main emission bands, two blue centered at 360 and 418 nm and a main green band at 505 nm, and it was also observed that all CL measurements corresponded to the PL emission bands, which indicates that the electron beam did not have an effect on the electron energy level distribution of the doped ion transitions. Furthermore, the broad bluish-green emission extending from 350 to 600 nm is only allocated to the $^3P_1 \rightarrow {}^1S_0$ transitions of the Bi^{3+} ions. It is noticeable that there was a slight broadening in the wavelength range in the CL emission for all samples compared to the PL emission. This broadening might be a result of the large energy difference in addition to the different mechanisms for the excitation. As indicated in PL studies the emission under electrical pumping, high energy electrons can excite Bi^{3+} ions at both lattice sites C_2 and S_6 excitation energy at both sites in the host lattice. Abdelrehman *et al.* [24] reported that CL excitation sources for Gd_2O_3:Bi^{3+} had expanded at longer wavelengths in the CL emission as a result of the large energy difference upon excitation in addition to their different mechanisms. Also in this case there was no change between the PL measurements shown in figure 6.7(a) and CL maximum intensity positions in figure 6.13(a) in addition to their correspondence to the CL emission of $Gd_{2-x}O_3$:Bi_x^{3+} at different concentrations of Bi^{3+} as presented in our previous study [24]. Thus, the CL emission of $Gd_{1.997-x}O_3$: $Bi_{x=0.003}^{3+}$, Yb_x^{3+} samples, when adding Yb^{3+} concentrations did not change the emission peak positions. There was a decrease in the CL intensity of the Bi^{3+} emission with an increased the Yb^{3+} concentration, which is expected due to the energy transfer from the Bi^{3+} activator to the Yb^{3+} ions as discussed for PL. Figure 6.13(b) displays the CL spectra of the $Gd_{1.997-x}O_3$: $Bi_{x=0.003}^{3+}$,Er_x^{3+}. The emission consists of two strong blue and green-yellow emission bands. The phosphor has two emission bands centered at 360 and 418 nm in the blue region allocated to the $^3P_1 \rightarrow {}^1S_0$ transitions of the Bi^{3+} ions. The green-yellow emission bands observed in the range 500 to 600 nm correspond to overlap between $^3P_1 \rightarrow {}^1S_0$ transitions of the Bi^{3+} and $^2H_{11/2}$, $^4S_{3/2} \rightarrow {}^4I_{15/2}$ transitions of Er^{3+} ions. Boruc *et al.* [5] reported that an Gd_2O_3:Bi^{3+},Er powder excited by an ion beam, had emission consisting of a chain of narrow lines in a green band which were assigned to Er^{3+} ions and also there was blue-violet broadband emission resulting from Bi^{3+} ions. The inset of figure 6.13(b) displays the variation of the CL emission intensity at 418, 520 and 560 nm as a function of Er^{3+}

concentration of $Gd_{1.997-x}O_3$: $Bi_{x=0.003}^{3+}$,Er_x^{3+}. The sample with a concentration of x = 0.015 of Er^{3+} ion exhibited the greatest CL intensity and then decreased due to concentration quenching, while at 560 nm the maximum emission intensity peak was at a concentration of 0.020 The variation of maximum intensity peaks may be due to the effect by overlapping between $^3P_1 \rightarrow {}^1S_0$ transitions of the Bi^{3+} ions and $^2H_{11/2}$, $^4S_{3/2} \rightarrow {}^4I_{15/2}$ transitions of the Er^{3+} ions.

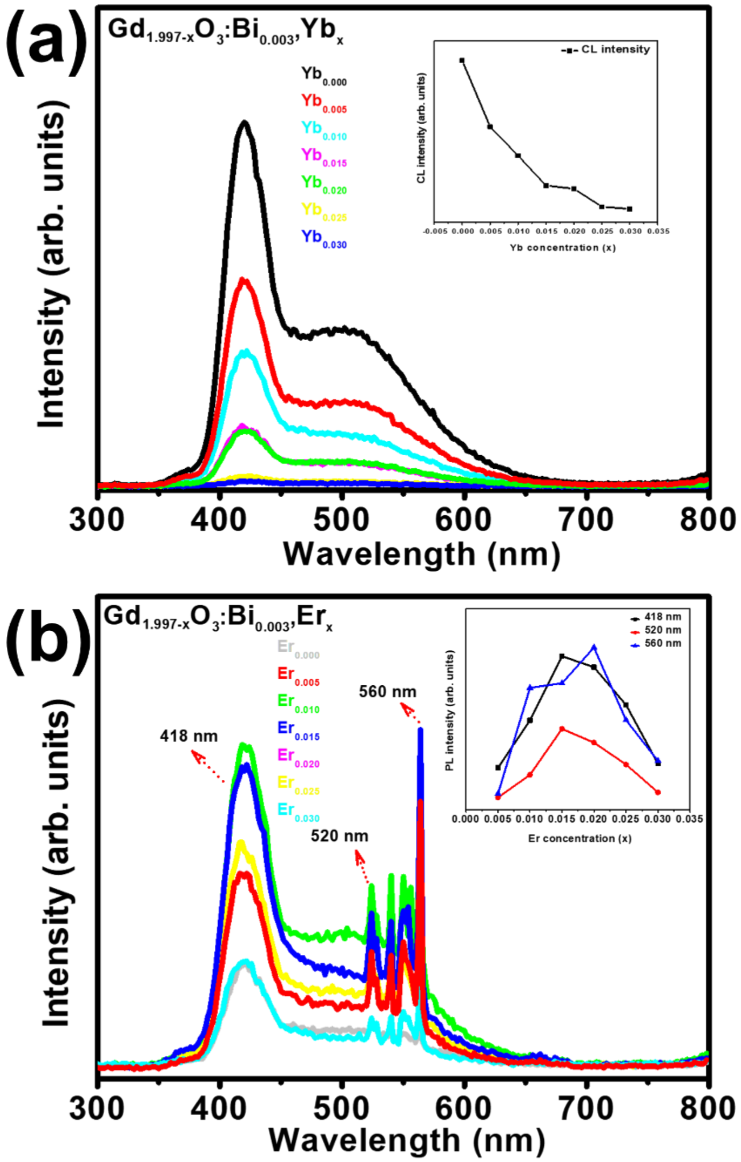

Figure 6.13: (a) CL spectra of the $Gd_{1.997-x}O_3$: $Bi_{x=0.003}^{3+}$, Yb_x^{3+} powder. The inset displays the CL peak intensity as a function of Yb^{3+} doping concentration. (b) CL spectra of the $Gd_{1.997-x}O_3$: $Bi_{x=0.003}^{3+}$, Er_x^{3+} powder. The inset displays the CL peak intensity as a function of Er^{3+} doping concentration.

6.4 Conclusion

Using the combustion method Er^{3+}/Yb^{3+} co-doped $Gd_2O_3:Bi^{3+}$ has been successfully synthesized. XRD results revealed that all the samples crystallized to a single-phase cubic structure matching to the Gd_2O_3 standard with an $Ia\overline{3}$ space group. The bandgap was determined from reflectance measurements which increased slightly with added Bi^{3+}, Yb^{3+} and Er^{3+} ions. This may be due to the distortion of the crystal lattice and the structural deformation in the Gd_2O_3 powder caused due to the replacement of either substitutional Gd^{3+} ions in the Gd_2O_3 lattice by Bi^{3+} and Yb^{3+} or Er^{3+} ions. The visible emission confirmed the $Gd_2O_3:Bi^{3+}$, Yb^{3+} emission located in the blue and extending to the green regions centered at 360, 418 and 505 nm, which were ascribed to the Bi^{3+} under S_6 and C_2 symmetry. The visible emission intensity of the co-doped phosphor samples reduced in the presence of increasing Yb^{3+} concentration due to the higher potential for energy transfer between the Bi^{3+} and Yb^{3+} ions. NIR emission of Yb^{3+} consisted of a sharp maximum centered at 976 nm accompanied by several weaker peaks centered at 950 nm, 1025 nm and 1065 nm caused by the crystal field Stark splitting of the $^2F_{5/2}$ and $^2F_{7/2}$ energy levels. The NIR emission was confirmed for the Yb^{3+} doped Gd_2O_3 samples with and without the presence of Bi^{3+}. NIR emission displayed that the Bi^{3+} ion steadily improved the Yb^{3+} emission intensity in the Gd_2O_3 matrix and by increasing the Yb^{3+} concentration led to an enhancement in the NIR emission intensity. On the other hand, the UC emissions of the visible-red and NIR emissions were confirmed for Er^{3+} doped Gd_2O_3 samples with and without the presence of Bi^{3+} pumped by 980 nm. The CL emission of Er^{3+} co-doped $Gd_2O_3:Bi^{3+}$ confirmed blue emission bands assigned to the $^3P_1 \rightarrow {}^1S_0$ transitions of the Bi^{3+} ions and the green-yellow emission bands that corresponded to an overlap between the $^3P_1 \rightarrow {}^1S_0$ transitions of the Bi^{3+} ions and the $^2H_{11/2}$, $^4S_{3/2} \rightarrow {}^4I_{15/2}$ transitions of the Er^{3+} ions. These results demonstrated that Gd_2O_3 materials based on the Bi^{3+}–Yb^{3+} and Bi^{3+}–Er^{3+} couples maybe an attractive excellent proposal for use in increasing and enhancing the efficiency of silicon SC through DC and UC processes.

References

[1] B. S. Richards. Luminescent layers for enhanced silicon solar cell performance: Down-conversion. *Solar Energy Materials and Solar Cells,* **90(9)** (2006) 1189–1207. doi:10.1016/j.solmat.2005.07.001.

[2] X. Y. Huang and Q. Y. Zhang. Near-infrared quantum cutting via cooperative energy transfer in Gd_2O_3:Bi^{3+},Yb^{3+} phosphors. *Journal of Applied Physics,* **107(6)** (2010) 063505–5. doi:10.1063/1.3354063.

[3] M. Bryan van der Ende, Linda. Aarts, Andries. Meijerink. Lanthanide ions as spectral converters for solar cells. *Physical Chemistry Chemical Physics*, **11(47)** (2009) 11081-11095. doi:10.1039/B913877C.

[4] J. Day, S. Senthilarasu, T. K. Mallick. Improving spectral modification for applications in solar cells: a review. *Renewable Energy,* **(132)** (2018) 186-205. doi:10.1016/j.renene.2018.07.101.

[5] Y. Zhydachevskyy, V. Tsiumra, M. Baran, L. Lipińska, P. Sybilski and A. Suchocki. Quantum efficiency of the down-conversion process in Bi^{3+}–Yb^{3+} co-doped Gd_2O_3. *Journal of Luminescence,* **196,** (2018) 169–173. doi:10.1016/j.jlumin.2017.12.042.

[6] N. A. M. Saeed, E. Coetsee, H. C. Swart. Down-conversion of YOF: Pr^{3+}, Yb^{3+} phosphor. *Optical Materials,* **110**, (2020) 110516–10. doi:10.1016/j.optmat.2020.110516.

[7] Y. Jia, Y. Yulin, F. Ruiqing, L. Danqing, W. Liguo, C. Shuo, L. Liang, Y. Bin and C. Wenwu. Enhanced Near-Infrared to Visible Upconversion Nanoparticles of Ho^{3+}-Yb^{3+}-F– Tri-Doped TiO_2 and Its Application in Dye-Sensitized Solar Cells with 37% Improvement in Power Conversion Efficiency. *Inorganic Chemistry*. **53 (15)** (2014) 8045-8053. doi: 10.1021/ic501041h.

[8] M. Back, E. Trave, R. Marin, N. Mazzucco, D. Cristofori, P. Riello. Energy Transfer in Bi- and Er-Codoped Y_2O_3 Nanocrystals: An Effective System for Rare Earth Fluorescence Enhancement. *The Journal of Physical Chemistry C*, **118(51)** (2014) 30071–30078. doi:10.1021/jp5080016.

[9] D. Li, W. Qin, P. Zhang, L. Wang, M. Lan, P. Shi. Efficient luminescence enhancement of Gd_2O_3:Ln^{3+} (Ln = Yb/Er, Eu) NCs by codoping Zn^{2+} and Li^{+} inert ions. *Optical Materials Express*, **7(2)** (2017) 329-7-2. doi:10.1364/ome.7.000329.

[10] E. Lee, R. E. Kroon, J. J. Terblans, H. C. Swart. Luminescence properties of Y_2O_3:Bi^{3+},Yb^{3+} co-doped phosphor for application in solar cells. *Physica B: Condensed Matter*, **(535)** (2017) 102-105. doi:10.1016/j.physb.2017.06.072.

[11] D. Serrano; A. Braud; J.-L. Doualan; P. Camy; A. Benayad; V. Ménard; R. Moncorgé. Ytterbium sensitization in KY_3F_{10}:Pr^{3+}, Yb^{3+} for silicon solar cells efficiency enhancement. *Optical Materials*, **33(7)** (2011) 1028–1031. doi:10.1016/j.optmat.2010.07.023.

[12] J. J. Eilers, D. Biner, J. T. Van Wijngaarden, K. Krämer, H. Güdel, A. Meijerink. Efficient visible to infrared quantum cutting through downconversion with the Er^{3+}–Yb^{3+} couple in $Cs_3Y_2Br_9$. *Applied Physics Letters*, **96(15)** (2010) 151106/1-151106/3. doi:10.1063/1.3377909.

[13] M. Qu, R. Wang, Y. Zhang, K. Li, H. Yan. High efficient antireflective down-conversion Y_2O_3:Bi,Yb films with pyramid preferred oriented nano-structure. *Journal of Applied Physics*, **111(9)** (2012) 093108-5. doi: 10.1063/1.4712461.

[14] Q. Xu, B. Lin. Y. Mao. Photoluminescence characteristics of energy transfer between Er^{3+} and Bi^{3+} in Gd_2O_3: Er^{3+}, Bi^{3+}. *Journal of Luminescence*, **128(12)** (2008) 1965–1968. doi:10.1016/j.jlumin.2008.06.007.

[15] G. Hai, L. Yunfeng, W. Dianyuan, Z. Weiping, Y. Min, L. Liren, X. Shangda. Blue upconversion of cubic Gd_2O_3:Er produced by green laser. *Journal of Alloys and Compounds*. **376(1-2)**, (2004) 0–27. doi:10.1016/j.jallcom.2003.12.020.

[16] J. Xue, X. Wang, J. H. Jeong, X. Yan. Spectrum and Energy transfer in Bi^{3+}-Re^{n+} (n = 2, 3, 4) co-doped phosphors studies for extended optical applications. *Physical Chemistry Chemical Physics*. **(20)**, (2018) 11516-11541. doi:10.1039/C8CP00433A.

[17] R. Nagai, Y. Shan, J. Yue, K. Tezuka. Examination on red emission of up-conversion phosphors with Bi-containing host materials. *Journal of the Ceramic Society of Japan*, **127(6)** (2019) 409–413. doi:10.2109/jcersj2.18217.

[18] R. K. Tamrakar, D. P. Bisen and N. Brahme. Comparison of photoluminescence properties of Gd2O3 phosphor synthesized by combustion and solid state reaction method. *Journal of Radiation Research and Applied Sciences*, **7(4)** (2014) 550–559. doi: 10.1016/j.jrras.2014.09.005.

[19] Y. Zou, L. Tang, J.-L. Cai, L.-T. Lin, L.-W. Cao and J.-X. Meng. Combustion synthesis and luminescence of monoclinic Gd_2O_3:Bi phosphors. *Journal of Luminescence*, **153**, (2014) 210–214. doi:10.1016/j.jlumin.2014.03.02.

[20] Q. B. Li, J. M. Lin, J. H. Wu, Z. Lan, J. L. Wang, Y. wang, F. G. Peng, M. L. Huang, Y. M. Xiao. Preparation of Gd_2O_3:Eu^{3+} downconversion luminescent material and its application in dye-sensitized solar cells. *Chinese Sci Bull*, **56(28-29)**, (2011) 3114–3118. doi:10.1007/s11434-011-4664-z.

[21] G. Tian, Z. Gu, X. Liu, L. Zhou, W. Yin, L. Yan, S. Jin, W. Ren, G. Xing, S. Li, Y. Zhao. Facile Fabrication of Rare-Earth-Doped Gd_2O_3 Hollow Spheres with Upconversion Luminescence, Magnetic Resonance, and Drug Delivery Properties. *The Journal of Physical Chemistry C*, **115(48)** (2011) 23790–23796. doi:10.1021/jp209055t.

[22] H. Jamnezhad and M. Jafari. Structure of Gd_2O_3 nanoparticles at high temperature. *Journal of Magnetism and Magnetic Materials*, **408** (2016) 164–167. doi:10.1016/j.jmmm.2016.02.041.

[23] B. Antic, A. Kremenovic, I. Draganic, P. Colomban, Vasiljevic-Radovic, D. Blanusa, J. Blanusa, M. Tadic and M. Mitric. Effects of O^{2+} ions beam irradiation on crystal structure of rare earth sesquioxides. *Applied Surface Science*, **255(17)** (2009) 7601–7604. doi:10.1016/j.apsusc.2009.04.035.

[24] M. H. M. Abdelrehman, R. E. Kroon, A. Yousif, H. A. A. Seed Ahmed and H. C. Swart. Photoluminescence, thermoluminescence, and cathodoluminescence of optimized cubic Gd_2O_3:Bi phosphor powder. *J. Vac. Sci. Technol.* **A 38,** (2020) 063207–15. doi.org/10.1116/6.0000567.

[25] G. Ju, Y. Hu, L. Chen, X. Wang, Z. Mu, H. Wu, F. Kang. Luminescence properties of Y_2O_3:Bi^{3+}, Ln^{3+} (Ln=Sm, Eu, Dy, Er, Ho) and the sensitization of Ln^{3+} by Bi^{3+}. *Journal of Luminescence*, **132(8)** (2012) 1853–1859. doi:10.1016/j.jlumin.2012.03.020.

[26] G.-X. Liu, R. Zhang, Q.-L. Xiao, S.-Y. Zou, W.-F. Peng, L.-W. Cao and J.-X. Meng. Efficient Bi^{3+}→Nd^{3+} energy transfer in Gd_2O_3:Bi^{3+}, Nd^{3+}. *Optical Materials*, **34(1)** (2011) 313–316. doi:10.1016/j.optmat.2011.09.003.

[27] S. K. Singh, K. Kumar and S. B. Rai. Optical properties and switching behavior in Gd_2O_3:Er^{3+} nanophosphor. *Journal of Applied Physics*, **106(9)** (2009) 093520-093520-6. doi:10.1063/1.3259370.

[28] X. Y. Huang, J. X. Wang, D. C. Yu, S. Ye, Q. Y. Zhang and X. W. Sun. Spectral conversion for solar cell efficiency enhancement using YVO_4:Bi^{3+}, Ln^{3+} (Ln = Dy, Er, Ho, Eu, Sm, and Yb) phosphors. *Journal of Applied Physics*, **109(11)** (2011) 1135261- 1135267. doi:10.1063/1.3592889.

[29] H. C. Swart and R. E. Kroon. Ultraviolet and visible luminescence from bismuth doped materials. *Optical Materials*: X, **2** (2019) 100025–20. doi:10.1016/j.omx.2019.100025.

[30] R. D. Shannon, Revised Effective Ionic Radii and Systematic Studies of Interatomic Distances in Halides and Chalcogenides, *Acta Crystallographica Section A*, **A(32)** (1976) 751–767. doi: 10.1107/s0567739476001551.

[31] Z. Liu, D. Chen. Color tunable upconversion luminescence and optical thermometry properties of mixed Gd_2O_3:Yb^{3+}/Ho^{3+}/Er^{3+} nanoparticles prepared via laser ablation in liquid. *Journal of Materials Science: Materials in Electronics*. **31,** (2020) 9321–9327. doi.org/10.1007/s10854-020-03471-y.

[32] L. Lutterotti, S. Matthies, H-R. Wenk, AS. Schultz, JW. Richardson. Combined texture and structure analysis of deformed limestone from time-of-flight neutron diffraction spectra. *Applied Physics,* **81** (1997) 594–600. https://doi.org/10.1063/1.364220.

[33] Marlene C. Morris, Howard F. McMurdie, Eloise H. Evans, Boris Paretzkin, Harry S. Parker, Winnie Wong-Ng, and Donna M. Gladhill. Standard X-ray Diffraction Powder Patterns Section 21 — Data for 92 Substances. International Centre for Diffraction Data 1601 Park Lane Swarthmore, (1985) 8-148. doi:10.6028/NBS.MONO.25-21.

[34] R.A. Young, D.B. Wiles. Profile shape functions in Rietveld refinements. *Applied Crystallography,* **15** (1982) 430–438. doi:10.1107/s002188988201231x.

[35] W. A. I. Tabaza, H. C. Swart and R. E. Kroon. Optical properties of Bi and energy transfer from Bi to Tb in $MgAl_2O_4$ phosphor. *J. Lumin.* **148**, (2014) 192–197. doi: 10.1016/j.jlumin.2013.12.018.

[36] P. S. V. Mocherla, C. Karthik, R. Ubic, M. S. Ramachandra Rao, and C. Sudakar. Tunable bandgap in BiFeO3 nanoparticles: The role of microstrain and oxygen defects. *Applied Physics Letters,* **103(2)** (2017) 022910–5. doi:10.1063/1.4813539.

[37] S. Gai, P. Yang, D. Wang, C. Li, N. Niu, F. He, X. Li. Monodisperse Gd_2O_3:Ln (Ln = Eu^{3+}, Tb^{3+}, Dy^{3+}, Sm^{3+}, Yb^{3+}/Er^{3+}, Yb^{3+}/Tm^{3+}, and Yb^{3+}/Ho^{3+}) nanocrystals with tunable size and multicolor luminescent properties. *CrystEngComm*, **13(17)** (2011) 5480-5487. doi:10.1039/C1CE05455D.

[38] M. C. Ferrara, D. Altamura, M. Schioppa, L. Tapfer, E. Nichelatti, L. Pilloni and M. Montecchi. Growth, characterization and optical properties of nanocrystalline gadolinia thin films prepared by sol–gel dip coating. *Journal of Physics D: Applied Physics*, **41(22)** (2008) 225408-10. doi:10.1088/0022-3727/41/22/225408.

[39] Y. A. Kuznetsova, A. F. Zatsepin, R. A. Tselybeev, V. N. Rychkov and V. A. Pustovarov. Luminescence of rare-earth ions and intrinsic defects in Gd_2O_3 matrix. *Journal of Physics: Conference Series*, **741** (2016) 0120890-0120896. doi:10.1088/1742-6596/741/1/012089.

[40] A. Maurya, R. S. Yadav, R. V. Yadav, A. Bahadur and S. B. Rai. Enhanced green upconversion photoluminescence from Ho^{3+}/ Yb^{3+} co-doped $CaZrO_3$ phosphor via Mg^{2+} doping. *Royal Society of Chemistry*. **6(114)** (2016) 113469–113477. doi:10.1039/C6RA23835A.

[41] Y. Zhang, B. Chen, S. Xu, X. Li, J. Zhang, J. Sun, X. Zhang, H. Xia, R. Hua. A universal approach for calculating the Judd–Ofelt parameters of RE^{3+} in powdered phosphors and its application for the β-$NaYF_4$:Er^{3+}/Yb^{3+} phosphor derived from auto-combustion-assisted fluoridation. *Physical Chemistry Chemical Physics*, **20** (2018) 15876-15883. doi:10.1039/C8CP02317D.

[42] D. Jia, L. Liu, and W. M. Yen. Erbium energy levels relative to the band gap of gadolinium oxide. *Optics Communications*. **212(1-3)**, (2002) 97–100. doi: 10.1016/S0030-4018(02)01999-5.

[43] S. Som and S. K. Sharma. Eu^{3+}/Tb^{3+}-codoped Y_2O_3 nanophosphors: Rietveld refinement, bandgap and photoluminescence optimization. *Journal of Physics D: Applied Physics*, **45(41)** (2012) 415102-(11p). doi:10.1088/0022-3727/45/41/415102.

[44] M. H. M. Abdelrehman, R. E. Kroon, A. Yousif, H. A. A. Seed Ahmed and H. C. Swart. Luminescence properties and cathodoluminescence degradation of Bi doped SrO powder. *Journal of Vacuum Science & Technology B*, **37(1)** (2019) 011206-(11p). doi:10.1116/1.5075492.

[45] Y. A. Kuznetsova and A. F. Zatsepin. Optical properties and energy parameters of Gd_2O_3 and Gd_2O_3:Er nanoparticles. *Journal of Physics: Conference Series*, **917** (2017) 062001-(5p). doi:10.1088/1742-6596/917/6/062001.

[46] H. Fukada, K. Ueda, J. Ishino, T. Miyata and T. Minami. Blue PL and EL emissions from Bi-activated binary oxide thin-film phosphors. *Thin Solid Films*, **518(11**) (2010) 3067–3070. doi:10.1016/j.tsf.2009.08.014.

[47] L. J. Xiao, F. Q. Yan, Y. Xie, F. Zeng, Y. J. Chen and W. Z. Li. Preparation and fluorescent properties of Bi (3+) Doped, Yb (3+) doped and Bi (3+), Yb (3+) co-doped Gd (2) O (3) phosphors. *Chinese Journal of Luminescence*, **33(4)**, (2012) 383-388. doi: 10.3788/fgxb20123304.0383.

[48] P. I. Paulose, G. Jose, V. Thomas, N. V. Unnikrishnan, M. K. R. Warrier. Sensitized fluorescence of Ce^{3+}/Mn^{2+} system in phosphate glass. *Journal of Physics and Chemistry of Solids.* **64(5)** (2003) 841–846. doi:10.1016/s0022-3697(02)00416-x.

[49] M. Back, M. Boffelli, A. Massari, R. Marin, F. Enrichi and P. Riello. Energy transfer between Tb^{3+} and Eu^{3+} in co-doped Y_2O_3 nanocrystals prepared by Pechini method. *Journal of Nanoparticle Research*, **15(7)** (2013) 1753–(11p). doi:10.1007/s11051-013-1753-8.

[50] X. Pang, Y. Zhang, L. Ding, Z. Su, W. F. Zhang. Upconversion Luminescence Properties of Er^{3+}–Bi^{3+} Codoped $CaSnO_3$ Nanocrystals with Perovskite Structure. *Journal of Nanoscience and Nanotechnology*. **10(3)** (2010) 1860–1864. doi:10.1166/jnn.2010.2135.

[51] M. Back, E. Trave, P. Riello, and J. J. Joos. Insight into the Upconversion Luminescence of Highly Efficient Lanthanide-Doped Bi_2O_3 Nanoparticles. *The Journal of Physical Chemistry C*. **122 (13)**, (2018) 7389-7398. doi: 10.1021/acs.jpcc.8b00637.

[52] S. Pyshkin. Luminescence - OLED Technology and Applications || Mechanism of Photoluminescence in Erbium-Doped Chalcogenide. I*ntechopen*. **10.5772** (2020) 78903(Chapter3). doi:10.5772/intechopen.81445.

[53] Y. Jiao, X. Gao, J. Lu, Y. Chen, W. He, X. Chen, X. Li, R. Li. Hydrothermal synthesis of the intense green photoluminescence of hexagonal phase $NaYF_4$:Yb^{3+}/Er^{3+} microcrystals. *Journal of Alloys and Compounds*. **549,** (2013) 245−253. doi:10.1016/j.jallcom.2012.09.056.

[54] S. Pattnaik and V. K. Rai. NIR to green light upconversion emission in Er^{3+} doped $CaTiO_3$ phosphors. *2018 3rd International Conference on Microwave and Photonics (ICMAP)*, (2018) 1-4. doi: 10.1109/ICMAP.2018.8354548.

[55] R. Luo, L. Chen, Q. Li, J. Zhou, L. Mei, Z. Ning, Y. Zhao, M. Liu, X. Lai, J. Bi, W. Yin and D. Gao. Bi^{3+}-Doped $BaYF_5$:Yb,Er Upconversion Nanoparticles with Enhanced Luminescence and Application Case for X-ray Computed Tomography Imaging. *Inorganic Chemistry*. **59(24)** (2020) 17906-17915. doi:10.1021/acs.inorgchem.0c01818.

[56] M. Yang, Y. Sui, S. Wang, X. Wang, Y. Wang, S. Lü, Z. Zhang, Z. Liu, T. Lü, W. Liu. Effects of Bi^{3+} doping on the optical properties of Er^{3+}:Y_2O_3. *Journal of Alloys and Compounds*, **509(3)**, (2011) 827–830. doi:10.1016/j.jallcom.2010.09.100.

[57] A. K. Choudhary, A. Dwivedi, A. Bahadur, T. P. Yadav, S.B. Rai. Enhanced upconversion emission and temperature sensor sensitivity in presence of Bi^{3+} ions in Er^{3+} /Yb^{3+} co-doped $MgAl_2O_4$ phosphor. *Ceramics International*, **44(8)** (2018) 9633-9642. doi:10.1016/j.ceramint.2018.02.190.

[58] Z. Boruc, G. Gawlik, B. Fetliński, M. Kaczkan, M. Malinowski. Temperature dependence of Er^{3+} ionoluminescence and photoluminescence in Gd_2O_3:Bi nanopowder. *Review of Scientific Instruments.* **85(6)** (2014) 064901–(6p). doi:10.1063/1.4880456.

Chapter 7

Effect of Yb^{3+} on the luminescence of Bi^{3+}/Er^{3+} co-doped Gd_2O_3 phosphor powder

In this chapter, the luminescence properties of visible light emission of $Bi^{3+}/Er^{3+}/xYb^{3+}$ tri-doped Gd_2O_3 phosphor powders for SC efficiency enhancement as well as the energy transfer mechanism are reported. The effect of different Yb^{3+} concentrations on the visible emission of Er^{3+} by different excitation wavelengths and the improvement of the UC emission of Er^{3+} by incorporation of Bi^{3+} and Yb^{3+} were also explored and discussed.

7.1 Introduction

To improve the efficiency of solar energy to electricity using crystalline silicon cells, developers have focused on applying spectral conversion to solar cells to take advantage of the extra part of the solar spectrum in the ultraviolet and infrared region [1]. The need for the improvement of solar cells arises because a large part of the solar energy in the photovoltaic processes is lost due to the thermalization of electron-hole pairs with an energy greater than the energy gap in c-Si [2]. The UC conversion process is an effective way to circumvent transmission loss by converting two photons from the subband gap to one photon above the bandgap, thus UC effect helps to harvest low energy photons that usually have too little energy to be absorbed. Once UC occurs, new photons can be absorbed and contribute to the generation of electron-hole pairs. Lanthanide (Ln^{3+}) ions are some of the best ions used as optical activators in phosphor materials for the use in photon conversion processes due to their unique properties such as narrow emission bands and long lifetime emissions [3]. Ln^{3+} ions can convert near infrared (NIR) light into visible or ultraviolet light, and they can also convert high energy photons into visible and near-infrared light to promote efficient use of sunlight for photocatalysts and solar cells [4]. Trivalent erbium (Er^{3+}) ions in multiple hosts were well suited for UC studies due to their intense green emission after 980 nm generation from two thermally coupled levels, namely $^2H_{11/2}$ and $^4S_{3/2}$ [5]. Er^{3+} ions in UC phosphors generally show strong green emission and weak red emission, although this can be affected by the concentration and the presence of a sensitizer. It has been observed that energy transfer from Bi^{3+} to Ln^{3+} ions can significantly improve the fluorescence of the Ln^{3+} ions [6,7]. Yb^{3+} is an excellent sensitizer due to its large absorption cross-section at about 980 nm and the efficiency of the energy transfer from Yb^{3+} to Er^{3+} [5]. Er^{3+} ions also absorb energy at about 980 nm, but Yb^{3+} ions are about 10 times more efficient [8]. Er^{3+} UC luminescence efficiency depends on the excited state dynamics of the Er^{3+} ions, the sensitizers and their interactions with the host matrix. Among the rare earth oxides, cubic Gd_2O_3 is a promising host matrix that can be used in photon conversion processes for wide application in various fields [9]. Gd_2O_3 is an attractive candidate in optical applications due to its high quality, based on the thermodynamic energy considerations due to its high dielectric constant, good thermal stability, wide band gap of more than 5 eV [10] and low phonon cut-off energy (600 cm^{-1}) [11] which reduces non-radiation relaxations [12]. Previously the luminescence-induced optical effect on Er^{3+} co-doped Gd_2O_3:Bi phosphor powder has been studied. Bi^{3+} ions can be used as a significant sensitizing ion due to the excellent properties of Bi^{3+} ions, with an adjustable luminescence energy transfer between Bi^{3+} and other luminescent ions or hosts. The most important feature of the Bi^{3+} ion is that it can efficiently absorb ultraviolet light and transfer energy to other luminescent centers, which significantly increases the acceptor ion emission intensity [13]. It has been reported in several studies [12,14,15] that when the Bi^{3+} ion is incorporated into Er^{3+}/Yb^{3+} -doped phosphors, a significant improvement in UC emission intensity is obtained. This is an extension of previous work on the effect of different concentrations of Yb^{3+} ions on the luminescence of $Gd_2O_3:Bi^{3+}$,Er phosphor powder prepared by the combustion method. The investigation is done on the suitability of the related energy levels among Bi^{3+}, Er^{3+} and Yb^{3+} ions for possible energy transfer and sensitization of the visible and NIR emissions.

7.2 Experimental

7.2.1 Materials and method

The $Gd_{1.977-x}O_3:Bi_{0.003},Er_{0.02},Yb_x$ phosphor powder samples with x = 0.0, 0.01, 0.03, 0.06, 0.09 and 0.12 were synthesized by using the solution combustion method [15] with the concentrations of Bi^{3+} and Er^{3+} ions fixed at 0.003 and 0.02, respectively. For a typical preparation,

$Gd(NO_3)_3 \cdot 6H_2O$ was used as the host precursor as the starting material and H_2CONH_2 for the fuel. Then $Bi(NO_3)_3 \cdot 5H_2O$, $Er(NO_3)_3 \cdot 5H_2O$ and $Yb(NO_3)_3$ were introduced by substituting for some $Gd(NO_3)_3 \cdot 6H_2O$. All starting powders were homogeneously mixed according to the designed stoichiometric ratio [29] by stirring using a magnetic stirrer for 2 h in deionized water at 100 °C. Then the final solution was kept in a furnace already heated to a temperature of 600 °C for combustion. The powders were put in crucibles and then sintered at 1000 °C for 2 h in an air atmosphere to obtain the final product.

7.2.2 Instruments

The structure of the prepared samples was characterized by X-ray diffraction (XRD) using a Bruker Advance D8 diffractometer (40 kV, 40 mA) with Cu Kα X-rays ($\lambda = 0.154$ nm). A JEOL JSM-7800F scanning electron microscope (SEM) was used to investigate the morphology, chemical composition and cathodoluminescence with the electron beam voltage maintained at 5 keV. UV–visible absorption by diffuse reflectance spectra measurements were collected by a Lambda 950 UV–Vis spectrophotometer. The UC spectra and NIR luminescence spectra were produced using a photoluminescence system consisting of a fiber-coupled 980 nm diode laser as the excitation source. The NIR emission was dispersed by a Horiba iHR 320 monochromator and detected by a solid-state DSS-IGA020T detector. An Edinburgh Instruments FS5 spectrophotometer with a 150 W CW ozone-free xenon lamp as an excitation source was used for the PL excitation and emission measurements. All measurements were done at room temperature.

7.3 Results and discussion

7.3.1 Structure analysis

Figure 7.1(a) illustrates the XRD patterns of the phosphor powder samples with different concentration of Yb^{3+} ions as compared with the pure host sample and the JCPDS standard #43-1014 of the cubic phase of Gd_2O_3 [16]. All observed XRD peaks confirmed the formation of a single phase cubic structure of Gd_2O_3 with a space group $Ia\overline{3}$ without any secondary phases. It is clear that incorporation of Bi, Er and Yb did not change the structure of the Gd_2O_3 host matrix, which means that these ions have been successfully doped in the Gd_2O_3 host sites by substitution of the Gd. The strongest peak detected at $2\theta = 28.27°$ represents the plane (2 2 2). In figure 7.1(b) a slight shift in the 222 peaks was observed towards a higher Bragg angle with an increase in the Yb^{3+} ion concentration, which indicates a decrease in the lattice parameter. This shift maybe due to a result of lattice distortions caused by the difference in the ionic radius of the Bi^{3+} (103 pm), Er^{3+} (89.0 pm) and Yb^{3+} (86.8 pm) dopant ions and the Gd^{3+} (93.8 pm) ions of the Gd_2O_3 host lattice [17].

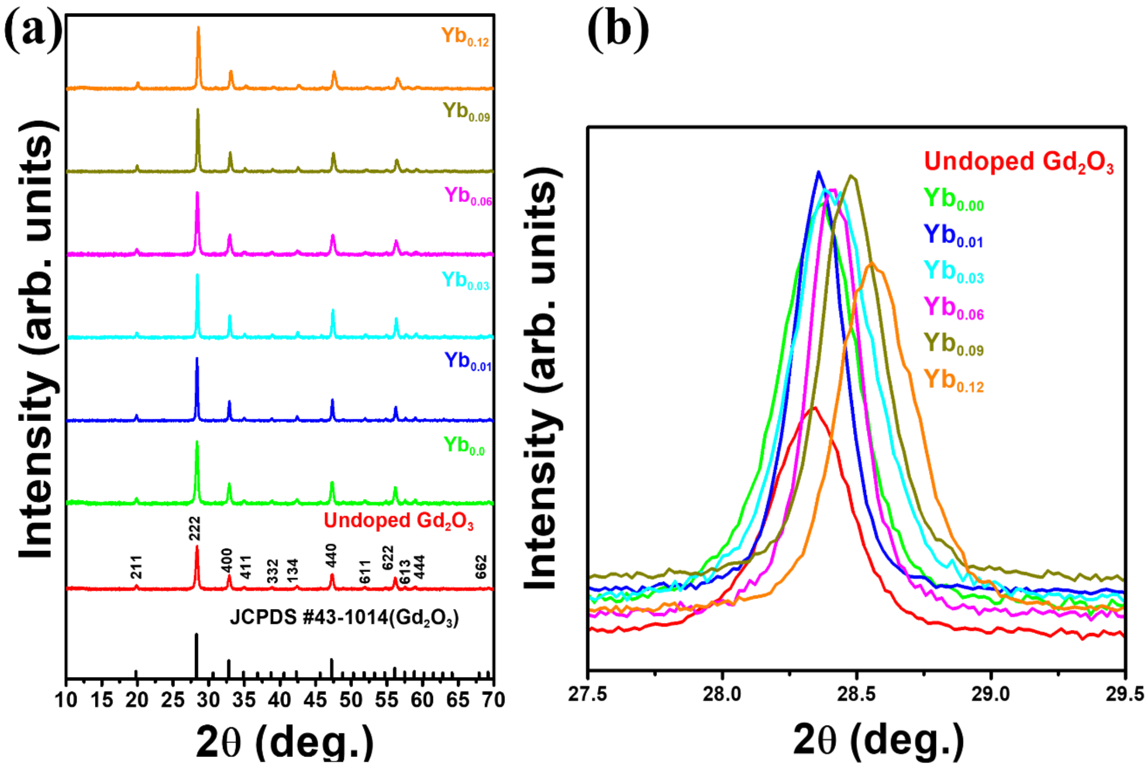

Figure 7.1: (a) XRD patterns of Gd_2O_3 and tri-doped $Gd_{1.977-x}O_3$:$Bi_{0.003}$,$Er_{0.02}$,Yb_x powder (b) magnified region of the 222 peaks.

By using all Miller indexes shown in Figure 7.1(a), the crystallite size and microstrain for both the undoped and doped materials were calculated using their FWHM by Williamson-Hall plots, Figure 7.2 [18]. There were changes in crystallite size as well as the strain present in the lattice with an increase in the Yb^{3+}concentration as given in table 7.1. The crystal size decreased from 52 nm for the host sample to 38 nm for the sample doped with x = 0.12 of Yb^{3+} ions. Kumar *et al.* [19] report that for an increase in Yb concentration of doped Y_2O_3 the main peak was broadened and the crystallite size reduced, and lattice strain was induced in the crystal. Therefore, in our case since all samples were analyzed under the same conditions and using the same system parameters, the decrease in crystallite size with an increase in doping concentration may be due to the enhanced incorporation of dopant ions into the Gd^{3+} sites of the host Gd_2O_3 lattice. Thus, the slight difference in size may have caused a stress field which perturbed the grain growth process, or some of the dopants may have formed a diffusion barrier at the grain boundary.

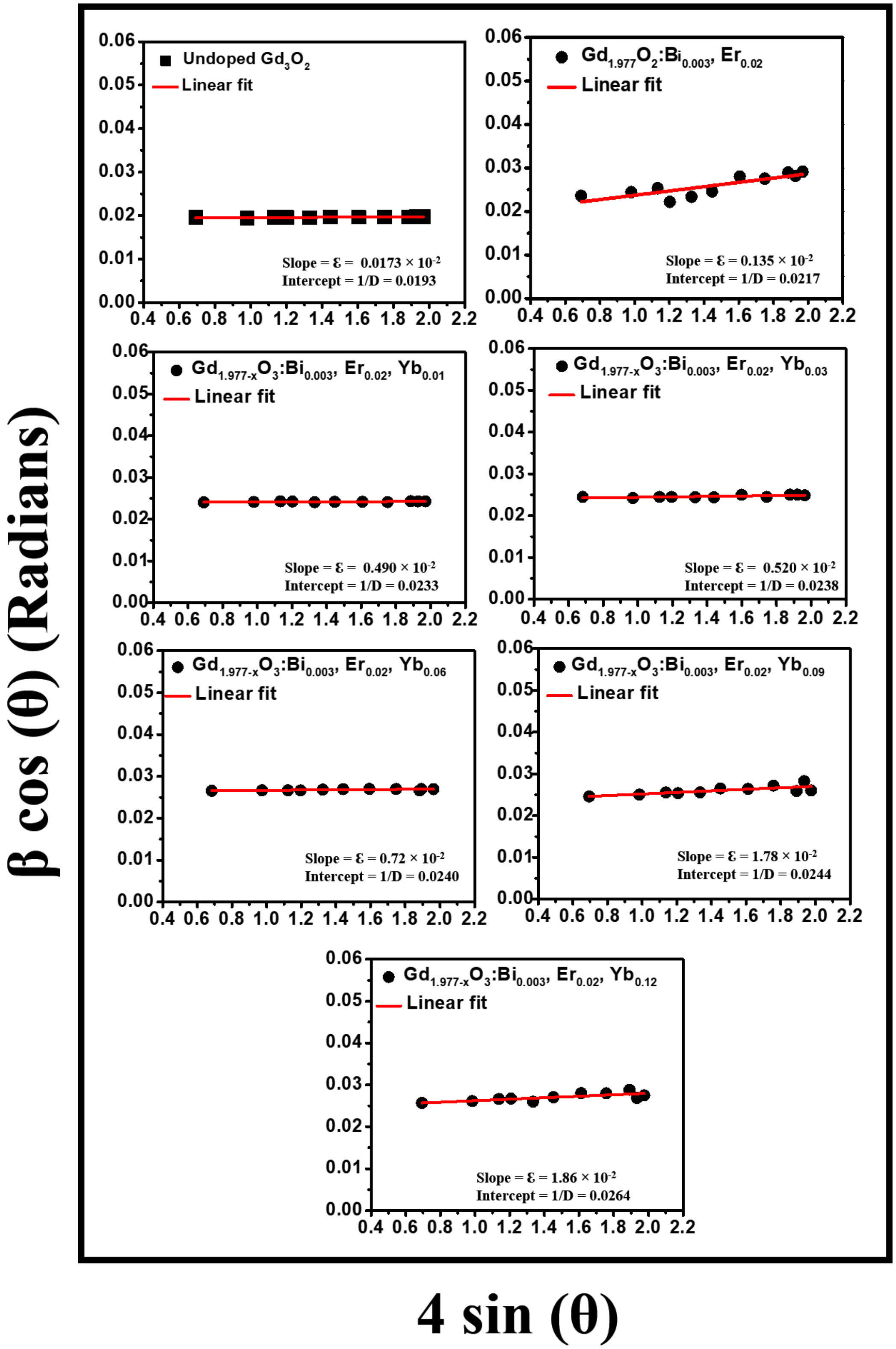

Figure 7.2: Williamson-Hall plots of Gd_2O_3 and $Gd_{1.977-x}O_3$:$Bi_{0.003}$,$Er_{0.02}$,Yb_x synthesized with different Yb^{3+} concentrations.

Table 7.1. The crystallite size and micro-strain of Gd_2O_3 and $Gd_{1.977-x}O_3$:$Bi_{0.003}$,$Er_{0.02}$,Yb_x synthesized with different Yb^{3+} concentrations.

Sample	Crystallite size D (nm)	Micro-strain ε (%)
Gd_2O_3	52	0.02
$Gd_{1.977}O_3$:$Bi_{0.003}$,$Er_{0.02}$	46	0.1
$Gd_{1.977-x}O_3$:$Bi_{0.003}$,$Er_{0.02}$,$Yb_{x=0.01}$	42	0.5
$Gd_{1.977-x}O_3$:$Bi_{0.003}$,$Er_{0.02}$,$Yb_{x=0.03}$	42	0.5
$Gd_{1.977-x}O_3$:$Bi_{0.003}$,$Er_{0.02}$,$Yb_{x=0.06}$	41	0.7
$Gd_{1.977-x}O_3$:$Bi_{0.003}$,$Er_{0.02}$,$Yb_{x=0.09}$	41	1.8
$Gd_{1.977-x}O_3$:$Bi_{0.003}$,$Er_{0.02}$,$Yb_{x=0.12}$	38	1.9

7.3.2 Morphological analyses

The surface morphology and the effect of Yb^{3+} ion concentration on the morphology of the $Gd_{1.977-x}O_3$:$Bi_{0.003}$,$Er_{0.02}$,Yb_x powders were investigated using SEM. Figure 7.3 illustrates the variation of the morphology with different concentrations of Yb^{3+} ions with the pure host for comparison. The host sample in Figure 7.3(a) consisted of a mixture of spheroids and small cubic particles clumped with each other. After adding Bi^{3+} and Er^{3+} in Figure 7.3(b) the size of the cubic particles remained about the same but the faces of the individual crystallites became more agglomerated. The authors earlier reported no methodical change in the morphology [15]. However, with the adding of different concentration of Yb^{3+}, a variety of irregularly shaped nanoplates with a smoother surface agglomerated with angular, particles were observed (Figure 7.3 (c-f)). In general, after adding Er^{3+} and Yb^{3+} the doped powders morphology remained the same, and the particles grew into large clusters consisting of particles of smaller sizes than those of non-doped powders. In the case of a high concentration of the Yb^{3+} ion at x= 0.12 in Figure 7.3(e), the image shows a mixture of homogeneous flake-like agglomerated particles with some grainy sides of cubic particles free of cracks or voids. The agglomeration of small particles in all samples may have occurred during high temperature annealing [20]. It was reported earlier that Gd_2O_3 phosphorous particles agglomerate upon sintering at 1000 °C [15].

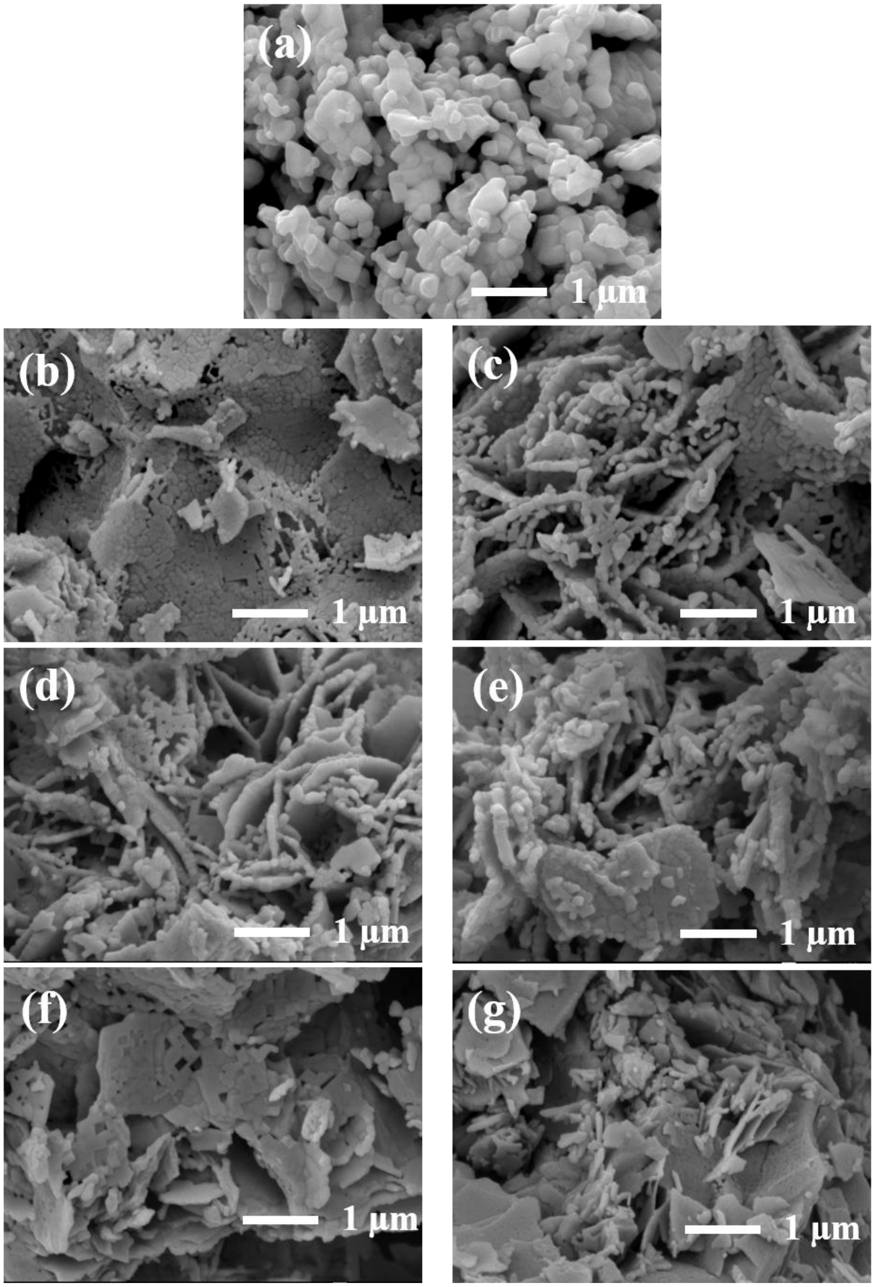

Figure 7.3: SEM micrographs of (a) Gd_2O_3 and $Gd_{1.977-x}O_3$:$Bi_{0.003}$,$Er_{0.02}$,Yb_x synthesised with different concentrations of Yb^{3+} (b) x = 0.00, (c) x = 0.01, (d) x = 0.03, (e) x = 0.06, (f) x = 0.09 and (g) x = 0.12.

7.3.3 Compositional analyses

To detect the constituent elements on the phosphor, EDS measurements were made and are shown in figure 7.4 for (a) Gd_2O_3, (b) $Gd_{1.977}O_3$:$Bi_{0.003}$,$Er_{0.02}$ and (c) $Gd_{1.977-x}O_3$:$Bi_{0.003}$,$Er_{0.02}$,$Yb_{x=0.12}$. The presence of the major elements Gd and O was observed in all samples as expected. The presence of carbon (C) was also observed, which may have come from the carbon tape on which the samples were attached during the measurement, or perhaps from atmospheric hydrocarbons that were introduced into the sample during synthesis and due to atmospheric processing. In Figure 7.4(b) the EDS spectrum shows the main elements in addition to Er as a result of its doping in the sample. There were no Bi peaks recorded in the spectra as they are envisaged to occur at 2.4, 2.7 and 3.4 keV [21], which may be due to its low concentration. Figure 7.4(c) shows the major elements Gd and C as well as Er and Yb as expected as a result of doping within the sample.

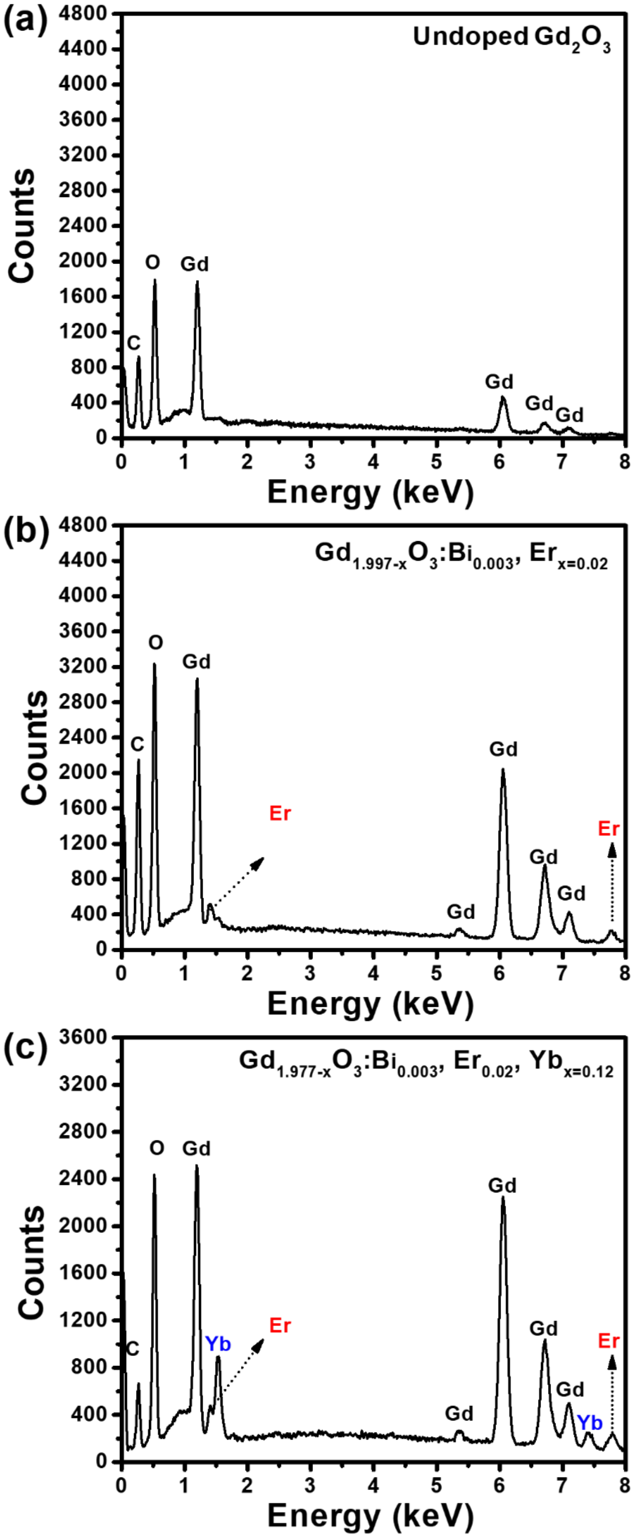

Figure 7.4: EDS spectra of (a) Gd_2O_3, (b) $Gd_{1.977}O_3$:$Bi_{0.003}$,$Er_{0.02}$, and (c) $Gd_{1.977-x}O_3$:$Bi_{0.003}$,$Er_{0.02}$,$Yb_{x=0.12}$.

7.3.4 Optical properties

7.3.4.1 Diffuse reflectance (DR) spectra

Figure 7.5 illustrates the DR measurements for the Gd_2O_3 host sample and $Gd_{1.797-x}O_3$:$Bi_{0.003}$,$Er_{0.02}$,Yb_x samples. There was a strong absorption at a wavelength of about 227 nm, which was due to the inter-band transitions of Gd_2O_3 [22]. In the host sample, there were additional absorption bands at 275, 315 nm, and 250 nm that were ascribed to the 4f-4f optical transitions of the Gd^{3+} ion from the ground $^8S_{7/2}$ to the excited ^6I_J, ^6P_J and ^6D_J states, respectively [23]. After doping the Bi^{3+}, Er^{3+} and Yb^{3+} ions into the phosphor, there were additional absorption bands in the visible and NIR spectral regions. The absorption bands located around 260, 335 and 375 nm, are due to the excitation transitions of the Bi^{3+} ions [24]. The bands at 260 and 375 nm were allocated to the transitions $^1A_g \rightarrow {}^3A_u$ and $^1A_g \rightarrow {}^3E_u$ of Bi^{3+} ion at the S_6 site. While the absorption band at 335 was attributed to the transitions $^1A \rightarrow {}^3A$ and $^1A \rightarrow {}^3B$ of the Bi^{3+} ion under C_2 symmetry [24]. The absorption bands are observed around 520, 655 and 802 nm, which can be attributed to the optical transitions in the Er^{3+} ions from the ground $^4I_{15/2}$ to the excited $^2H_{11/2}$, $^4F_{9/2}$ and $^4I_{9/2}$ energy levels, respectively [25]. An intense broad absorption band is also observed at 880-1050 nm, which may be due to the $^2F_{7/2} \rightarrow {}^2F_{5/2}$ transition of the Yb^{3+} ion [26], which increased significantly with increasing Yb^{3+} concentration. Since the absorption band of the Yb^{3+} ion is very wide, it can absorb a large number of incident photons, which may generate the large UC intensity of the Er^{3+} ion.

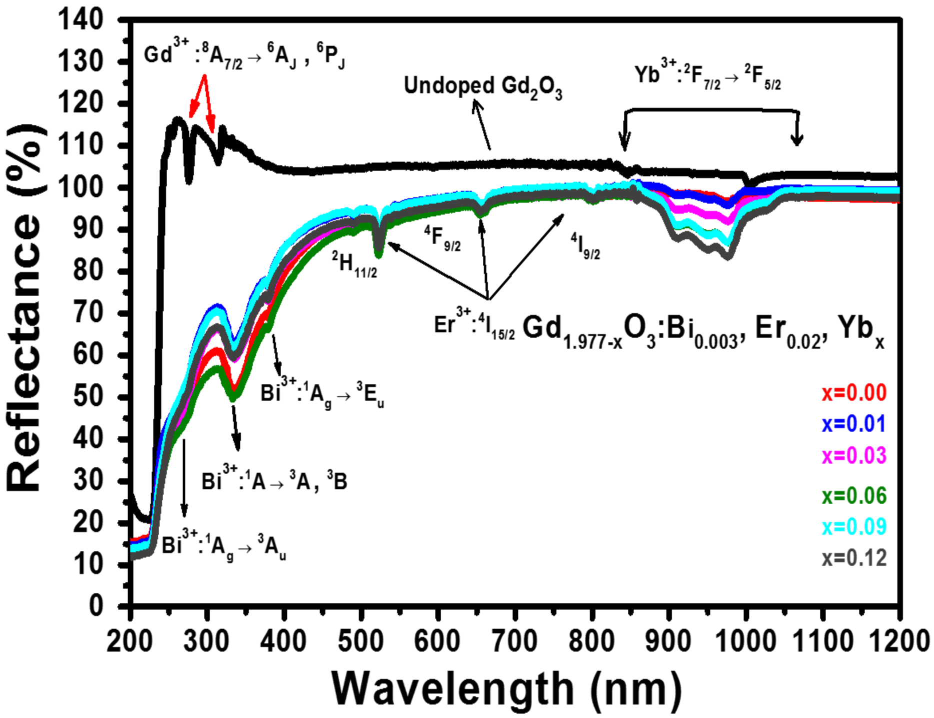

Figure 7.5: DR spectra of Gd_2O_3 and $Gd_{1.977-x}O_3$:$Bi_{0.003}$,$Er_{0.02}$,Yb_x.

7.3.4.2 Photoluminescence investigations

The room temperature UC spectra of $Gd_{1.977-x}O_3$:$Bi_{0.003}$,$Er_{0.02}$,Yb_x were measured for excitation with 980 nm radiation in the 500 – 800 nm emission region as shown in figure 7.6(a). The phosphor samples gave a variation in the emission intensity depending on the Yb^{3+} concentration, with several emission peaks in two prominent bands in the green and red regions. The emission bands peaking around 520, 537, 550, 560 and 670 nm and are attributed to $^4F_{5/2}$, $^4F_{7/2}$, $^2H_{11/2}$, $^4S_{3/2}$, and $^4F_{9/2}$ transitions to $^4I_{15/2}$ of the Er^{3+} ion, respectively [27]. There was a noticeable splitting of the peaks into several sharp components due to the crystal field effect (Stark splitting). This splitting probably describes the strength of the crystal field around the dopant ions in the host [14]. The inset in Figure 7.6(a) shows that UC emission intensity was optimized by changing the concentration of the Yb^{3+} ions of $Gd_{1.977-x}O_3$:$Bi_{0.003}$,$Er_{0.02}$,Yb_x. The intensity of the Er^{3+} ion emission strongly increased initially when the concentration of the Yb^{3+} ions was increased up to x = 0.03 and then decreased due to the concentration quenching effect that was probably due to the excitation energy migration from one activator ion to another. Khajuriaa *et al.*

[20] reported that the UC emission intensity of $Na_3Y(PO_4)_2:Er^{3+}/Yb^{3+}$ was reduced due to concentration quenching that happened as a result of the rate of energy back transfer from Er^{3+} to Yb^{3+} that becomes active with a further concentration increase. Furthermore, Haung *et al.* [28] reported that there was a clear quenching in the Er^{3+} UC emission when increasing the Yb^{3+} concentration. For high Yb concentrations, instead of transferring energy from Yb^{3+} to Er^{3+}, the migration between Yb^{3+} will continue. Therefore, high concentrations of Er^{3+} and Yb^{3+} act to constrain the efficiency of the UC energy transfer. The integrated intensity of all UC emission bands is sufficiently enhanced when co-doping with Yb^{3+} but the emission in the red region is significantly increased compared to the green light region.

To determine the effect of Bi^{3+} and Yb^{3+} on the UC emission of Er^{3+}, four samples were prepared. The first sample was doped with Er^{3+} only, the second was co-doped with Bi^{3+}, the third was co-doped with Yb^{3+} while the fourth sample was co-doped with both Bi^{3+} and Yb^{3+} (see Figure 7.6(b)). For the sample $Gd_2O_3:Er_{0.02}$ the UC intensity of the green and red emission was approximately the same. After being co-doped with Bi^{3+} the emission was strongly enhanced in the green area while the red emission increased slightly. When instead Yb^{3+} ions were added to form $Gd_{1.98-x}O_3:Er_{0.02},Yb_{x=0.03}$ the UC intensity of the red emission became six times higher than the green emission, as a result of the efficient transfer of energy from the Yb^{3+} sensitizer to the Er^{3+} which is called sensitized energy transfer UC [29]. UC emission of the $Gd_{1.977-x}O_3:Bi_{0.003},Er_{0.02},Yb_{x=0.03}$ was relatively enhanced in both the red and green regions. In general, the absorption of the lanthanide ions doped materials can be enhanced by increasing the doping concentration. However, a significant enhancement of the emission intensities of Er^{3+} ions was observed after Bi^{3+} and Yb^{3+} were doped. The improvement in the UC emission after Bi^{3+} doping was perhaps caused by the modification of the local crystal field around the Er^{3+}. Substitution of Bi^{3+} for Gd^{3+} can modify the crystal field in the lattice and enhances the radiative transition rate in favor of enhancing the UC emission intensity. The improvement in the UC emission after Yb^{3+} doping might be attributed to ET between Yb^{3+} and Er^{3+} ions. The presence of Yb^{3+} ions contributes significantly to the population of the states responsible for the emission in this region due to the increase of nonradiative mechanisms [30]. Although, the multi-phonon relaxation can neutralize the population of intermediate and emitting levels and thus determine the efficiency of the conversion process.

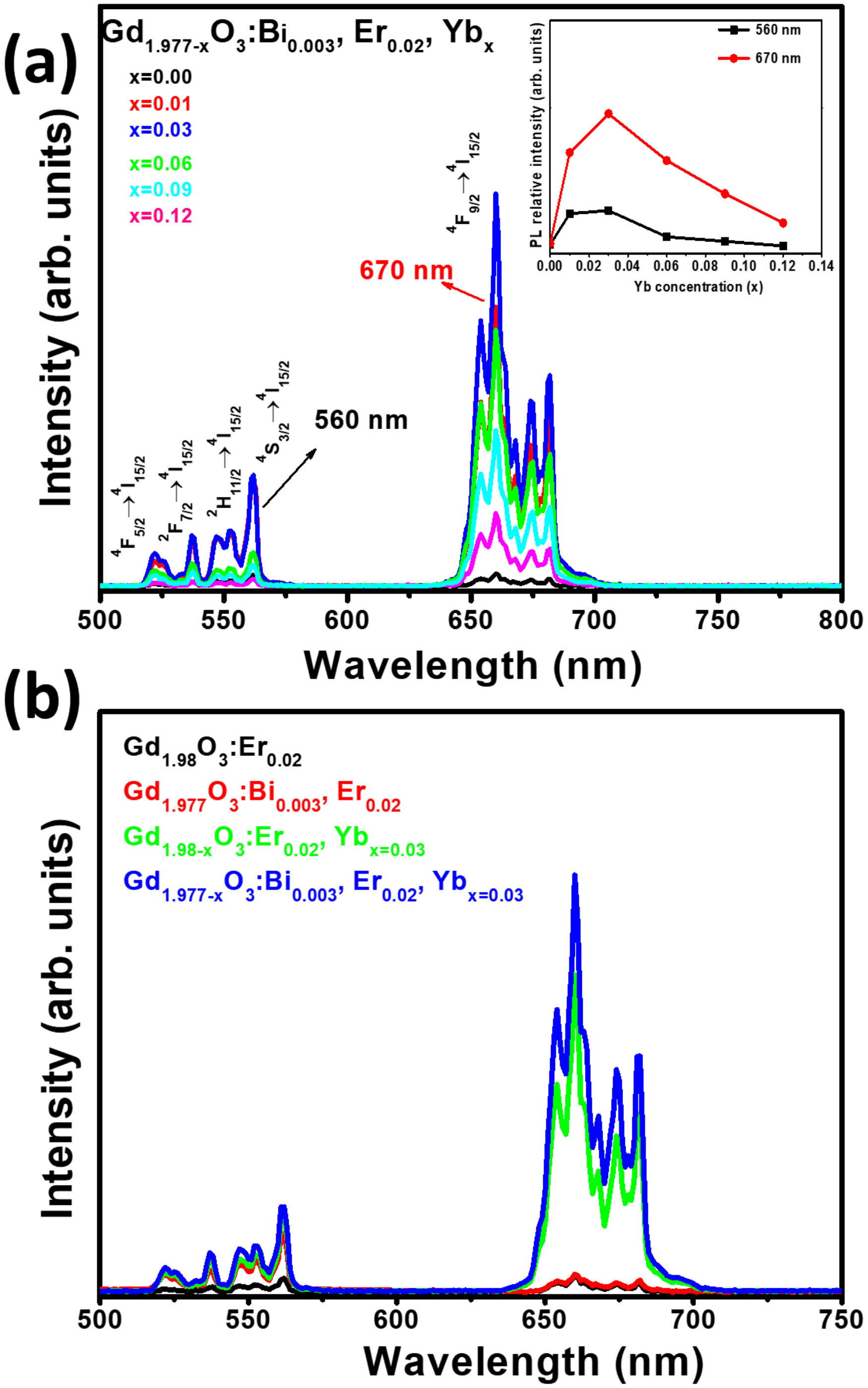

Figure 7.6: (a) The UC visible emission spectra of $Gd_{1.977-x}O_3$:$Bi_{0.003}$,$Er_{0.02}$,Yb_x for different Yb^{3+} concentration under 980 nm infrared excitation. The inset shows the variation of the 560 and 670 nm emission PL intensity as a function of Yb^{3+} concentration. (b) The UC visible emission spectra of $Gd_{1.98}O_3$:$Er_{0.02}$, $Gd_{1.977}O_3$:$Bi_{0.003}$,$Er_{0.02}$, $Gd_{1.98-x}O_3$:$Er_{0.02}$,$Yb_{x=0.03}$ and $Gd_{1.977-x}O_3$:$Bi_{0.003}$,$Er_{0.02}$,$Yb_{x=0.03}$.

In order to understand and explain the mechanism behind the UC emission, figure 7.7 shows the schematic energy level diagram of Er^{3+} and Yb^{3+} in the $Gd_{1.98-x}O_3$: $Er_{0.02}$,$Yb_{x=0.03}$ matrix. At a 980 nm pump photon wavelength the electrons in the Yb^{3+} ions are promoted from their ground state ($^2F_{7/2}$) to the excited state ($^2F_{5/2}$) due to a large absorption cross-section (~ 11.2×10^{-21} cm^2) for this wavelength [28]. The excited Yb^{3+} ions transfer their energy to Er^{3+} ions, promoting them to the $^4I_{11/2}$ level. The energy transfer procedure dominates the ground state absorption process in terms of exciting Er^{3+} ions because of the much larger absorption cross-section of Yb^{3+} ions compared to Er^{3+} ions. The Er^{3+} ions in the $^4I_{11/2}$ state may relax to the lower $^4I_{13/2}$ level. Electrons in either the $^4I_{11/2}$ or $^4I_{13/2}$ states may again receive energy via transfer from another excited Yb^{3+} ion and be up-converted to the $^4F_{7/2}$ and $^4F_{9/2}$ energy levels, respectively. It is worth mentioning the doping of Bi^{3+} ions did not have an obvious effect on the characteristics of the emission peaks in terms of position and the shape of the emission peaks of the Er^{3+} ions upon excitation by 980 nm [31]. The population in the $^4F_{7/2}$ state may relax nonradiatively to the $^2H_{11/2}$ and $^4S_{3/2}$ levels, while radiative emission can occur from any of these levels to the ground state $^4I_{15/2}$ by emitting a green photon around 520 nm, 550 and 560 nm, respectively. Electrons occupying the $^4F_{9/2}$ level may relax radiatively to the ground state $^4I_{15/2}$, giving red emissions centered around 670 nm. These emission transitions are efficiently enhanced by ET from the Yb^{3+} ions to different excited states of the Er^{3+} ions since the absorption cross-section of Yb^{3+} is stronger than that of Er^{3+} when excited at 980 nm [32].

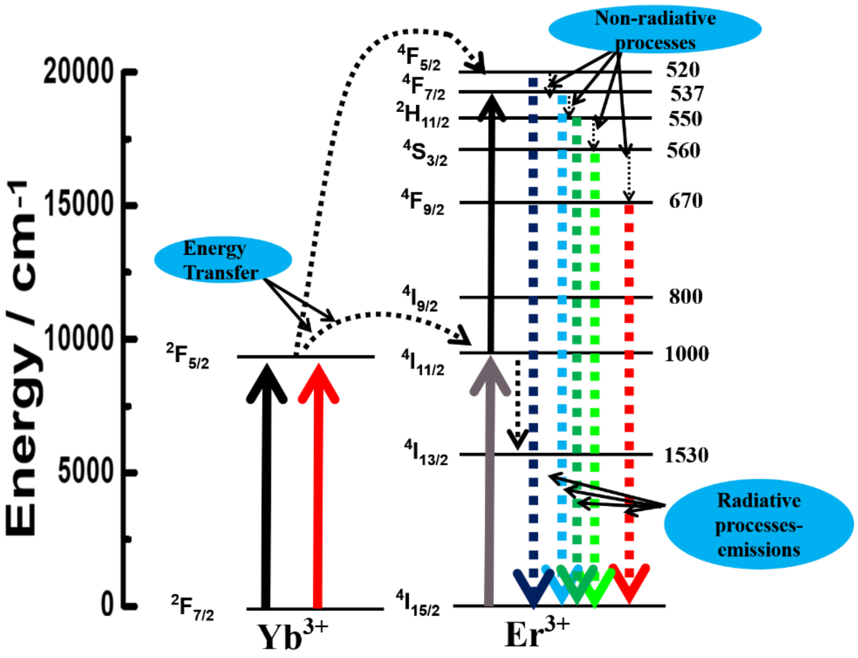

Figure 7.7: Schematic energy level diagram upon excitation energy (980 nm, up arrow), proposed the possible UC processes for the green and red mechanism of $Gd_{1.98-x}O_3$: $Er_{0.02}$,$Yb_{x=0.03}$ phosphors.

The study of the luminescence properties of the Bi^{3+} ions in Gd_2O_3 has been the focus of a previous study [15], in which it was confirmed that the activity levels of the ions are from two specific sites of the host, named C_2 and S_6. Moreover, in our measurements here we used the same excitation values as before to investigate the effect of the Yb^{3+} concentration on the emission of the $Gd_{1.977-x}O_3$:$Bi_{0.003}$,$Er_{0.02}$,Yb_x phosphors. The ultraviolet excitation and visible emission are illustrated in figure 7.8. The emission spectra are shown in Figure 7.8(a) upon excitation at 375 nm in the range from the blue extending into the red region in the 400−700 nm range centred at 418 nm. The strong emission band at 418 nm is corresponding to the $^3P_1 \rightarrow {}^1S_0$ transition of the Bi^{3+} ion at the S_6 site as reported previously [15]. The strong broad excitation spectra centered at 375 nm is due to the $^1S_0 \rightarrow {}^3P_1$ transitions of the Bi^{3+} ions. The PL intensity at 418 nm decreased monotonically with increasing the Yb^{3+} concentration, as shown by the inset. The decrease in intensity might be due to the energy transfer from the Bi^{3+} ions to the neighboring Yb^{3+} ions at the 375 nm wide excitation range. Lee *et al.* [33] reported that the visible emission PL spectrum of Y_2O_3:Bi^{3+},Yb^{3+} when monitored by visible excitation, has been quenched with an increase in Yb^{3+} ion concentration due to the ET from the Bi^{3+} to the Yb^{3+} ions. Also, Sawla *et al.* [34] reported that the visible emission of $Y_{2.99-x}Al_5O_{12}$: $Bi_{0.01}$,Yb_x when excited by UV decreased with increasing Yb^{3+} concentration. The emission spectra also include a series of narrow emission peaks for Er^{3+} ions in the 450−700 nm range, corresponding to the transitions $^3H_{9/2}\rightarrow{}^4I_{15/2}$ (blue emission) $^2P_{9/2}$, $^2F_{7/2}$, $^2H_{11/2}$ and $^2S_{9/2}\rightarrow{}^4I_{15/2}$ (green-yellow emission) and $^4F_{9/2} \rightarrow {}^4I_{15/2}$ (red emission). To better understand the effect of the Yb^{3+} ions on these emissions, the excitation and emission spectra were monitored at 560 and 379 nm in the same range, which are correlated with excitation and emission occurring by transitions of the Er^{3+} ion, as are shown in Figure 7.8(b). The emission spectra of Er^{3+} monitored for 379 nm excitation exhibited quenching in the intensity of Er^{3+} peaks with an increase of the Yb^{3+} concentration, which indicates energy transfers from Er^{3+} to Yb^{3+} by cross-relaxation. There is a high probability that an energy transfer process can occur between the Er^{3+} and Yb^{3+} ions, which is responsible for the improvement of the UC emission. This may be the reason for the reduction of the visible emission intensity. On the contrary, the UC emission intensity of the $^4F_{9/2} \rightarrow {}^4I_{15/2}$ transition of Er^{3+} previously was enhanced with an increasing Yb^{3+} concentration, indicating a different mode of energy transfer in this case.

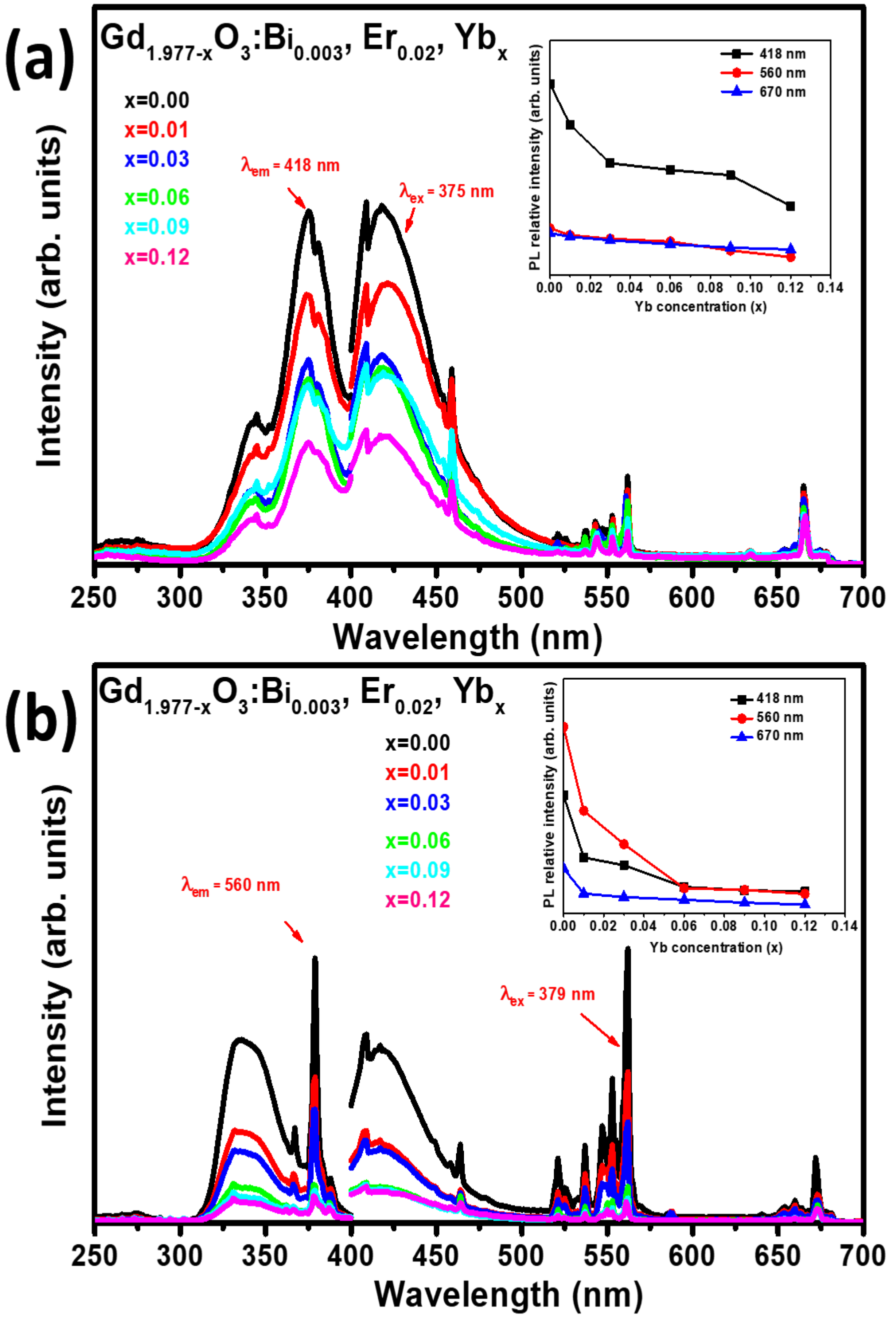

Figure 7.8: PL excitation and emission spectra of $Gd_{1.977-x}O_3$:$Bi_{0.003}$,$Er_{0.02}$,Yb_x powder (a) excitation and emission spectra monitored at 418 and 375 nm. (b) The excitation and emission spectra monitored at 560 and 379 nm.

To determine the effect of Bi^{3+} on the excitation and emission of Er^{3+} into the host matrix, two samples were prepared, one with and the other without Bi^{3+} as shown in figure 7.9. The PL emission from the $Gd_{1.977}O_3$:$Bi_{0.003}$,$Er_{0.02}$ was evaluated under 379 nm excitation as shown in Figure 7.9(a), which was also the wavelengths of an absorption band noted earlier for the Er^{3+}. A blue emission with a single broad peak at about 418 nm was observed due to the Bi^{3+} transitions with a narrow emission series extending from blue at 408 to 690 nm. On Figure 7.9(b) for the sample $Gd_{1.98}O_3$:$Er_{0.02}$, under the same excitation at 379 nm, all PL emission peaks were narrow with a series from 400-700 nm with maxima at 409, 465, 520, 537, 550, 560 and 670 nm corresponding to transitions of the Er^{3+} ion levels, which are clearly shown in the energy diagram of Figure 7.10. Monitoring the excitation at 560 nm of the Er^{3+} emission the excitation peaks located at 366 and 379 nm are corresponding to the $^4I_{15/2} \rightarrow {}^4G_{9/2}$ and $^4I_{15/2} \rightarrow {}^4G_{11/2}$ transitions of the Er^{3+}, while monitoring the 670 nm emission revealed an excitation only at 379 nm.

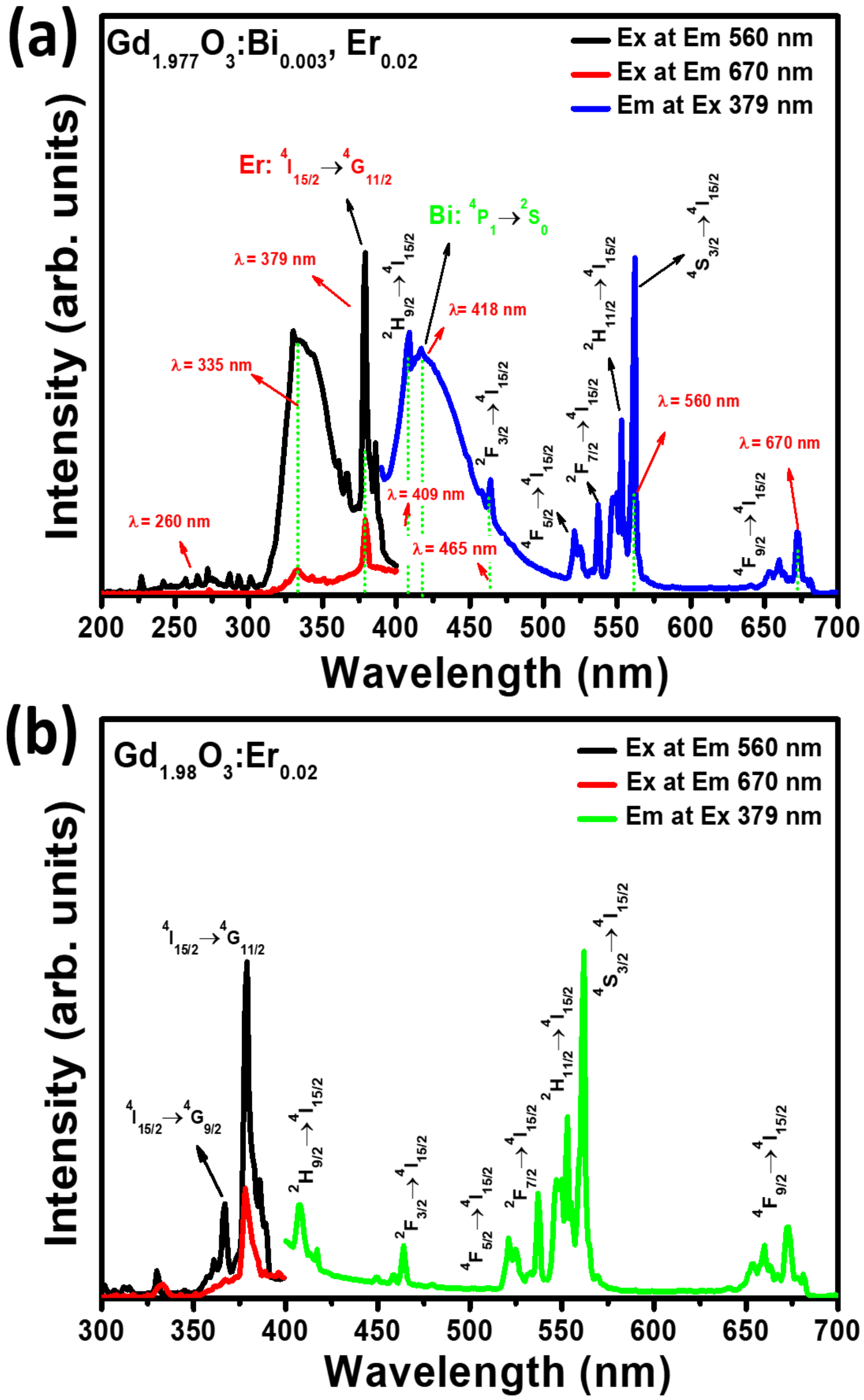

Figure 7.9: PL excitation and emission spectra of (a) $Gd_{1.977}O_3$:$Bi_{0.003}$,$Er_{0.02}$ (b) $Gd_{1.98}O_3$:$Er_{0.02}$.

Figure 7.10 displays a schematic energy level diagram of Bi^{3+}, Er^{3+} doped Gd_2O_3. The excitation peaks of Bi^{3+} can occur for transitions from $^1S_0$ to $^3P_1$, $^3P_2$ and $^1P_1$ which are usually denoted as A, B and C, respectively [35]. In the case of the presence of the Bi^{3+} ion, when pumping the photon by 375 nm (see Figure 7.8(a)), the emission band at 418 nm can be assigned to the transition $^3E_u \rightarrow {}^1A_g$ of Bi^{3+} at the S_6 site. Thus, the excitation bands of the blue emission centered at 260 and 375 nm can be assigned to the transitions $^1A_g \rightarrow {}^3A_u$ and $^1A_g \rightarrow {}^3E_u$ of the Bi^{3+} ion at the S_6 site. As we reported previously [15] the excitation band at 335 nm was due to the $^3A \rightarrow {}^1A$ transition of Bi^{3+} at the C_2 site. The excitation band of Bi^{3+} at the S_6 at 375 nm is close to the excitation band $^4I_{15/2} \rightarrow {}^4G_{11/2}$ of Er^{3+}, which causes some overlap in the excitation band of Bi^{3+} and the excitation band of the Er^{3+} ion, which makes the energy exchange between them possible, and thus the excitation of the Er^{3+} ion can occur at 379 nm as presented in Figure 7.9(a). Upon excitation at 379 nm the Er^{3+} ions are excited directly to the $^4G_{11/2}$ state through the ground state. The population in the $^4G_{7/2}$ states relaxes nonradiative to the $^2H_{9/2}$ and then to the ground state $^4I_{15/2}$ by emitting a blue photon around 409 nm. There were more non-radiative relaxation populations from $^2H_{9/2}$ to the lower levels with 4f-4f emissions (in the green-yellow region) which are corresponding with: $^4F_{3/2} \rightarrow {}^4I_{15/2}$ at 465 nm, $^4F_{5/2} \rightarrow {}^4I_{15/2}$ at 520 nm, $^4F_{9/2} \rightarrow {}^4I_{15/2}$ at 537 nm, $^2H_{11/2} \rightarrow {}^4I_{15/2}$ at 550 nm and $^4S_{3/2} \rightarrow {}^4I_{15/2}$ at 560 nm. The last recombination from the $^4F_{9/2}$ level to the ground state $^4I_{15/2}$ emitting a red photon at 670 nm.

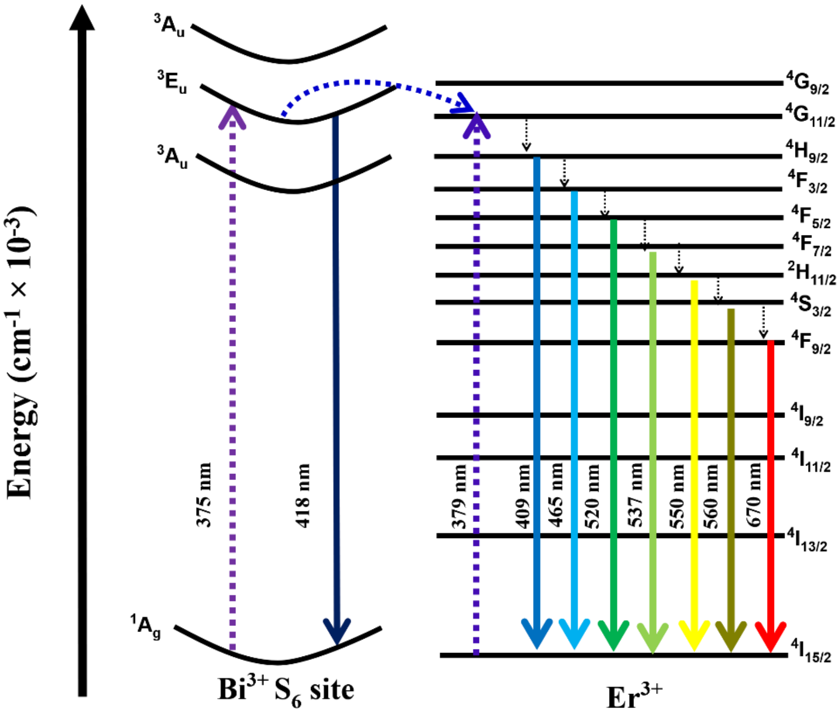

Figure 7.10: Schematic energy level diagram of $Gd_{1.977}O_3$:$Bi_{0.003}$,$Er_{0.02}$.

The Commission Internationale de l’Eclairage (CIE) chromaticity diagram [36] was used to explore the colour of the $Gd_{1.98}O_3:Er_{0.02}$, $Gd_{1.977}O_3:Bi_{0.003},Er_{0.02}$ and $Gd_{1.977-x}O_3:Bi_{0.003},Er_{0.02},Yb_{x=0.03}$ samples as shown in figure 7.11. The color coordinate for sample doped only with Er^{3+} ions is situated in the blue-green region under the 379 nm excitation wavelength. This is in contrast to the co-doped sample with Er^{3+} and Bi^{3+} ions which emitted in the blue region. The addition of Yb^{3+} ions did not alter the emission colour.

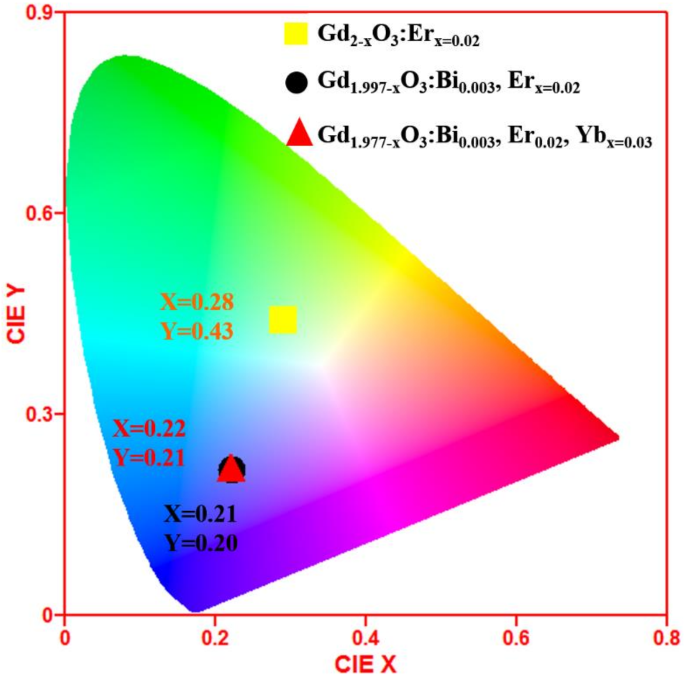

Figure 7.11: The calculated chromaticity coordinates for the emission for the $Gd_{1.98}O_3:Er_{0.02}$, $Gd_{1.977-x}O_3:Bi_{0.003},Er_{0.02}$, and $Gd_{1.977-x}O_3:Bi_{0.003},Er_{0.02},Yb_{x=0.03}$ samples.

7.3.5 Cathodoluminescence properties

The CL spectra of the $Gd_{1.977-x}O_3:Bi_{0.003},Er_{0.02},Yb_x$ powder samples were excited using an electron energy of 5 keV in a vacuum of the order of 10^{-5}–10^{-6} Torr as illustrated in figure 7.12. The CL spectra are located in the wide emission range from 300 to 800 nm, consisting of three main emission bands in the visible region. The blue emission centered at 418 nm, branched green-yellow emission bands in the range from 500 to 680 nm centered at 560 nm, and a weakly branched red band in the range from 640 to 700 nm centered at 670 nm. The blue emission centered at 418 nm is due to the $^3P_1 \rightarrow {}^1S_0$ transitions of the Bi^{3+} ions. As reported in [30] the blue emissions at 418 nm of Bi-doped Gd_2O_3 phosphors under electron energy of 5 keV were ascribed to Bi^{3+} under S_6 symmetry. The green-yellow emission bands in the range from 500 to 680 nm correspond to transitions of the Er^{3+} ions. As mentioned earlier those emission bands are attributed to $^4F_{5/2}$, $^4F_{7/2}$, $^2H_{11/2}$, $^4S_{3/2}$ and $^4F_{9/2}$ level transitions to $^4I_{15/2}$ of the Er^{3+} ions, respectively. Boruc *et al.* [37] reported that for Gd_2O_3:Bi,Er powder under excitation under an ion beam, the emission contained a series of narrow lines in the green region and was attributed to transitions of Er^{3+} ions. There was also a broad blue-violet band due to transitions of the Bi^{3+} ions. Doping with Yb^{3+} and the increase in Yb^{3+} concentration did not affect the positions or shape of the CL emission peaks, implying that the emission comes only from Bi^{3+} and Er^{3+} ions. The inset in Figure 7.12 displays the variation of the CL peak intensity as a function of Yb^{3+} doping concentration and the un-doped Yb^{3+} sample had the highest CL intensity. The decrease in the CL intensity when Yb^{3+} was added may be due to the energy transfer from the Bi^{3+} and Er^{3+} ions to the Yb^{3+} ions. In addition, it is known that the nature of the Bi^{3+} emission in different systems is greatly influenced by the surrounding bonds and the effect of the co-doping concentration [39]. Therefore, the intensity of the Bi^{3+} emissions may be due the presence of Yb^{3+} and some defects which were generated during doping or during the electron beam irradiation.

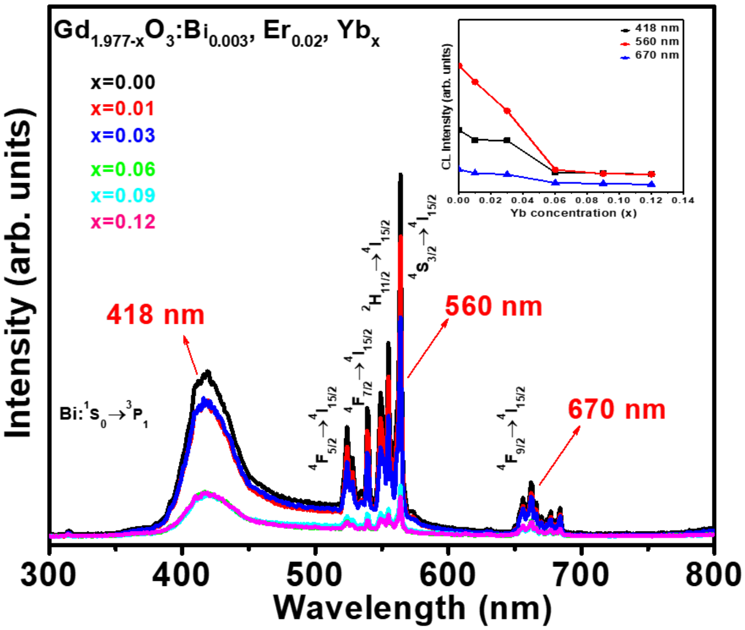

Figure 7.12: CL spectra of the $Gd_{1.977-x}O_3$:$Bi_{0.003}$,$Er_{0.02}$,Yb_x powder. The inset displays the CL peak intensity as a function of Yb^{3+} doping concentration.

7.4 Conclusion

The visible light emission of $Bi^{3+}/Er^{3+}/xYb^{3+}$ tri-doped Gd_2O_3 phosphor powders was successfully studied. The XRD results showed all the samples had the single cubic crystal structure phase. The average crystallite size of the nanoparticles decreased with an increase in the Yb^{3+} doping concentration. Using the EDS technique, the presence of the main elements of Gd_2O_3 and the dopants Er^{3+} and Yb^{3+} were confirmed, but there was no Bi^{3+} detected due to its low concentration. The DR spectra for the undoped sample showed two absorbance bands located around 275 and 315 nm which were attributed to the 4f-4f optical transitions of Gd^{3+}. In the doped samples three bands located around 260, 335 and 375 nm were observed due to the excitation transitions of Bi^{3+} ions into the different sites (C_2 and S_6). There were peaks in the range 500-820 that were observed that correspond to the optical transitions in Er^{3+} ions, while the broad absorption band at 880-1050 nm was due to the transition of the Yb^{3+} ion. The optical properties and the effect of Yb^{3+} concentration on the $Gd_{1.977-x}O_3$:$Bi_{0.003}$,$Er_{0.02}$,Yb_x samples were evaluated in the visible region. The phosphor emits in the green and a strong red upconverted emission band upon 980 nm excitation. For the sample $Gd_{1.98}O_3$:$Er_{0.02}$ the UC intensity of the green and red emission was approximately the same, but after co-doping with Bi^{3+} the UC green emission was strongly enhanced. The UC red emission intensity was enhanced many times higher in the presence of an optimum concentration of the Yb^{3+} ions. The upconversion mechanisms of the 520, 537, 550, 560 and 670 nm peaks are ascribed to $^4F_{5/2}$, $^4F_{7/2}$, $^2H_{11/2}$, $^4S_{3/2}$ and $^4F_{9/2}$ levels to the ground state $^4I_{15/2}$ transitions of the Er^{3+} ions, respectively. The intensity for both the visible emission spectra of the Er^{3+} monitored for 379 nm excitation and CL at 5 keV, exhibited a reduction in the intensity of the Er^{3+} peaks with an increase of Yb^{3+} concentration due to the energy transfers from Er^{3+} to Yb^{3+} by cross-relaxation. These results demonstrated the ability of the phosphor powders to be utilized as a luminescence layer to enhance the efficiency of silicon solar cells via spectral modification using UC processes.

References

[1] Y. Tai, G. Zheng, H. Wang, J. Bai. Broadband down-conversion based near infrared quantum cutting in Eu^{2+}–Yb^{3+} co-doped $SrAl_2O_4$ for crystalline silicon solar cells. *Journal of Solid State Chemistry,* **226** (2015) 250–254. doi:10.1016/j.jssc.2015.02.020.

[2] W. G. J. H. M. van Sark, A. Meijerink, R. E. I. Schropp, J. A. M. van Roosmalen. E. H. Lysen. Enhancing solar cell efficiency by using spectral converters. *Solar Energy Materials & Solar Cells,* **87(1-4)** (2005) 395–409. doi:10.1016/j.solmat.2004.07.055.

[3] M. Bryan van der Ende, L. Aarts, A. Meijerink. Lanthanide ions as spectral converters for solar cells. *Physical Chemistry Chemical Physics,* **11(47)** (2009) 11081–11095. doi:10.1039/B913877C.

[4] Y. Wang, C. Xu, C. Zheng, X. Wang, X. Wang, L. Gong, L. Sun. Ho^{3+}/Yb^{3+} codoped Vernier phase $Y_7O_6F_9$ powders with efficient near-infrared quantum cutting, intense upconversion and downshifting from visible to mid-infrared. *Infrared Physics & Technology,* **104** (2019) 304180-3041809. doi:10.1016/j.infrared.2019.103004.

[5] W. Xu, X. Gao, L. Zheng, P. Wang, Z. Zhang, W. Cao. Optical Thermometry through Green Upconversion Emissions in Er^{3+}/Yb^{3+}-Co-doped $CaWO_4$ Phosphor. *Applied Physics Express,* **5(7)** (2012) 072201–072203. doi:10.1143/apex.5.072201.

[6] X. Y. Huang and Q. Y. Zhang. Near-infrared quantum cutting via cooperative energy transfer in Gd_2O_3:Bi^{3+},Yb^{3+} phosphors. *Applied Physics,* **107(6)** (2010) 0635050-0635054. doi:10.1063/1.3354063

[7] G. Ju, Y. Hu, L. Chen, X. Wang, Z. Mu, H. Wu, F. Kang. Luminescence properties of Y_2O_3:Bi^{3+}, Ln^{3+} (Ln=Sm, Eu, Dy, Er, Ho) and the sensitization of Ln^{3+} by Bi^{3+}. *Journal of Luminescence,* **132(8)** (2012) 1853–1859. doi:10.1016/j.jlumin.2012.03.020.

[8] L. A. Rocha, S. J. L. Ribeiro, A. C. Pereira, M. A. Schiavon, J. L. Ferrari. Upconversion and infrared emission of Er^{3+}/Yb^{3+} co-doped SiO_2-Gd_2O_3 obtained by sol-gel process. *Processing and Application of Ceramics,* **9(1)** (2015) 23–31. doi: 10.2298/PAC1501023R.

[9] Y. Zou, L. Tang, J.-L. Cai, L.-T. Lin, L.-W. Cao and J.-X. Meng. Combustion synthesis and luminescence of monoclinic Gd_2O_3:Bi phosphors. *Journal of Luminescence,* **153** (2014) 210–214. doi:10.1016/j.jlumin.2014.03.026.

[10] Q. B. Li, J. M. Lin, J. H. Wu, Z. Lan, J. L. Wang, Y. wang, F. G. Peng, M. L. Huang, Y. M. Xiao. Preparation of Gd_2O_3:Eu^{3+} downconversion luminescent material and its application in dye-sensitized solar cells. *Chinese Science Bulletin,* **56(28-29)** (2011) 3114–3118. doi:10.1007/s11434-011-4664-z.

[11] I. Kamińska, A. Wosztyl, P. Kowalik, B. Sikora, T. Wojciechowski, K. Sobczak, R. Minikayev, K. Zajdel, M. Chojnacki, W. Zaleszczyk, K. Łysiak, W. Paszkowicz, J. Szczytko, M. Baniewicz, W. Stryczniewicz and K. Fronc. Synthesis and characterization of Gd_2O_3:Er^{3+}, Yb^{3+} doped with Mg^{2+}, Li^+ ions—effect on the photoluminescence and biological applications. *Nanotechnology,* **32(24)** (2021) 245705-2467013. doi:10.1088/1361-6528/abed02.

[12] R. S. Yadav, Dinesh Kumar, A. K. Singh, Ekta Raia and S. B. Rai. Effect of Bi^{3+} ion on upconversion-based induced optical heating and temperature sensing characteristics in the Er^{3+}/Yb^{3+} co-doped La_2O_3 nano-phosphor. *The Royal Society of Chemistry,* **8** (2018) 34699–34711. doi:10.1039/c8ra07438k.

[13] J. Xue, X. Wang, J. H. Jeong, X. Yan. Spectrum and Energy transfer in Bi^{3+}–Re^{n+} (n = 2, 3, 4) co-doped phosphors studies for extended optical applications. *Physical Chemistry Chemical Physics,* **20** (2018) 11516-11541. doi:10.1039/C8CP00433A.

[14] A. K. Choudhary, A. Dwivedi, A. Bahadur, T. P. Yadav, S.B. Rai. Enhanced upconversion emission and temperature sensor sensitivity in presence of Bi^{3+} ions in Er^{3+} /Yb^{3+} co-doped $MgAl_2O_4$ phosphor. *Ceramics International,* **44(8)** (2018) 9633-9642. doi:10.1016/j.ceramint.2018.02.190.

[15] M. H. M. Abdelrehman, R. E. Kroon, A. Yousif, H. A. A. Seed Ahmed and H. C. Swart. Photoluminescence, thermoluminescence, and cathodoluminescence of optimized cubic Gd_2O_3:Bi phosphor powder. *Vacuum Science & Technology A,* **38** (2020) 063207 (15 pages). doi:10.1116/6.0000567.

[16] Marlene C. Morris, Howard F. McMurdie, Eloise H. Evans, Boris Paretzkin, Harry S. Parker, Winnie Wong-Ng, and Donna M. Gladhill. Standard X-ray Diffraction Powder Patterns Section 21 — Data for 92 Substances. International Centre for Diffraction Data 1601 Park Lane Swarthmore, (1985) 8-148. doi:10.6028/NBS.MONO.25-21.

[17] R. D. Shannon, Revised Effective Ionic Radii and Systematic Studies of Interatomic Distances in Halides and Chalcogenides. *Acta Crystallographica Section A,* **32** (1976) 751-767. doi: 10.1107/s0567739476001551.

[18] Y. Prabhu, K. Rao, V. Kumar and B. Kumari. X-Ray Analysis by Williamson-Hall and Size-Strain Plot Methods of ZnO Nanoparticles with Fuel Variation. *World Journal of Nano Science and Engineering,* **4** (2014) 21-28. doi:10.4236/wjnse.2014.41004.

[19] S. Kumar, H. Tripathi, J.D. Sharma, U. Batra. Structural, morphological and opto-electrical properties of $Y_{2-x}Yb_xO_3$ nanoparticles synthesized using co-precipitation method. *International Journal of Applied Ceramic Technology,* **18** (2021). 12-23. doi:10.1111/ijac.13603.

[20] P. Khajuriaa, A.K. Bedyala, M. Manhasa, H.C. Swart, F. Duranic, V. Kumara. Spectral, surface and thermometric investigations of upconverting Er^{3+}/Yb^{3+} co-doped $Na_3Y(PO_4)_2$ phosphor. *Alloys and Compounds,* **877** (2021) 160327-160338. doi:10.1016/j.jallcom.2021.160327.

[21] P. Ju, P. Wang, B. Li, H. Fan, S. Ai, D. Zhang and Y. Wang. A novel calcined $Bi_2WO_6/BiVO_4$ heterojunction photocatalyst with highly enhanced photocatalytic activity. *Chemical Engineering Journal,* **236** (2014) 430–437. doi:10.1016/j.cej.2013.10.001.

[22] M. C. Ferrara, D. Altamura, M. Schioppa, L. Tapfer, E. Nichelatti, L. Pilloni and M. Montecchi. Growth, characterization and optical properties of nanocrystalline gadolinia thin films prepared by sol–gel dip coating. *Journal of Physics D: Applied Physics,* **41(22)** (2008) 2254080-2254089. doi:10.1088/0022-3727/41/22/225408.

[23] Y. A. Kuznetsova and A. F. Zatsepin. Optical properties and energy parameters of Gd_2O_3 and Gd_2O_3:Er nanoparticles. *Journal of Physics: Conference Series,* **917** (2017) 062001-062005. doi: 10.1088/1742-6596/917/6/062001.

[24] Y. Zou, J. -L. Cai, L. -T. Lin, L. Tang and J. -X. Meng. Combustion Preparation and Near-infrared Phosphors of Gd_2O_3:Bi^{3+},Nd^{3+}. *Chinese Journal of Luminescence,* **35(5)** (2014) 531-535. doi: 10.3788/fgxb20143505.0531.

[25] D. Jia, L. Liu, and W. M. Yen. Erbium energy levels relative to the band gap of gadolinium oxide. *Optics Communications,* **212(1-3)** (2002) 97–100. doi: 10.1016/S0030-4018(02)01999-5.

[26] A. Maurya, R. S. Yadav, R. V. Yadav, A. Bahadur and S. B. Rai. Enhanced green upconversion photoluminescence from Ho^{3+}/ Yb^{3+} co-doped $CaZrO_3$ phosphor via Mg^{2+} doping. *Royal Society of Chemistry,* **6(114)** (2016) 113469–113477. doi: 10.1039/C6RA23835A.

[27] X. Pang, Y. Zhang, L. Ding, Z. Su, W. F. Zhang. Upconversion Luminescence Properties of Er^{3+}–Bi^{3+} Codoped $CaSnO_3$ Nanocrystals with Perovskite Structure. *Nanoscience and Nanotechnology,* **10(3)** (2010) 1860–1864. doi: 10.1166/jnn.2010.2135.

[28] F. Huang, Y. Gao, J. Zhou, J. Xu, Y. Wang. Yb^{3+}/Er^{3+} co-doped $CaMoO_4$: a promising green upconversion phosphor for optical temperature sensing. *Alloys and Compounds,* **639** (2015) 325–329. doi:10.1016/j.jallcom.2015.02.228.

[29] B. Huang, M. Sun, A. W. Dougherty, H. Dong, Y. Xu, L. Sun, C. Yan. Unravelling the energy transfer of Er^{3+}-self-sensitized upconversion in Er^{3+}–Yb^{3+}–Er^{3+} clustered core@shell nanoparticles. *Nanoscale,* **9** (2017) 18490-18497. doi:10.1039/C7NR06729A.

[30] Z. Wang, A. Meijerink. Concentration Quenching in Upconversion Nanocrystals. *Physical Chemistry, C* **122** (2018) 26298−26306. doi:10.1021/acs.jpcc.8b09371.

[31] R. Luo, L. Chen, Q. Li, J. Zhou, L. Mei, Z. Ning, Y. Zhao, M. Liu, X. Lai, J. Bi, W. Yin and D. Gao. Bi^{3+}-Doped $BaYF_5$:Yb,Er Upconversion Nanoparticles with Enhanced Luminescence and Application Case for X-ray Computed Tomography Imaging. *Inorganic Chemistry,* **59(24)** (2020) 17906-17915. doi:10.1021/acs.inorgchem.0c01818.

[32] D. K. Mohanty, V.K. Rai, Y. Dwivedi, Y. Dwivedi and S. B. Rai. Enhancement of upconversion intensity in Er^{3+} doped tellurite glass in presence of Yb^{3+}. *Applied Physics B,* **104** (2011) 233–236. doi.org/10.1007/s00340-011-4422-6.

[33] E. Lee, R. E. Kroon, J. J. Terblans, H. C. Swart. Luminescence properties of Y_2O_3:Bi^{3+},Yb^{3+} co-doped phosphor for application in solar cells. *Physica B: Condensed Matter,* **(535)** (2017) 102-105. doi:10.1016/j.physb.2017.06.072.

[34] N. S. Sawala, S. K. Omanwar. Near-infrared DC approach by Bi^{3+}–Yb^{3+}co-doped YAG phosphor. *Research on Chemical Intermediates,* **43(2)** (2017) 693–702. doi:10.1007/s11164-016-2646-0.

[35] H. Fukada, K. Ueda, J. Ishino, T. Miyata and T. Minami. Blue PL and EL emissions from Bi-activated binary oxide thin-film phosphors. *Thin Solid Films,* **518(11**) (2010) 3067–3070. doi:10.1016/j.tsf.2009.08.014.

[36] A. D. Broadbent. A critical review of the development of the CIE1931 RGB color-matching functions. *Color Research & Application,* **29(4)** (2004) 267–272. doi:10.1002/col.20020.

[37] Z. Boruc, G. Gawlik, B. Fetliński, M. Kaczkan, M. Malinowski. Temperature dependence of Er^{3+} ionoluminescence and photoluminescence in Gd_2O_3:Bi nanopowder. *Review of Scientific Instruments,* **85(6)** (2014) 064901–064906. doi:10.1063/1.4880456.

[38] A. Yousif, R. M. Jafer, S. Som, M. M. Duvenhage, E. Coetsee, H. C. Swart, Ultrabroadband luminescent from a Bi-doped CaO matrix. *Royal society of chemistry advances,* **5 (67)** (2015) 54115–54122. doi.org/10.1039/c5ra09246a.

Chapter 8

Conclusions and future work

This chapter provides a summary of the general conclusion of the results obtained in this research study as well as some suggestions for future work that could be continued.

8.1 Summary

The work presented in this thesis discusses an analytical description of luminescence properties of Gd_2O_3:Bi^{3+} co-doped Ln^{3+} (namely Yb^{3+} and Er^{3+}) as powder and thin films phosphors for solar cell applications. The obtained phosphors showed good optical behavior for emissions of the Bi^{3+}-Yb^{3+}, Bi^{3+}-Er^{3+} and Bi^{3+}, Yb^{3+}-Er^{3+} systems with respect to down-conversion (DC) and up-conversion (UC) which are certainly excellent potential candidates for c-Si SC efficiency enhancement.

$Gd_{2-x}O_3$:Bi_x was successfully synthesized by using the solution combustion method with H_2CONH_2 as a fuel. The photoluminescence (PL), thermoluminescence (TL) and cathodoluminescence (CL) properties of Bi doped Gd_2O_3 powders were investigated for different doping concentrations and different annealing temperatures. All the powder phosphors exhibited the cubic phase structure of the Gd_2O_3. The powder morphology was strongly affected as a result of increasing the annealing temperature. From reflectance data of the pure host sample the bandgap of Gd_2O_3 was found to be 5.09 eV. The 4f-4f optical transitions of Gd^{3+} have been observed as well as the excitation transitions of Bi^{3+} ions. The luminescent properties of G_2O_3:Bi^{3+} phosphor revealed that the emissions are affected by different preparation parameters, such as Bi^{3+} concentration, the environment around Bi^{3+} ions and annealing temperatures. Both PL and CL results showed that the Bi^{3+} ion-doped Gd_2O_3 has two emission bands centred at 365 and 418 nm for blue emission and a third band centred at 505 nm for green emission, corresponding to the $^3P_1 \rightarrow ^1S_0$ transitions in the Bi^{3+} ion in two different sites (S_6 and C_2) of the Gd_2O_3 host matrix. The TL results indicated that the trap depth and frequency factors are reasonably good for Gd_2O_3:Bi under UV exposure and the high trap density peak may be suitable for dosimeter studies. The stability of the surface, chemical and luminescence properties of the highest luminescence intensity sample under electron beam irradiation was investigated and it was found to be very stable under electron beam irradiation for samples prepared in both the base vacuum and back-filled O_2 environments.

A ceramic pellet made of $Gd_{2-x}O_3$:$Bi_{x=0.003}$ powder was used for the growth of the thin films using the PLD technique in the presence of a base pressure and oxygen (O_2) gas on Si (100) substrates at different substrate temperatures. The background atmosphere and substrate temperature played a critical role in the film crystallinity, morphology and luminescence properties. The film deposited in vacuum exhibited an amorphous structure at the lower substrate temperature and then a strong preferential growth on the (211) and (222) planes of the cubic phase up to 200 °C. At higher temperatures of 350 and 500 °C, it changed to the orthorhombic phase of $Gd_2Si_2O_7$. The films deposited in O_2 showed that the crystallinity improved with an increase in the substrate temperature, changing from amorphous to a cubic structure. The thickness of the film was not appreciably affected by the substrate temperature, although the film thickness was slightly affected by the deposition atmosphere. PL revealed that the films fabricated in vacuum first have an enhancement in the PL emission intensities with an increasing substrate temperature, and then a reduction with the appearance of another peak at 700 nm at the highest substrate temperatures due to the formation of orthorhombic $Gd_2Si_2O_7$. The optimum deposition conditions for maximum PL emission intensity were found to be at the substrate temperature of 350 °C in an O_2 atmosphere. The CL degradation studies showed a different degradation behavior in the two atmospheres. The CL intensity reduced slightly during the degradation in vacuum in the beginning up to a dose of 15 C/cm^2 and subsequently a 10–20% slight increase during further electron bombardment, while in O_2 the CL intensity initially increased up to a dose of 90 C/cm^2 and then stabilized during further exposure. Gd_2O_3:Bi^{3+} thin film samples were more stable than the powders under the same experimental conditions. The results exhibited that the Gd_2O_3:Bi^{3+} phosphor material has a lot of possibilities to be used in co-doped systems as DC and UC material.

The $Gd_{1.997-y}O_3$:$Bi_{0.003}$, Yb_y phosphors were also investigated for DC applications for Si-SCs. While keeping the Bi^{3+} concentration constant the Yb^{3+} concentration was varied from (y = 0.005 to 0.03). The XRD showed that the Gd_2O_3:Bi^{3+},Yb^{3+} samples still remained in the single phase cubic structure of the host material. The Bi^{3+} was an efficient sensitizer to Yb^{3+} and by non-radiative transfer of energy the 4f-4f excitation of Yb^{3+} was increased under UV excitation of Bi^{3+}, resulting in good NIR emissions. The best sample that can be used as a DC material was at the highest concentration of the Yb^{3+} which has the highest intensity. The NIR-DC emission was significantly enhanced by doping with the Bi^{3+} ions compared with the sample doped by only Yb^{3+} ions.

The luminescence properties of $Gd_{1.997-z}O_3:Bi_{0.003}$ co-doped by Er_z phosphor powders were examined with different concentrations of Er^{3+} (z = 0.005, 0.01, 0.015, 0.02, 0.025 and 0.03) for UC processes. The samples exhibited multiple UC emission peaks in the green-orange-red region and other peaks in the NIR region that belong only to the 4f-4f transitions characteristic to the transitions of the Er^{3+} ions. A possible mechanism of energy transfer was studied. The PL emission intensity of the Er^{3+} ions was related to the difference in the concentration of the Er^{3+} ions in the various excitation states. The highest intensity sample of the green-orange UC emission, as well as CL emission, was found to be at the concentration of z = 0.015, while the highest intensity sample of UC red emission was found to be at the concentration at z = 0.025 of Er^{3+} ions. The Bi^{3+} enhances the visible UC emission as a result of the modification of the local crystal field around the Er^{3+} ion. According to previous PL investigations, the $Gd_2O_3:Bi^{3+}$ phosphor co-doped with Yb^{3+} and Er^{3+}, Bi^{3+} is a suitable candidate to be applied as a sensitizer with other Ln^{3+} ions.

An investigation was done on the suitability of the related energy levels among Bi^{3+}, Er^{3+} and Yb^{3+} ions doped in Gd_2O_3 powder for possible energy transfer and sensitization of the visible and NIR emissions for possible increased enhancement of UC emission of Er^{3+}. Bi^{3+} and Er^{3+}-Yb^{3+} ions were successfully incorporated into the Gd_2O_3 host material. The $Gd_{1.977-y}O_3:Bi_{0.003},Er_{0.02},Yb_y$ phosphor powder samples were prepared with varied Yb^{3+} concentration of (y = 0.0, 0.01, 0.03, 0.06, 0.09 and 0.12). The spectral conversion from 980 nm to 500-760 nm was achieved. The highest PL UC emission was recorded for the sample doped with a y = 0.03 concentration of Yb^{3+} after which quenching occurred. The emission intensity of the Er^{3+} ions was greatly enhanced in the co-doped systems. Furthermore, it was shown that despite the efficient energy conversion in the Bi^{3+}, Er^{3+} and Yb^{3+} system for enhancement of the UC emissions, the visible emission intensity monitored by using both UV and CL excitation exhibited a reduction with an increase in the Yb^{3+} concentration indicating a different mode of energy transfer in both cases. The results suggested that the Bi^{3+} ions are well suited to sensitize the Yb^{3+}-Er^{3+} couple in the current system and can be used as a solar spectral converter for the c-Si solar cells application.

In conclusion, the different studies in this thesis have in common that they are related to the question of whether the luminescent properties of the Bi^{3+} ion co-doped by Ln^{3+} ions in Gd_2O_3 can be used to improve the efficiency of SCs. It was found that doping Bi^{3+} is an effective and facile method to improve the DC and UC emission of the Ln^{3+} ions. Overall, Bi^{3+} in combination with a high concentration of Yb^{3+} appears to have a great potential for future DC applications as it strongly improves the NIR emission of Yb^{3+} by a cooperative ET process from Bi^{3+} to Yb^{3+}. On the other hand, there is no ET between Bi^{3+} and Er^{3+}, although the Bi^{3+} contributes to enhancing the visible UC emission of Er^{3+} especially in the green region that was strongly enhanced, due to the modification of the local crystal field around the Er^{3+} ion, which might be useful for other research interest. For a more efficient enhancement of the UC red emission, there was the incorporation of Yb^{3+} co-doped Bi^{3+}/Er^{3+} ions. The UC emission intensity was efficiently enhanced by ET from the Yb^{3+} ions for an optimum concentration of the Yb^{3+} ions. Thus from luminescence results it is suggested that the sample with a combination of Bi^{3+}/Er^{3+} and Yb^{3+} in the Gd_2O_3 matrix is the most suitable and best sample for UC applications.

8.2 Suggestions for future work

This work considered materials to be applied for spectral DC and UC layers to be coated on a solar cell. Some additional investigations need to be done.

1. The Yb^{3+} an Er^{3+} ions were successfully doped into the $Gd_2O_3:Bi^{3+}$ phosphor powder as possible candidates for DC and UC luminescent layers, but more detailed studies are needed for these phosphors in the form of thin films.
2. The UC emission of the Bi^{3+}/Er^{3+} co-doped Gd_2O_3 phosphor powder has been greatly enhanced by co-doping Yb^{3+} ions, but further investigations are needed of this phosphor in thin film forms before use in SCs applications.
3. From analysis, the stability of $Gd_2O_3:Bi$ powder was studied under electron beam irradiation. The luminescence properties of Yb^{3+} co-doping $Gd_2O_3:Bi^{3+},Er^{3+}$ phosphor powders must still be investigated during prolonged electron bombardment.
4. Investigation of other rare earth ions such as Tb^{3+}, Tm^{3+} and Ho^{3+} in $Gd_2O_3:Bi$ aiming at the Si-SC efficiency enhancement needs to be done.

5. Preparing thin films of the obtained phosphors to check their performance on Si-SC devices and to study the energy efficiencies.
6. The application of the thin film to a commercial solar cell and its effect on current, voltage, and power output to establish if the efficiency of the solar cell can be improved. Then, if efficiency improves, more studies need to be done to find ways to produce such thin films on a larger scale for potential commercial use.

Appendix

Publications

The following list of publications have brought about from this thesis. We gratefully acknowledge the assistance of the co-authors in preparing these publications:

[1] M. H. M. Abdelrehman, R. E. Kroon, A. Yousif, H. A. A. Seed Ahmed and H. C. Swart. Photoluminescence, thermoluminescence, and cathodoluminescence of optimized cubic Gd_2O_3:Bi phosphor powder. *Vacuum Science & Technology A.* **A 38,** (2020) 063207-15. https://doi.org/10.1116/6.0000567.

[2] M. H. M. Abdelrehman, R. E. Kroon, E. Coetsee, A. Yousif, H. A. A. Seed Ahmed and H. C. Swart. Photoluminescence, cathodoluminescence degradation and surface analysis of Gd_2O_3:Bi pulsed laser deposition thin films. *Physica B Condensed Matter*. **631** (2022) 413618 (14 pages). https://doi.org/10.1016/j.physb.2021.413618.

[3] M. H. M. Abdelrehman, R. E. Kroon, A. Yousif, H. A. A. Seed Ahmed and H. C. Swart. Luminescence properties of Yb^{3+} and Er^{3+} co-doped into Gd_2O_3:Bi phosphor powder, *Journal of Alloys and Compounds.* **908** (2022) 163856 (14 pages). https://doi.org/10.1016/j.jallcom.2022.163856.

[4] M. H. M. Abdelrehman, R. E. Kroon, A. Yousif, H. A. A. Seed Ahmed and H. C. Swart. Effect of Yb^{3+} on the luminescence of Bi^{3+}/Er^{3+} co-doped Gd_2O_3 phosphor powder. (In preparation, November 2021).